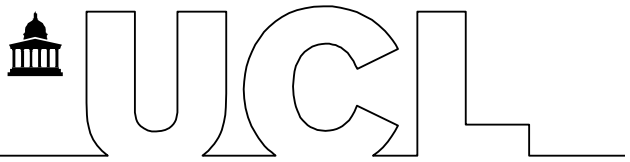

GNSS-Seismometry Integration for Rapid Far-Field Displacement Estimation

Chia-Yuan (Naomi) Li

Space Geodesy and Navigation Laboratory

Dept. of Civil, Environmental and Geomatic Engineering

University College London

A thesis submitted for the degree of

Doctor of Philosophy

July 2015

Declaration

I, *Chia-Yuan Li*, also known as *Naomi Li*, confirm that the work presented in this thesis is my own. Where information has been derived from other sources, I confirm that this has been indicated in the thesis.

……

Abstract

Accurate and rapid estimation of permanent surface displacement is required immediately after a slip event for earthquake monitoring or tsunami early warning. It is difficult to achieve the necessary accuracy at high- and low-frequencies using GNSS or seismometry alone, particularly where the sensor network has a low spatial resolution, such as in the third world or developing countries. Kalman filter algorithms with displacement and velocity states have been developed to combine GNSS and accelerometer observations to overcome the limitations of each other and to obtain the optimal displacement solutions. However, sawtooth-like phenomena caused by the bias or tilting of the sensor decrease the accuracy of the displacement estimates. In this study, a three-dimensional Kalman filter algorithm with an additional baseline error state has been developed. An experiment with both a GNSS receiver and a strong motion seismometer mounted on a movable steel plate on the platform and subjected to known displacements was carried out on the roof of the National Physical Laboratory. The results clearly show that the additional baseline error state enables the Kalman filter to estimate the instrument's sensor bias and tilt effects and correct the state estimates. Additional validation was conducted using data from the University of California, San Diego large outdoor shake table experiment. Finally, the proposed Kalman filter algorithm has been validated with data sets from the 2010 Mw 7.2 El Mayor-Cucapah Earthquake. The results indicate that the additional baseline error state cannot only eliminate the linear and quadratic drifts but also reduce the sawtooth-like effects from the displacement solutions. Conventional seismometric baseline-corrected results fail to resolve the permanent displacements after an earthquake; the two-state Kalman filter can only provide stable and optimal solutions if the strong motion seismometer had not been moved or tilted by shaking. The proposed Kalman filter algorithm can achieve rapid and stable displacements by estimating and correcting for the baseline error at each epoch. The integration filters out noise-like distortions and thus improves the real-time detection and measurement capability. The proposed approach includes not only a new form of state but also a new approach in seismometry for tuning the Kalman filter. Including baseline error state in the Kalman filter improves accuracy and information content (both permanent displacements and earthquake waveforms) in the output of integrated GNSS and accelerometer systems, both of which are vital in earthquake monitoring.

Acknowledgements

I would like to thank my supervisor, Professor Marek Ziebart and Dr. Paul Groves, for their full support and guidance over the course of my research as well as their careful review and comments on the early version and the draft of this thesis.

I would also like to thank my colleagues in the Space Geodesy and Navigation Laboratory at UCL. Particular thanks to Dr. Alex Parkins for working with me on developing the software in Python and sharing his knowledge as well as experience of integration methods at the early stage of this study; Chris Atkins for planning/running experiments with me and processing GNSS data; also Dr. Santosh Bhattarai for his kind assistance and advice throughout.

I am very thankful to all my friends who shared this journey with me, in particular to: Dr. Jenny Roan for her company, support, and advice; Dr. Sarah Wise for proofreading this thesis thoroughly.

I am especially grateful to my family's support, over these years, mentally and financially. Finally, special thanks to my fiancé, Lee Chapman, who took care of me, encouraged me, and shared life with me during this study.

This work was mostly funded by my parents and partially funded by the Taiwanese Government Scholarship to Study Abroad.

Contents

List of Figures

List of Tables

List of Acronyms and Abbreviations

1D, 2D, or 3D	One-dimension, Two-dimension, or Three-dimension
ADC	Analog-to-Digital Converter
AGU	American Geophysical Union
AVG	AVeraGe displacement solutions
BAP	Basic Strong-Motion Accelerogram Processing Software
C/A Code	Coarse/Acquisition Code
Caltech	California Institute of Technology
CESMD	Center for Engineering Strong Motion Data
CGS	California Geological Survey
CISN	California Integrated Seismic Network
CODE	Centre for Orbit Determination in Europe
CRTN	California Real-Time GPS Network
DGPS	Differential GPS
ECEF	Earth-Centered Earth-Fixed
FFT	Fast Fourier Transformation
GLONASS	GLObalnaya Navigatwionnaya Spurnikovaya Sistema
GNSS	Global Navigation Satellite System
GPS	Global Positioning System
GPST	GPS Time
GSN	Global Seismological Network
IGS	International GNSS Service
IMU	Inertial Measurement Unit
INS	Inertial Navigation System
IRIS	Incorporated Research Institutions for Seismology
JPL	Jet Propulsion Laboratory
KFB	Kalman Filter with the Baseline error state
KFNB	Kalman Filter with No Baseline error state
LHPOST	Large High Performance Outdoor Shake Table
m_b	Body wave Magnitude scale
MEMS	Micro-Electro-Mechanical Systems
M_L	Local Magnitude scale
M_s	Surface wave Magnitude scale
M_w	Moment Magnitude scale
NEES	Network for Earthquake Engineering Simulation
NPL	National Physical Laboratory
NSMP	National Strong Motion Project
NZ	New Zealand
P-wave	Primary wave

PBO	Plate Boundary Observatory
PPP	Precise Point Positioning
PSD	Power Spectral Density
RMS	Root Mean Square
RTS	Rauch Tung Striebel
S-wave	Secondary Wave
SCSN	Southern California Seismic Network
SGNL	Space Geodesy and Navigation Laboratory
SHM	Structural Health Monitoring
SKF	Smoothed Kalman filter
SMS	Strong Motion Seismometer
STD	Standard Deviation
TVC	Three-Variable Control
UCL	University College London
UCSD	University of California, San Diego
USGS	United States Geological Survey

List of Symbols

a	the accelerometer measurement
b	the baseline error state of the accelerometer
d	the computed displacement of the accelerometer
k	the epoch of the measurement
v	the computed velocity of the accelerometer
$\boldsymbol{q_a}$	the PSD of the accelerometer noise
$\boldsymbol{q_b}$	the PSD of the accelerometer baseline error variation
u_{k-1}	the control input
w_m	the measurement noise, with an assumed zero-mean Gaussian distribution
w_s	the system noise, with an assumed zero-mean Gaussian distribution
x_0	the first true value of the state vector;
$\hat{x}_0^-$	the initial predicted state *n*-vector estimate
x_k	the state vector
$\hat{x}_k^-$	the propagated state estimate
$\hat{x}_k^+$	the updated state estimate
$\hat{x}_{k,N}^s$	the smoothed state estimate
z_k	the displacement measurement from GPS position solutions
δt_a	the time interval of the accelerometer measurements
δt_{GPS}	the time interval of the GPS measurements
$\delta\hat{x}_0^-$	the state vector residual, the difference between the true values and the estimate
δz_k^-	the measurement innovation
$\boldsymbol{\Phi}$	the state transition matrix
$\rho_{i,j}$	the correlation coefficient between the *i*th and *j*th state estimates
σ_{be}	the standard deviation of the baseline error variation
σ_i	the uncertainties of the *i*th state estimate
σ_j	the uncertainties of the *j*th state estimate
τ_s	the propagation interval
A_k	the smoothing gain

B_{k-1} the control input matrix at the previous epoch (k-1)

E the expectation operator in accelerometers

F_{k-1} the system matrix at the previous epoch (k-1)

G the generator constant in accelerometers

G_{k-1} the system noise distribution matrix at the previous epoch (k-1)

H_k the measurement matrix

M the proof mass of accelerometers

P_0^- the initial predicted error covariance matrix

P_k^- the propagated state error covariance

P_k^+ the updated state error covariance

$P_{k,N}^s$ the smoothed error covariance

$\boldsymbol{Q}$ the system noise covariance matrix

$\boldsymbol{R}$ the measurement noise covariance matrix

R_1 the resistance of the feedback path in accelerometers

V the output voltage in accelerometers

Chapter 1 Introduction

Earthquake monitoring and early warning systems have been an active research area for many years, involving the rapid determination of earthquake co-seismic displacements and moment magnitude. The limitations of sensors have restricted developments by using either geodetic networks or seismic networks alone. The work presented in this thesis addresses the aspects of the far-field displacement estimation during earthquakes using global navigation satellite systems (GNSS) or global navigation systems (GPS) and seismometry integration technology. In this chapter, the background and developments of the integrated GNSS/GPS-seismometry system are introduced as well as the motivation for this research. An outline of the chapters in the thesis is also presented.

1.1 Background

Destructive and lethal earthquakes, often giving rise to tsunami, are a frequent occurrence in the world. Many countries located on seismic zones, such as Japan, United States, and New Zealand, have suffered the effects of earthquakes or tsunamis over the last decade (GNS Science 2011a; National Research Institute for Earth Science and Disaster Prevention 2011; United States Geological Survey 2011). To mount an effective and timely response to such events requires real-time and accurate estimation of various parameters, such as the moment magnitude, the fault location, and the probability of the generation of a lethal tsunami. Japan, United States, and New Zealand have set up extensive seismic networks with various sensors for earthquake monitoring, for example, strong motion seismometers. Strong motion seismometers are accelerometers, which output the accelerations of the land surface due to seismic displacements with high sampling rates (100-200 Hz). For decades, seismologists have been using strong motion seismometer observations to determine the strength of earthquakes. The most well known method is the Richter magnitude scale developed by Charles Richter (Richter 1935). However, for large earthquakes, the strong motion seismometer observations cannot describe the total amount of energy released precisely. Moreover, the size of each earthquake is always underestimated and hence so is the estimate of the damage caused. In 1978, Hiroo Kanamori published an article in *Nature Magazine,* which quantified the sizes of the earthquakes, and introduced the moment magnitude scale (M_w) based on physical mechanical theories (Kanamori 1978; Hanks & Kanamori 1979). Offsetting the limitations and underestimation of the Richter magnitude for large earthquakes, the moment magnitude scale is now widely used in the seismological field for describing the earthquake size and the energy released, especially for large earthquakes with a large rupture area. The moment magnitude scale

can model the strength of the earthquakes mathematically, and the mean displacement of the mean slipped fault is one of the critical parameters in the mathematical model.

The ground accelerations provided by strong motion seismometers are numerically integrated to obtain velocities and positions or displacements for the mathematical model. However, instrumental biases and errors can distort the computed positions and velocities, rendering them unsuitable for the estimation, especially for large earthquakes and places where seismic networks are sparse. These instrumental biases and errors are categorised as the accelerometer baseline error, which changes significantly during or after violent earthquake shaking when the strong motion seismometers are moved or disturbed (Chiu 1997). A series of papers was first published by a seismologist, Trifunac Miilailo, in one of the top journals, *Bulletin of the Seismological Society of America,* to discuss the effects of baseline errors (Trifunac et al. 1973; Trifunac 1971; Trifunac & Lee 1974). The accelerometer baseline error has become a combination of multiple instrument errors that has been a critical issue in the seismological field since then. Based on the papers published in the seismological field, the baseline error includes constant drifts and shifts in the acceleration outputs, low-frequency noise of the sensors, background noise, operational errors of sensors, tilts, rotations, and misalignments (Trifunac & Todorovska 2001; Chiu 1997). The main challenge is that baseline errors are integrated when doubly integrating the accelerometer observations over time, which results in linear trends in the velocity error and quadratic drifts in the displacement error (Clinton 2004; Javelaud et al. 2011). Seismologists have relied on a general strong motion data procedure, known as the baseline correction, to reduce the baseline error effects in the velocity and displacement solutions. A standard baseline correction includes removing the mean acceleration and velocity before/during the numerical integration and applying noise filters on the accelerometer observations (Shakal et al. 2003). The National Strong Motion Project (NSMP) from United States Geological Survey (USGS) has provided a software tool for strong motion data processing (United States Geological Survey 2011). However, although the baseline correction can reduce most velocity and displacement errors successfully, it also filters out the actual displacements caused by earthquake shaking during earthquakes. As the slipped displacement is one of the core components for determining earthquake magnitudes, a method that can provide accurate mean fault displacements during or after earthquakes is needed.

The Global Positioning System (GPS) has been assessed by seismologists to provide real-time position or displacement solutions and applied in earthquake monitoring. GPS seismology became an important subject gradually in the seismological fields since the 1990s (Larson et al. 1991). Pioneers in seismological field like Kristine M Larson and Yehuda Bock have published several papers on the GPS seismology topic in the global leading journals, for example, *Journal of Geophysical Research, Science*, and *Journal of Geodesy*. GPS solutions of geodetic networks, where are in areas adjacent to, or

surrounding, the epicentres, can efficiently provide the actual mean displacement of the faults and crustal deformation measurements during earthquakes. This is particularly useful for determining the earthquake magnitude and earthquake early warning during large earthquakes because GPS provides comparative information across a wider scale of energies compared to other possible methods. GPS seismology, including fault displacement, crustal deformation and earthquake magnitude determination, has been studied and also applied to real earthquakes, for example, 2002 M_w 7.9 Denali Earthquake (Yehuda Bock et al. 2004; Bilich et al. 2008; Larson et al. 2003), 2004 M_w 9.2 Sumatra Earthquake (Blewitt et al. 2006; Vigny et al. 2005) and 2011 M_w 9.0 Tohoku-Oki Earthquake (Larson 2007; Wright et al. 2012). However, the low sampling rate (0.5-10 Hz) and the sensitivity of GPS measurements sometimes restrict the usefulness of the GPS-alone solutions. Earthquakes often involve low- to high-frequency movements, and both movements are important elements in earthquake monitoring systems for determining the size of the earthquakes. Thus, latterly in a summary article "*GPS Seismology"* written by Kristine M Larson, a system that can provide both low- and high-frequency measurements rapidly during earthquakes was suggested as the future focus in the GPS seismological field (Larson 2009).

At the early stage of GPS and strong motion seismometer integrations, GPS displacement outputs were used separately to augument the accelerometer/strong motion seismometer outputs to recover the seismic displacements or to monitor large structures during an earthquake (Roberts et al. 2004; Li et al. 2006; Emore et al. 2007). The first GPS and seismometer integration was proposed by Smyth and Wu (2006) for structural health monitoring (SHM). The measurements of both GPS and accelerometers were integrated via an optimal recursive data processing algorithm, the Kalman filter. One advantage of using the Kalman filter is that it outputs high-sampling rate optimal estimates (based on the sampling rate of the accelerometers), which indicates that the integrated system can provide high-rate accelerations, velocities, and displacements. Hammond et al. (2010) showed the results and advantages of the Kalman filter integration by combining the strong motion seismometer data and GPS observations in the M_w 7.2 El Mayor-Cucapah Earthquake. Later in 2011, Bock et al. (2011) at the University of California, San Diego built a large outdoor shake table and mounted several sets of GPS receivers and accelerometers on the seven-floor building on the platform. Kalman filter integration was investigated to combine the advantages and overcome the disadvantages of each instrument. High-sampling rate optimal solutions can be obtained for near real-time earthquake monitoring. Since then, the Kalman filter algorithm has become the key method for GPS and accelerometer/strong motion seismometer integrations. Related studies have shown that developing the Kalman filter algorithm and improving the performance of the Kalman filter integrations have become an important subject for earthquake monitoring (Tu et al. 2013; Geng, Bock, et al. 2013; Geng, Melgar, et al. 2013).

1.2 Motivation

Since in recent years, several devastating earthquakes and tsunamis have damaged peoples' assets and lives, a reliable earthquake monitoring system is required. One of the core components in the earthquake monitoring system is the rapid and accurate measurement of mean fault displacements, which is used to determine the earthquake magnitude immediately after earthquakes.

Currently, although the Kalman filter integration algorithm has been developed and implemented in the seismological field for years, existing integrated systems are still unstable and under tests. For example, due to the design of the Kalman filter algorithm, the strong motion seismometer/accelerometer instrumental biases and errors would severely affect the accuracy and performance of the Kalman filtered velocity and displacement solutions. As these instrumental biases and errors are associated to the accelerometer baseline error, an integrated Kalman filter algorithm that combines the seismological accelerometer baseline correction is to be studied in this thesis. The Kalman filter has been applied in multi-sensor integration in the navigation field for decades, in this study, GPS and strong motion seismometer/accelerometer integration field is investigated to improve the performance of the integrated solutions for earthquake monitoring. It is hoped that a stable integrated system that integrates GPS observations and measurements from strong motion seismometers or accelerometers will be able to provide accurate and rapid real-time ground displacements caused by earthquakes, especially large earthquakes.

1.3 Outline of Thesis

The section briefly shows the contents of the following chapters of this thesis.

Chapter 2 presents the literature review of this study introducing the relevant research. In this literature review, the material is organised into four topics, which are earthquake science, strong motion seismometry, GPS seismometry, and GPS/accelerometer integrations. Finally, the aims and objectives of this study, which states the research problems to be addressed, are described as well. The methodology of this study is also stated in this chapter.

In Chapter 3, the core algorithm used in this study is introduced, the Kalman filter algorithm. The concepts, definitions and architecture of the Kalman filter algorithm are explained in detail. The most important contributions of this study related to the implemented Kalman filter are also described.

The proposed Kalman filter algorithm is tested with the University of California, San Diego outdoor large shake table GPS and accelerometer data sets in Chapter 4, and the related results and analysis are also shown.

Chapter 5 provides a performance analysis of the designed displacement experiment that took place on the rooftop of the National Physical Laboratory, and the proposed three-dimensional Kalman filter algorithm is validated with the collocated GNSS receiver and strong motion seismometer data sets.

In Chapter 6, the proposed Kalman filter algorithm is implemented and validated with collocated GPS and strong motion seismometer data sets from the existing geodetic and seismic networks in a real earthquake, the 2010 El Mayor-Cucapah Earthquake.

Chapter 7 is the final chapter of this thesis, where the conclusions of this study are described, and a discussion of implications of the results is presented comprehensively.

Chapter 2 Overview and Literature Review

Foundational knowledge of both the earthquake and navigation/geodesy fields is needed in order to appreciate the integration of strong motion seismometers and GPS receivers. This chapter presents a review of books and papers in both subjects, and introduces the problems, concepts, and aims of this study. In order to provide a general and better understanding of this research, the following sections will go through the background of earthquakes and seismometry, the introduction of GPS seismology, and the advantages of the GPS and accelerometer integration.

2.1 Earthquakes and Seismometry

This chapter follows the earthquake and seismology terminology utilised by Bolt (2006) and Shearer (2009), as these are the canonical textbooks in those fields. Further history, theory, and wider applications of the methods explored here in earthquake and seismology fields can also be found in other textbooks, including Howell (1990), Towhata (2008), Vallina (1999), and Yeats (2012).

An earthquake occurs when the crust of the Earth releases energy and moves rapidly. The released energy is transmitted through the Earth and produces waves of energy known as seismic waves. A seismic wave as a term describes the size and travel speed of earthquakes or other energy releasing activities, such as explosions or volcanoes. Based on their different propagation modes, seismic waves caused by earthquakes can be divided into three types: primary wave, secondary wave, and surface wave (Bolt 2006).

A Primary wave, known as a P wave, is a body wave and is similar to a sound wave that can propagate through gases, solids and liquids. Because they can propagate through so many different media, P waves always travel faster than any other waves during an earthquake. A P wave is also called a pressure wave, as there are dilatations and compressions during propagation as shown in Figure 2.1.

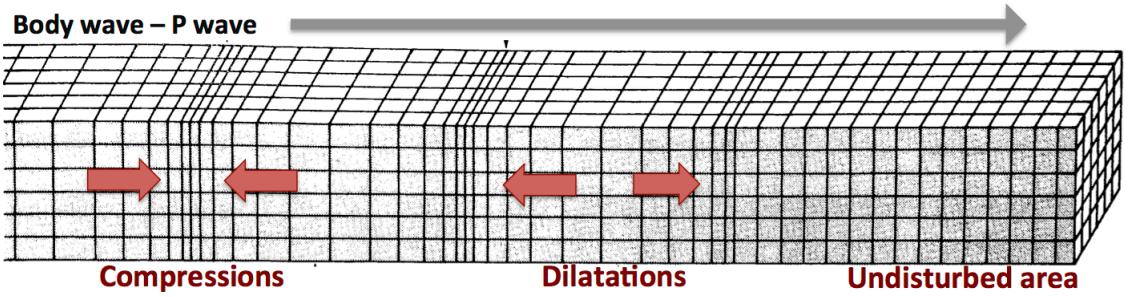

Figure 2.1: The propagation and ground motion of P wave during an earthquake (figure adapted from (Bolt 2006))

Figure 2.2 illustrates another body wave, a secondary wave, also known as an S wave or

shear wave. An S wave can only propagate through solid materials, which means that S waves cannot travel through the liquids inside or on the Earth, for example through magma or oceans. The propagation time of P and S waves depend on the solids and materials the waves have actually traveled through during an earthquake, and a P wave travels faster than an S wave in most cases. The ground motion caused by an S wave contains both vertical and horizontal movements, and these movements damage the structures of buildings more than P waves.

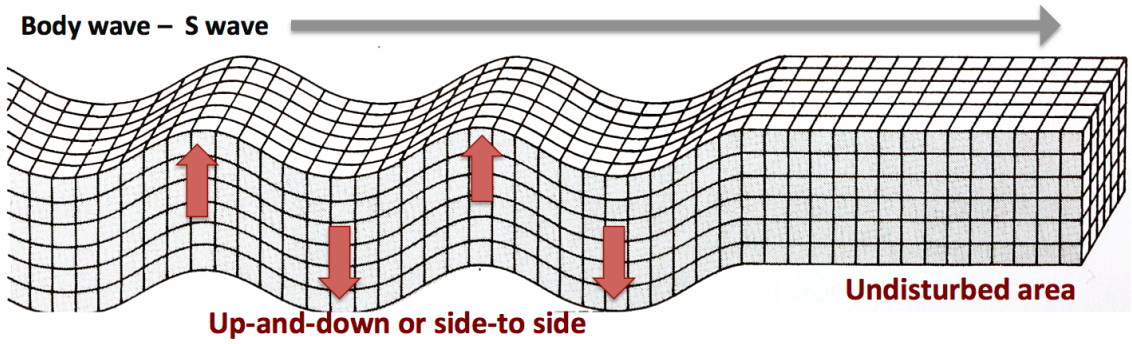

Figure 2.2: The propagation and ground motion of S wave during an earthquake (figure adapted from (Bolt 2006))

Unlike the body waves, which travel through the body of the Earth, there are also surface waves that are only transmitted near the surface of the ground during earthquakes. Surface waves can be divided into two main kinds: Love waves and Rayleigh waves. A Love wave (see Figure 2.3) usually propagates faster than a Rayleigh wave and moves the ground surface horizontally without vertical movement. A Love wave is similar to an S wave in that it cannot travel through liquids.

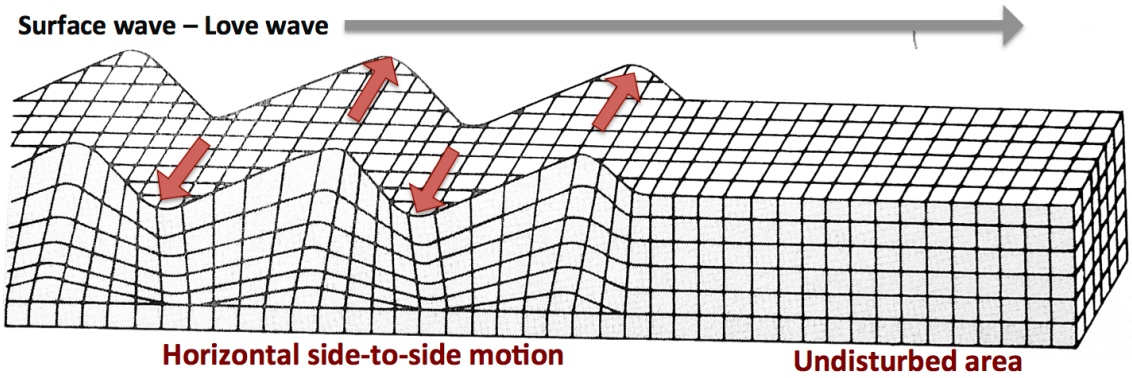

Figure 2.3: The propagation and ground motion of Love wave during an earthquake (figure adapted from (Bolt 2006))

Another type of surface wave, the Rayleigh wave, is characterized by a rolling motion during propagation, as shown in Figure 2.4. Rayleigh waves are transmitted through both liquids and solids, and the rolling motion of the wave causes both horizontal and vertical movement near the ground surface.

These seismic waves are the general wave propagations in earthquakes, and the

movements and effects while shaking might actually consist of multiple wave types at the same time.

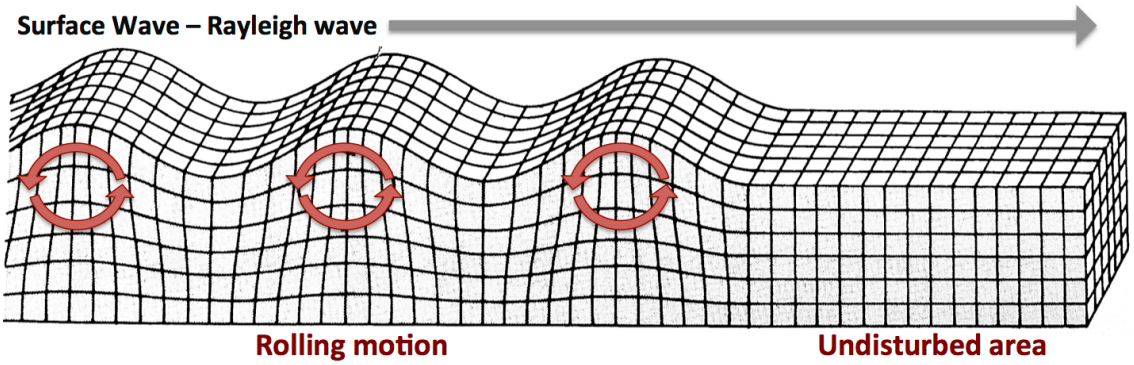

Figure 2.4: The propagation and ground motion of Rayleigh wave during an earthquake (figure adapted from (Bolt 2006))

When an earthquake occurs, the seismic waves start to travel radially from a location called the hypocentre, which refers to the place where crust or faults move originally underneath the earth. The corresponding point on the ground surface vertically above the hypocentre is called the epicentre. The vicinity around the epicentre is usually where properties and structures are most damaged during an earthquake. Observations of ground motion during earthquakes are used to estimate the positions of the hypocentre and epicentre.

Seismometry includes the investigation of motion of the ground, the development of devices for detecting motion, and also providing seismic wave information about earthquakes to seismologists. A sensor known as a seismometer is used to measure the displacement, the velocity, and the accelerations of ground motion due to phenomena that range from the natural noise of the earth to large ground movements. The term seismograph refers to the entire system of measuring, signal amplifying, time tagging, and data recording. The output of the recorded ground motion as a time series is known as a seismogram (Stein & Wysession 2003).

2.2 Seismic Scale and Earthquake Magnitudes

The seismic scale is a method used to describe the size and severity of earthquakes. Intensity and magnitude scales are the most common seismic scales. After earthquakes, seismologists observe the differences of elevation on the ground surface due to shaking to create seismic contour maps to illustrate places with similar levels of damage and effects on structures, facilities, human beings, and animals. This kind of method is known as an intensity scale, and seismologists can use it to define the locations of earthquake epicentres. The intensity scale is always presented in Roman numerals, and the definitions and the levels of the contour lines might be varied in different regions. Therefore, to be able to compare the severity and size of earthquakes widely and

globally, a more standard scheme is required.

The magnitude scale, always presented in Arabic numbers, is defined by the energy released during earthquakes based on the measurements from the seismic sensors. Combining observations of acceleration with velocity and displacement estimates from a network of seismic sensors enables the approximate magnitude of the earthquake to be determined. The magnitude scale provides seismologists with a uniform method to describe the size and severity of earthquakes globally. Several magnitude scales have been created and applied, beginning with the local magnitude (M_L), also known as the Richter magnitude scale, which was first developed for southern California earthquakes by Charles Richter in 1935 (Richter 1935). Richter took measurements of earthquake wave amplitude, obtained using Wood-Anderson seismographs (Bolt, p164, 2006), and used them to calculate the local magnitude. The local magnitude can be determined by measuring the time difference between the arrival of the P-wave and the S-wave and the maximum amplitude of the seismic wave (Bolt 2006). As shown in Figure 2.5, the time difference of arrival in seconds of P- and S-waves is related to the distance between the epicentre and the sensor in kilometres. The maximum amplitude of the shaking is also determined from the seismogram. The local magnitude is then estimated by drawing a straight line on the scale between the calculated distance and the maximum amplitude (as shown in Figure 2.5). So in this example, the local magnitude in Figure 2.5 is estimated as 5.0. However, the local magnitude scale was designed only for southern Californian earthquakes, and the distance between the epicentre and the seismograph was assumed to be at a maximum of 1000 km, as the Wood-Anderson seismograph was limited by its natural frequency (1.25 Hz) and not able to record seismic waves with lower frequencies produced by large earthquakes (Stein & Wysession 2003; Yeats 2012). Hence, the local magnitude performs better at determining local earthquakes but is not necessarily useful for global and great earthquakes.

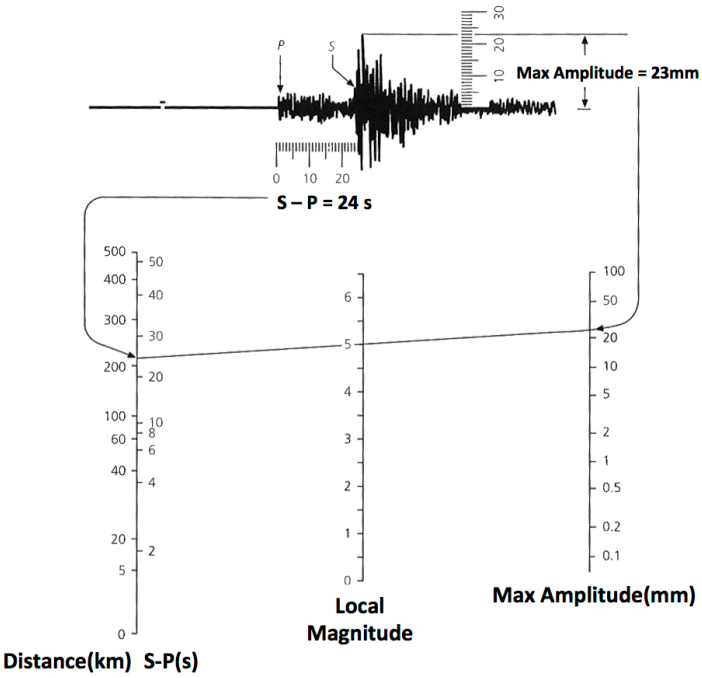

Figure 2.5: Example of the method to determine the local magnitude (figure adapted from (Bolt 2006))

In addition, Charles Richter and Beno Gutenburg also developed the body wave magnitude scale (m_b) and the surface wave magnitude scale (M_s) for determining the magnitude of different kinds of seismic waves individually (Gutenberg & Richter 1955; Gutenberg & Richter 1956). The body wave magnitude scale is derived from the largest amplitude of the P-wave, and the surface wave magnitude scale is obtained from the maximum amplitude measurement of the surface wave within a 20-second period. These magnitude scales provide different values and information for earthquakes; however, neither of them have estimated the magnitudes correctly when severe earthquakes occurred (Bolt 2006). For large earthquakes with a large rupture area, the peaks of the seismic waves cannot describe the total amount of the energy released precisely, and the size or the damage of earthquakes are always underestimated. A uniform and now widely used scale, the moment magnitude scale (M_w), is based on physical mechanical theories and introduced by Hiroo Kanamori in the 1970s (Kanamori 1978). The moment magnitude scale uses the seismic moment (M_0) to determine the size of the earthquakes. The seismic moment is the product of the rock rigidity of the faults ($\boldsymbol{\mu}$) in dyn/cm^2 (1 dyn = 1 g • cm/s^2), the mean displacement of the slipped fault (D) in cm, and the rupture area during the earthquake (A) in cm^2. The rock rigidity, also known as the shear modulus of elasticity, is usually constant for any particular material, and the average displacement and rupture area can be mathematically modelled using observations from seismograph network data. More recently, the mean displacement now can be derived directly from the GPS solutions of the geodetic networks (Shearer 2009), provided they are of sufficient station density and in areas adjacent to, or surrounding, the epicentre. The moment magnitude has become

the standard number to describe the energy released in an earthquake because it provides useful and comparative information across a wider scale of energies compared to other possible methods. This is particularly apparent for very large earthquakes.

One of the key factors of determining earthquake magnitude for the purposes of planning emergency response and potential tsunami forecasting is obtaining reliable and accurate ground displacement immediately after the earthquake has taken place. The ranges of the amplitude and frequency of seismic waves are very large when measuring from the natural ground noise of the Earth to the large earthquakes. The displacement of ground motions is possibly from 1 nm up to 10 m, and the frequency range can be measured from 0.00001 Hz to 1000 Hz, as shown in Table 2.1. The design of instrumentation in earthquake seismology is an important and challenging topic (Havskov & Alguacil 2010).

Table 2.1: Different seismic sources and the corresponding frequencies (Havskov & Alguacil 2010)

Frequency (Hz)	**Type of source**	**Period**
0.00001-0.0001	Earth tides	12 days – 0.1 days
0.0001-0.001	Earth free oscillations, earthquakes	0.1 days – 1000 seconds
0.001-0.01	Surface waves, earthquakes	1000 – 100 seconds
0.01-0.1	Surface, P and S waves, earthquakes with $M_w > 6$	100 – 10 seconds
0.1-10	P and S waves, earthquakes with $M_w > 2$	10 – 0.1 seconds
10-1000	P and S waves, earthquakes with $M_w < 2$	0.1 – 0.001 seconds

2.3 Strong Motion Seismometer

When a strong earthquake occurs, it produces substantial ground shaking in the seismic zone around the source of the earthquake. This high-amplitude motion of the ground cannot always be recorded by seismometers with restricted dynamic ranges, whereas strong motion seismometers can measure the specific force caused by the ground motion with a large dynamic range; they are also known as accelerometers (Bolt 2006). Strong motion seismometers or accelerometers are designed based on the force-feedback or force-balance principle as shown in Figure 2.6. When the ground motion produces an external force applied to the casing of an accelerometer, an internal force of the sensor that keeps the mass of the instrument at its equilibrium position will be generated electronically by an electromagnetic transducer (Havskov & Alguacil 2010).

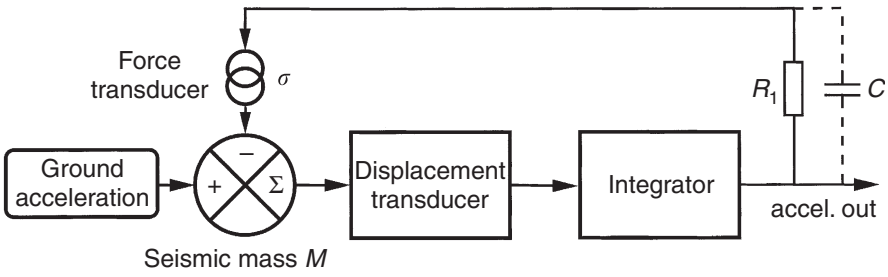

Figure 2.6: Force-balance accelerometer feedback circuit (Wielandt 2002)

Based on the force balance principle, the acceleration and the output voltage can be derived from the seismic mass, the feedback resistor, and the force transducer (Wielandt 2002; Havskov & Alguacil 2010). The coil generated force equals the external force on the accelerometer mass:

$$\sigma \cdot \frac{V}{R_1} = M \cdot a \tag{2-1}$$

$$G = \frac{V}{a} = \frac{MR_1}{\sigma} \tag{2-2}$$

where σ : the motor constant of the feedback coil (in Newtons/Ampere);

M : the proof mass of the seismometer;

R_1 : the resistance of the feedback path;

V : the output voltage;

a : the acceleration;

G : the generator constant.

The generator constant is the ratio of the output voltage to the acceleration and can be derived from three passive components: the seismic mass, the resistor, and the force transducer. The force balance accelerometers can be precise because the seismic mass which defines the inertial reference is assumed to be error-free; the resistor is considered an ideal component; and the small transformed motion makes the force transducer very precise (Wielandt 2002; Havskov & Alguacil 2010). After the measurement of the voltage, an internal analogue-to-digital converter (ADC) of the seismometer then converts the analogue signals to digital records, and the seismometer can output the acceleration of the ground motion (Shakal et al. 2003; Havskov & Alguacil 2010). As G is a calibrated constant of the instrument, the voltage is varied to maintain the proof mass in a particular position, which (when the correct voltage is applied) maintains a constant ratio, equal to G. The value of G is then taken as the constant of proportionality to convert measured voltages to the "measured" accelerations.

2.4 Strong Motion Data and The Seismometer Baseline Error

The first strong motion seismometer measured seismic waves during the Long Beach Earthquake, California, in 1933 (Ruge and McComb 1937; Trifunac 1971). Since then, local and national strong motion seismic networks have been established around the world for earthquake monitoring. Many countries have set up extensive strong motion seismograph networks for earthquake monitoring, such as GeoNet in New Zealand, KiK-net in Japan, and the National Strong-Motion Network in the United States (GNS Science, 2011; Hammond, Bürgmann, & Heaton, 2010; United States Geological Survey (USGS), 2011). There are thousands of strong motion seismometers and accelerometers that have been installed to record data every day for global and regional earthquake monitoring. Recording strong motion seismic data has helped seismologists and governments understand and identify situations and areas of seismic risk and then make critical decisions. The seismic information has been also widely used in various research fields, such as seismology, earth science, earthquake engineering, and structural engineering.

A strong motion seismometer outputs ground accelerations, and in order to obtain measurements of ground displacement, the observed accelerations are numerically integrated twice. Hence, the velocity and the displacement can (ideally) be obtained from the numerical integration directly. However, some errors do affect strong motion seismometer data. As an earthquake takes place ground displacement may cause physical misalignment of a seismic sensor, which results in changes in vertical position and vertical accelerations being sensed along the horizontal sensor axes. This error can change during an earthquake when the instrument is disturbed, and there can also be changes in the errors of the sensors themselves, which further contribute to the baseline error. The baseline error is a combination of multiple instrument errors: it includes constant drifts and small shifts in the acceleration outputs and low-frequency noise of the sensors as well as the background. Meanwhile, operational errors of sensors, such as tilts, rotations, or misalignments can also be considered as baseline errors (Chiu 1997). When doubly integrating the acceleration over time, the baseline errors are integrated as well, which results in linear trends in the velocity error and quadratic growth in the displacement error (Clinton 2004). The drifts of the uncorrected velocity and displacement shown in Figure 2.7 illustrate the baseline error problem of strong motion seismometer output, which have been developed and studied from different perspectives for several decades (Javelaud et al. 2011). A general and standard strong motion data procedure implemented for obtaining the corrected ground velocity and displacement has been drawn from Shakal, Huang, & Graizer (2003) and USGS NSMP Data Center (2012):

(1) **First-order baseline correction:** apply a first-order baseline correction to remove the mean of the strong motion data during a static period and make the

acceleration zero-mean during the earthquake events;

(2) **Numerical integration:** numerically integrate the zero-mean acceleration to velocity;

(3) **Higher-order baseline correction:** remove a parabola or a higher-order function if there is any obvious linear trend from the velocity (e.g. the uncorrected data in Figure 2.7.b);

(4) **High-pass and low-pass filtering:** apply the high-pass and low-pass filter to attenuate the low-frequency and high-frequency noise of the acceleration;

(5) **Numerical integration**: numerically integrate and doubly integrate the baseline-corrected and filtered acceleration to velocity and displacement;

(6) **Response spectra computation:** use the corrected and filtered acceleration to calculate the Fourier amplitude spectra and the response spectra.

A strong motion data processing method, Basic Strong-Motion Accelerogram Processing Software (BAP), programmed and provided by USGS (Converse & Brady 1992) has been widely used to obtain corrected acceleration, velocity, and displacement results from the input strong motion specific force time series (Douglas & Boore 2010).

The purpose of the baseline correction method is to obtain the accurate velocities and displacements during earthquakes, as the amplitudes and frequencies of the ground accelerations, velocities, and displacements during the earthquakes all play parts in Earthquake Engineering for determining the sizes, the acting faults, and the properties of the earth crust of the seismic activities (Lam & Wilson 2004). However, with the current baseline correction method (e.g. the BAP software), the applied baseline corrections and noise filters not only reduce the baseline errors and noises within the accelerations but also eliminate the permanent co-seismic displacements after earthquakes. As an attempt to overcome this problem, GPS networks providing absolute position have been investigated as an adjunct form of seismometry.

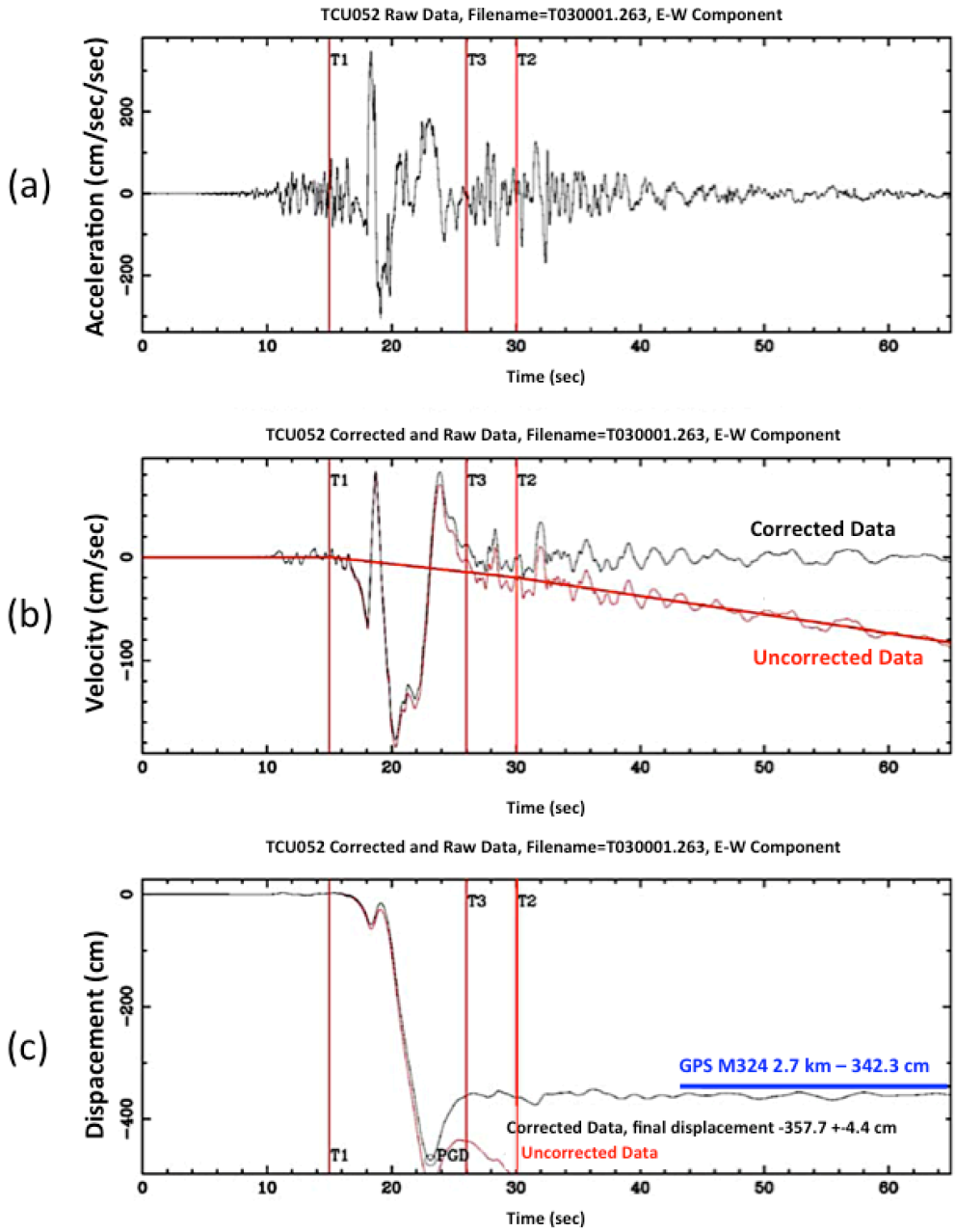

Figure 2.7: An example of integrating the raw and the baseline-corrected accelerations at strong motion station TCU052 from 1999 Chi-Chi (M_w 7.6). (a) The raw east-west strong motion acceleration (b) The uncorrected (red) and corrected (black) velocities (c) The uncorrected (red) and baseline-corrected (black) displacements (Wu & Wu 2007). Notably in (c), the corrected displacement, -357.7 ± 4.4 cm, was also compared with the GPS displacement, -342.3 cm, from the nearest GPS station M324 (2.7 km away from the strong motion station TCU052).

2.5 GPS Seismometry

The original motive for developing GPS for the U.S. government was to offer the accurate estimation of position, velocity, and time for military services. GPS was designed to comprise a constellation of at least 24 satellites orbiting at an altitude of

approximately 20200 km and transmitting signals from satellites to users continuously. The satellites broadcast timing signals over two carrier frequencies: L1 at 1575.42 MHz and L2 at 1227.60 MHz (Kaplan 2005). The antenna of the GPS receiver then receives line-of-sight signals from at least four satellites for the receiver to calculate its position in both horizontal and vertical domains; the signals are also used to determine the receiver clock offset. For precision applications there are several GPS data processing approaches available: the two principal methods are relative network positioning (e.g. Genrich and Bock (1992)) and precise point positioning (PPP) methods (Zumberge et al. 1997).

Differential GPS (DGPS) has been widely used for GPS positioning in relative network positioning. DGPS always uses GPS data from two or more receivers to improve the position estimates at what is commonly known as a rover station. At least one receiver is placed over a point of known coordinates, this being termed a reference station. Satellites are tracked at both the reference and rover stations simultaneously, and this data is then combined (either in real time or after the event) and processed using differencing strategies. These algorithms help to reduce the conventional positioning errors that degrade GPS position estimates. The error sources in GPS solutions include the differences between the true and broadcast ephemeris and satellite clock errors, signal propagation delays through ionosphere and troposphere, and receiver measurement errors due to delays in responding to dynamics, receiver noise, radio frequency interference, and signal multipath (Groves 2013). The common GPS signal propagation errors, including ionosphere, troposphere, multipath effects, and signal blockage are shown in Figure 2.8. By DGPS processing, most error sources can be eliminated by differential dual-frequency measurements, and relative network positioning can provide real-time sub-decimetre-accuracy position or displacement solutions (Misra & Enge 2010). In the 1990s, while GPS accuracy was controlled and restricted by U.S. military, Larson and Agnew (1991) and Bock et al. (1997) proposed using GPS to measure the deformation of the Earth. Larson (1993) published GPS positions and crustal movement analysis from five years of data (1986-1991) from the southern California Borderlands, and the results indicated that precise geodetic observations could be made using DGPS. This encouraged GPS devices to be applied widely in geodetic monitoring networks, seismic displacement detection, and earthquake observations (Langbein & Bock 2004; Y Bock et al. 2004; Ji et al. 2004). In 2003, Larson et al. (2003) used 1 Hz GPS data recorded from the 2002 Alaska Denali fault earthquake (M_w 7.9) to analyse the significant surface movements and proposed that 1 Hz GPS could measure the large surface waves with a large range of velocities between ~1 to 4 km/s, which had exceeded the recording limits of the high-dynamic range and broad-bandwidth seismometers. Unlike a conventional seismometer, the range of ground movements that can be measured by GPS has no upper limit (although conversely very small ground movements, for example, sub-mm, cannot be measured

successfully with GPS). The important distinction is that a seismometer tends to "clip" once the earthquake acceleration amplitude exceeds a certain threshold, whereas GPS can measure large displacements of strong earthquakes.

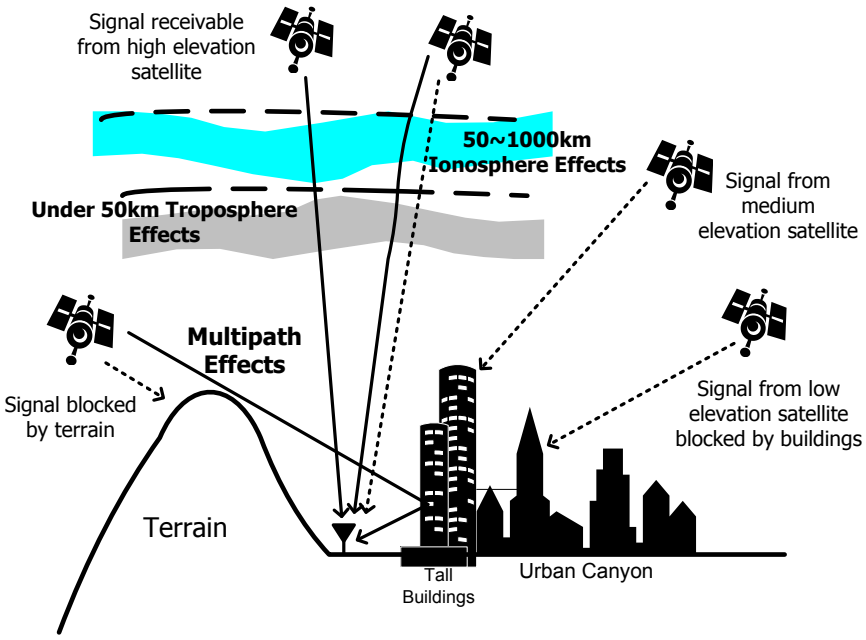

Figure 2.8: GPS signal blockages and error sources (Li 2010)

However, problems occur if the relative reference stations have been also moved by the earthquakes (Li et al. 2013). Whereas the PPP method under a global reference frame (defined by the satellite orbits and clocks) and the precise GPS satellite orbits and clocks (provided by the International GNSS Service (IGS)) provides the position solutions of the GPS receivers without the need of GPS reference stations (Takasu 2006) in the vicinity of the seismic zone. Although PPP is currently used mainly for post-processing applications and still developing for further real-time applications, it has been tested for some large earthquakes, such as the 2002 Alaska Denali Fault earthquake, the 2004 Sumatra-Andaman earthquake, and the 2011 Tohoku-Oki earthquake. PPP has been used to measure the ground movement, monitor the crustal deformation, and determine the magnitude of the earthquakes (Kouba 2003; Wright et al. 2012; Takasu 2006).

Blewitt et al. (2006) used GPS solutions and seismic data from the 2004 Sumatra earthquake (M_w 9.2-9.3) to discuss one of the most lethal tsunamis ever recorded. They showed that when using conventional seismic instruments alone to measure and to calculate the seismic wave propagation and magnitude of the earthquakes, it took about 45 minutes to obtain the magnitude of the earthquake at M_w 8.5. It then took 5 hours to correct the magnitude to M_w 9.0 and to realize the possible threat of the strong tsunami. Whereas, by using the real-time 30 second GPS observations to obtain the mean displacement of the seismic zone and the seismic moment M_0, it was possible to estimate the earthquake's size at M_w 9.0 in about 15 minutes. Similar to Blewitt et al.

(2006), Wright et al. (2012) also demonstrated the dangers of underestimating and delaying the earthquake magnitude determination by using conventional seismic networks and the advantages and efficiency of using the dense GPS networks during the 2011 Japan M_w 9.0 Tohoku Oki Earthquake. In addition, rapid and accurate GPS solutions can be used for setting the initial values of tsunami monitoring models, such as the difference of the sea levels, and this can help to identify the danger and risk of the potential tsunami in a shorter time period. Thus, GPS has been proposed as a component of a tsunami warning system. Nevertheless, although the main studies showing effective use of GPS (both for the Sumatra and the Tohoku Oki earthquakes) have been very large earthquakes (M_w 9.0), the effectiveness of GNSS for more frequent, smaller (and yet still lethal) earthquakes has yet to be demonstrated.

2.6 Limitations of Existing Seismic Networks and GPS Networks

A limitation of strong motion seismometer data processing is that the baseline correction and low/high-pass filters not only eliminate the baseline errors but also the permanent co-seismic displacements (Li et al. 2013). An example is shown in Figure 2.9; during the 2010 El Mayor-Cucapah earthquake (M_w 7.2), the baseline corrected and filtered displacement of a strong motion seismometer shows no permanent movement after the large shaking, yet there is an approximate 0.2 m permanent shift in PPP solutions measured by a co-located GPS station. This illustrates perfectly the problem of using only the seismic network to obtain the ground motion displacement.

Meanwhile, although GPS can provide accurate and permanent co-seismic displacements of the ground motion, compared to the 100 Hz output rate of the seismometer or accelerometer, the low output rate (0.5~10 Hz) might limit the usefulness of the GPS solutions for showing the high-frequency motion of the ground during earthquakes (Larson et al. 2003). To overcome the limitations of using either strong motion seismometer networks only or GPS networks only, a two-state (displacement and velocity) Kalman filter integration technique was first developed to combine these two types of measurement in order to provide real-time, rapid (up to 100 Hz sampling rate), and reliable (centimetre accuracy) displacement solutions for structural health monitoring (SHM) during earthquakes (Smyth & Wu 2006). This paper was particularly important and fundamental, as this was the first approach to propose a detailed Kalman filter integration algorithm using GPS and seismic data in the seismological field.

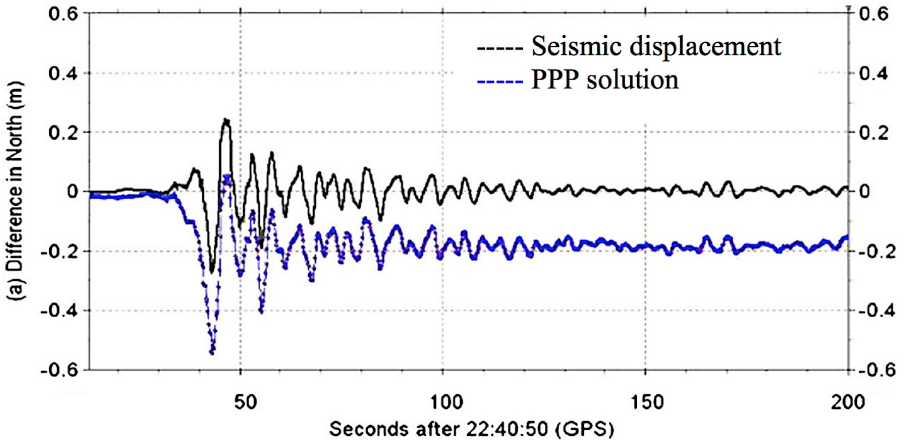

Figure 2.9: The corrected seismic displacement (black) and GPS PPP (blue) displacement in the north-south direction of the co-located seismic station 5058 and GPS station P496 during the 2010 El Mayor-Cucapah earthquake (Li et al. 2013).

2.7 GPS and Strong Motion Seismometer/Accelerometer Integration

In order to monitor deformation during large earthquakes (M_s 7.0+) and typhoons, Li et al. (2006) installed a GPS antenna and accelerometers on a 108-metre tall steel tower in Tokyo, Japan. In the paper, 10 Hz GPS observations and 20 Hz accelerometer measurements were compared to each other. The displacement from GPS was numerically doubly differentiated to obtain acceleration, and the acceleration from the accelerometer has been doubly integrated to obtain displacement. Meanwhile, the time-frequency analysis method, Fast Fourier Transformation (FFT), was applied to analyse the responses of GPS and accelerometer measurements during seismic activity and wind gusts. The results in both events showed that GPS solutions provide more information at the low frequency end of the displacement waveform, whereas the accelerometer measurements provide more details at the high frequency end of the acceleration waveform. Hence, it was suggested that by using the measurements from both GPS and accelerometers, a full-scale structural monitoring system could be developed.

Instead of using a single type of instrument, Hammond et al. (2010) show the results and advantages of the Kalman filter integration combining the strong motion seismometer data and GPS observations in the M_w 7.2 El Mayor-Cucapah Earthquake. In Figure 2.10 (a), Hammond et al. (2010) applied the baseline correction method proposed by Boore et al. (2002) to show the 0^{th}, 1^{st}, and 2^{nd}-order baseline corrected displacement solutions with acceleration outputs of the strong motion seismometer. The results indicate that with acceleration outputs only, the numerical double-integrated displacements result in linear and quadratic drifts after applying 0^{th} and 1^{st}-order baseline corrections, respectively. Meanwhile, when applying the higher order

correction, the drift has been eliminated but the permanent displacement caused by the earthquake has also been filtered out. In contrast, using the two-state (displacement and velocity) Kalman filter integration method proposed by Smyth and Wu (2006), the combined results of 1 Hz GPS observation and 100 Hz 0th-order baseline corrected accelerometer data (shown as the black line in Figure 2.10 (b)) can provide a more accurate result with earthquake shaking information and the permanent displacement in near real-time compared with the numerically integrated the 1st order corrected acceleration results (grey line) and the post-processed 1 Hz GPS solutions (red dots).

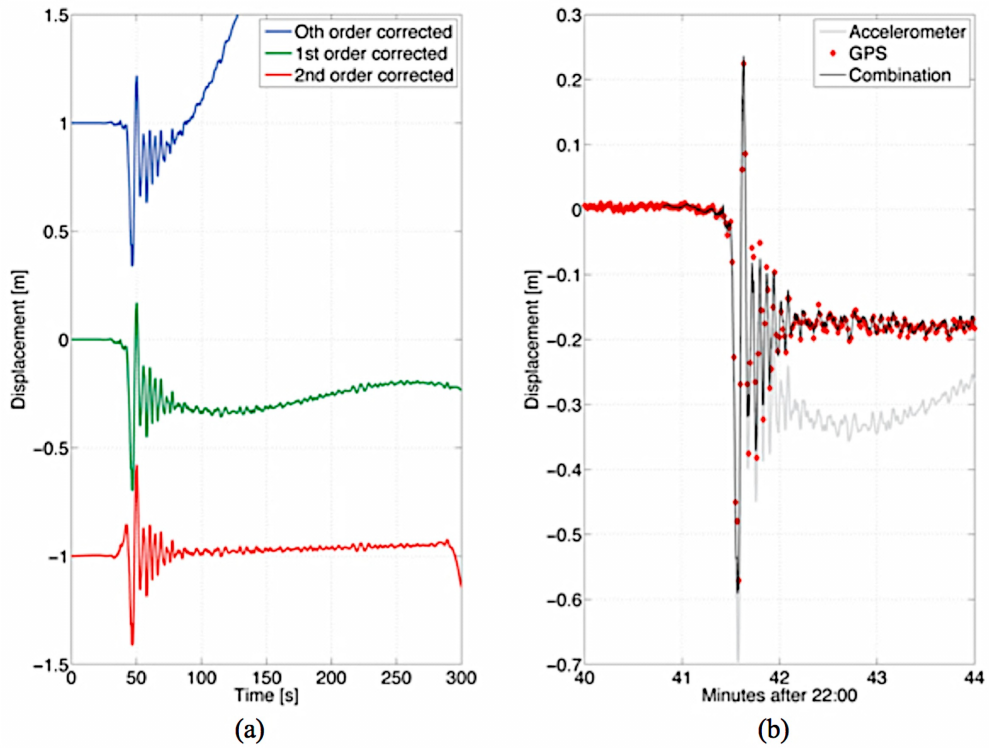

Figure 2.10: The comparison of the displacement results at the seismic station WES during the 2010 El Mayor-Cucapah Earthquake (Mw 7.2) (a) the 0th, 1st, and 2nd-order baseline corrected numerically integrated results from the strong motion seismometer measurements (b) the 100 Hz numerically integrated 1st-order corrected acceleration (grey), 1Hz GPS solutions (red), and the combined GPS and strong motion seismometer results (black) (Hammond et al. 2010)

Although the GPS solutions were still post-processed, it shows that the low-latency GPS data helps to improve the seismic-alone data via the Kalman filter integration. Furthermore, the authors proposed that potential real-time integrated GPS and seismometer technology will lead seismology related studies, including the studies of earthquakes, tsunamis, volcanoes, and glaciers etc., to the next scientific era. Combining the instruments to provide the accurate and precise displacement solutions in short time periods for more accurate earthquake magnitude estimations became a subject for establishing a near real-time earthquake alarm system.

In Bock et al. (2011), an outdoor large shake table was established with 15 Micro-Electro-Mechanical Systems (MEMS) accelerometers and 7 GPS receivers in 2003, and a loosely coupled Kalman filter algorithm was applied to integrate the observations of the collocated MEMS accelerometers and GPS receivers. The outdoor shake table simulated the seismic wave of the 1971 San Fernando (M_w 6.6) and 1994 Northridge (M_w 6.7) earthquakes. A high output rate (1024 Hz) displacement truth model was provided by a multivariable MTS 469DU digital controller to compare with the displacement results of the GPS-only, accelerometer-only, and integrated GPS and accelerometer. Notably, the displacement truth model provided the accurate and precise amplitude of the oscillations of the platform rather than any permanent displacement during shaking. The differences between displacement solutions and the displacement truth model are used to calculate root mean square (RMS) statistics for discussing the precision of each method. For accelerometer-only solutions, the RMS displacement differences of the 15 accelerometers are between 12.0-19.3 mm. For GPS-only solutions, the RMS displacement differences of the 7 GPS receivers are between 2.6-4.0 mm. For integrated Kalman filter results, the RMS displacement differences of several combinations of the GPS receivers and MEMS accelerometers are between 1.6-2.0 mm. The results clearly showed the improvement from using the Kalman filter integration. Although there are some issues from the shake table simulation, for example, only dynamic motions and no permanent displacement available after shaking, the experiment and results have set a milestone for this research field. Furthermore, in Bock et al. (2011), the Kalman filter algorithm is also tested with collocated GPS and accelerometer data (within 0.5 km) from the California Real-Time GPS Network (CRTN) and California Integrated Seismic Network (CISN) during the 2010 El Mayor-Cucapah earthquake (M_W 7.2) and compared with 1 Hz GPS-only solutions. In addition, the authors discussed the sawtooth-like phenomena (as shown in Figure 2.11) within the integrated solutions and the Kalman filter error variances due to the absence of GPS solutions. This means that while the Kalman filter estimates the displacement by accelerometer measurements only and without regular GPS updates, the results drift due to accelerometer errors until the next GPS observation is available. To minimize the sawtooth-like phenomena, a method known as Kalman filter tuning is usually applied in the calculation. The Kalman filter tuning is a process to try and set the variables, such as the measurement error covariance matrix and the system noise covariance matrix, in a Kalman filter properly in order to obtain the optimal solutions, (Groves 2013). The Kalman filter tuning is often empirical and can be very complicated. Therefore, in Bock et al. (2011), instead of changing and testing the variables in the Kalman filter, the authors proposed to solve these problems by applying a Rauch Tung Striebel (RTS) smoother; they indicated that the 3-dimensional precise integrated displacement solutions at high output rate (100 Hz) can be derived via the Kalman smoother within a short time period.

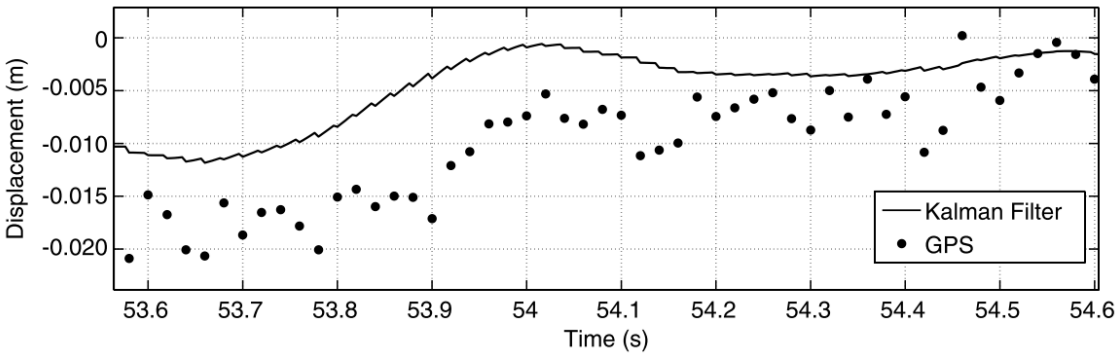

Figure 2.11: The 250 Hz forward loosely-coupled Kalman filter GPS/accelerometer integrated displacement with the sawtooth-like abnormalities (black line) and the 50 Hz GPS-only displacement (black dots) in the University of California, San Diego (UCSD) large shake table experiment (Bock et al. 2011)

The RTS smoother is a post-processing method and consists of a common forward Kalman filter (Figure 2.12.a) and a backward fixed-interval smoothing filter (Figure 2.12.b). The $\hat{X}_{0,0} \sim \hat{X}_{N,N}$ in Figure 2.12.a denote the state estimates at point 0~N with a total amount of 0~N measurements, for example, $\hat{X}_{5,5}$ means the states estimate at point 5 with six measurements (points 0~5) so far. Whereas the $\hat{X}_{0,N} \sim \hat{X}_{N,N}$ in Figure 2.12.b denote the smoothed state estimates at point 0~N with a fixed amount of N measurements, for example, $\hat{X}_{5,N}$ means the states estimate at point 5 with N+1 measurements (points 0~N) in the calculation. The smoother uses the processed forward filter information, such as the filtered estimates and the corresponding covariances, to do a backward estimate epoch by epoch and usually could obtain better solutions (Brown & Hwang 2012). However, although the smoothed results are usually more accurate than forward Kalman filtered results, the Kalman filter smoother is an after-event method, which requires the entire desired data series to calculate the optimal estimates, and the longer the time period, the longer the processing time (Shin 2005). Thus, instead of applying the smoothed Kalman filter, other methods, for example, an improved forward Kalman filter integration with proper error corrections, for data processing are seeking to provide the similar accuracy at near real-time.

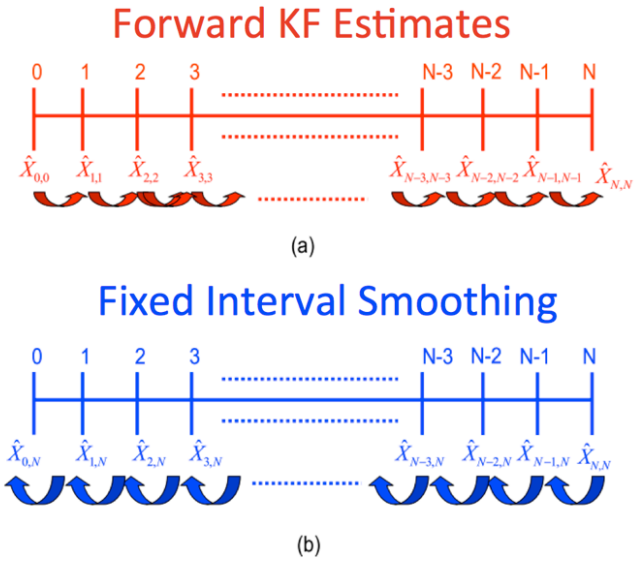

Figure 2.12: A forward Kalman filter and a backward smoother with state estiamtes at 0~N epochs (Li, 2009).

GPS aiding in inertial navigation systems (INS) has been investigated and implemented in the navigation field for about three decades, and the advantages and disadvantages of GPS and INS are complementary (Farrell & Barth 1999). An INS consists of an Inertial Measurement Unit (IMU) and navigation computers to estimate and output high-rate position, velocity, attitude, and attitude rate solutions. They have been applied widely in military and navigation fields (Grewal et al. 2001). An IMU contains two main components: gyroscopes and accelerometers for measuring the rotation and the specific force, respectively. The navigation computer calculates the navigation solution by using the orientation information, the local gravity vector, and the velocity and position from numerically integrating the acceleration (Gleason & Gebre-Egziabher 2009). The limitation of an INS is that while numerically integrating the acceleration, the sensor errors would be integrated at the same time, and the navigation solution drifts with time. Also, the price of an INS is usually proportional to its accuracy, especially that of the gyroscopes. Since GPS can be used for the initialisation of inertial navigation algorithms, and it is significantly cheaper to use accelerometers alone, the gyro-free INS/GPS (accelerometer/GPS) integrated system was developed (Mostov et al. 1997). However, the accuracy and precision of this gyro-free INS/GPS integrated system are not accurate and precise enough to be used for all navigation applications. Since gyros are much cheaper nowadays, partial IMUs (three accelerometers and one gyro) can be used for road vehicles. However, for earthquake monitoring, the GPS receivers and strong motion seismometers/accelerometers are always located in open-sky and more stable environments compared to navigation applications. Therefore, based on the knowledge and experience in the INS/GPS integration navigation fields, the techniques in INS/GPS integration have been modified to develop strong motion seismometer/GPS (accelerometer/GPS) integrated systems. Different combined techniques have been investigated and applied in structural and earthquake monitoring (Roberts et al. 2004;

Bock et al. 2011). In Roberts et al. (2004), the GPS antenna and an accelerometer in a designed cage were placed on a footbridge for the bridge structural dynamic and deflection monitoring. The GPS/accelerometer integration method in the paper used GPS velocity and position solutions to correct the baseline corrected and low-pass filtered accelerometer data: the numerically integrated velocity and position. This means the observations of sensors were processed separately first, and then the processed results were combined afterwards. Whereas Bock et al. (2011) used a Kalman filter algorithm (which has been widely used in navigation) to integrate the raw accelerometer data and DGPS solutions, which as shown earlier demonstrates the feasibility of the combined GPS/accelerometer technology for earthquake or structural monitoring. Table 2.2 summarises the features of strong motion seismometer /accelerometers and GPS, showing they are complementary.

Table 2.2: Comparisons of individual sensors and integrated system

	Accelerometer/Strong Motion Seismometer	**GPS**	**Integrated System**
Advantages	• High output rate (100-400 Hz) • Lower noise • Precise specific force measurements and acceleration outputs	• Measures position • Does not clip • Less susceptible to rotation	• High output rate (100-400 Hz) • Precise displacement, velocity, and acceleration outputs • A full-scale system: providing information at both high- and low-frequency ends
Disadvantages	• The bias of sensor may induce linear or quadratic errors on the numerically integrated velocity and displacement • The effect of sensor rotations or tilts on baseline corrections • May clip	• Low output rate (1-10 Hz) • Higher noise • Erroneous signals by multipath and time correlated noise	

2.8 Problem Statement and Study Aims

The Background and Literature Review section describes the heritage of both strong motion and GPS seismology. Building on that body of work, two major research questions are addressed in this study:

(1) In the rapid determination of ground displacement immediately after an earthquake, what improvement in performance can be achieved by integrating GPS and accelerometer instruments using an improved loosely-coupled Kalman filter compared to existing methods?

(2) Can a similar level of performance improvement be achieved during real earthquakes using the GPS observations from existing geodetic networks and strong motion seismometer data from existing seismic networks?

The overall aim in this study is to integrate accelerometer-based instruments (strong motion seismometers or accelerometers) with geodetic level GPS receivers to obtain real-time accurate ground displacements rapidly for accurate earthquake magnitude determination and tsunami early warning systems.

2.9 Study Objectives

In order to address the research questions and achieve the aims, the study objectives are described as follows:

- Develop a loosely-coupled accelerometer and GPS integrated Kalman filter algorithm to include the accelerometer baseline error correction in the Kalman filter algorithm;
- Develop a software package that includes the proposed loosely-coupled Kalman filter algorithm;
- Solve the time synchronisation problems between instruments;
- Validate the Kalman filter algorithm with experiments designed to suit different situations and uses;
- Test the data processing techniques on real earthquake observations from existing seismic and geodetic networks.

2.10 Overview of the Method

An improved loosely-coupled Kalman filter integration incorporating the built-in accelerometer baseline error correction will be developed. Experiments will be performed based on comparisons between the improved Kalman filter algorithm and other loosely-coupled Kalman filter methods. In the experiments, besides the strong motion seismometers, other low-cost accelerometer instruments are tested as well, such as new MEMS accelerometers. Furthermore, the loosely-coupled Kalman filter algorithm is designed to apply to real earthquakes using observations from existing earthquake monitoring networks to obtain ground displacements of improved accuracy.

2.10.1 Development of a Kalman filter algorithm and its software implementation

A major component of this study's objectives is to develop an improved loosely-coupled Kalman filter algorithm and to build the accelerometer baseline error correction into GPS/strong motion seismometer integration. The determination of the optimum

design and the parameter tuning of the algorithm will be approached based on knowledge and techniques of GPS/INS integration in the navigation field.

The proposed Kalman filter algorithm will be programmed into a software package and tested with observations from different instrument combinations, such as the strong motion seismometer and multi-frequency GPS receiver integration, or the MEMS accelerometers and multi-frequency GPS receiver integration. The Kalman filter tuning process is usually semi-empirical, and the initial values and error covariance are usually varied between instruments.

2.10.2 Time synchronisation approaches for tuning will be developed and tested between instruments

An anticipated and fundamental problem will be the time synchronisation between all the instruments while comparing the results from every sensor and combining either the strong motion seismometer or the accelerometer with the GPS. Groves (2013) pointed out that different navigation systems log data with varied time delays, and while using a Kalman filter algorithm within the data processing, a communication delay might occur. Generally speaking, not only in navigation solutions, time synchronisation is a critical issue in any kind of multi-sensor implementation, especially when a Kalman filter processor is implemented in the application. For example, the timing systems and the sampling rates between sensors are different, or using sensors in the same timing system but with different sampling rates or with simply offsets. Hence, a time synchronisation method must be developed, and several physical and numerical methods could be applied to solve this difficulty, which will be investigated and considered further in this research.

2.10.3 Validation of the Kalman filter algorithm via designed experiments

As it is difficult to obtain true movements in real earthquakes, designed and controlled experiments with collocated accelerometers/strong motion seismometers and GPS receivers will be implemented before applying the proposed Kalman filter algorithm on real earthquakes. In the designed experiments, displacement truth models can be provided to validate the performance and accuracy of the proposed Kalman filter algorithm. Furthermore, according to the different dimensions of the data resources, the proposed Kalman filter algorithm needs to be modified and adapted to the computations. Corresponding file readers and processors for different data resources are also required to obtain the correct data format for feeding the proposed Kalman filter technique.

2.10.4 Tests of data processing techniques on real earthquake data of the existing seismic and geodetic networks

The core algorithm is aimed to provide accurate displacement results for determining the magnitude of an earthquake rapidly. Hence, experiments with real earthquake data sets from existing strong motion seismometer networks and existing GPS networks, e.g. USGS networks, for providing accurate ground displacements will be carried out. Collocated strong motion seismometer stations and GPS stations (distances < 500 m) in the networks are desired. The GPS and strong motion seismometer integrated solutions will be compared with results provided by geological institutes or those published in international journals to show if any improvement has been achieved by the proposed Kalman filter during real earthquakes.

2.11 Summary

This chapter has introduced the background and also reviewed the literature of strong motion seismology, GPS seismology, and accelerometer-based instruments/GPS integration applied to seismology. The limitation of current seismic and GPS networks in seismological applications has been described. This research is focusing on using the integration of accelerometer instruments and GPS to improve the current limitations in seismological field, for example, providing accurate displacements rapidly for determining the magnitude of an earthquake.

In this chapter, the research problems, aims, and objectives of this study have also been addressed. An overview of the methods used in the research has been given.

Chapter 3 will present in detail the main methodology of this study, including the fundamental Kalman filter algorithm, the Kalman filter integrations, and the proposed Kalman filter algorithm with the accelerometer baseline error correction.

Chapter 3 Integration Method

In this study, the Kalman filter algorithm is the core estimation engine for the integrated system. This section describes the Kalman filter and its architectures comprehensively. Besides the Kalman filter algorithm, the instrument integration architecture is developed based on knowledge of the field of GNSS/INS navigation. Nowadays, depending on diverse system requirements and measurements, several integration architectures have been developed for navigation or other applications, such as uncoupled, loosely-coupled, and tightly-coupled systems (Farrell & Barth, 1999). This study will focus on the loosely-coupled integration particularly, which will be illustrated in detail in this chapter. Most symbols, equations, and algorithms in this study are based on Groves (2013). Deeper discussion and more complete descriptions of other integration schemes

can be found in some navigation textbooks, such as Farrell (2008), Gleason and Gebre-Egziabher (2009), and Groves (2013).

3.1 Kalman Filter Algorithm

The Kalman filter first proposed by R. E. Kalman in 1960 is a numerical technique to correct measurements and predict optimal estimations (Kalman 1960). After half a century, the Kalman filter has been widely applied and become one of the main algorithms in the control systems and integrated navigation fields (Welch & Bishop 1995). Figure 3.1 shows the standard Kalman filter algorithm based on Groves (2013). The steps and equations of the algorithm are then introduced and described in detail in the following sections.

A standard Kalman filter can be divided into three parts: **initialisation, system propagation** (also known as the time propagation), **and correction** (also known as the measurement update). The initialisation includes setting up the initial state vector and error covariance matrix. The state vector is a set of numbers that quantifies the state of a system, e.g. its position, velocity, acceleration and noise, which is designed based on different systems or requirements. For example, in this study, the state vector consists of the estimates of displacement, velocity, and acceleration bias. The error covariance matrix shows the uncertainties and the error distribution of the estimates in the state vector, and it also describes the error correlations between the estimates. For example, the diagonal elements of the covariance matrix in this study describe the uncertainties of the displacement, velocity, and acceleration bias; the off-diagonal coefficients in the matrix show the error correlations between the state estimates.

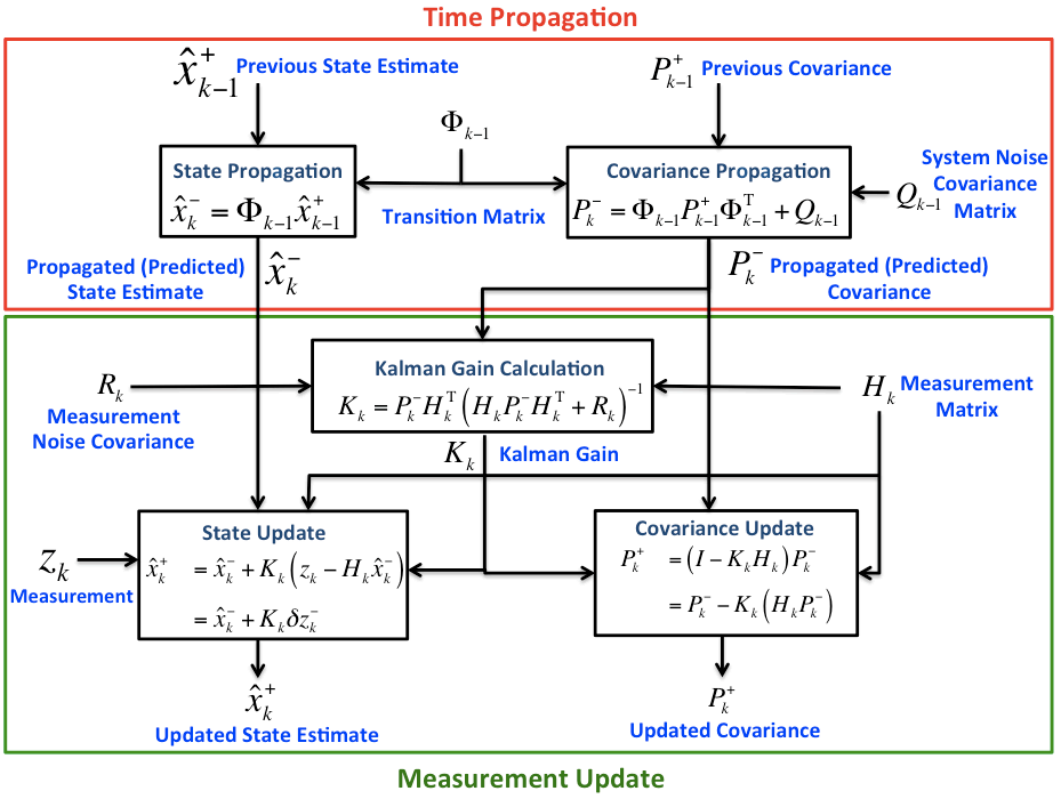

Figure 3.1: Kalman filter integration algorithm (after Groves (2013))

The **system propagation** is a time-propagation method modelling the changes in the Kalman filter state vector and error covariance matrix with time. The system model is also known as a prediction process, which uses the known information of the previous state to predict the next state until there is a new measurement available. During this period, due to the absence of new measurement information, the uncertainties in the state and system could be built up since there might be some unknown or unexpected errors between the truth and the state estimate. When a measurement and its uncertainty have input into the processing, a **measurement innovation** is calculated using the measurement data and predicted state. At the same time, the noise covariance of the measurement will be used to calculate with the estimated covariance and obtain a weighting parameter, known as the **Kalman gain**. The measurement innovation and predicted covariance are then weighted by the Kalman gain to update the predicted state and covariance for the optimal solution. This process is known as **correction or measurement update** of a Kalman filter. After the measurement update, the updated estimate and covariance are used as the previous estimate and covariance in the next iteration.

In this study, for example, the displacement state is numerically integrated using the velocity state, and the velocity state is the integral of the acceleration from the accelerometer or seismometer. Hence, whenever there is an acceleration input, the system model will calculate the predicted displacement and velocity states based on the acceleration input and the sampling rate of the acceleration. The uncertainties of the

displacement and velocity should be accumulated with time, as the uncertainties will also be integrated with time. Once a measurement input (GPS displacement solution) is available, the predicted state vector (displacement, velocity, and baseline error) and covariance will be updated according to the measurement noise covariance and the predicted covariance. The corrected state vector and covariance will be the optimal estimates for this epoch, and they will be used as the previous estimate and covariance for the next epoch.

An example showing the relationships between initialisation, propagation, measurement update, and the iterations of a Kalman filter algorithm can be seen in Figure 3.2. In Figure 3.2, the inputs and outputs of estimates and covariance are at 5 Hz sampling rate, and the measurement is at 1 Hz sampling rate.

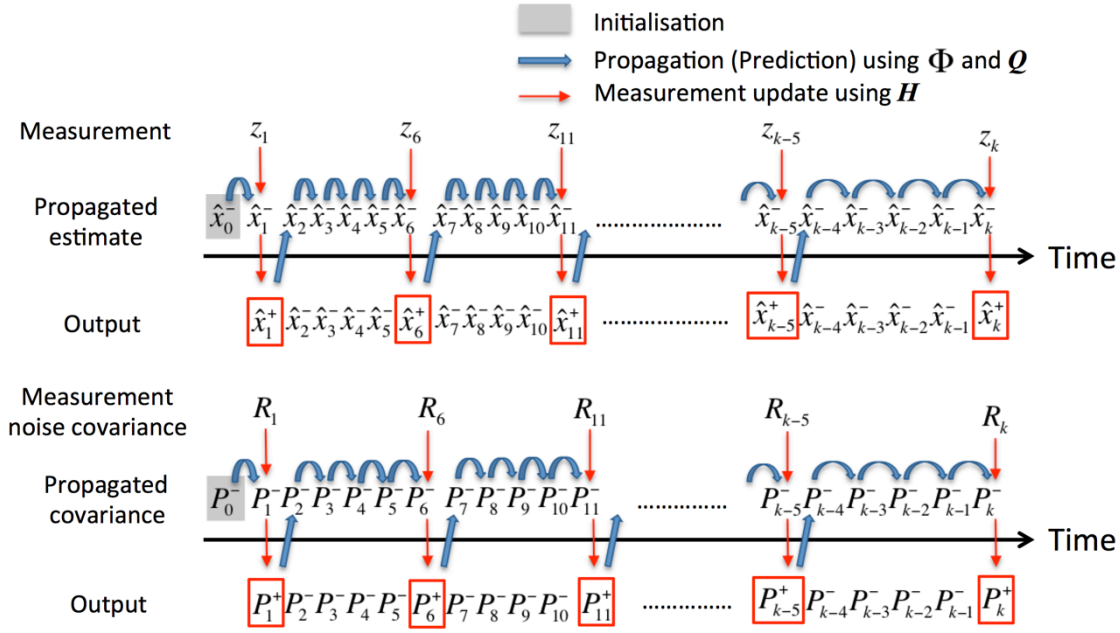

Figure 3.2: An example of the initialisation, system propagation and measurement update of a standard Kalman filter; symbols are referred to Figure 3.1

3.2 System Model

With reference to Figure 3.1, both the system and measurement updates of the Kalman filter algorithm consist of several steps. The Kalman filter algorithm can be divided into the system model and the measurement model. The system model is used for the time propagation, whereas the measurement model is a model of the measurement in terms of the state. This and the following section aim to introduce the system and measurement models comprehensively by explaining each step and the corresponding equations. All notations, equations, and definitions in these two sections are based on *Chapter 3 Kalman Filter-Based Estimation* in Groves (2013).

A standard Kalman filter is a linear algorithm that assumes states are derived from a linear function of other states and white noise. Following the formulation in Maybeck

(1982) and Lewis et al. (2007), Eq. 3-1 describes the discrete system dynamic model of the Kalman filter used in this study:

$$x_k = F_{k-1}x_{k-1} + B_{k-1}u_{k-1} + G_{k-1}w_{s,k-1} \tag{3-1}$$

where

x_{k-1}: the true state *n*-vector;

F_{k-1}: the system matrix ($n \times n$) at the previous epoch ;

B_{k-1}: the control input matrix ($n \times m$) at the previous epoch (k-1)

u_{k-1}: the control input *m*-vector;

G_{k-1}: the system noise distribution matrix ($n \times l$);

$w_{s,k-1}$: the system noise *l*-vector, with an assumed zero-mean Gaussian distribution.

The design of the system model is based on the known properties of the true state vector and its correlation to the known functions, *F, B,* and *G*. The control input vector is known as the system input, which is the raw accelerometer output in this study.

At the initialisation of the filter, the initial state vector and the initial covariance can be defined according to some assumptions and statistics. For example, the initial state vector is usually set as zero in Kalman filter implementations of this study by assuming there is zero displacement, velocity, and acceleration prior the earthquake as shown in Eq. (3-2). The initial covariance is the expectation of the state vector residual between the initial state and the true state, as shown in Eq. (3-3).

$$\hat{x}_0^- = \begin{bmatrix} 0_1 \\ \vdots \\ 0_n \end{bmatrix} \tag{3-2}$$

$$P_0^- = E[(\hat{x}_0^- - x_0)(\hat{x}_0^- - x_0)^T] = E[\delta\hat{x}_0^-(\delta\hat{x}_0^-)^T] \tag{3-3}$$

where

$\hat{x}_0^-$: the initial predicted state *n*-vector estimate;

P_0^-: the initial predicted error covariance matrix;

E: the expectation operator;

x_0: the first true value of the state vector;

$\delta\hat{x}_0^-$: the state vector residual, the difference between the true values and the estimate.

The state error covariance, *P*, is always a symmetric matrix, and the diagonal elements of the matrix consists of the state variances; the off-diagonal elements of the matrix describe how one state estimate error is correlated with another state estimate error:

$$P_{ii} = \sigma_i^2 \tag{3-4}$$

$$P_{ij} = P_{ji} = \sigma_i \sigma_j \rho_{i,j} \tag{3-5}$$

where

σ_i and σ_j are the uncertainties of the *i*th and *j*th state estimates;

$\rho_{i,j}$ is the correlation coefficient between the *i*th and *j*th state estimates.

The Kalman filter estimate is denoted $\hat{x}$, and $\hat{x}_k^-$ and P_k^- represent the time-propagated state estimates and error covariance, whereas the measurement updated estimates and error covariance are denoted $\hat{x}_k^+$ and P_k^+. In the system model, following Maybeck (1982), Lewis et al. (2007), and Groves (2013), the first step is to derive the **transition matrix**, **control input matrix**, and **system noise covariance matrix**:

$$\Phi_{k-1} = e^{F_{k-1}\tau_s} \tag{3-6}$$

$$B_{k-1} = \int_0^{\tau_s} e^{F_{k-1}t} B_{k-1} dt \tag{3-7}$$

$$Q_{k-1} = E[w_k w_k^T] \tag{3-8}$$

where

Φ_{k-1} : the state transition matrix at the previous epoch (k−1);

τ_s : the propagation interval;

Q_{k-1} : the system noise covariance matrix at the previous epoch (k−1).

The state transition matrix, Φ_{k-1}, expresses the changes with time between observations and time-propagated estimates. The propagation interval, τ_s, is the time interval between observations for the system update. The system noise covariance matrix, Q_{k-1}, describes how the uncertainties of state estimate might accumulate during the propagation due to any unknown parameter that is not estimated as a state. These parameters are assumed by the Kalman filter to be white noise.

The state estimate and covariance at the previous epoch ($k-1$) are then propagated to the current epoch (k) using

$$\hat{x}_k^- = \Phi_{k-1}\hat{x}_{k-1}^+ + B_{k-1}u_{k-1} \tag{3-9}$$

$$P_k^- = \Phi_{k-1}P_{k-1}^+\Phi_{k-1}^{\mathrm{T}} + Q_{k-1} \tag{3-10}$$

where

$\hat{x}_k^-$: the propagated state estimate;

$\hat{x}_{k-1}^+$: the previous state estimate;

P_k^- : the propagated state error covariance;

P_{k-1}^+ : the previous state error covariance.

3.3 Measurement Model

After the system propagation, the measurement model is then used to correct the predicted estimate and covariance. The measurement model at discrete intervals at the current epoch (k) is as follows:

$$z_k = H_k x_k + w_{mk} \tag{3-11}$$

where

z_k : the measurement p-vector;

H_k : the measurement matrix ($p \times n$);

w_{mk} : the white noise sources of measurements.

The measurement matrix relates the measurement vector and the state vector. The measurement noise covariance is the expectation of the measurement error vector, and the covariance matrix is defined as

$$R = E[(z_k - H_k x_k)(z_k - H_k x_k)^T] = E[w_m w_m^T] \tag{3-12}$$

where

R_k is the measurement noise covariance matrix.

The Kalman gain for weighting and updating the predicted estimate and covariance is:

$$K_k = P_k^- H_k^{\mathrm{T}} \left(H_k P_k^- H_k^{\mathrm{T}} + R_k \right)^{-1} \tag{3-13}$$

The predicted state estimate and covariance are then updated by using the Kalman gain to weight the measurement innovation and predicted covariance, respectively:

$$\begin{aligned} \hat{x}_k^+ &= \hat{x}_k^- + K_k \left(z_k - H_k \hat{x}_k^- \right) \\ &= \hat{x}_k^- + K_k \delta z_k^- \end{aligned} \tag{3-14}$$

$$\begin{aligned} P_k^+ &= \left(I - K_k H_k \right) P_k^- \\ &= P_k^- - K_k \left(H_k P_k^- \right) \end{aligned} \tag{3-15}$$

where

$\hat{x}_k^+$: the updated state estimate;

δz_k^- : the measurement innovation;

P_k^+ : the updated state error covariance.

The measurement innovation, δz_k^-, describes the difference between the measurement and the predicted state estimate. The updated state estimate and covariance are the optimal solutions for the current epoch. As shown in Figure 3.2, the updated solutions will be used as the previous state estimate and its error covariance in the next iteration.

3.4 Open-Loop and Closed-Loop Correction Architectures

The Kalman filter algorithm for multi-sensor integrated systems can usually be divided into the open-loop and closed-loop schemes based on the feedback and correction methods in the algorithm. In the open-loop scheme (Figure 3.3), the computed velocity and position of the strong motion seismometer/IMU/accelerometer are corrected by GPS position solutions and velocity solutions in the integration Kalman filter without computed acceleration measurement feedback. On the contrary, in the closed-loop correction depicted in Figure 3.4, the integrated Kalman filtered outputs are fed back to correct the measurements of the strong motion seismometer/IMU/accelerometers. The state elements and the linearization errors of the system model are decreased in the closed-loop correction. In this study, the closed-loop correction is implemented in the loosely coupled Kalman filter, which will be introduced in the next section.

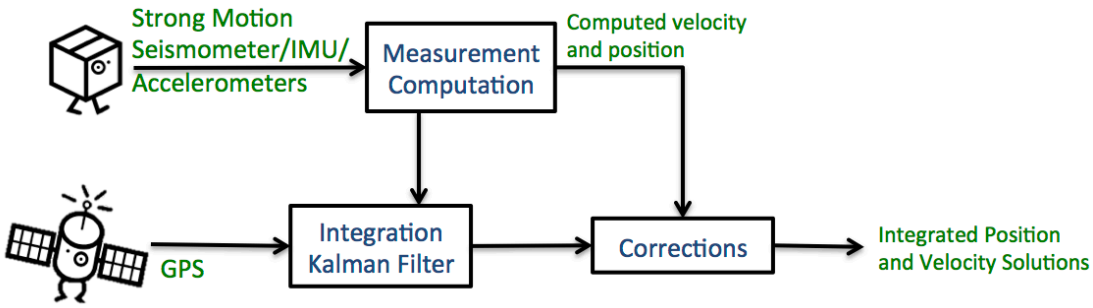

Figure 3.3: Open-loop correction scheme

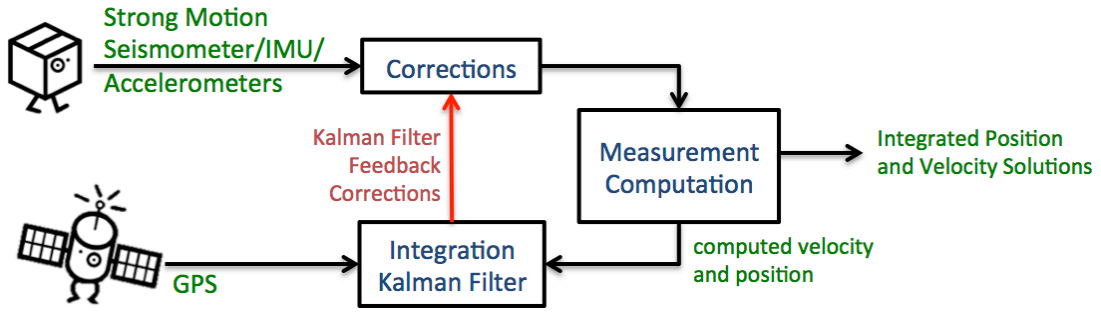

Figure 3.4: Closed-loop correction scheme

3.5 Loosely Coupled Integration

Loosely coupled integration has been developed and implemented widely in current navigation applications. In loosely coupled integration (Figure 3.5), the accelerometers measure the specific force and use a gravity model to derive the acceleration from specific force for computing the velocity and position or displacement numerically. Meanwhile, the GPS provides the displacement/position and velocity solutions using an individual positioning algorithm. In many navigation applications, both computed positions and velocities are then inputs to the integration Kalman filter. In this study, the small and sudden movement of the sensors is the most important and interesting issue; therefore, instead of inputting the GPS position and velocity solution, the computed GPS solution is the displacement of GPS receiver. Over long observation periods, the displacements or positions and velocities of GPS have less drift and are more stable than the displacement or position and velocity derived from acceleration sensors. Therefore, the GPS solutions are used for the measurement updates in the Kalman filter calculation to correct the rapid drifts from acceleration integrals. Compared to other integration architectures, the loosely coupled is relatively simple to implement; furthermore, it provides independent GPS navigation solutions from the separate GPS Kalman filter. However, since the integration Kalman filter requires the displacements or positions and velocities from the GPS Kalman filter, the observability of GPS

receivers becomes critical in the loosely coupled integration. At least four satellite measurements are necessary for a sustainable GPS navigation solution. If there are no GPS solutions inputting to the integration Kalman filter, the displacement or position and velocity solutions will be numerically calculated from the measurements of the accelerometers only, which may lead to linear or quadratic drifts in the integrated solution.

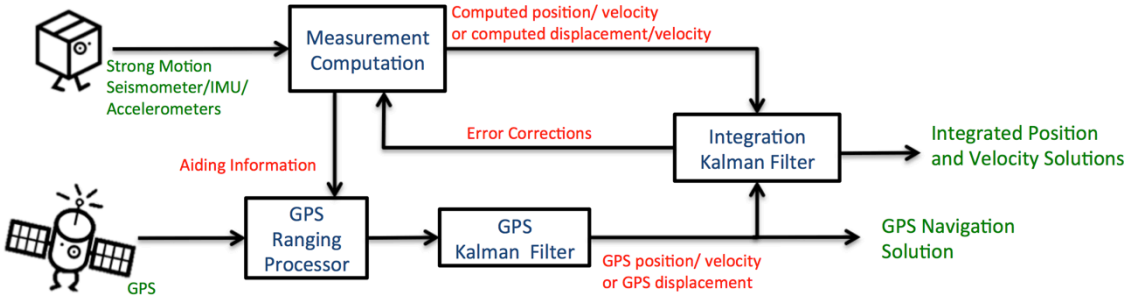

Figure 3.5: Closed-loop loosely coupled integration

3.6 Tightly Coupled Integration

Figure 3.6 shows the tightly coupled integration architecture. Unlike a loosely coupled integration, in tightly coupled integration, there is no separate GPS Kalman filter. The observations from the GPS ranging processor, GPS pseudo-range and pseudo-range rates, are input to the integration Kalman filter to correct the position and velocity computed from the accelerometer measurements. The tightly coupled integration decreases the potential error propagation problems by implementing one Kalman filter. Furthermore, since GPS solutions are no longer required, the tightly coupled integration can provide integrated solutions even while there is only one satellite observable. For navigation applications, a tightly coupled integration algorithm is usually more stable than a loosely coupled integration algorithm, especially in urban canyons where GPS signals are blocked or reflected by tall buildings (as previously shown in Figure 2.8). However, for seismological applications, for example the integrated GPS and seismometer system in this study, most geodetic GPS receivers are located in open-sky fields. The GPS solutions are usually achievable for inputting a loosely coupled Kalman filter. In this case, the advantage of using a tightly coupled Kalman filter might not be that significant. Recently, some seismogeodetic approaches of applying a tightly coupled Kalman filter GPS/accelerometer integration to obtain the precise and accurate displacements have been investigated in Geng et al. (2013) and Tu and Chen (2014). This study will focus on improving the precision and accuracy of the displacement solutions via estimating the baseline error in a loosely coupled Kalman filter integration.

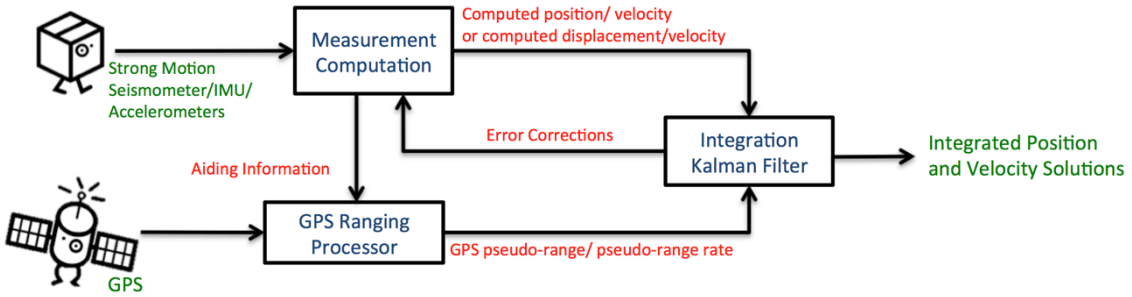

Figure 3.6: Closed-loop tightly coupled integration

3.7 Baseline Error State Estimate

As discussed in Chapter 2, although the traditional baseline correction could eliminate the baseline offsets from the accelerometer data, there are other issues to be considered as well. First, as the traditional baseline correction removes the mean of the acceleration and velocity for minimizing the linear or quadratic effects from the numerical integrals, the true movements of the earthquakes might be filtered out at the same time. Second, the baseline may be changed during or after shaking, which means that the average of the acceleration will be varied. The lack of additional information, such as the tilt or rotation angles of the instrument, may lead the baseline correction to be invalid while there are sensor biases or tilts. Hence, to reduce the effects from the baseline error, other correction methods are needed for adjusting the bias or error of the measurements.

Generally speaking, the accelerometer baseline error might include a combination of the sensor bias, scale factor errors, cross-coupling error and tilts of instruments. Some of the instrument bias presents a constant error in the sensor, which is independent of forces; some of it is temperature dependent; some of it changes when turning the instrument off and on; some of it varies slowly. The scale factor error refers to a gradient difference between the inputs and outputs, which does not depend on the forces and will be propagated throughout the true measurements of the sensor. The cross-coupling error is a sinusoidal function of the misalignment error, which is due to the misalignment of the sensor's vertical and horizontal axes (Groves 2013). The conventional correction method assumes that the instrument bias is not changing overtime, however, in the reality, the rapid shaking of earthquakes often causes the instruments to tilt and affects the specific force of the sensor as well as the processing to determine its acceleration outputs. A more sophisticated method to evaluate the baseline error is using an additional state to estimate the baseline error on each iteration in the Kalman filter algorithm. The aim is to include a new parameter in the Kalman filter state: the baseline error state, $\boldsymbol{b}$, to absorb all the instrumental biases and errors. This approach is similar to the method used in navigation systems; however, in navigation, the accelerometer biases and attitude errors are estimated as separate states. With the baseline error state estimate, a pre-event mean is not required to be subtracted from the

raw acceleration outputs. The baseline error will be estimated and used to correct the measurements during each Kalman filter calculation.

3.8 Loosely Coupled Kalman Filter with a Baseline Error State

This section will explain the implementation of the loosely coupled Kalman filter algorithm with the baseline error state adopted in this study. The algorithm in this section can be adjusted into one-dimension (1D), two-dimension (2D), or three-dimension (3D), depending on the implementations and data resources. For example, it is one-dimensional computation in Chapter 4 and three-dimensional computation in Chapter 5 and 6. A total-state Kalman filter has been implemented, and the state vector, displacement, velocity, and baseline error are defined as follow:

$$x_k = \begin{bmatrix} d \\ v \\ b \end{bmatrix}_k \tag{3-16}$$

where

x_k : the state vector;

d : the computed displacement of the accelerometer;

v : the computed velocity of the accelerometer;

b : the baseline error state of the accelerometer;

k : the epoch of the accelerometer.

According to Eq. (3-1), the system model for the loosely coupled Kalman filter in this study is defined as below:

$$\begin{bmatrix} d \\ v \\ b \end{bmatrix}_k = \begin{bmatrix} 1 & \delta t_a & \frac{-\delta t_a^2}{2} \\ 0 & 1 & -\delta t_a \\ 0 & 0 & 1 \end{bmatrix}_{k-1} \begin{bmatrix} d \\ v \\ b \end{bmatrix}_{k-1} + \begin{bmatrix} \frac{\delta t_a^2}{2} \\ \delta t_a \\ 0 \end{bmatrix} a_{k-1} + \begin{bmatrix} \frac{\delta t_a^2}{2} \\ \delta t_a \\ 0 \end{bmatrix} w_{acc,k-1} \tag{3-17}$$

where

δt_a : the time interval of the accelerometer measurements;

a_{k-1} : the acceleration measurement;

$w_{acc,k-1}$: the associated measurement noise of the accelerometer.

A critical part is to define the system and measurement noise covariance. With reference to Groves (2013), the system noise covariance matrix is formulated as:

$$Q_{k-1} = \begin{bmatrix} \frac{q_a \delta t_a^3}{3} & \frac{q_a \delta t_a^2}{2} & 0 \\ \frac{q_a \delta t_a^2}{2} & q_a \delta t_a & 0 \\ 0 & 0 & q_b \delta t_a \end{bmatrix} \tag{3-18}$$

where

q_a is the power spectral density (PSD) of the accelerometer noise (in m^2s^{-3});

q_b is the PSD of the accelerometer baseline error variation (in m^2s^{-3}).

A way to determine the initial q_a is to log the accelerometer noise during static periods and obtain the PSD, or it can be determined based on the accelerometer laboratory datasheet provided by the manufacturers. For determining the initial q_b, it can be calculated from the standard deviation of the baseline error during static periods and obtain the PSD of the baseline error variation. As the accelerometer provides the inputs for the system model, GPS provides the inputs into the measurement model. The measurement inputs are the GPS displacements calculated from GPS position solutions, and the measurement model based on Eq. (3-11) can be illustrated as follows:

$$H_k = \begin{bmatrix} 1 & 0 & 0 \end{bmatrix}_k \tag{3-19}$$

$$z_k = \begin{bmatrix} 1 & 0 & 0 \end{bmatrix}_k \begin{bmatrix} d \\ v \\ b \end{bmatrix}_k + w_{GPS} \tag{3-20}$$

where

H_k : the measurement matrix;

z_k : the displacement measurement from GPS position solutions;

w_{GPS} : the GPS measurement noise.

With reference to *Chapter 14 INS/GNSS Integration* in Groves (2013), ideally, the measurement noise covariance accounts for the error covariance of the GPS solution. However, in reality, the measurement noise covariance is hardly achievable purely by the error covariance of the GPS solution. The time synchronisation errors and the dynamic excitements between GPS receivers and accelerometers while shaking are accounted for in the measurement noise covariance as well. Thus, the measurement noise covariance is determined as a product of the GPS position error variance (m^2), the error correlation time (s), and the output rate (Hz) of the GPS measurement. Usually, the measurement noise covariance is determined with an empirical constant:

$$R_k = R_{GPS} \tag{3-21}$$

where R_{GPS} is the measurement noise covariance of GPS.

Based on the data sets provided in the experiments, in Chapter 4, the adapted equations and the integrated results are in the 1D domain. The detailed 3D loosely coupled integration based on the Kalman filter algorithms in this section is performed in Chapter 5 and 6.

3.9 Kalman Smoothing

As described in previous sections, the Kalman filter is a forward filter providing real-time solutions. It can predict and update estimates continuously until there is no more input. For post-processing and testing during certain time periods, a Kalman smoother can also be applied for improving the accuracy of solutions. The Kalman smoother is a forward-backward filter that uses the forward filtered information to reduce the errors or drifts in the solutions. An example is shown in Figure 3.7. When GPS measurements are not available in a GPS/accelerometer integrated Kalman filter, the position/ displacement error may increase rapidly with time. After smoothing, the error and the uncertainty of state decrease. The Kalman smoother uses the solved estimates and covariance of the entire desired period from the forward Kalman filter. A key point here is that the forward Kalman filter uses only measurement data from before the time of interest, whereas, the smoother uses measurement data from before and after. Hence, the Kalman smoother is usually used to obtain the optimal but non-real-time solutions. The forward-backward filter and Rauch, Tung, and Striebel (RTS) smoother are the most commonly used techniques (Rauch et al. 1965). In this study, the RTS smoother is used and explained in the following section. Details about the forward-backward filter can be found in Fraser and Potter (1969) and Gelb (1974).

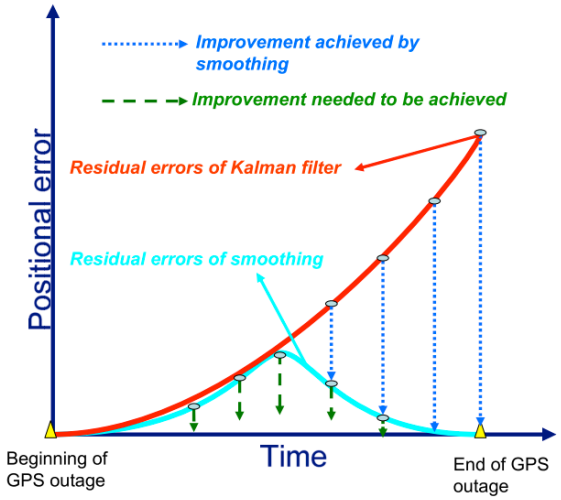

Figure 3.7: An example of the positional error before and after applying a Kalman smoother (Chiang et al. 2010)

3.9.1 Rauch, Tung, and Striebel (RTS) smoother

The RTS smoother is a fixed-interval backward filter method for linear dynamic systems, such as Kalman filter (Rauch et al. 1965). As shown in Figure 3.8, a series of data is processed via a forward Kalman filter first, and the state estimates, x, error covariance, P, and transition matrix, Φ, are stored after the system propagation and measurement update on each iteration. After forward Kalman filtering, the smoother begins the backward filtering from the last epoch ($t = N$) to the first epoch ($t = 0$). The $\hat{x}_{0,0} \sim \hat{x}_{N,N}$ in Figure 3.8 represent the state estimates at point 0~N with unlimited 0~N measurements, for example, $\hat{x}_{5,5}$ means the states estimate at point 5 with six measurements (points 0~5) so far. Whereas the $\hat{X}_{0,N} \sim \hat{X}_{N,N}$ in Figure 2.12.b denote the smoothed state estimates at point 0~N with a fixed amount of N measurements, for example, $\hat{X}_{5,N}$ means the states estimate at point 5 with N+1 measurements (points 0~N) in the calculation. The following contents and algorithms are with reference to Brown and Hwang (2012) and Groves (2013).

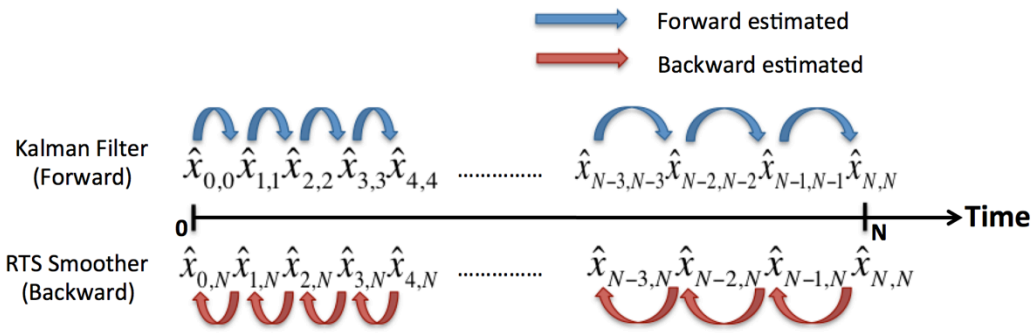

Figure 3.8: The state estimates of a Kalman filter and an RTS smoother

In an RTS smoother, a smoothing gain is derived by the Kalman filtered predicted and updated noise covariance and transition matrix. The smoothing gain defines the weight of the difference between the smoothed state estimate at epoch (k+1) and the Kalman filter updated state estimate at epoch (k+1):

$$A_k = P_k^+ \Phi_k^T (P_{k+1}^-)^{-1} \tag{3-22}$$

where A_k is the smoothing gain.

The initial smoothed state estimate is the last forward filtered estimate, $\hat{x}_{N,N}^s = \hat{x}_N^+$. The smoothed state estimate, for $k = N-1, N-2 \ldots\ldots 0$, is given by:

$$\hat{x}_{k,N}^s = \hat{x}_k^+ + A_k(\hat{x}_{k+1,N}^s - \hat{x}_{k+1}^-) \tag{3-23}$$

where $\hat{x}_{k,N}^s$ is the smoothed state estimate.

For the error covariance, the first smoothed error covariance is also the error covariance from the last epoch, $P_{N,N}^s = P_N^+$. The error covariance matrix propagation is:

$$P_{k,N}^s = P_k^+ + A_k(P_{k+1,N}^s - P_{k+1}^-)A_k^T \tag{3-24}$$

where $P_{k,N}^s$ is the smoothed error covariance for $k = N-1, N-2, N-3 \ldots\ldots 0$.

The advantage of using an RTS smoother is that it processes the measurements with the information from both before and after the time of interest instead of the entire period. The RTS smoother can improve the forward filtered estimates and derive the optimal solutions more efficiently than other forward-backward filters. However, the smoother requires more processing power and time than a basic Kalman filter. Therefore, for a real time implementation in this study, the smoothed Kalman filter solutions are used as a truth model in some experiments to test and validate the proposed forward Kalman filtered solutions.

3.10 Software Tools and Data Sources

The software tools, including the methods and implementations, that were developed in this research are presented in this section. As there was no existing software package that contained the functions of the proposed Kalman filter integration, the developing and testing of the new software was the primary task of this study. The developed software package contains several core functions, including data-fetching, Kalman filter calculations, data-storing, and numerical analysis. This software that comprised several

scripts and modules was programmed in Python and Matlab. Figure 3.9 illustrates the flow chart of the software used in this study.

Figure 3.9 shows that the data-fetching process involves the files from the two main instruments used in this study: GPS/GNSS and accelerometer-based sensors. For GPS, apart from the GPS displacement files in Chapter 4 which was given by the UCSD, all other GPS/GNSS displacement solutions provided by Christopher Atkins using a PPP software developed by Dr. Alexander Parkins and Christopher Atkins in the Space Geodesy and Navigation Laboratory at the Department of Civil, Environmental and Geomatic Engineering of University College London (UCL). Detailed information related to the PPP processing and the developed software used in this study are described and given in Section 5.1.3.

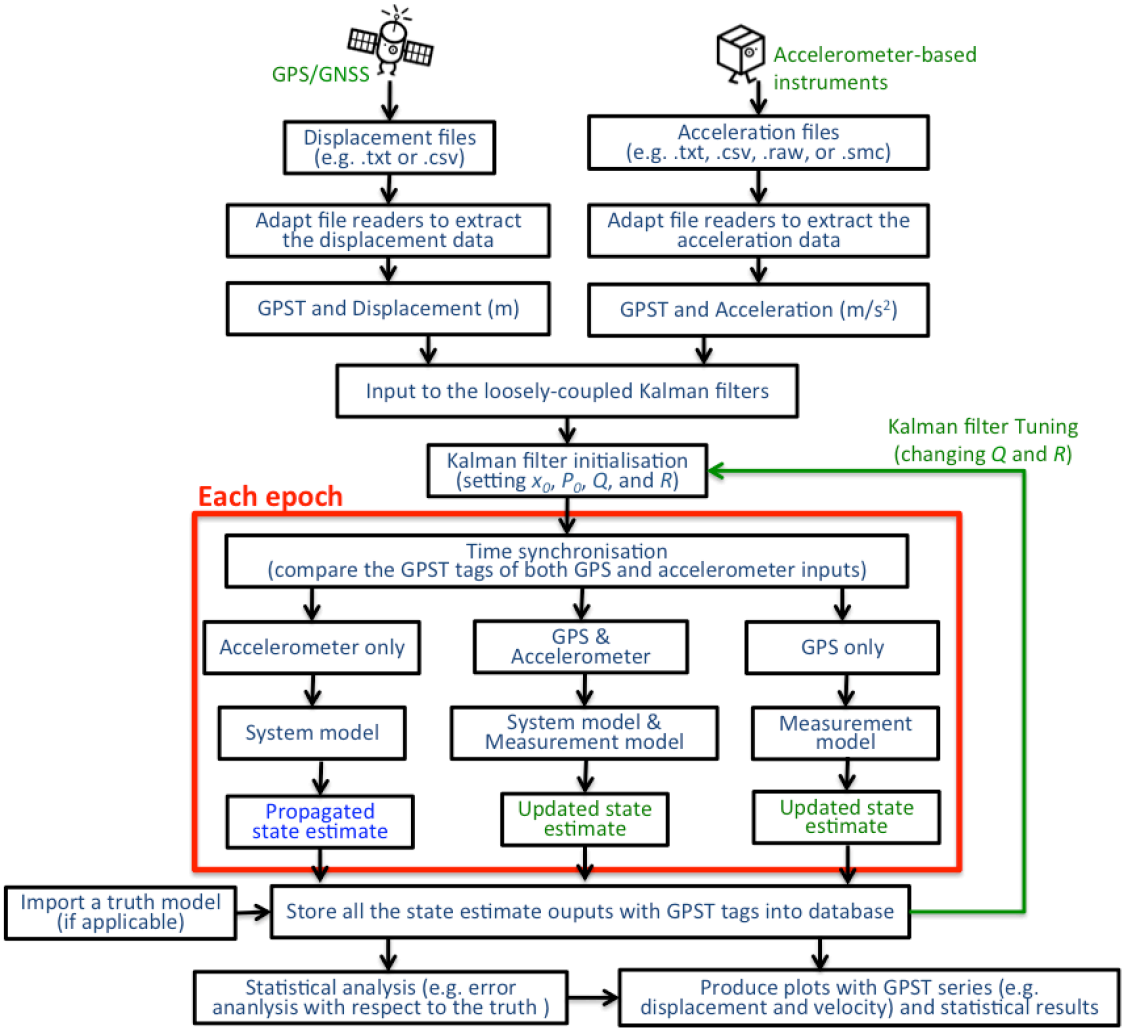

Figure 3.9: A flow diagram of the software developed and used in this study

The GPS/GNSS displacement solutions with GPS time (GPST) tags are usually archived in .txt or .csv format. File readers were adapted to extract the GPS displacement data with the corresponding GPST and to store them in a database. For accelerometer-based instruments, the acceleration files were often archived in various

formats due to the variety of the accelerometer-based instruments, including accelerometers, IMU, and strong motion seismometers. For example, based on the acceleration files received in this study, the acceleration file formats in Chapter 4, Chapter 5, and Chapter 6 were .txt, .smc, and .raw, respectively. Normally, the three-axial (also known as three-channels) accelerations are archived in three acceleration files separately. Thus, the acceleration file readers were usually rewritten to extract the acceleration data from different file formats and to store the data with the corresponding GPST tags in the database.

The stored GPS displacements and accelerations were then input into the Kalman filter calculation as shown in Figure 3.9. The Kalman filter calculation, as described in Sections 3.1~3.3, involves the Kalman filter initialisation, the system model, and the measurement model. After the initialisation, the GPS displacement and acceleration data sets in the database were then input to the time synchronisation function according to the sequence of their GPST tags. Noted that only one GPST tag (one epoch) was input to the time synchronisation process, and each epoch might contain acceleration only, GPS displacement only, or both GPS displacement and acceleration. As displayed in Figure 3.9, if there was only acceleration available at this epoch, the Kalman filter would only process the system model and output the propagated state estimates. Whereas, if only GPS displacement was available at the epoch, the Kalman filter would update the previous propagated state estimate. For the epoch that contained both observations, the Kalman filter would run both system and measurement models and provide the updated state estimate. The Kalman filter calculation would be implemented repeatedly for each epoch until the last epoch of data sets. Finally, all the state estimate outputs, including the propagated and updated state estimate outputs from each epoch, were stored into a GPST-series in the database for further statistical analysis.

The developed software has been adapted and implemented in every experiment in this study. Furthermore, as there were some similarities between the software programmed in this study and the code for the UCSD large shake table project in Bock et al. (2011), the results of the two were compared to validate the developed software tools.

3.11 Summary

This chapter has described the fundamental Kalman filter algorithm and its architecture comprehensively. Besides the Kalman filter algorithm, different instrument integration architectures are also introduced. The main method for the integrated system, a loosely-coupled Kalman filter algorithm with the accelerometer baseline correction, has been proposed in this chapter as well. The improved loosely-coupled Kalman filter algorithm with the accelerometer baseline error state estimate has been described in detail in this chapter. Furthermore, a smoothing technique, RTS smoother, for providing smooth and accurate solutions has also been presented.

A software package has been developed in this study based on the proposed Kalman filter algorithm via programming languages, Python and Matlab. Later in Chapter 4 and Chapter 5, two designed experiments will be carried out for testing and validating the proposed Kalman filter algorithm. After validating the proposed Kalman filter algorithm with the controlled experiments, the developed software will be implemented with a real earthquake data set in Chapter 6.

Chapter 4 UCSD's Large Outdoor Shake Table Experiment

For validating the proposed Kalman filter algorithm, collocated GPS and accelerometer data sets have been searched for at the beginning of this study. After contacting the authors of Bock et al. (2011), the authors have generously provided the data sets of their large shake table experiment and the code they used to analyse the data. The data sets will be used to validate this study's algorithm and also to investigate the performance of each method with respect to a displacement truth model.

4.1 Experiment Introduction

In 2003, the George E. Brown, Jr. Network for Earthquake Engineering Simulation (NEES) project established and simulated earthquake measurements from the Large High Performance Outdoor Shake Table (LHPOST) (Einde et al. 2004; Ozcelik, Luco, Conte, et al. 2008). Figure 4.1 illustrates the LHPOST scheme including the large steel platform (12.2 m × 7.6 m × 2.2 m) and the MTS System Corporation shake table (Einde et al. 2004). The shake table system was designed and implemented with low friction and high performance capabilities (Thoen & Laplace 2004). The shake table controller is the MTS Three-Variable Controller, which controls three state variables: displacement, velocity, and acceleration (Ozcelik 2008). More information of implementation and the mechanicals of the MTS control system can also be found in Thoen and Laplace (2004) and Ozcelik (2008). Since the LHPOST was built, its large size, controllable platform, and accurate mechanical system have provided an ideal experimental environment for researches in various fields, such as Earthquake Engineering, Structural Engineering, and as well as Seismology (Luco et al. 2011; Ozcelik, Luco & Conte 2008; Bock et al. 2011).

A seven-floor high concrete building was then built on the LHPOST, as shown in Figure 4.2, for further earthquake engineering as well as structural engineering experiments. For example, two large earthquakes, the 1971 M_w 6.6 San Fernando Earthquake and the 1994 M_w 6.7 Northridge Earthquake, were simulated via the LHPOST as described in Bock et al. (2011).

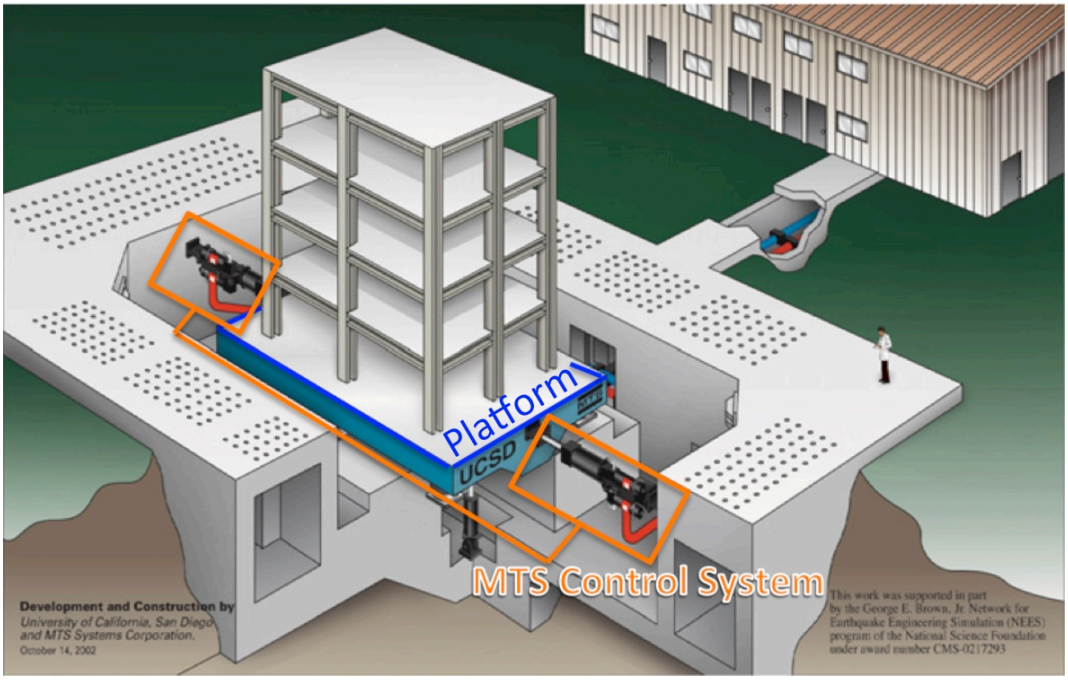

Figure 4.1: The NEES/UCSD LHPOST: the large shake table (the steel platform) and the MTS control system (photograph from Luco et al. (2011))

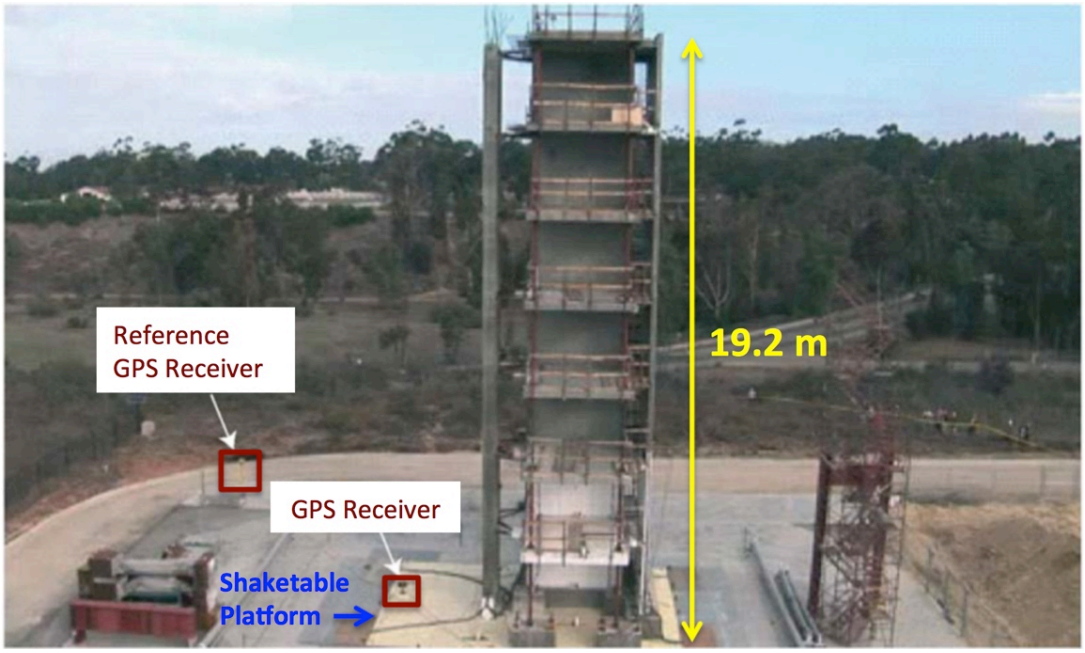

Figure 4.2: NEES/UCSD LHPOST experiment with a seven-floor high concrete building on the steel platform (photograph from Bock et al. (2011))

In this chapter, the same 1994 M_w 6.7 Northridge Earthquake simulated data was provided by Professor Yehuda Bock from UCSD, and all movements were in one dimension and measured in the East-West direction. The data provided includes 50 Hz displacement solutions of 5 GPS receivers, 240 Hz accelerations output of 18 accelerometers, 250 Hz forward and smoothed Kalman filter integrated results, and 1024 Hz accurate displacement measurements from a multivariable MTS 469DU digital controller (Bock et al. 2011). All the measurements or solutions from these instruments

were GPS time tagged. The MTS 469DU digital controller plays an important role in the LHPOST experiments as it can provide real-time three-variable control (TVC) of displacement, velocity, and acceleration (Thoen & Laplace 2004; Thoen 2004). Following the methodology of Bock et al. (2011), the MTS 469DU digital recorder is used to provide the displacement truth model during the earthquake simulations. Bock et al. (2011) used a loosely-coupled Kalman filter integration that estimates two states, displacement and velocity. For the purposes of this study, the raw data was processed with the addition of the baseline error state to the loosely-coupled Kalman filter state vector. In this chapter, several sets of observations of the co-located GPS receivers and the accelerometers on the building and platform of the LHPOST have been selected, processed, and analysed based on the data sets used in Bock et al. (2011) to show the improvement from using a three-state state vector in the Kalman filter algorithm. These data sets have provided an excellent opportunity to test and validate the proposed loosely-coupled Kalman filter algorithm.

4.2 Baseline Error Estimation for UCSD's Outdoor Shake Table Experiment

This section will describe the loosely coupled Kalman filter algorithm used to analyse the data of the outdoor shake table experiment provided by UCSD. As mentioned in the previous section, the data set is the same high-intensity Northridge event data in Bock et al. (2011), which provides a great opportunity to test the proposed algorithms as the MTS data can provide the high-rate true displacement. All data sets provided are in 1D and oriented East-West in this experiment. The accelerometer outputs are given in accelerations (m/s^2). The GPS solutions were displacements in metres obtained by the differential carrier-phase GPS calculation from the GPS receivers mounted on the platform or the building on the shake table and one GPS reference receiver just off the shake table (as shown in Figure 4.2). With respect to the two-state Kalman filter algorithm in Bock et al. (2011), in this research, a baseline error state is added to the algorithm. The following are the details and definitions for the modified loosely coupled Kalman filter algorithm to be used for UCSD's LHPOST data sets.

In this LHPOST experiment, the computed displacement and velocity are calculated from the initial position of the shake table before shaking. The state vector, 1D displacement, velocity, and baseline error according to Eq. (3-16) at the epoch k are modified as below:

$$x_k = \begin{bmatrix} d_e \\ v_e \\ b_e \end{bmatrix}_k \tag{4-1}$$

where

x_k : the state vector;

d_e : the computed displacement in the East-West direction of the accelerometer;

v_e : the computed velocity in the East-West direction of the accelerometer;

b_e : the baseline error state in the East-West direction of the accelerometer.

The system model of the 1D Kalman filter according to Eq. (3-1) is then defined as:

$$\begin{bmatrix} d_e \\ v_e \\ b_e \end{bmatrix}_k = \begin{bmatrix} 1 & \delta t_{ae} & \frac{-\delta t_{ae}^2}{2} \\ 0 & 1 & -\delta t_{ae} \\ 0 & 0 & 1 \end{bmatrix}_{k-1} \begin{bmatrix} d_e \\ v_e \\ b_e \end{bmatrix}_{k-1} + \begin{bmatrix} \frac{\delta t_{ae}^2}{2} \\ \delta t_{ae} \\ 0 \end{bmatrix} a_{e,k-1} + \begin{bmatrix} \frac{\delta t_{ae}^2}{2} \\ \delta t_{ae} \\ 0 \end{bmatrix} w_{acc,e,k-1} \tag{4-2}$$

where

δt_{ae} : the time interval of the accelerometer's East-West measurements;

$a_{e,k-1}$: the acceleration measurements in the East-West direction at epoch $k-1$;

$w_{acc,e,k-1}$: the associated East-West measurement noise of accelerometers at epoch $k-1$.

The actual displacement since last epoch is $d_{e,k-1} + v_{e,k-1}\delta t_{ae} + \frac{1}{2}(a_{e,k-1} - b_{e,k-1} + w_{acc,e,k-1})\delta t_{ae}^2$. In practical application, the error in the acceleration ($w_{acc,e,k-1}$) is unknown, hence the actual mechanisation of the filter is $d_{e,k} = d_{e,k-1} + v_{e,k-1}\delta t_{ae} + \frac{1}{2}(a_{e,k-1} - b_{e,k-1})\delta t_{ae}^2$. In this experiment, the sampling rate of the accelerometer is 240 Hz; therefore, the time interval of the acceleration inputs, δt_{ae}, is (1/240) s.

The system noise covariance matrix based on Eq. (3-18) is formulated as:

$$Q_{k-1} = \begin{bmatrix} \frac{q_{ae}\delta t_{ae}^3}{3} & \frac{q_{ae}\delta t_{ae}^2}{2} & 0 \\ \frac{q_{ae}\delta t_{ae}^2}{2} & q_{ae}\delta t_{ae} & 0 \\ 0 & 0 & q_{be}\delta t_{ae} \end{bmatrix} \tag{4-3}$$

where

q_{ae} is the PSD of the accelerometer East-West noise (in m^2s^{-3});

q_{be} is the PSD of the accelerometer East-West baseline error variation (in m^2s^{-3}).

As mentioned in Section 3.8, the initial q_{ae} (the PSD of the accelerometer noise) usually can be determined by keeping the accelerometer static for a period and calculate the PSD of the accelerometer noise or by using the manufacturer's instrument datasheet. However, in this experiment, the initial q_{ae} is determined based on the setting in Bock et al. (2011) to test if the additional baseline error state in the Kalman filter can provide more accurate and precise solutions.

$$q_{ae} = 1.0(m^2 s^{-3}) \tag{4-4}$$

The initial q_{be} (the PSD of the accelerometer baseline error variation) is obtained from the standard deviation of the baseline error from the pre-event accelerometer observations when the accelerometer was static and calculating the PSD of the baseline error variation. The initial q_{be} is:

$$q_{be} = \frac{\sigma_{be}^2}{\delta t_{ae}} = \frac{\sigma_{be}^2}{(1/240)}(m^2 s^{-3}) \tag{4-5}$$

where σ_{be} is the standard deviation of the baseline error variation.

As the accelerometer provides the inputs for the system model, GPS provides the displacements solutions into the measurement model. The GPS displacements are calculated from the initial position of the GPS receivers where the shake table started shaking. Following the Eq. (3-11) and Eq. (3-19), the measurement matrix, H_k, and the measurement vector, z_k, can be formulated as

$$H_k = \begin{bmatrix} 1 & 0 & 0 \end{bmatrix} \tag{4-6}$$

$$z_k = \begin{bmatrix} 1 & 0 & 0 \end{bmatrix} \begin{bmatrix} d_e \\ v_e \\ b_e \end{bmatrix}_k + w_{GPS,e} \tag{4-7}$$

where $w_{GPS,e}$ is the GPS measurement noise in the East-West direction.

As discussed in Section 3.8, the measurement noise covariance, R_k, accounts for the error covariance of the GPS solution, which is usually defined with a constant value.

$$R_k = R_{GPS,e} \tag{4-8}$$

where $R_{GPS,e}$ is the measurement noise variance of GPS in the West-East direction.

As Bock et al. (2011) stated that the variance for GPS measurement has been set as the optimal value determined in Genrich and Bock (2006), hence the same measurement noise covariance was first set for comparing the use of the additional baseline error state.

$$R = \frac{(0.003(m))^2}{\delta t_{GPS,e}} = \frac{0.000009(m^2)}{1/50(s)} = 0.00045(m^2/s) \tag{4-9}$$

where $\delta t_{GPS,e}$ is the time interval of the GPS measurements.

Notably, as defined in the Eq. (3-12), the measurement noise covariance is the covariance of the measurement error vector. With further reference to Grewal et al. (2007), Gleason and Gebre-Egziabher (2009), Singhal et al. (2012), and Groves (2013), the correct measurement noise covariance unit should be m^2 from the Eq. (4-10). The unit of the measurement noise covariance R was set as m^2/s incorrectly in Bock et al. (2011) based on Smyth and Wu (2006) instead of the correct unit m^2, which has been assumed to be a mistake in both papers. However, in order to validate the results and analysis shown in Bock et al. (2011), the same numerical value of R has been given in our Kalman filter by assuming a 1 s correlation time and multiplying the Eq. (4-9).

$$R = \frac{0.000009(m^2)}{1/50(s)} \times 1(s) = 0.00045(m^2) \tag{4-10}$$

In this experiment, the high-sampling rate (1024 Hz) displacement truth model provided a great opportunity to compare the accuracy and precision of the two-state and three-state Kalman filter integrated results from setting different measurement noise covariance values. Moreover, several measurement noise covariance values are set in the three-state Kalman filter algorithm to seek the optimal measurement noise covariance, and the results are shown in the following sections.

4.3 Experimental Results and Analysis

From Bock et al. (2011), the UCSD's integrated results were computed by using the re-sampled 250 Hz accelerations from the accelerometers at 240 Hz and 50 Hz GPS displacement measurements, so that while Kalman filtering, the GPS measurement could update at every 5^{th}-epoch of the accelerometer measurements. However, the up-sampling and down-sampling process may potentially increase the noise level of accelerometer measurements and increase the noise in the integrated results during the interpolation. Therefore, in this research, unlike the resampling process from the UCSD, the loosely coupled Kalman filter algorithm has been designed to time-tag and calculate the 240 Hz acceleration measurements with the GPS measurement updated at 50 Hz without either up-sampling or down-sampling the observations. The accelerations and GPS displacements have been input to the Kalman filter algorithm when there is an observation available as shown in Figure 3.2. According to the accelerometer data sets and instruction provided by Professor Bock (in an email in October 2012), the start time of accelerometer data was given in GPS time (GPST), and the 240 Hz accelerometer data are complete (no data gaps). Thus, the time-synchronisation in this experiment was approached by assigning GPS time-tags to the accelerometer data based on the initial GPST and the sampling rate of the accelerometer. The observations are from an accelerometer and GPS receiver pair placed on the LHPOST platform which were chosen based on the results published in Bock et al. (2011) for comparison.

Figure 4.3 shows the displacement results of the simulated 1994 Northridge (M_w 6.7) earthquake with different algorithms. Displacements shown in Figure 4.3 are the calculations from numerically integrating the seismometer baseline corrected acceleration (labelled as SBC in Figure 4.3), the outputs from the MTS controller, the GPS solutions from the DGPS process, and the Kalman filtered estimates from the UCSD's Kalman filter with no baseline error state (UCSD KFNB), the proposed Kalman filter with the baseline error state (KFB), and the smoothed Kalman filter (SKF). The smoothed Kalman filter used in this experiment is the RTS smoother as described in Section 3.9.

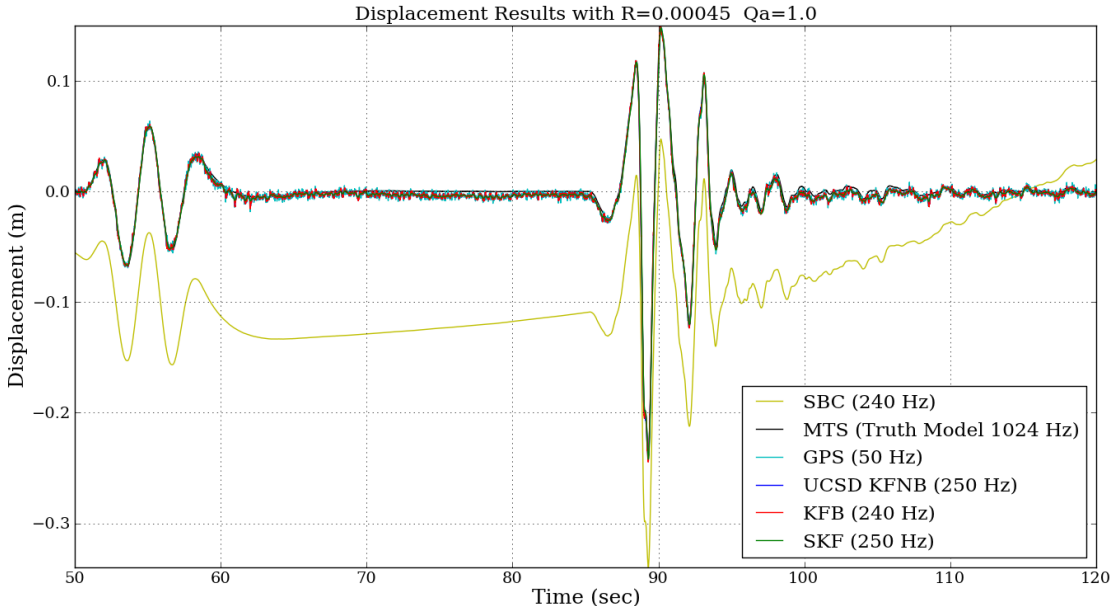

Figure 4.3: The displacement results from different methods with the system noise covariance and the measurement noise covariance setting in the Kalman filter algorithms based on Bock et al. (2011)

The traditional baseline correction, the yellow line in Figure 4.3, used in this experiment is the basic one implemented by removing the baseline error (the mean acceleration of the non-seismic periods) from pre-event observations and applying a high-pass filter to eliminate the low-frequency noise before the numerical integration as described in Boore and Bommer (2005) and Bock et al. (2011). As mentioned in Chapter 2, the traditional baseline corrected result in Figure 4.3 is obviously affected by the linear and quadratic drifts, which is due to the baseline error not being corrected completely and then being doubly integrated during the numerical integration. Since other displacement results in Figure 4.3 have similar accuracy, the further discussion in this chapter will focus on comparing the results of other methods without the baseline corrected results. Figure 4.4 illustrates the displacement results from the MTS controller, GPS receivers, and Kalman filter integrations individually.

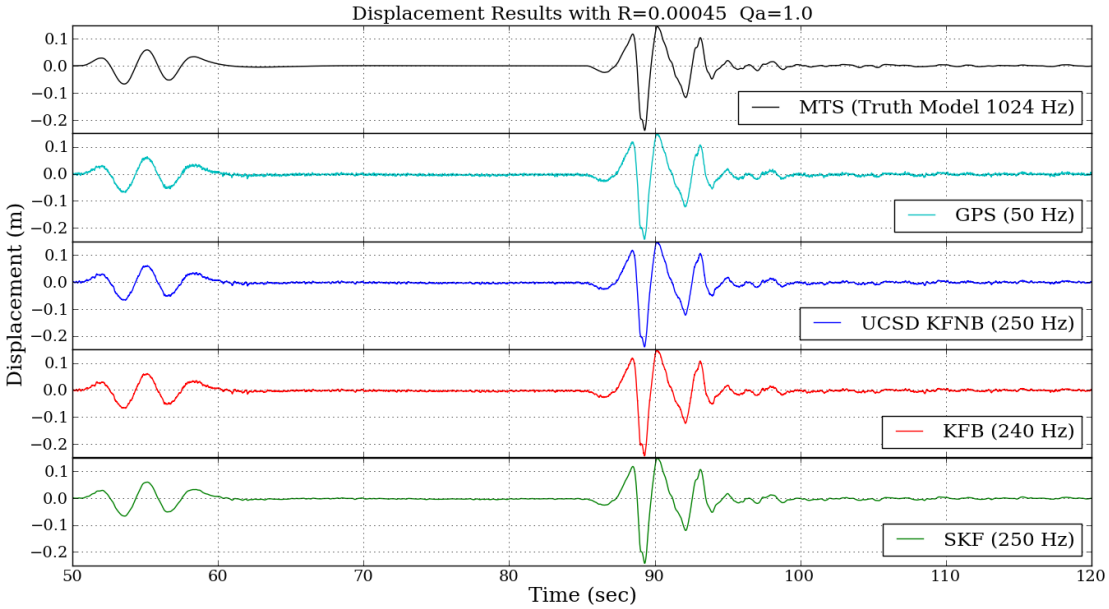

Figure 4.4: The displacement results from the various methods with the system noise covariance and the measurement noise covariance setting in the Kalman filter algorithms based on Bock et al. (2011)

Figure 4.4 shows that the MTS controller as a truth model can provide a smooth and continuous displacement at a high sampling rate. The MTS result also shows that there is actually no offset of the platform after shaking, which is different from a real earthquake event. The LHPOST is implemented to simulate the acceleration waveform of the earthquake, however, no permanent displacement is available due to the design of the shake table system. Nevertheless, although there is no offset of the platform after shaking, and some critical information for understanding the baseline shift and error might be incomplete, the data sets from this LHPOST experiment are still helpful for examining and validating the proposed integrated methods during shaking. From Figure 4.3 and Figure 4.4, during this earthquake simulation, there is a small shaking at 50~60 sec and a large shaking at 85~100 sec.

The displacement waveforms in Figure 4.4 show that during the earthquake simulation, the maximum movement of each instrument is about 0.35 m peak to trough. As the performance of GPS and Kalman filter integrations is expected to achieve the centimetre-level accuracy, the displacement waveforms in Figure 4.3 and Figure 4.4 can only show that the displacement results of GPS and Kalman filter integrations are with some variations during the static period (65~80 sec). Hence, for understanding the error and noise levels of each technique, the MTS displacement result is subtracted from each of the methods as shown in Figure 4.5. Figure 4.5 illustrates the difference between different methods and the MTS outputs. As the MTS controller is used as the truth model, the difference between MTS and each method is considered to be the error of the displacement results.

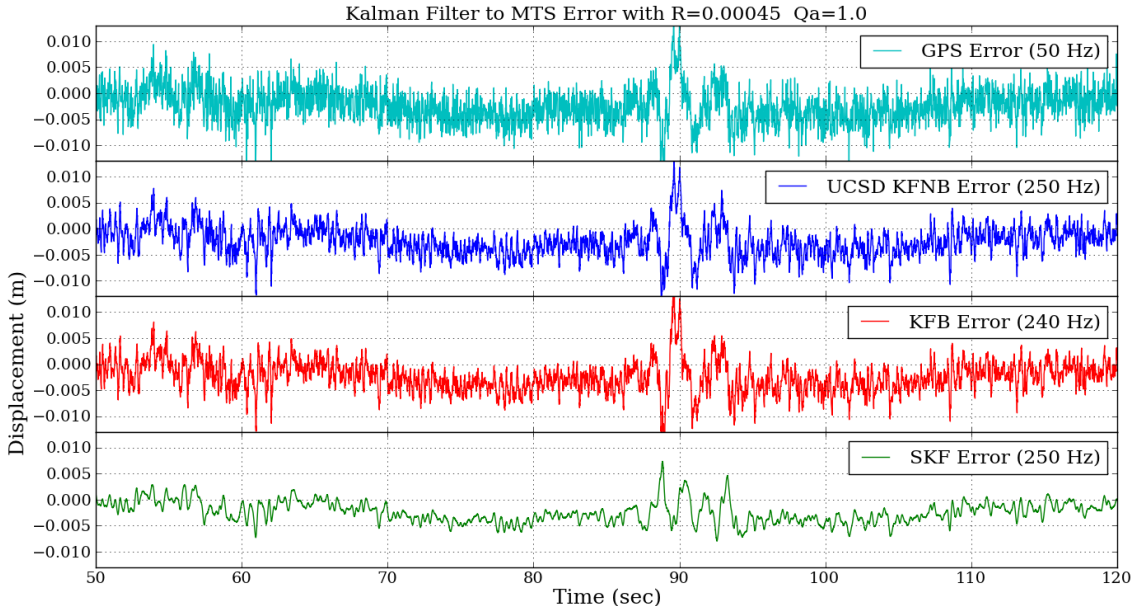

Figure 4.5: The error of the displacement results from different techniques with respect to the MTS displacement truth model

The errors presented in Figure 4.5 show that each displacement determination method can achieve centimetre-level accuracy, and large errors are observed while the earthquake took place (85~100 sec). The error of the GPS results shown in Figure 4.5 is relatively noisy compared to the other Kalman filter integrated results as the GPS with lower sampling rate is expected to contain more high-frequency noises. The Kalman filtered solutions in Figure 4.5 show that the high-frequency noise of the displacement result is reduced by adding the accelerometer information, especially the smoothed Kalman filtered result. The statistical results of the difference between each method and the MTS solution are shown in Table 4.1.

Table 4.1: The performance of different methods with respect to the MTS outputs

	Displacement Error Relative to MTS		
	Mean (m)	**STD (m)**	**RMS (m)**
GPS	-0.0017	0.0033	0.0037
UCSD KFNB	-0.0019	0.0028	0.0034
KFB	-0.0018	0.0028	0.0034
SKF	-0.0019	0.0028	0.0028

*Root Mean Square (RMS) and Standard Deviation (STD)

Table 4.1 shows clearly that the RTS smoothed Kalman filter performs better than the forward Kalman filter results and that both forward Kalman filters show a similar performance. However, the results also indicate that introducing the proposed baseline error state did not improve the performance. This might due to the LHOST is a fixed

and well-calibrated platform, which means there is no permanent shift during and after shaking. Figure 4.6 shows the raw acceleration and the baseline error state (taken from the KFB state time series), and the baseline error state estimates are very close to zero without big changes. As there is no baseline change when the earthquake simulation took place, the baseline error state might be neglected during the Kalman filter computation. Therefore, the advantage of using a baseline error state will be investigated further in Chapter 5 by setting permanent shifts of the sensors in the experiment. In this chapter, as the improvements and effects of changing the system and measurement noise covariance are more significant, the following section will show the changes between various system and measurement noise covariance settings. This process is also known as the Kalman filter tuning process.

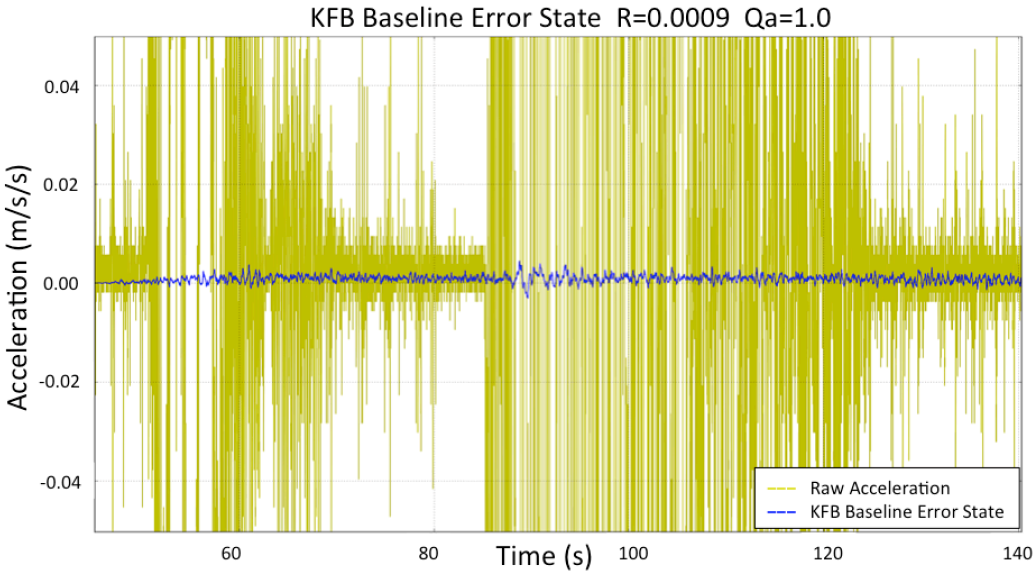

Figure 4.6: The raw accelerometer data and the KFB baseline error state (taken from the KFB state time series)

4.4 Kalman Filter Tuning

When using a Kalman filter, the initial error covariance, the system noise covariance matrix, and the measurement noise covariance matrix need to be set properly to obtain optimal solutions, this process is known as Kalman filter tuning. The tuning process is usually empirical and time consuming. One approach to achieve the Kalman filter tuning is varying one error covariance and fixing the other error covariance in the Kalman filter algorithm (Groves 2013), for example, keeping the initial error and system noise covariance the same values and changing the measurement noise covariance. Ideally, the most suitable covariance combinations for the optimal estimates will be found by Kalman filter tuning. The MTS truth model in this experiment has provided the ideal opportunity for tuning. The optimal solutions are defined by minimising the values of RMS error with respect to the MTS truth model. This section will show and discuss the results and statistical analysis of changing either the system

noise covariance or the measurement noise covariance in the KFB algorithm. Meanwhile, to show the significant effects and improvement of the KFB tuning process, the initial values are set based on the settings in Bock et al. (2011).

4.4.1 Fixed System Noise Covariance, q_{ae} and q_{be}

The first approach is to fix the system noise covariance and vary the measurement noise covariance. The acceleration variance, $\boldsymbol{q_{ae}}$, in the system noise covariance is set as 1.0 (m^2/s^3), whereas the accelerometer baseline error variance, $\boldsymbol{q_{be}}$, is set as shown in Eq. (4-5). The statistical analysis shown in Table 4.2 is of the Kalman filter displacement solution with different values of the measurement noise covariance, $\boldsymbol{R}$, with respect to the MTS truth model. The MTS outputs were at 1024 Hz sampling rate, whereas the Kalman filter results were at 240 Hz sampling rate. The method to calculate the statistical results is derived from interpolating the 1024 Hz MTS solutions into 240 Hz solutions.

Table 4.2: The performance of KFB by fixing $\boldsymbol{P_0}$ and $\boldsymbol{Q}$ and varying $\boldsymbol{R}$ with respect to the MTS truth model

	KFB Displacement Error to MTS				KFB Displacement Error to MTS		
R (m^2)	**Mean (m)**	**STD (m)**	**RMS (m)**	**R (m^2)**	**Mean (m)**	**STD (m)**	**RMS (m)**
4.5e-4	-0.00179	0.00288	0.00339	**16.0**	-0.00197	0.00184	0.00269
1e-2	-0.00179	0.00255	0.00312	**24.0**	-0.00200	0.00180	0.00269
0.1	-0.00180	0.00238	0.00299	**32.0**	-0.00203	0.00178	0.00270
1.0	-0.00184	0.00217	0.00284	**64.0**	-0.00213	0.00175	0.00275
2.0	-0.00186	0.00209	0.00279	**128.0**	-0.00226	0.00174	0.00285
4.0	-0.00188	0.00199	0.00275	**256.0**	-0.00244	0.00178	0.00302
8.0	-0.00192	0.00191	0.00271	**512.0**	-0.00267	0.00187	0.00328

The results in Table 4.2 show that with the increasing measurement noise covariance, the STD and RMS of the KFB error are getting smaller until $\boldsymbol{R}$ = 32.0 (m^2), and the value of the mean error kept getting larger when increasing the $\boldsymbol{R}$. Notably, the first value in Table 4.2, $\boldsymbol{R}$ = 4.5e-4 (m^2), was set based on the setting in Bock et al. (2011) as described in Eq. (4-10). While setting the value of $\boldsymbol{R}$ to more than 32.0 (m^2), the RMS and STD errors are increasing slightly as well. Figure 4.7 illustrates the STD and RMS results in Table 4.2, and as the scale of the value is large, the x-axis is a logarithmic-scale axis. The smallest STD and RMS of the KFB error is between $\boldsymbol{R}$ = 16.0 (m^2) and $\boldsymbol{R}$ = 24.0 (m^2), and usually, the smallest value that can provide the optimal and stable estimates will be chosen (Groves 2013). Therefore, $\boldsymbol{R}$ = 16.0 (m^2) is considered to be the optimal value of $\boldsymbol{R}$ in this case. The STD and RMS of the KFB error have been improved 37.5% and 20.6%, respectively, from setting $\boldsymbol{R}$ = 4.5e-04 (m^2) to $\boldsymbol{R}$ = 16.0 (m^2).

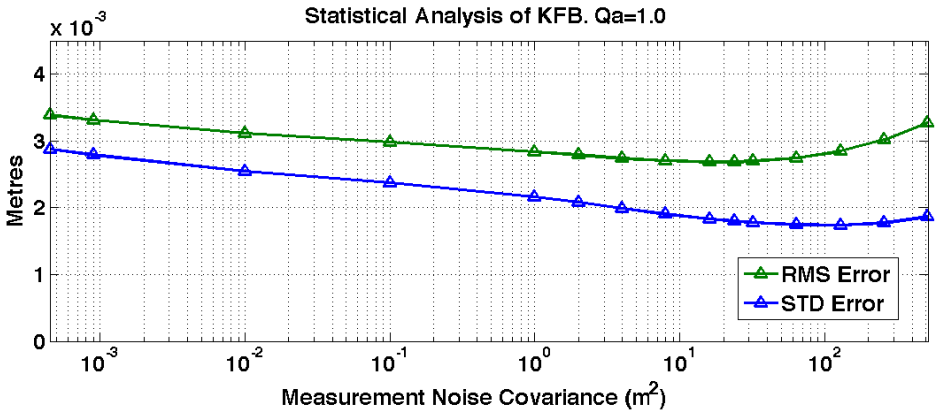

Figure 4.7: The statistical analysis of the KFB integrated solutions by fixing $\boldsymbol{P_0}$ and $\boldsymbol{Q}$ and varying $\boldsymbol{R}$ with respect to the MTS truth model

As shown in Table 4.2 and Figure 4.7, while tuning the Kalman filter, every parameter in the algorithm needs to be set delicately, and finding the optimal parameters are mainly by trial and error. The changes between varied measurement noise covariance can be seen not only from the statistical analysis but also from plotting. Figure 4.8 illustrates the error of the KFB displacement with respect to the MTS truth model with different values of $\boldsymbol{R}$.

The errors of the KFB results with respect to the MTS truth model in Figure 4.8 are plotted with the same scale for comparison. By comparing these figures, it can be seen that the noise level decreased when increasing the value of the $\boldsymbol{R}$. However, although the noise level seems to drop down from plot (a) to plot (c) in Figure 4.8, the statistical analysis indicates that the mean and RMS of the error are actually raised when the measurement noise covariance exceeds a certain value. This might be due to the linear or quadratic effects in the system model caused by the double integral being transferred to the estimates. In Kalman filter calculations, the ratio of $\boldsymbol{P/R}$ will decide the Kalman gain and then influence the state estimates. When exaggerating the values of $\boldsymbol{R}$, the Kalman gain in the algorithm becomes relatively small, which means the weighting function "trusts" the system estimates more than the measurement updates. This impact can also been seen in the following section while fixing the measurement noise covariance and varying the system noise covariance.

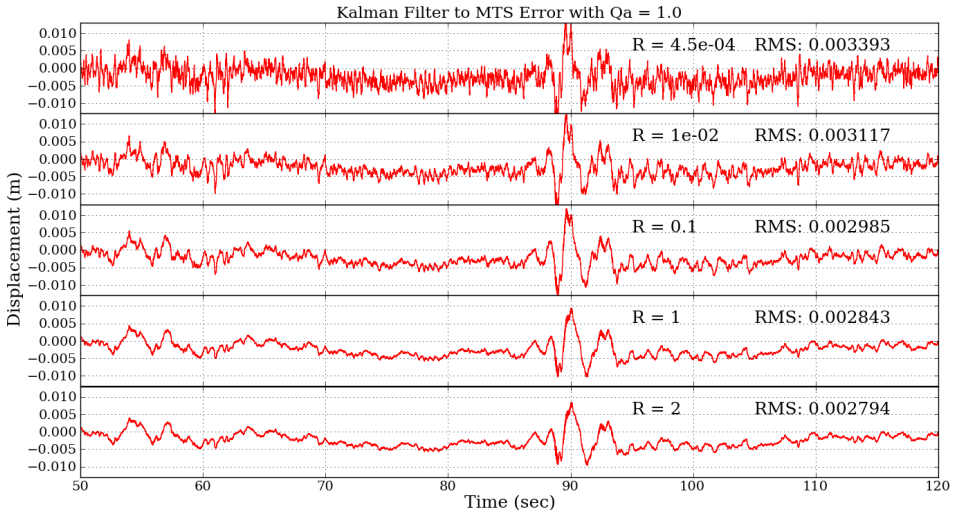

(a)

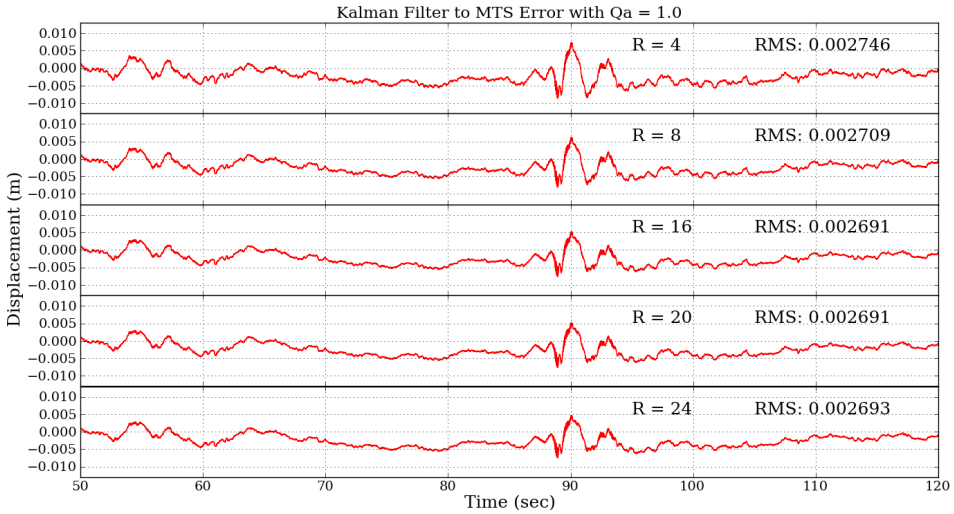

(b)

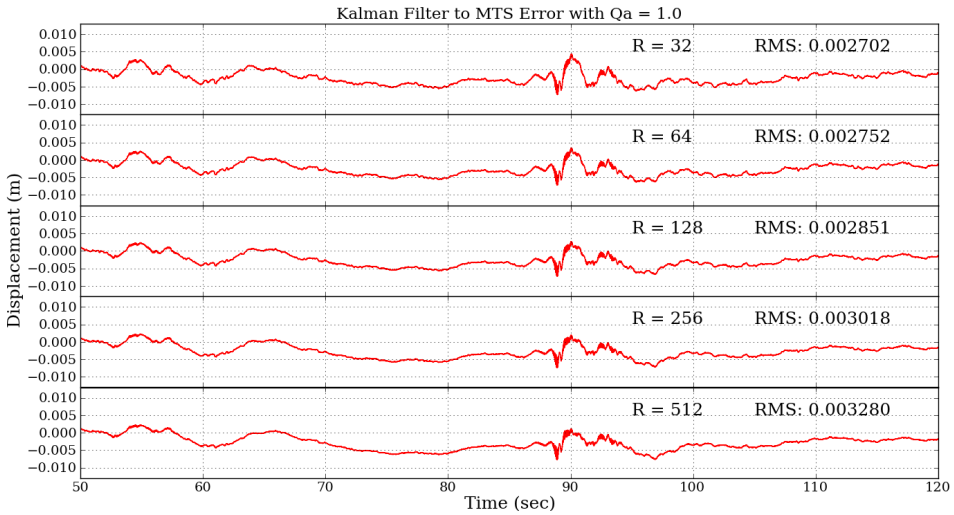

(c)

Figure 4.8: KFB tuning: fixed system noise covariance, $\boldsymbol{Q}$ and varied measurement noise covariance, $\boldsymbol{R}$.

4.4.2 Fixed measurement noise covariance, R = 4.5e-04 (m^2), variable process noise

Similarly, in order to assess the potential improvement of the accuracy by the Kalman filter tuning of the process noise, the fixed value of the measurement noise covariance is held at the same setting as in Bock et al. (2011), $\boldsymbol{R}$ = 4.5e-04 (m^2). By assuming the noise level of the accelerometer outputs is not large as the LHOST is a well calibrated system, the initial value of $\boldsymbol{Q}$ was set with a relatively small acceleration variance, q_{ae} = 1.0e-08 (m^2/s^3). Furthermore, as two values of q_{ae}, 1.0 and 1000.0, were set in Bock et al. (2011), both values are also set in this tuning process for comparison. Table 4.3 shows the statistical analysis of the displacement error with varied system noise covariance with respect to the MTS displacement truth model.

Table 4.3: The performance of the KFB solutions by fixing $\boldsymbol{P_0}$ and $\boldsymbol{R}$ ($\boldsymbol{R}$ = 4.5e-04 (m^2)) and setting different q_{ae} with respect to the MTS truth model

	KFB Displacement Error to MTS				KFB Displacement Error to MTS		
q_{ae} (m^2/s^3)	Mean (m)	STD (m)	RMS (m)	q_{ae} (m^2/s^3)	Mean (m)	STD (m)	RMS (m)
1.0e-08	-0.00184	0.00184	0.00260	**0.01**	-0.00179	0.00244	0.00303
1.0e-07	-0.00184	0.00184	0.00260	**0.1**	-0.00179	0.00262	0.00317
1.0e-06	-0.00184	0.00184	0.00260	**1.0**	-0.00179	0.00288	0.00339
1.0e-05	-0.00184	0.00185	0.00261	**10.0**	-0.00179	0.00319	0.00366
1.0e-04	-0.00183	0.00202	0.00273	**100.0**	-0.00179	0.00365	0.00406
0.001	-0.00180	0.00227	0.00290	**1000.0**	-0.00179	0.00433	0.00469

As the initial number is relatively small and the need of setting q_{ae} = 1.0 (m^2/s^3) and q_{ae} = 1000.0 (m^2/s^3) for comparison, the values of q_{ae} in this tuning process are increased by multiplying by ten.

Unlike the results in Table 4.2, the results in Table 4.3 show that while increasing the value of the system noise covariance, the STD and RMS of the KFB error are becoming larger and more unstable. As the ratio of $\boldsymbol{P/R}$ becomes larger, the Kalman gain in the algorithm is getting larger, which might make the state estimates influenced or biased by the measurement noise too much. In this tuning process, the STD and RMS of the KFB error become larger for any value of q_{ae} > 1.0e-05 (m^2/s^3). Compared to the statistics in Bock et al. (2011), the STD and RMS of the KFB error have been improved 36.1% and 23.3%, respectively after tuning.

Figure 4.9 displays the STD and RMS results in Table 4.3, and the x-axis in Figure 4.9 is logarithmic-scaled due to the wide range of q_{ae} values. Compared to the results in Figure 4.7, the statistical results in Figure 4.9 show a different trend as the STD and

RMS of the KFB error become stable and converge when the value of $\boldsymbol{Q}$ is decreasing. This is also related to the ratio of $\boldsymbol{P/R}$ and as well as the Kalman gain as discussed in the previous section.

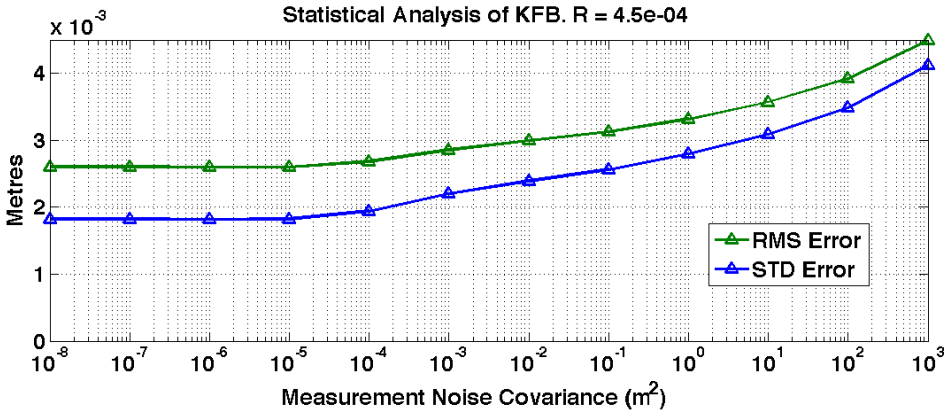

Figure 4.9: The statistical analysis of the KFB integrated solutions ($\boldsymbol{R}$ = 4.5e-04 (m^2)) with respect to the MTS truth model

Figure 4.10 illustrates the tuning results of the Kalman filter integration with respect to the MTS truth model by fixing the measurement noise covariance, $\boldsymbol{R}$ = 4.5e-04 (m^2), and setting varied system noise covariance, $\boldsymbol{Q}$. From plot (a) to plot (c) in Figure 4.10, it can be seen clearly that the noise of the KFB error accumulates significantly while increasing and exaggerating the value of $\boldsymbol{q_{ae}}$. The optimal system noise covariance with the fixed measurement noise covariance, $\boldsymbol{R}$ = 4.5e-04 (m^2), is considered to be calculated by $\boldsymbol{q_{ae}}$ = 1.0e-06 (m^2/s^3) in this case.

As $\boldsymbol{q_{ae}}$ = 1.0 (m^2/s^3) was decided as the initial and optimal setting in Bock et al. (2011), the results in Table 4.3 and Figure 4.9 disagree that $\boldsymbol{q_{ae}}$ = 1.0 (m^2/s^3) in the forward Kalman filter can obtain the optimal state estimates. The results also show that with appropriate tuning, the statistical results can achieve the similar accuracy to the RTS smoothed results shown in Table 4.1.

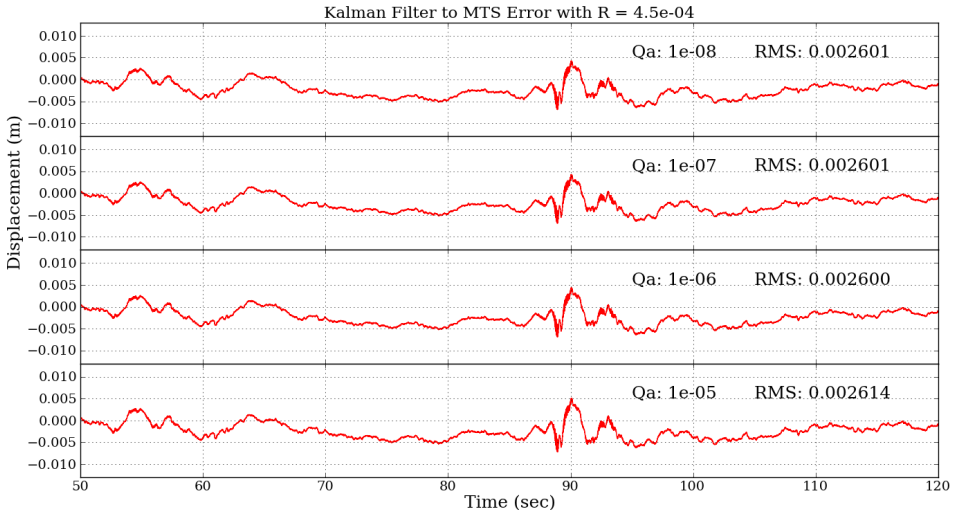

(a)

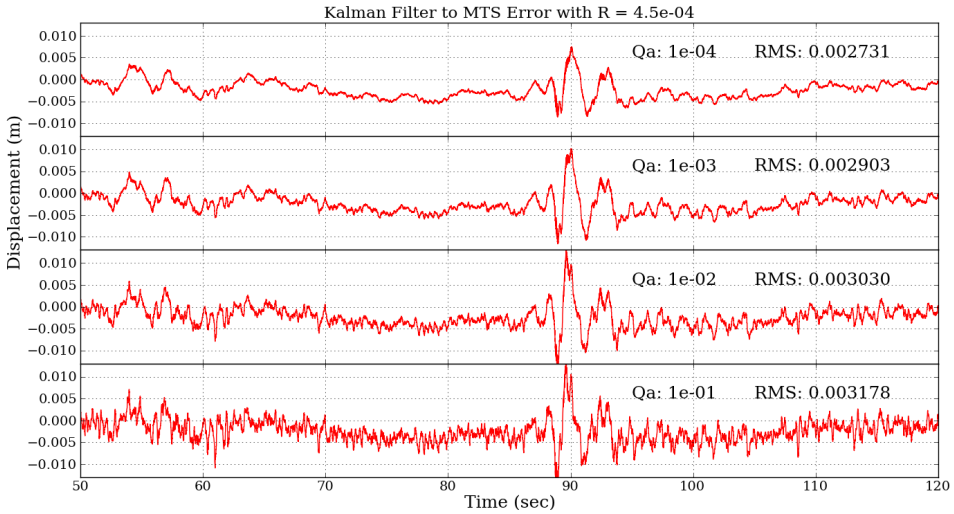

(b)

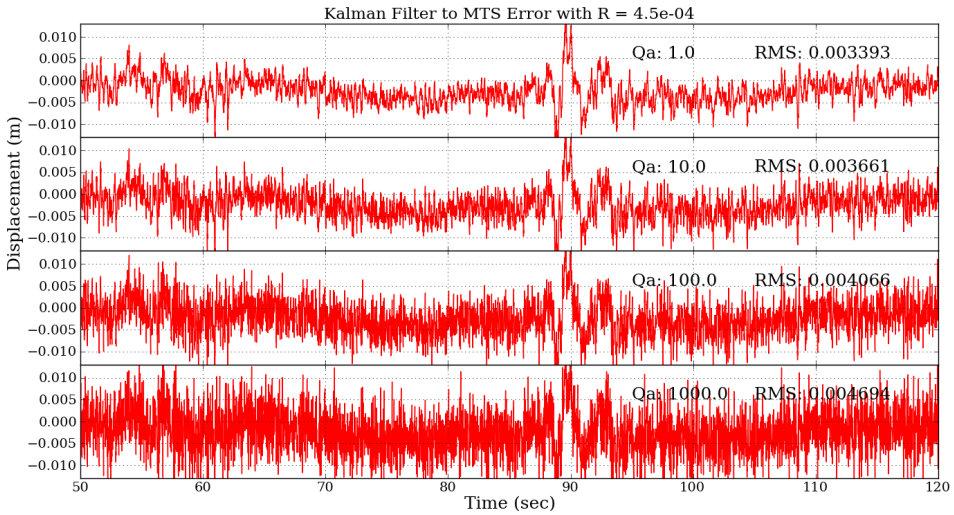

(c)

Figure 4.10: KFB tuning: fixed measurement noise covariance, $\boldsymbol{R}$ = 4.5e-04 (m^2), and varied system noise covariance, $\boldsymbol{Q}$.

4.4.3 Fixed Measurement Noise Covariance, R = 9.0e-06 (m^2)

According to Bock et al. (2011), if the measurement noise variance was not mistakenly used in the algorithm (see Eq. 4-10 and Eq. 4-11), the measurement noise variance of the Kalman filter integration was supposed to be the GPS measurement noise variance, $\boldsymbol{R}_{GPS}$ = 3 (mm) × 3 (mm) = 9.0e-06 (m^2). The value of $\boldsymbol{R}_{GPS}$ in Bock et al. (2011) was determined from the statistical analysis of the GPS solutions with respect to the MTS truth model as shown in Table 4.1. Thus, for validating the algorithm with a more realistic value, $\boldsymbol{R}$ = 9.0e-06 (m^2) is used as the fixed measurement noise covariance in this KFB tuning process. Based on the results in previous section, the optimal system noise covariance for the fixed $\boldsymbol{R}$ = 9.0e-06 (m^2) is expected to be smaller as the state estimate converged when the ratio of $\boldsymbol{P/R}$ is getting smaller. Hence, the initial system noise covariance is set with $\boldsymbol{q}_{ae}$ = 1.0 (m^2/s^3) and divided by ten in this case as shown in Table 4.4. The statistical results in Table 4.4 are also plotted as Figure 4.11, and similarly, the x-axis in Figure 4.11 is plotted in the logarithmic scale for a better illustration.

Table 4.4: The performance of the KFB solutions by fixing $\boldsymbol{P}_0$ and $\boldsymbol{R}$ ($\boldsymbol{R}$ = 9e-06 (m^2)) and varying $\boldsymbol{q}_{ae}$ with respect to the MTS truth model

	KFB Displacement Error to MTS				KFB Displacement Error to MTS		
q_{ae} (m^2/s^3)	Mean (m)	STD (m)	RMS (m)	q_{ae} (m^2/s^3)	Mean (m)	STD (m)	RMS (m)
1.0e-11	-0.00180	0.00210	0.00276	**1.0e-05**	-0.00179	0.00226	0.00289
1.0e-10	-0.00180	0.00210	0.00276	**1.0e-04**	-0.00179	0.00241	0.00300
1.0e-09	-0.00180	0.00210	0.00276	**1.0e-03**	-0.00179	0.00256	0.00313
1.0e-08	-0.00180	0.00210	0.00276	**0.01**	-0.00179	0.00280	0.00332
1.0e-07	-0.00180	0.00210	0.00277	**0.1**	-0.00179	0.00309	0.00358
1.0e-06	-0.00180	0.00214	0.00278	**1.0**	-0.00179	0.00349	0.00392

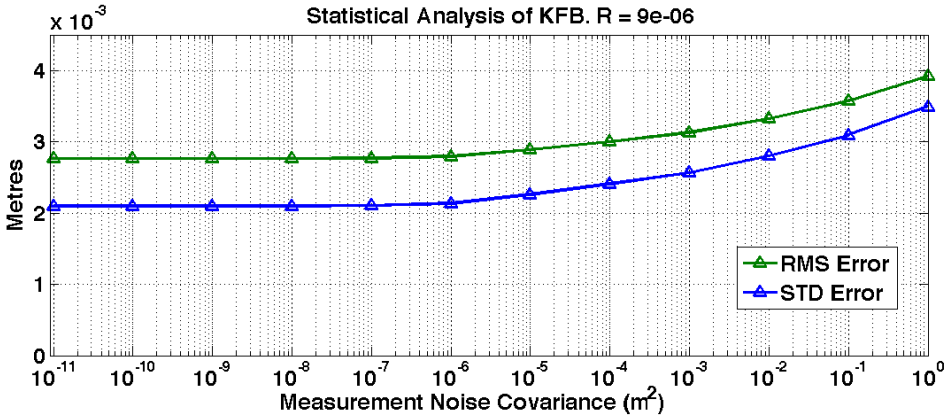

Figure 4.11: The statistical analysis of the KFB integrated solutions ($\boldsymbol{R}$ = 9e-06 (m^2)) with respect to the MTS truth model

As discussed previously, the statistical results show that when the fixed measurement noise covariance is smaller, the system noise covariance required for the state estimate to become stable and converge will also be smaller. Table 4.4 and Figure 4.11 show that the RMS and STD of the KFB error begin to converge when $\boldsymbol{q_{ae}}$ is smaller than 1.0e-06 (m^2/s^3). In addition, it has been noticed that when the fixed measurement noise covariance is set too small, the values of the RMS and STD error convergence seem to be larger. The STD and RMS error by setting $\boldsymbol{q_{ae}}$ = 1.0e-07 (m^2/s^3) has been improved 39.8% and 29.3%, respectively, from setting $\boldsymbol{q_{ae}}$ = 1.0 (m^2/s^3).

Figure 4.12 illustrates the error of the KFB by fixing the measurement noise covariance and setting different system noise covariances. Similarly, from plot (a) to plot (c) in Figure 4.12, the noise level of the error increases when increasing the system noise covariance in the algorithm.

Although the $\boldsymbol{R}$ = 9e-06 (m^2) is set based on the statistical analysis of the $\boldsymbol{R_{GPS}}$, the tuning results show the need to enlarge the measurement uncertainties in order to enhance the stability of the system. As the assumption of Kalman filter algorithm is a system in an ideal environment with white noise only, the uncertainties and errors of the estimates are always underestimated. In reality, the errors and uncertainties of the state estimates are always more complicated and unpredictable. Hence, it is normal to double or triple the corresponding error standard deviation when implementing Kalman filter algorithms (Groves 2013). This might also explain why the results from the setting of $\boldsymbol{R}$ (see Eq. 4-10 and Eq. 4-11) in Bock et al. (2011) could provide more stable estimates. As based on Eq. 4-10, while dividing $\boldsymbol{R_{GPS}}$ by the measurement time interval (1/50 s), the value of the GPS standard deviation is then about seven times bigger than the original GPS standard deviation.

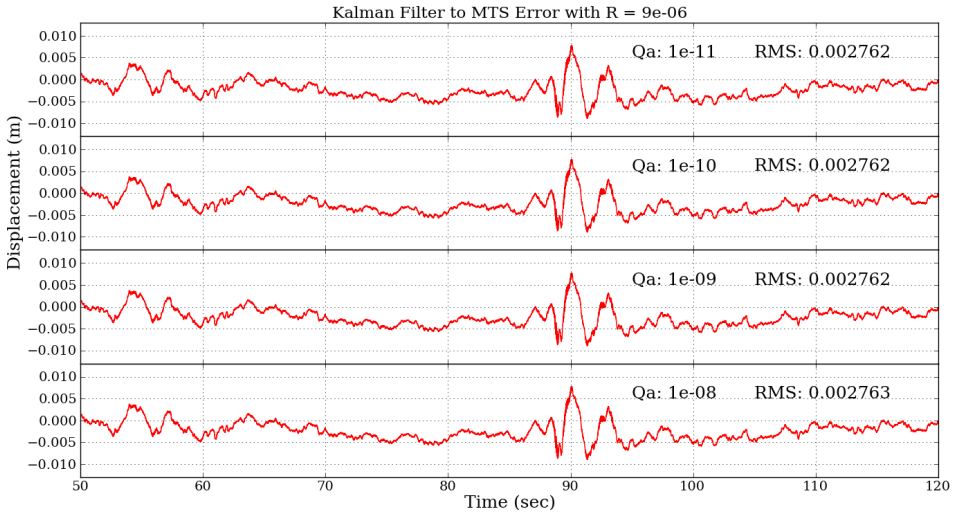

(a)

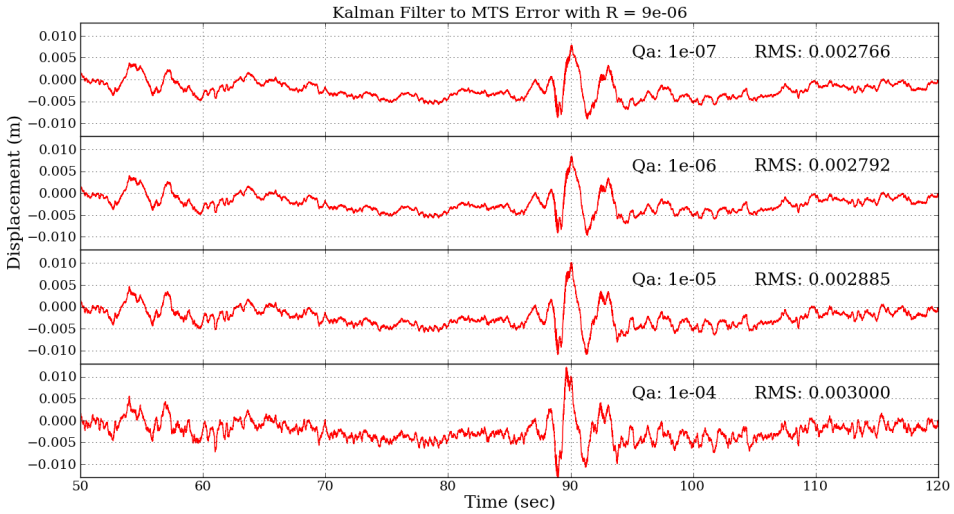

(b)

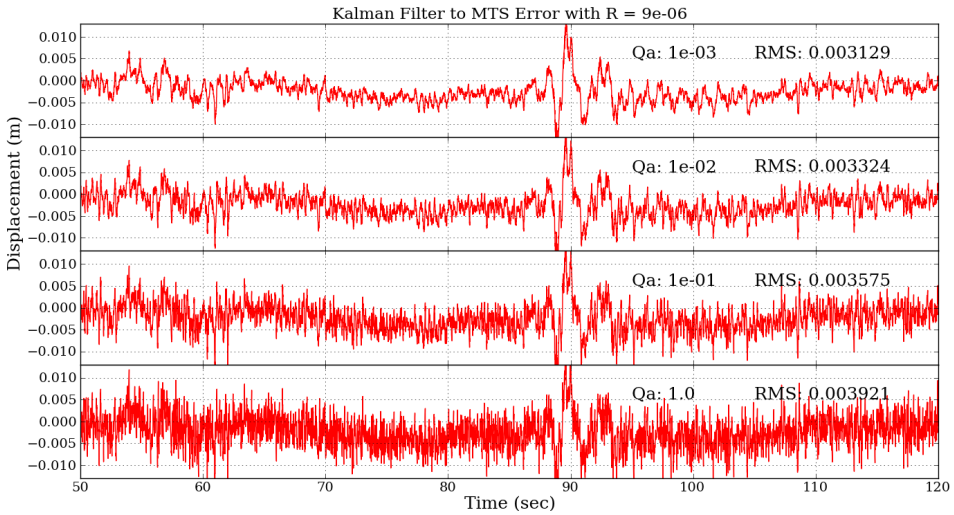

(c)

Figure 4.12: KFB tuning: fixed measurement noise covariance, $\boldsymbol{R}$ = 9e-06 (m^2), and varied system noise covariance, $\boldsymbol{Q}$.

4.5 Summary

A large earthquake, 1994 M_w 6.7 Northridge Earthquake, has been simulated via the LHPOST in the experiment. This chapter demonstrates the proposed loosely coupled Kalman filter integration using the LHPOST data sets from high-sampling rate GPS receivers and accelerometers and comparing the results with a displacement truth model. The same parameters in the Kalman filter algorithm have been given for comparing with the results in Bock et al. (2011). Furthermore, to improve the accuracy of the estimates, a Kalman filter tuning process has been introduced and demonstrated. In the Kalman filter tuning process, the variable Kalman filter parameters include the initial state covariance, $\boldsymbol{P_0}$, the system noise covariance, $\boldsymbol{Q}$, and the measurement noise covariance, $\boldsymbol{R}$. The Kalman filter tuning process is usually approached by varying either $\boldsymbol{Q}$ or $\boldsymbol{R}$ at one time and fixing the other two parameters. The results show that the accuracy of the tuned results can be improved more than 36% and 20% in terms of the STD and RMS of the error, respectively.

Notably, in Bock et al. (2011), the authors state that determining the system noise covariance is more complicated and unpredictable due to the rotational motion and tilt of the sensors during earthquakes. Hence, an exaggerated value of the system noise covariance, $\boldsymbol{q_{ae}}$ = 1000.0 (m^2/s^3), was set in the Kalman filter algorithm with fixed $\boldsymbol{R}$ and $\boldsymbol{P_0}$ by assuming that the noise level of the accelerometer observations is very high, and the calculated results are compared to the results with setting $\boldsymbol{q_{ae}}$ = 1.0 (m^2/s^3). Bock et al. (2011) then concluded that the improvement of the accuracy is not significant by varying the system noise covariance and that applying a Kalman smoother after the forward Kalman filter integration can actually provide the optimal estimates. However, the results in this section show that with the proper tuning, the accuracy of the estimates can actually be improved.

Furthermore, the result from setting $\boldsymbol{q_{ae}}$ = 1000.0 (m^2/s^3) shows that tuning a Kalman filter algorithm needs to be approached delicately instead of setting an extreme value and assuming it can cover all the instrument error and bias, for example, the rotational motion and tilt effects. These error effects might be corrected by the additional baseline error state in the proposed Kalman filter integration. However, the fixed platform in the LHOST experiment might have limited the rotational motion and tilt effects on the instruments. Therefore, the improvement from using additional baseline error state will be discussed more in the following chapters when a permanent displacement takes place in the experiments.

Chapter 5 National Physical Laboratory Rooftop Experiment

In order to test and validate further the proposed Kalman filter algorithm discussed in Section 3.8, an experiment was carried out at the National Physical Laboratory (NPL) in the United Kingdom. This experiment has been designed to examine whether the proposed Kalman filter integration can process three-dimensional measurements successfully, and also to increase the measurement accuracy of small displacements of known magnitude and direction by using the additional baseline error state as well as the correct tuning in the algorithm. Section 5.1 gives the instruments and settings of the NPL rooftop experiment. In Section 5.2, the three-dimensional Kalman filter algorithm as the main algorithm in this experiment is presented. The related experimental results and analysis are shown in Section 5.3. This is followed by Section 5.4 where a Kalman filter tuning process with different parameter settings is presented. Section 5.5 summarises the findings and contributions of this experiment.

5.1 Experiment Description

As discussed in the previous chapter, during real earthquakes, the shaking can easily cause permanent shifts of the instruments. A permanent shift comprises both linear and rotational displacements. As GPS can update and provide the three dimensional position solutions itself in a short period, the permanent shifts of the GPS receivers do not disturb the GPS solutions at all. The effects of moving are more severe for seismometers or accelerometers, especially the linear and rotational displacements. The linear and rotational movements of the seismometer or the accelerometer normally change the baseline error of the sensor, which will lead to a quadratic error with time within displacement solutions while numerically double-integrating the acceleration (Brady 2009; Boroschek & Legrand 2006; Graizer 2005). Since the sampling rate of seismometers and accelerometers are always much higher than GPS receivers, the baseline errors of the seismometer or accelerometer will affect the estimates in the system model rapidly, which will lead to quadratic drifts on the displacement state estimates and linear drifts on the velocity state estimates. Hence, in order to reduce the error effects from the permanent shifts, the baseline error state in the proposed Kalman filter was designed to measure and estimate the small changes of the sensor's baseline during or after shaking. The baseline error state estimate will then feed back the small change of the baseline to the system to correct the acceleration observation before the numerical integration in the next iteration. Therefore, the main purposes of this experiment are for the proposed Kalman filter to measure and provide accurate displacement of sensors and for the baseline error state to detect the small baseline changes in the seismometer or accelerometer after moving.

5.1.1 NPL Rooftop Experiment

As GNSS receivers require open sky to receive signals from satellites, a building's rooftop at NPL was used to run the experiment. During this experiment, a Leica GNSS receiver was used in the tests on a designed platform with a movable steel plate on, as shown in Figure 5.1.

Figure 5.1: The NPL building and its rooftop where the experiment was carried out

A steel plate that can move laterally along the x-axis in the body frame of the designed platform is shown in Figure 5.2. A Güralp Systems CMG-5TD strong motion seismometer and a Leica Viva GNSS antenna were firmly attached to the movable steel plate on the platform. The steel plate was designed and constructed at University College London with help of Mr. Leslie Irwin from the departmental workshop to ensure the mounted sensors are aligned to the axes of the platform. The idea of the movable steel plate is to create a single 'sounding board' for measurements. Since the movable steel plate on the platform can only move along one direction, the steel plate was mounted on the platform along the moving direction, x_{body}, as shown in Figure 5.2.

Figure 5.3 illustrates the horizontal axes of the three body frames: the GNSS antenna, the strong motion seismometer, and the platform. In this experiment, for less confusion, the observations and analysis are converted into and discussed in the body frame of the platform. The y-axis of the strong motion seismometer was aligned along the x-axis in the body frame of the platform, which is also the direction of the movement. Similarly, the x-axis of the GNSS antenna was aligned with the x-axis of the platform body frame.

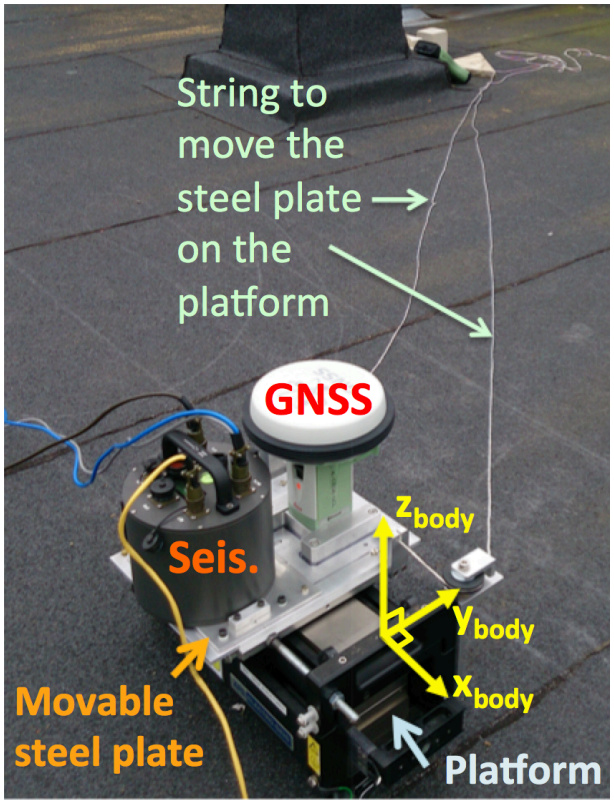

Figure 5.2: A Güralp CMG-5TD strong motion seismometer and a Leica Viva GNSS antenna collocated on a movable steel plate with the body frame axes shown and the adjustable string for moving the steel plate on the platform

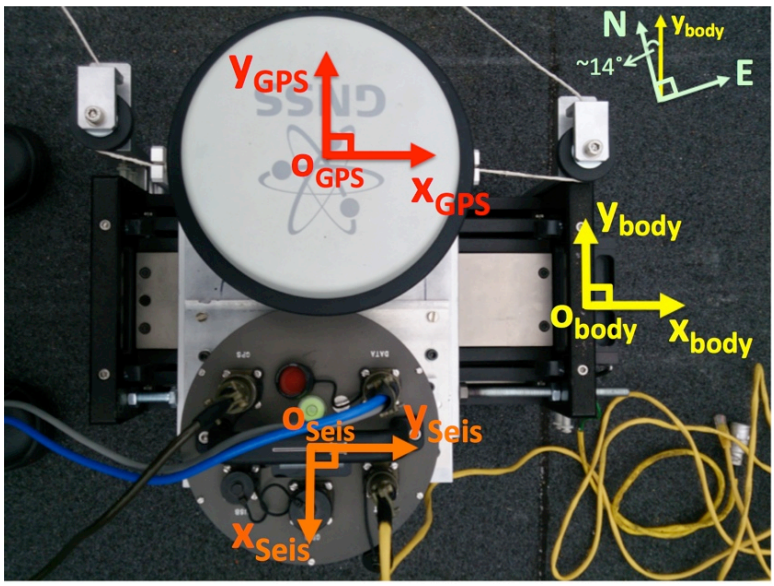

Figure 5.3: The body frames of the GNSS antenna (red), the strong motion seismometer (orange), and the platform (yellow)

Both sensors logged observations for the same 5-hour period on two consecutive days. The two-day observations were used so that a sidereal filter could be applied to the GNSS measurements. All the observations of both GPS and strong motion seismometer were GPS time tagged. During most of the time periods, the instruments and platform

were kept at the same position without any movement. During the last 90 minutes of the second day, the steel plate on the platform was subjected to various small displacements along the x-axis in the body frame of the platform, for example, 40 mm, 30 mm, 20 mm, and 10 mm. The strong motion seismometer observed the specific force of the ground motion and output accelerations along the x, y, and z directions of the seismometer body frame. The GNSS observations were processed several times using PPP to obtain the positions in an Earth-Centered Earth-Fixed (ECEF) reference frame and convert the positions into a body frame that aligns to the platform. The position solutions in the GNSS body frame were then calculated into displacements from the original position obtained from the GNSS static observations.

5.1.2 Güralp Systems CMG-5TD Strong Motion Seismometer

Figure 5.4 shows the Güralp Systems CMG-5TD strong motion seismometer used in this experiment. The CMG-5TD strong motion seismometer contains three single-axis force feedback accelerometers with low-noise components and large dynamic ranges. The device has a number of different settings varying from high sensitivity with a 0.1 g limit to lower sensitivity with a 4 g limit (Güralp Systems CMG-5TD Manual). The strong motion seismometer, as shown in Figure 5.1, measures the specific force of the ground motion and outputs accelerations (m/s^2) of the North-South, East-West, and Vertical components, respectively. The output rate of the CMG-5TD strong motion seismometer is 100 Hz.

Figure 5.4: Güralp Systems CMG-5TD strong motion seismometer

5.1.3 Leica Viva GNSS Multi-Frequency GNSS Receiver

GNSS plays an important role in this research, and Leica Viva GNSS multi-frequency GNSS receivers were used to integrate with the strong motion seismometer. The Leica Viva outputs data at a 20 Hz sampling rate, provides highly accurate GNSS observations, and receives almost all kinds of satellite signals from different satellite systems, for example, GPS, GLONASS (Global Navigation Satellite System), and the Galileo system. One feature of this receiver is that the observations can be transmitted via wireless communication ports while surveying. Figure 5.5 shows the Leica Viva GNSS antenna that has been mounted on a designed steel plate in the laboratory.

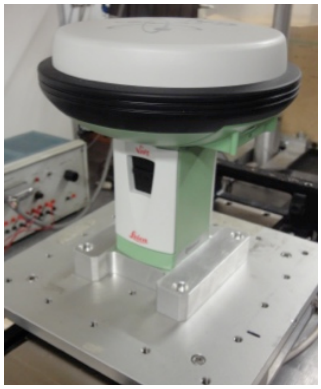

Figure 5.5: Leica Viva GNSS receiver on a designed platform in the laboratory

In this experiment, the GNSS position solutions were firstly computed in an ECEF frame and then converted into displacements along the x-, y-, and z-axes in the platform body frame for later input to the Kalman filter integrations.

As mentioned in Section 3.10, all of the GNSS observations in this experiment were processed by Christopher Atkins using PPP software developed by Dr. Alexander Parkins and Christopher Atkins. The PPP software made use of high-accuracy satellite orbits and clock offsets in order to process the 1 Hz GNSS observations of the GNSS receiver in order to derive its positions with centimetre to decimetre level accuracy (Atkins & Ziebart 2015). In order to provide this level of accuracy, certain error sources of the GNSS observations such as ionosphere delays, atmospheric errors, and other errors, have been minimised by applying the GPS ionosphere-free measurements in the PPP algorithm. The GPS ionosphere-free phase measurements are formed by a linear combination of GPS L1 and L2 phase measurements, which can largely reduce the ionosphere delays effect (Gao & Chen 2004). These phase measurements are then processed by a PPP Kalman filter algorithm in the aforementioned software. In the PPP Kalman filter, the position of the GNSS receiver, the receiver clock offset, zenith tropospheric delay, and an ionosphere-free phase ambiguity for every visible satellite are set as the Kalman filter states for estimating the GNSS solutions at each epoch. The PPP Kalman filter process in the software is also known as the ‘classical’ or ‘float’ PPP process, which estimates the slow-varying non-integer ionosphere-free phase ambiguity in the state vector for any visible satellite (Gao & Chen 2004). Furthermore, in order to provide centimetre level accuracy in this study, the PPP software post-processed the position solutions by using precise post-processed satellite orbit and high-rate (5-second) satellite clock data from the Centre for Orbit Determination in Europe (CODE) (Atkins & Ziebart 2015). More detailed information and settings related to the PPP Kalman filter as well as the PPP software that used in this study can be found in Atkins & Ziebart (2015).

5.2 Three-Dimensional Kalman Filter Algorithm

In this experiment, a three-dimensional Kalman filter integration has been applied to process the strong motion seismometer and GNSS observations. Compared to the one-dimensional Kalman filter integration in Chapter 4, the three-dimensional algorithm also follows the basic algorithm introduced in Chapter 3 but involves more settings and a more complicated numerical calculation. Thus, to fully understand the three-dimensional Kalman filter algorithm, the differences in the settings and calculation are introduced as follows. Notably, since the instruments are oriented to the body frame of the platform in this experiment, the equations are formulated with the x-, y-, and z-axes in the body frame of the platform.

First of all, based on Eq. (3-16), the **state vector**, x_k, must be defined in three dimensions. Eq. (5-1) shows the three-dimensional state vector including displacement, velocity, and baseline error along the x-, y-, and z-axes. A total-state Kalman filter has also been implemented in this experiment. The state vector is defined as follows:

$$x_k = \begin{bmatrix} d_x \\ d_y \\ d_z \\ v_x \\ v_y \\ v_z \\ b_x \\ b_y \\ b_z \end{bmatrix}_k \tag{5-1}$$

where d is the displacement, v is the velocity, and b is the baseline error. The **transition matrix** for the three-dimensional Kalman filter algorithm is:

$$\Phi_{k-1} = \begin{bmatrix} I_3 & \delta t_a I_3 & \frac{-\delta t_a^2}{2} I_3 \\ 0_3 & I_3 & -\delta t_a I_3 \\ 0_3 & 0_3 & I_3 \end{bmatrix}_{k-1} \tag{5-2}$$

where δt_a is the time interval of the strong motion seismometer observation, I_3 is a 3×3 identity matrix, and 0_3 is a 3×3 zero matrix. According to Eq. (3-1), Eq. (3-17), Eq. (5-

1), and Eq. (5-2), the **system model** for the three-dimensional Kalman filter can be formulated as follows:

$$\begin{bmatrix} d_x \\ d_y \\ d_z \\ v_x \\ v_y \\ v_z \\ b_x \\ b_y \\ b_z \end{bmatrix}_k = \begin{bmatrix} I_3 & \delta t_a I_3 & \frac{-\delta t_a^2}{2} I_3 \\ 0_3 & I_3 & -\delta t_a I_3 \\ 0_3 & 0_3 & I_3 \end{bmatrix}_{k-1} \begin{bmatrix} d_x \\ d_y \\ d_z \\ v_x \\ v_y \\ v_z \\ b_x \\ b_y \\ b_z \end{bmatrix}_{k-1} + \begin{bmatrix} \frac{\delta t_a^2}{2} I_3 \\ \delta t_a I_3 \\ 0_3 \end{bmatrix} \begin{bmatrix} a_x \\ a_y \\ a_z \end{bmatrix}_{k-1} + \begin{bmatrix} \frac{\delta t_a^2}{2} I_3 \\ \delta t_a I_3 \\ 0_3 \end{bmatrix} \begin{bmatrix} w_x \\ w_y \\ w_z \end{bmatrix}_{a,k-1} \tag{5-3}$$

where a is the control input (the acceleration measurements in the platform body frame), and w is the associated measurement noise of the strong motion seismometer on the x-, y-, and z-axes. The **system noise matrix** following Eq. (3-18) is defined in Eq. (5-4).

$$Q_{k-1} = \begin{bmatrix} \frac{q_a \delta t_a^3}{3} I_3 & \frac{q_a \delta t_a^2}{2} I_3 & 0_3 \\ \frac{q_a \delta t_a^2}{2} I_3 & q_a \delta t_a I_3 & 0_3 \\ 0_3 & 0_3 & q_b \delta t_a I_3 \end{bmatrix}_{k-1} \tag{5-4}$$

where q_a is the PSD of the strong motion seismometer random noise, and q_b is the PSD of the strong motion seismometer baseline error variation. As discussed in Chapter 3, the initial q_a is set according to the CMG-5TD strong motion seismometer datasheet provided by the manufacturer, Güralp Systems Limited. Since the instruments and platform have been kept at the same position for a long period without being moved in this experiment, the initial q_b is calculated from the standard deviation of the pre-event mean acceleration during the static period by assuming there is zero displacement.

Similarly, as the strong motion seismometer provides the observations into the system model, the measurement inputs in the measurement model are provided by GNSS displacement solutions with respect to the initial GNSS position in the platform body frame. The **measurement matrix** is defined in Eq. (5-5), and based on Eq. (3-11); the **measurement model** for the three-dimensional Kalman filter integration is formulated as Eq. (5-6).

$$H_k = \begin{bmatrix} I_3 & 0_3 & 0_3 \end{bmatrix}_k \tag{5-5}$$

$$z_k = \begin{bmatrix} d_{x,GNSS} \\ d_{y,GNSS} \\ d_{z,GNSS} \end{bmatrix}_k = \begin{bmatrix} I_3 & 0_3 & 0_3 \end{bmatrix}_k \begin{bmatrix} d_x \\ d_y \\ d_z \\ v_x \\ v_y \\ v_z \\ b_x \\ b_y \\ b_z \end{bmatrix}_k + \begin{bmatrix} w_{x,GNSS} \\ w_{y,GNSS} \\ w_{z,GNSS} \end{bmatrix}_k \tag{5-6}$$

where the $d_{x,GNSS}$, $d_{y,GNSS}$, and $d_{z,GNSS}$ are the GNSS displacement solutions of the x-, y-, and z-axes, respectively, in the platform body frame calculated from the initial GNSS position; $w_{x,GNSS}$, $w_{y,GNSS}$, and $w_{z,GNSS}$ are the GNSS measurement random noise parameters along the three axes in the body frame as well. The **measurement noise covariance matrix** in the three-dimensional Kalman filter is defined as follows:

$$R_k = \begin{bmatrix} R_{x,GNSS} & 0 & 0 \\ 0 & R_{y,GNSS} & 0 \\ 0 & 0 & R_{z,GNSS} \end{bmatrix} \tag{5-7}$$

where the $R_{x,GNSS}$, $R_{y,GNSS}$, and $R_{z,GNSS}$ are the measurement noise covariance of GNSS along x-, y-, and z-axes in the platform body frame. The sampling rate of GNSS observation in this experiment is 1 Hz. Following the suggestion in the *Section 14.3 Measurement Models* in (Groves 2013), the initial measurement noise covariance of GNSS was set as $(4\ \text{m})^2$.

5.3 Experimental Results and Analysis

Unlike the LHPOST experiment in Chapter 4, there are no displacement truth outputs with a time series and also no real earthquake or earthquake simulations in the NPL experiment. The movable steel plate on the platform was shifted along the x-axis manually by pulling a string, and the displacements were determined by using a spacer and a screw as shown in Figure 5.6. The spacer and the adjustable screw in Figure 5.6

ensure that the platform's range of movements is mechanically limited. The main purposes for this experiment are firstly to test whether the proposed three-dimensional Kalman filter algorithm with the baseline error state (KFB) can provide stable and accurate displacement estimates when there are small shifts, and secondly to understand whether the baseline error state can detect the baseline changes and improve the accuracy of the Kalman filtered estimates. Hence, in order to validate the proposed Kalman filter algorithm, a Kalman filter smoother, the RTS smoother, introduced in Section 3.9.1, has been applied after the KFB. The smoothed results are also used in this experiment to compare with the three-dimensional Kalman filter with no baseline error state (KFNB) and the KFB.

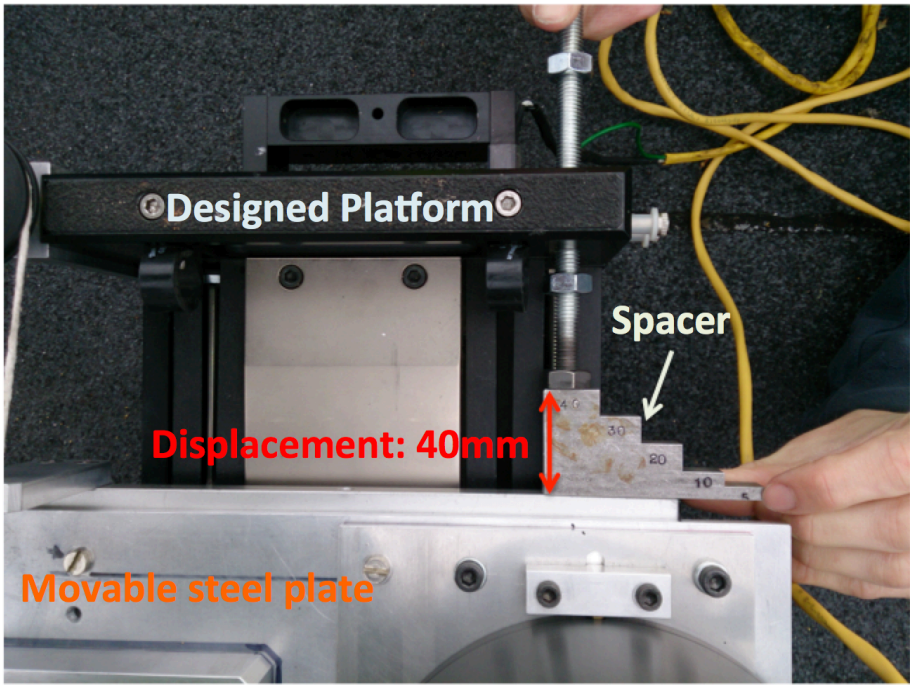

Figure 5.6: A spacer made with 40 mm, 30 mm, 20 mm, 10 mm, and 5 mm displacements on for adjusting the shifts of the movable steel plate on the platform

As mentioned before, the experiment took place at NPL during the same time periods on two consecutive days, and the sensors and platform were in the initial position without movement for most of the time periods. By doing this, the initial position of the GNSS receiver can be determined precisely for later calculating the displacement from moving. The movable steel plate on the platform was only adjusted by using the spacer and shifted various small displacements along the x-axis during the last 90 minutes of the second day. The platform was subjected to 40 mm, 30 mm, 20 mm, and 10 mm displacement along the x-axis in the body frame. These small displacements were implemented in the experiment, as the part of the point of the research is to be able to determine small shifts at distances of hundreds of kilometres from a fault immediately after an earthquake. Figure 5.7 shows the entire displacement results in the x-, y-, and z-

axes from GNSS and Kalman filter integrations when the platform and the sensors began to move laterally.

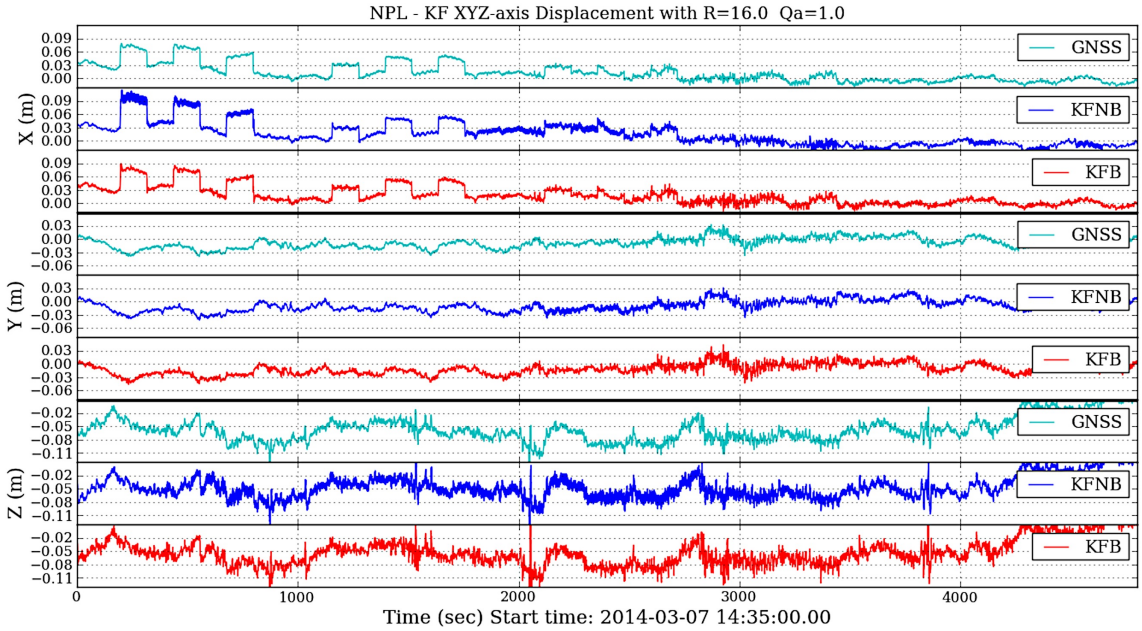

Figure 5.7: The three-dimensional displacement solutions from the GNSS PPP (GNSS), the Kalman filter with no baseline error state (KFNB), and the Kalman filter with baseline error state (KFB) with $\boldsymbol{q_a}$=1.0 (m^2/s^3), $\boldsymbol{R}$ =16 (m^2), and C_{q_b} = 4.0 (time span ~ 90 mins)

Since the platform was moving laterally along the x-axis, in Figure 5.7, the displacement solutions along the x-axis show obvious movements. As there was no significant vertical movement during this experiment, Figure 5.7 also illustrates that the results of the vertical direction are generally noisier than the horizontal results. As the effect of the GNSS signal geometry, the horizontal GNSS positioning is usually more accurate than vertical GNSS positioning (Groves 2013). Furthermore, the results in Figure 5.7 also show that when the movement along the x-axis is smaller than 30 mm, all three methods struggle to provide accurate displacement solutions; this can be seen in Figure 5.8 as well. By determining the x-axis displacement of the platform manually using the spacer (black line), the magnitudes and time periods of the platform movements are clearly shown as AVG in Figure 5.8. Since the movements of the sensors are mainly along the x-axis, the further discussion and analysis in this chapter are focusing on the x-axis solutions. As described previously, the RTS smoothed solutions (green line in Figure 5.8) are also shown in the results for comparison with other solutions. The AVG are expected to be relatively accurate solutions and are used as the true displacement in this experiment.

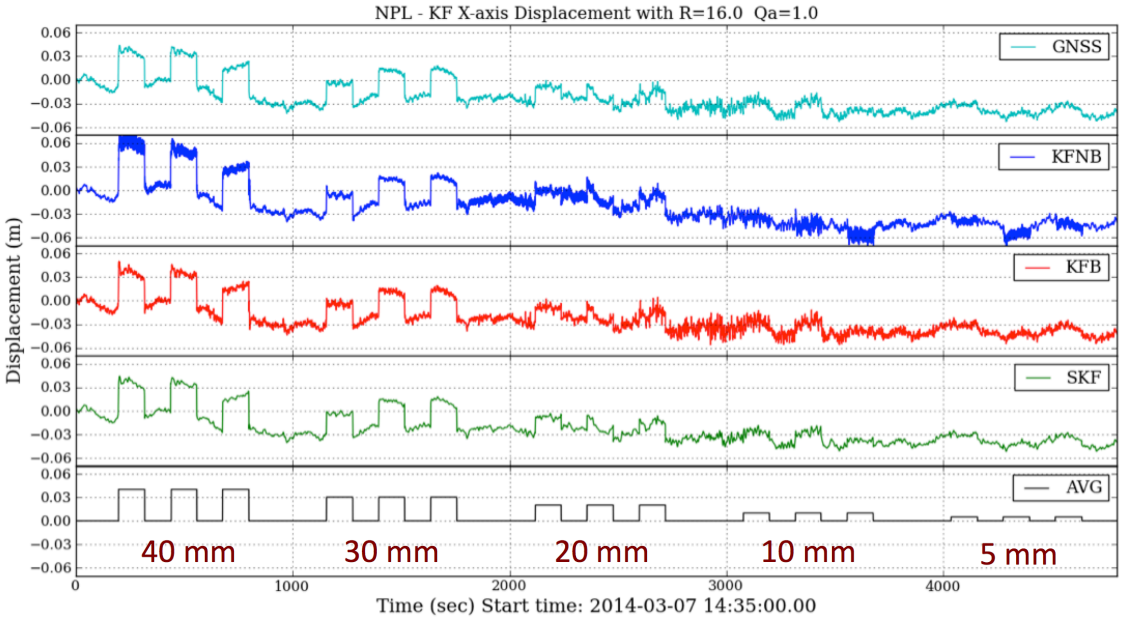

Figure 5.8: The displacement solutions with $\boldsymbol{q_a}$=1.0 (m^2/s^3), $\boldsymbol{R}$ =16 (m^2), and C_{q_b} = 4.0 along the x-axis of the entire period with the numerically generated displacment results (black) to illustrate the ideal magnitudes and periods of the platform movements

In the experiment, the movable steel plate was shifted side-to-side on the platform and kept static at one side for two minutes. Thus, there was no high-frequency earthquake-like shaking but only brief movements. This experiment was mainly designed to test whether, if there are permanent shifts after earthquakes, the proposed GNSS or Kalman filter methods can provide accurate displacement solutions. Visually comparing the GNSS, KFNB, and KFB displacements solutions in Figure 5.8, GNSS provides relatively stable and smooth solutions compared to KFB and KFNB when the platform movements are more than 30 mm, which can also be seen in Figure 5.9. However, Figure 5.8 also shows the noise level of GNSS is greater than a 20 mm displacement, so that GNSS is unable to provide accurate solutions when the displacements are smaller than 20 mm. Although the experiment was set on a rooftop with few surrounding reflectors relative to the GNSS receiver, there were still GNSS multipath effects in the environment. The geometry of the GNSS satellites and the surrounding environment of the GNSS receivers are related to the multipath error as well as the precision of the GNSS solutions (Genrich & Bock 1992). In the project of which this thesis is a part, a sidereal filter technique has also been applied on the GNSS solutions to identify and filter the repeating multipath error by taking the advantage of the approximately 23h 55m 55s ground-track repeat time of GNSS satellites (Choi et al. 2004). Research regarding GNSS PPP processing and improvements have been investigated by Christopher Atkins (Atkins & Ziebart 2015). This thesis concentrates on the GNSS and strong motion seismometer integration.

Because measuring the permanent displacements rapidly after shaking is the most important task in this study, the real displacements that are provided by the spacer are compared with the displacement solutions of GNSS and Kalman filter methods. The true movement marked as AVG in Figure 5.9 shows the real displacements along the x-axis when the movable steel plate was shifted by 40 mm and 30 mm on the platform. The mean displacements of each static period are displayed as yellow dots in Figure 5.9, and the orange arrows (d1)~(d12) represent the displacements of the twelve shifts in the experiment. Table 5.1 shows the twelve movement results of GNSS, KFB, KFNB, and SKF, calculating the differences of the mean values of the static displacements.

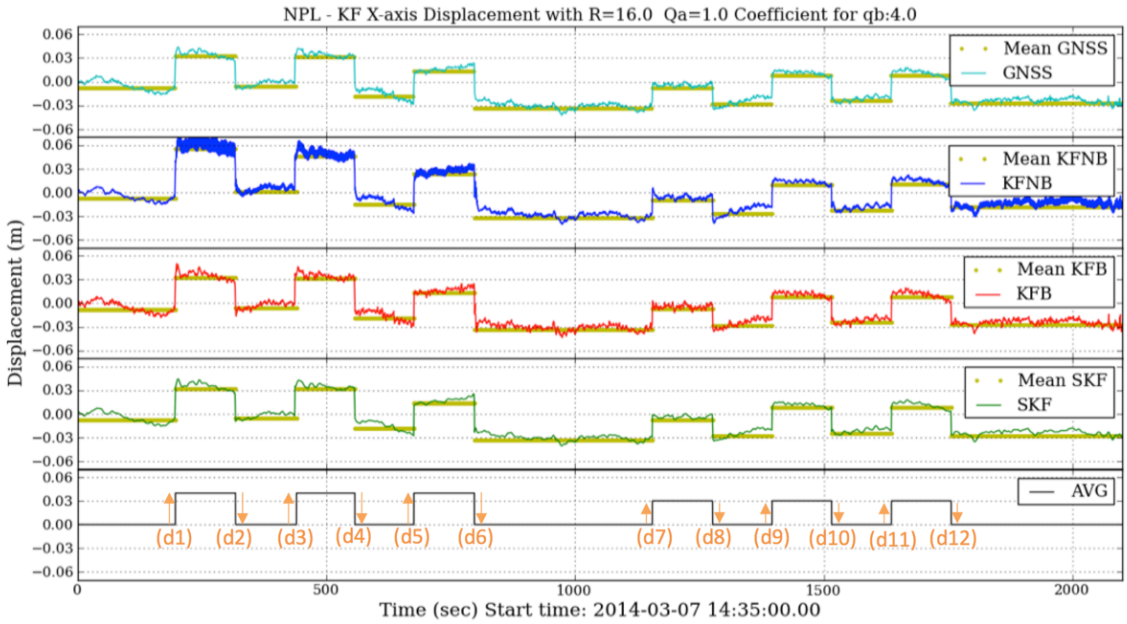

Figure 5.9: The displacement results with $\boldsymbol{q_a}$=1.0 (m^2/s^3), $\boldsymbol{R}$ =16 (m^2), and C_{q_b} = 4.0 along the x-axis when the movable steel plate was shifted by 40 mm and 30 mm. The orange arrows (d1)~(d12) represent the displacments of the twelve movements. The Mean GNSS, KFB, KFNB, and SKF (yellow dots) represent the mean values of the static displacments after movements.

The displacement error results in Table 5.1 show that apart from the KFNB solutions, the performances of GNSS, KFB, and SKF with respect to the AVG movements are similar. As the integration methods were expected to provide a better performance, especially SKF, the results in Table 5.1 indicate that the actual shift errors are dominated by GNSS errors with the data sets. This phenomenon might due to the improper setting of the measurement noise parameter, $\boldsymbol{R}$, in the Kalman filters, which results the weighting being too high for GNSS measurements. In this case, a Kalman filter tuning process is needed to find out the appropriate noise parameter settings in the Kalman filter calculations for a better performance.

Table 5.1: The displacements of GNSS, KFB, KFNB, and SKF from d1 to d12 (as marked in Figure 5.9) and their error statistics with respect to the AVG movements with $\boldsymbol{q_a}$=1.0 (m^2/s^3), $\boldsymbol{R}$ =16 (m^2), and C_{q_b} = 4.0

(mm)	d1	d2	d3	d4	d5	d6	Displacement Error to AVG		
AVG	40.00	-40.00	40.00	-40.00	40.00	-40.00	Mean	STD	RMS
GNSS	40.32	-37.64	36.82	-49.52	31.14	-46.58	0.33	6.16	6.15
KFNB	63.92	-55.05	44.52	-60.69	38.27	-54.68	12.86	15.63	8.89
KFB	40.41	-37.80	36.87	-49.71	31.49	-46.82	0.51	6.16	6.14
SKF	40.23	-37.52	36.73	-49.62	31.45	-46.77	0.39	6.16	6.15
(mm)	d7	d8	d9	d10	d11	d12	Displacement Error to AVG		
AVG	30.00	-30.00	30.00	-30.00	30.00	-30.00	Mean	STD	RMS
GNSS	26.01	-20.72	36.52	-32.70	32.35	-35.51	0.63	5.59	5.55
KFNB	22.16	-17.06	36.46	-32.17	33.20	-28.83	-1.68	6.91	6.70
KFB	26.22	-20.92	36.67	-32.94	32.54	-35.58	0.81	5.58	5.53
SKF	26.20	-20.99	36.72	-33.01	32.60	-35.61	0.85	5.59	5.53

By focusing on the first 40 mm displacement results along the x-axis, Figure 5.10 illustrates the displacement solutions from different methods in more details. In Figure 5.10, the KFNB results drifted and were biased by the changed baseline after the platform shifted. When the drifted and biased estimates in KFNB were updated by the GNSS measurements, the displacement result became sawtooth-like as shown in Figure 5.10. The main reason for the sawtooth-like effects is that the sensor bias of the strong motion seismometer might have been changed during or after moving, which means the accelerometer baseline has been changed from the pre-event accelerometer baseline. When the accelerometer baseline changes, the resulting accelerometer baseline error will lead to a quadratic drift within displacement estimates` during the Kalman filter system update processing until a measurement update is available. For example, the 100 Hz strong motion seismometer observations will be doubly integrated to the displacements in the system model until a 1 Hz GNSS observation has been put into the Kalman filter algorithm, and then the GNSS observations will correct and update the quadratic-drifted propagated estimates. The sawtooth-like effect related to the different sampling rates of the observations between the system model and measurement model is a common effect in the loosely coupled Kalman filter integration (Rios & White 2002; Emore et al. 2007; Geng, Bock, et al. 2013; Bock et al. 2011; Niu & Xu 2014). The

sawtooth-like effect can be significant when there are uncorrected sensor biases or baseline errors in the system model and when the time interval in the system model is much smaller than in the measurement model, for example, the 100 Hz accelerometer data in the system model and the 1 Hz GNSS observation in the measurement model in this study. Thus, by estimating the baseline error state and correcting the accelerometer observations at each epoch in the system model, ideally the sawtooth-like effect will be minimised. The KFB results in Figure 5.10 also show that while estimating the strong motion seismometer baseline error as a state in the KFB, the sawtooth-like effects are significantly reduced, and the displacement results have become more reliable.

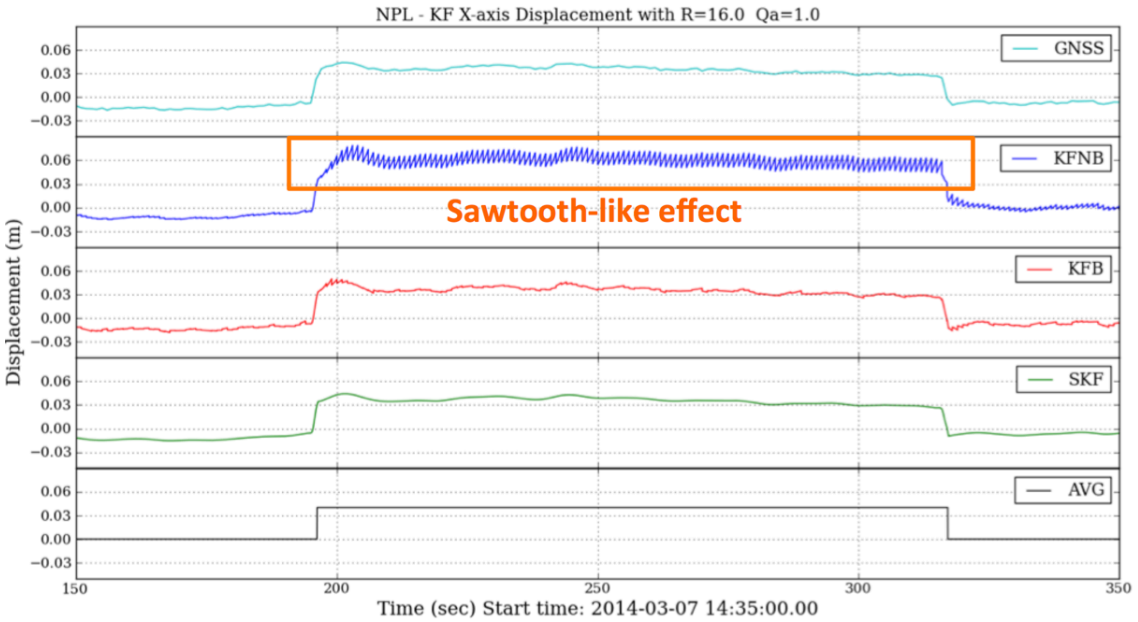

Figure 5.10: The sawtooth-like effect on the displacement results with $\boldsymbol{q_a}$=1.0 (m^2/s^3), $\boldsymbol{R}$ =16 (m^2), and C_{q_b} = 4.0 along the x-axis when the movable steel plate on the platform was shifted by 40 mm.

By assuming the sensors are static except when shifting the movable steel plate to one side of the platform from the other side, the strong motion seismometer outputs are expected to be zero-mean. However, when processing the accelerometer or strong motion seismometer data, the sensor bias or tilting usually biases the acceleration outputs and hence affects the displacement estimates, for example, the sawtooth-like effect. The influence sometimes can be eliminated by obtaining the mean acceleration outputs from the static sensors, also known as the pre-event acceleration baseline, and removing this mean acceleration from the accelerometer outputs. This process is known as the baseline correction. Theoretically, the corrected accelerometer outputs become zero-mean, and the accelerometer can provide the actual movement without biases. However, while moving or shaking the instruments, the acceleration baseline might be changed, and the accelerometer outputs are not zero-mean anymore. For example, in Figure 5.10, before the platform was shifted (150~195 seconds), the KFNB can provide smooth solutions; after the first movement (195~320 seconds), the accelerometer

outputs have been biased by the change in the baseline error, which magnifies the sawtooth-like effects on the displacement solutions. Hence, in order to sense the changes of the acceleration baseline error and correct them from the accelerometer observations, a baseline error state has been proposed in the KFB as described previously in Section 5.2 to estimate any small changes of the acceleration baseline. Figure 5.11 illustrates the first 2000 seconds of acceleration results of the strong motion seismometer including the raw accelerometer outputs (yellow), the baseline error state estimates (taken from the KFB state time series) (red), and the pre-event baseline error (green).

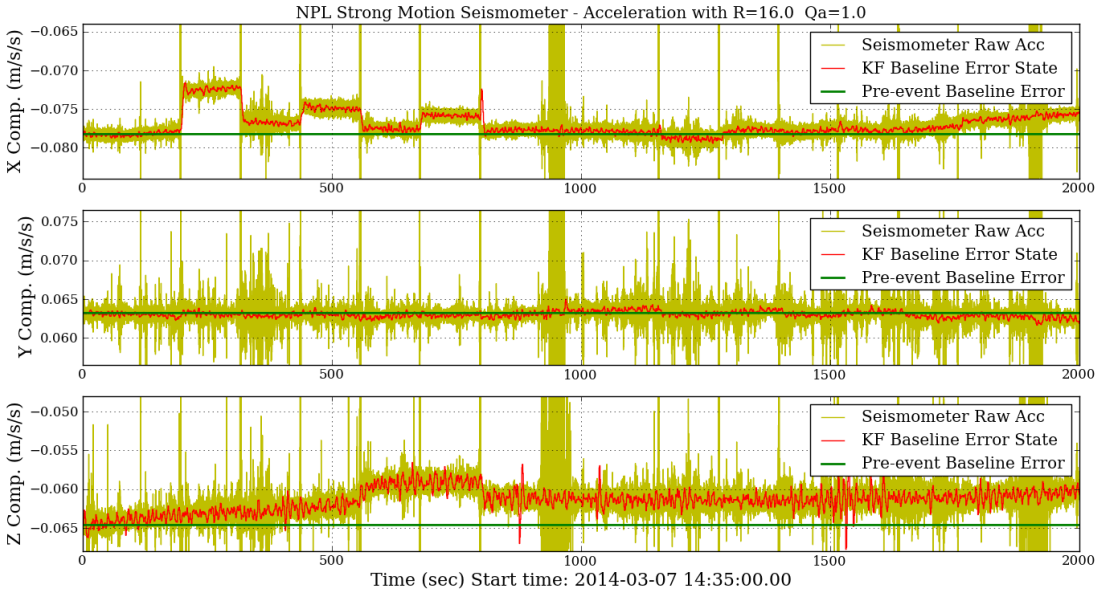

Figure 5.11: The acceleration results of the x-, y-, and z-component of the strong motion seismometer and the Kalman filter baseline error state estimates.

The pre-event baseline error (green line) in Figure 5.11 is the mean acceleration of a static period (200 seconds) before the first movement. Based on the design of this experiment, ideally, the raw acceleration should have been close to zero when the platform was static and only reached large values for a very short period when the platform was moved. However, the raw accelerometer outputs of the strong motion seismometer in Figure 5.11 show that in this experiment. The mean acceleration baseline errors of three components are non-zero from the beginning; further, whenever the movable steel plate was shifted side-to-side on the platform, the accelerometer outputs exceeded the range of the figure for a very short time and then returned to different mean values; and finally, the baseline error state estimates follow the changes of the acceleration baseline error.

As described in Chapter 4, the UCSD large shake table data was unable to show the greatest advantage of using the baseline error state estimates due to the lack of permanent displacement and baseline error changes after shaking. Thus, the NPL

experiment was designed purposely not to level the sensor carefully, in order to leave some potential baseline errors in the accelerometer observations. For example, although the strong motion seismometer on the platform was levelled at the beginning of the experiment, the uneven ground of the rooftop might leave the sensor unlevelled when shifting the sensor to the other side. Also, as the platform was not firmly fixed on the ground, when pulling the string and shifting the platform sharply during the experiment, the unfixed platform might be slightly moved or tilted. The seismometer raw data (yellow line) in Figure 5.11 shows that the mean baseline errors varied almost every time after laterally shifting the platform, especially the x-component. The acceleration baseline error is believed to be one important factor to cause the sawtooth-like effect in the displacement solutions during Kalman filter integrations. The KFB, by estimating the baseline error state epoch by epoch, can minimize the rapid drifts or the sawtooth-like effects and provide more reliable displacement solutions.

5.4 Kalman Filter Tuning

In Chapter 4, the MTS controller was used as a displacement truth model in the UCSD LHOPST experiment. The displacement truth model in Chapter 4 provided the standard to validate the accuracy of different methods and show the importance of the Kalman filter tuning process. However, often in real earthquakes, no displacement truth model is available; this is also the case in the movement in the NPL experiment. The RTS smoother was applied on the displacement solutions after KFB and considered to be the relatively accurate solutions and the 'near-true' movements. However, the RTS smoothed solutions actually varied when tuning the parameters in KFB because the RTS smoother was applied after KFB, which is difficult to provide a fair statistical analysis. Hence, instead of focusing on the displacement solutions, the velocity solutions of each Kalman filter algorithm are used to calculate the statistical results in this experiment. The movable steel plate on the platform remained static for 2 minutes after each shift, which means that the real velocity of the instruments during the static periods should be zero. The zero-velocity assumption has provided a relative truth in this experiment. Since the accelerometer baseline errors lead to linear drifts in the velocity solutions, the velocity error analysis will be helpful for obtaining the optimal parameters in the Kalman filter algorithms. Furthermore, this section will also discuss how each parameter actually impacts the state estimates when tuning the Kalman filter.

The Kalman filter tuning process mainly involves three parameters: the measurement noise covariance, $\boldsymbol{R}$, and the $\boldsymbol{q_a}$ and $\boldsymbol{q_b}$ in the system noise covariance, $\boldsymbol{Q}$. The technique used to tune the Kalman filter in this section is to fix two of the parameters and vary the third parameter. The $\boldsymbol{q_b}$ in KFB and SKF are the PSDs of the accelerometer baseline error variation obtained from the standard deviation of the baseline error from the pre-

event accelerometer observations. Following by Eq. (4-5), the technique to vary $\boldsymbol{q_b}$ is to increase the standard deviation of the baseline error:

$$C_{q_b} \cdot q_b = \frac{(c \cdot \sigma_b)^2}{\delta t_a} \tag{5-8}$$

where C_{q_b} is the coefficient of $\boldsymbol{q_b}$, and c is the coefficient to vary the standard deviation of the baseline error variation. The initial C_{q_b} was set as 4.0 in the tuning process. The initial $\boldsymbol{q_a}$ = 1.0 (m^2/s^3) and $\boldsymbol{R}$ = 16.0 (m^2) were set according to Eq. (5-4) and Eq. (5-7). The parameters in the KFB, KFNB, and SKF are set as the same values for comparison.

5.4.1 Fixed R and q_b with varied q_a

The first parameter to tune in the Kalman filter is the $\boldsymbol{q_a}$ in the system noise covariance matrix. The tuning process starts with the initial $\boldsymbol{q_a}$=1.0 (m^2/s^3) and increases/decreases the value of $\boldsymbol{q_a}$. Noted that when tuning $\boldsymbol{q_a}$ in the Kalman filter, the $\boldsymbol{q_a}$ in both KFB and KFNB are tuned to the same value, and the SKF solutions are the RTS smoothed KFB solutions. The velocity results of these three methods are compared with the zero-velocity truth model. The zero-velocity truth assumes that the velocity of the platform and sensors were zero for 2 minutes after each movement in the experiment. Notably, as it is difficult to know the exact time periods when the platform was moving, the velocity solutions for 4 seconds during each movement are removed when calculating the velocity error results. Since the KFNB is tuned at the same time, the advantages of using an additional baseline error state in KFB are more clear and significant. Moreover, the SKF results can show the advantage of applying a smoother after a forward Kalman filter. Table 5.2 shows the statistics of the tuned KFB, KFNB, and SKF error results with respect to the zero-velocity truth during the static periods.

Table 5.2: The performance of the KFNB, KFB, and SKF velocity solutions by fixing $\boldsymbol{R}$ =16 (m^2) and C_{q_b} = 4.0 and setting different $\boldsymbol{q_a}$ with respect to the zero-velocity truth model during the static periods

	KFNB X Velocity Error (m/s)			KFB X Velocity Error (m/s)			SKF X Velocity Error (m/s)		
q_a (m^2/s^3)	Mean	STD	RMS	Mean	STD	RMS	Mean	STD	RMS
1E-03	0.02045	0.02391	0.03147	-2.23E-05	0.00130	0.00130	-1.72E-05	0.00048	0.00048
1E-02	0.01153	0.01357	0.01782	-2.23E-05	0.00130	0.00130	-1.72E-05	0.00048	0.00048
1E-01	0.00651	0.00772	0.01010	-2.22E-05	0.00130	0.00130	-1.72E-05	0.00048	0.00048
1.0	0.00370	0.00446	0.00580	-2.22E-05	0.00117	0.00117	-1.72E-05	0.00044	0.00044
10.0	0.00216	0.00275	0.00350	-1.95E-05	0.00127	0.00127	-1.70E-05	0.00057	0.00057
100.0	0.00137	0.00213	0.00254	-1.64E-05	0.00146	0.00146	-1.62E-05	0.00083	0.00083
1000.0	0.00106	0.00230	0.00253	-3.33E-06	0.00196	0.00196	-1.41E-05	0.00131	0.00131

Generally speaking, in Table 5.2, the performance and stability of KFB are better than KFNB with respect to the zero-velocity truth, which also show the advantage of using a baseline error state in the Kalman filter algorithm. The KFB and SKF velocity error results in Table 5.2 indicate that when the value of q_a is decreasing, the error mean is decreasing yet the STD and RMS errors are increasing. Whereas the KFNB velocity error results show that the mean, STD, and RMS errors are decreasing when increasing q_a in Table 5.2. As q_a represents the noise level of the strong motion seismometer, the larger the q_a is, the more the Kalman filter trusts the GNSS observations. This explains the differences between the KFB and KFNB tuning results shown in Table 5.2. Since the KFB and SKF have estimated and corrected the baseline errors from the strong motion seismometer observations, the effects of changing q_a are not significant. As the mean error of KFB and SKF in Table 5.2are relatively small and similar compared to STD and RMS, the optimal estimates of KFB and SKF with the minimum STD and RMS velocity error when tuning q_a are obtained from setting q_a=1.0 (m^2/s^3) in this case.

In the following seven figures, the displacement results for KFNB and KFB are shown for each of the q_a values given in Table 5.2. By plotting the displacement and the acceleration results together in figures, the correspondences between both results during tuning q_a are illustrated more clearly. The velocity error results of KFB, KFNB, and SKF of varied q_a with respect to the zero-velocity truth are also displayed in **Appendix A.1** for more information.

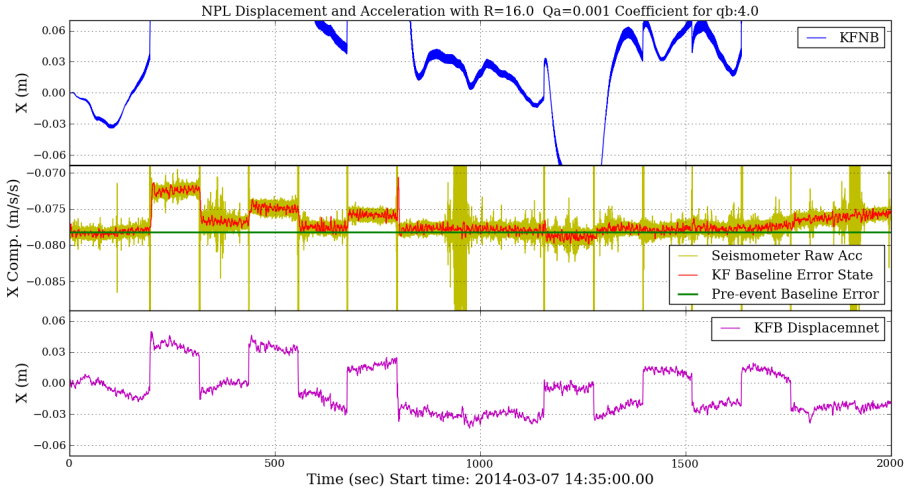

Figure 5.12: KFB and KFNB tuning: displacement and corresponding acceleration results with q_a=0.001 (m^2/s^3), $\boldsymbol{R}$ =16 (m^2), and C_{q_b} = 4.0

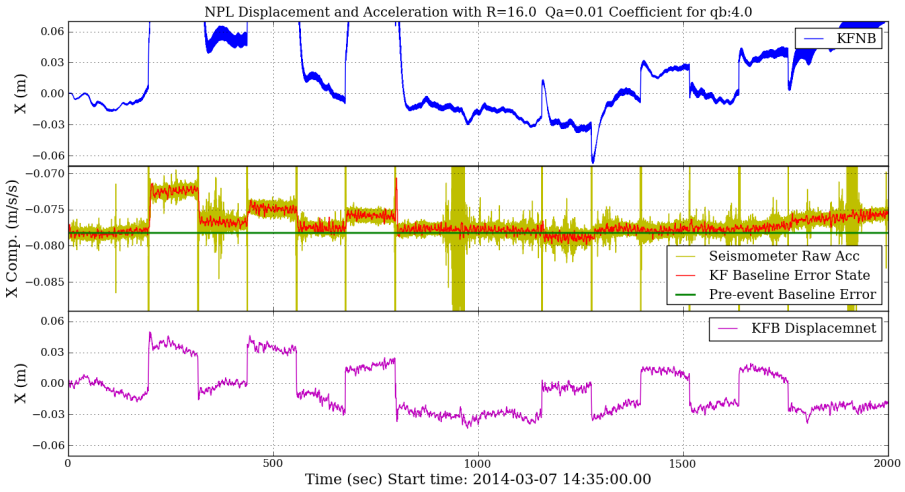

Figure 5.13: KFB and KFNB tuning: displacement and corresponding acceleration results with $\boldsymbol{q_a}$=0.01 (m^2/s^3), $\boldsymbol{R}$ =16 (m^2), and C_{q_b} = 4.0

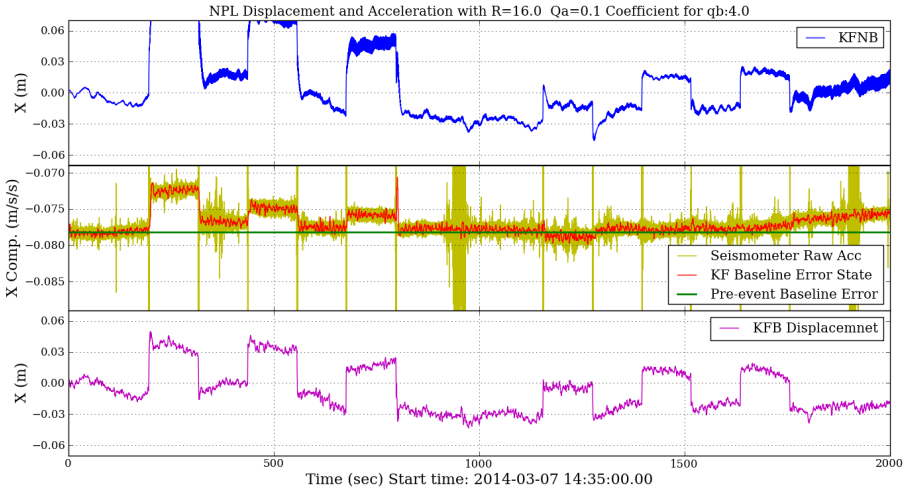

Figure 5.14: KFB and KFNB tuning: displacement and corresponding acceleration results with $\boldsymbol{q_a}$=0.1 (m^2/s^3), $\boldsymbol{R}$ =16 (m^2), and C_{q_b} = 4.0

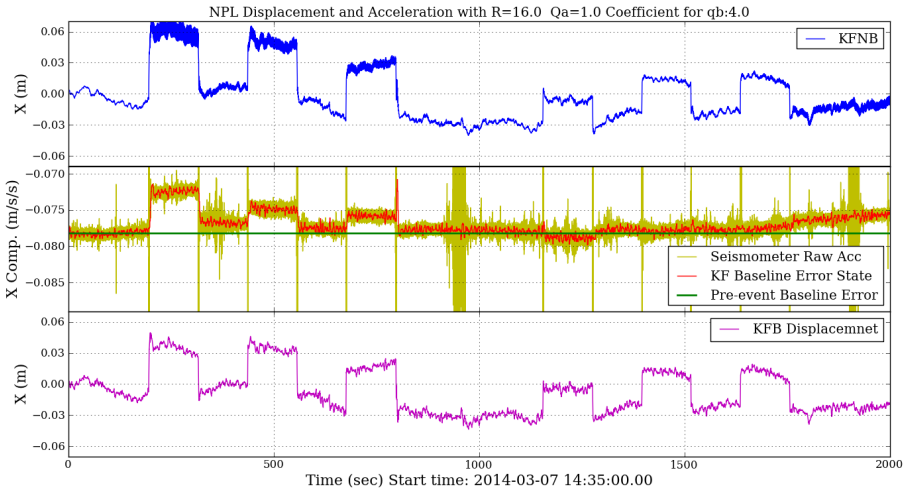

Figure 5.15: KFB and KFNB tuning: displacement and corresponding acceleration results with $\boldsymbol{q_a}$=1.0 (m^2/s^3), $\boldsymbol{R}$ =16 (m^2), and C_{q_b} = 4.0

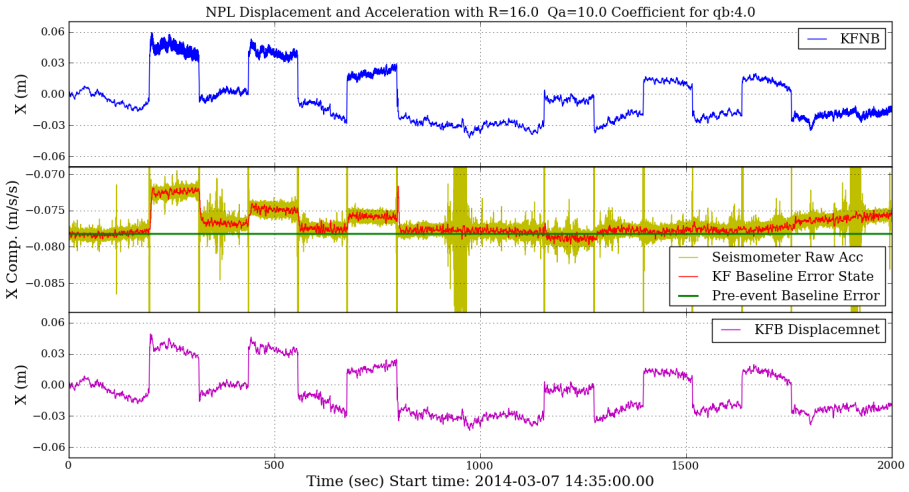

Figure 5.16: KFB and KFNB tuning: displacement and corresponding acceleration results with $\boldsymbol{q_a}$=10.0 (m^2/s^3), $\boldsymbol{R}$ =16 (m^2), and C_{q_b} = 4.0

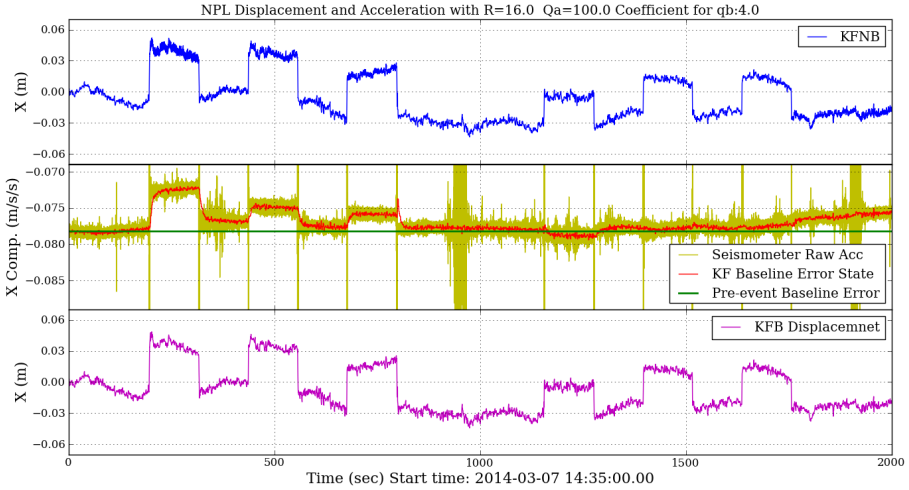

Figure 5.17: KFB and KFNB tuning: displacement and corresponding acceleration results with $\boldsymbol{q_a}$=100.0 (m^2/s^3), $\boldsymbol{R}$ =16 (m^2), and C_{q_b} = 4.0

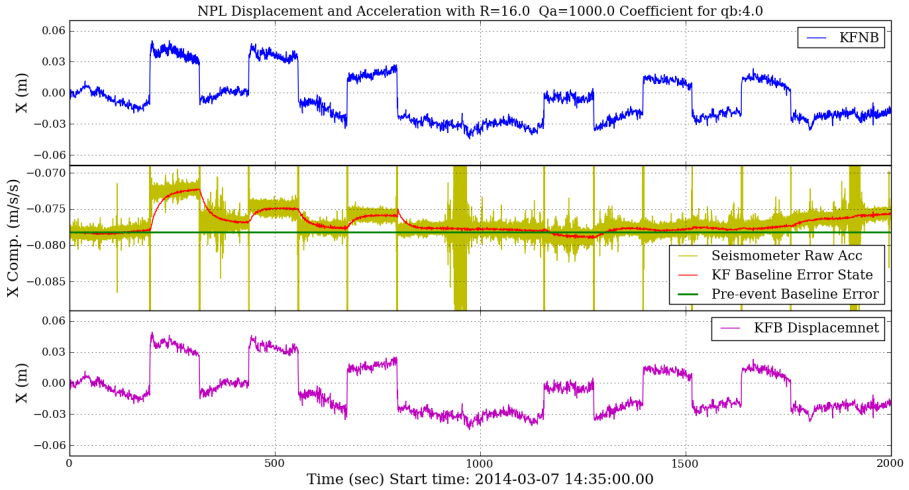

Figure 5.18: KFB and KFNB tuning: displacement and corresponding acceleration results with $\boldsymbol{q_a}$=1000.0 (m^2/s^3), $\boldsymbol{R}$ =16 (m^2), and C_{q_b} = 4.0

From Figure 5.12 to Figure 5.18, the KFB solutions with the baseline error state are generally more stable compared to the KFNB solutions. Figure 5.12 to Figure 5.15 show that when the q_a is set small (q_a=0.001~1.0 (m^2/s^3)), the KFNB displacement solutions drift rapidly with the sawtooth-like effects. The baseline error state estimates in the KFB can compensate the sensor bias and avoid the rapid quadratic drifts in the displacement solutions.

When increasing the value of q_a (in Figures 5.12~5.18), the trend of the baseline error state estimates in the KFB is also changing. The larger values of q_a indicate that the noise level of the strong motion seismometer observations is higher, and the Kalman filter will then trust the GNSS displacement solutions more due to the lack of confidence on the strong motion seismometer observations. Meanwhile, when q_a is large, the q_b for detecting the variations of the baseline error state estimates might be neglected and unable to reflect the small variations of the baseline error state estimates. For example, when q_a = 1000.0 (m^2/s^3), the baseline error state estimates become smoother and take more time to converge to the stability as shown in Figure 5.18; the STD and RMS errors of KFB and SKF velocity with respect to the zero-velocity truth shown in Table 5.2 are actually growing when q_a = 1000.0 (m^2/s^3).

From the error results and figures in this section, it is clear that tuning of q_a impacts the KFNB solutions more than the KFB solutions. When q_a > 1.0, the KFNB solutions are improved because the underlying mathematic model is insufficient. Although when q_a > 10.0, the increasing q_a degrades the estimation of the baseline error states in the KFB, the performance of the KFB is still better than the KFNB. Generally speaking, with the baseline error state in the KFB, the Kalman filter becomes steadier and provides relatively reliable displacement solutions over time.

5.4.2 Fixed q_a and q_b with varied R

After tuning the q_a in the system noise matrix, the measurement noise matrix, $\boldsymbol{R}$, is tuned in this section. Based on the results in previous section 5.4.1, the fixed q_a is set as 1.0 (m^2/s^3). The fixed q_b in the system noise matrix is still set with the C_{q^b} = 4.0. The initial $\boldsymbol{R}$ is set as 16.0 (m^2) based on the suggestion in Groves (2013). Noted that when tuning $\boldsymbol{R}$ in the Kalman filter, the $\boldsymbol{R}$ in both KFB and KFNB are also tuned to the same value, and the SKF solutions are the RTS smoothed KFB solutions. As discussed in the previous section, the velocity results of these three methods are compared with the zero-velocity truth model as well. Table 5.3 shows the statistics of the tuned KFB, KFNB, and SKF error results with respect to the zero-velocity truth during the static periods.

Table 5.3: The performance of the KFNB, KFB, and SKF velocity solutions by fixing $\boldsymbol{q_a}$ = 1.0 (m^2/s^3) and C_{q^b} = 4.0 and setting different $\boldsymbol{R}$ with respect to the zero-velocity truth during the static periods

	KFNB X Velocity Error (m/s)			KFB X Velocity Error (m/s)			SKF X Velocity Error (m/s)		
$R(m^2)$	Mean	STD	RMS	Mean	STD	RMS	Mean	STD	RMS
2.0	0.00227	0.00287	0.00366	-1.91E-05	0.00167	0.00167	-1.70E-05	0.00064	0.00064
4.0	0.00266	0.00329	0.00423	-1.93E-05	0.00151	0.00151	-1.70E-05	0.00058	0.00058
8.0	0.00313	0.00382	0.00494	-2.02E-05	0.00138	0.00138	-1.70E-05	0.00054	0.00054
16.0	0.00370	0.00446	0.00580	-2.16E-05	0.00129	0.00129	-1.71E-05	0.00049	0.00049
32.0	0.00438	0.00525	0.00683	-2.28E-05	0.00123	0.00123	-1.73E-05	0.00046	0.00046
64.0	0.00519	0.00619	0.00808	-2.35E-05	0.00119	0.00119	-1.72E-05	0.00043	0.00043
128.0	0.00616	0.00731	0.00956	-2.32E-05	0.00118	0.00118	-1.70E-05	0.00040	0.00040
256.0	0.00731	0.00866	0.01133	-2.17E-05	0.00121	0.00121	-1.63E-05	0.00039	0.00039

The $\boldsymbol{R}$ was set to 16 m^2 initially and then varied to find the optimal setting. Based on the error results in Table 5.3, $\boldsymbol{R}$=128.0 (m^2) can provide the most stable and optimal estimates during static periods in this case. The error results in Table 5.3 show that when tuning $\boldsymbol{R}$ in Kalman filters, the velocity error results of KFB do not vary much, whereas the KFNB velocity error results are dominated by the value of $\boldsymbol{R}$. While increasing $\boldsymbol{R}$ in the KFB, the mean, STD, and RMS velocity errors are accumulating as well. Figures 5.19~26 illustrate that the tuned KFB, KFNB, and SKF velocity error with respect to the zero-velocity truth.

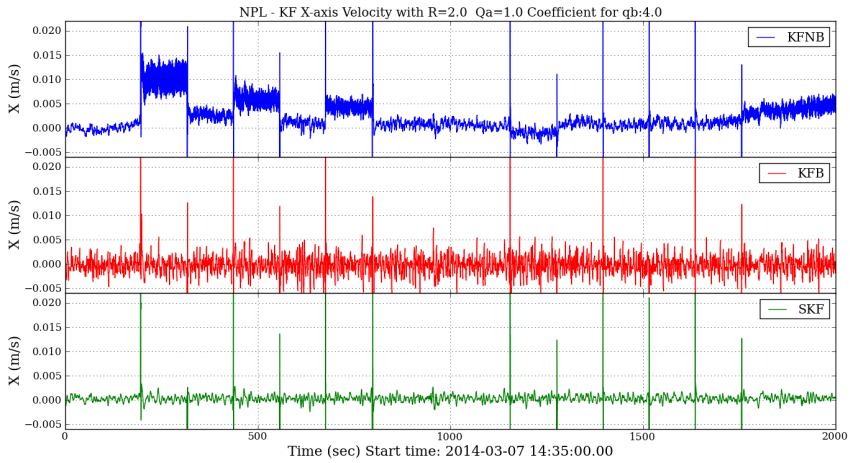

Figure 5.19: KFB and KFNB tuning: velocity error results with respect to the zero-velocity truth with with $\boldsymbol{R}$ =2.0 (m^2), $\boldsymbol{q_a}$=1.0 (m^2/s^3), and C_{q^b} = 4.0

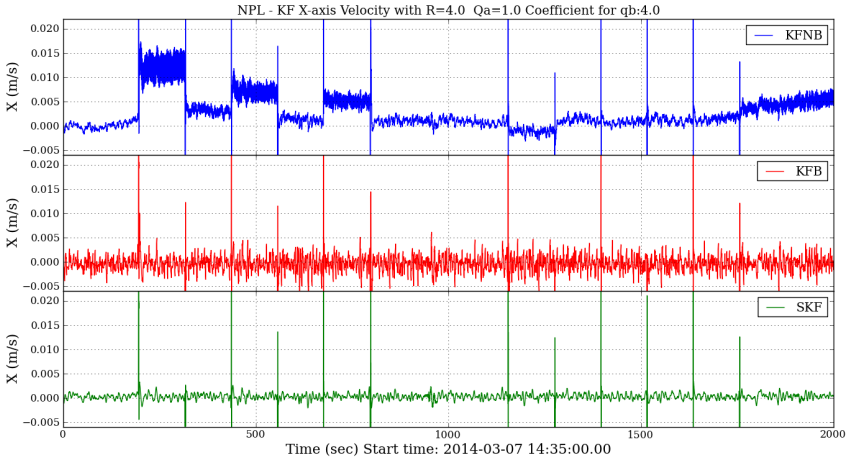

Figure 5.20: KFB and KFNB tuning: velocity error results with respect to the zero-velocity truth with with $\boldsymbol{R}$ =4.0 (m^2), $\boldsymbol{q_a}$=1.0 (m^2/s^3), and C_{q_b} = 4.0

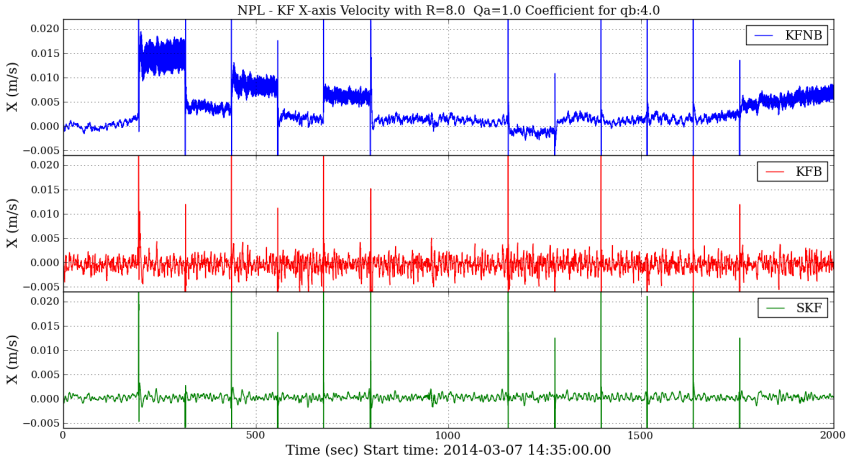

Figure 5.21: KFB and KFNB tuning: velocity error results with respect to the zero-velocity truth with with $\boldsymbol{R}$ =8.0 (m^2), $\boldsymbol{q_a}$=1.0 (m^2/s^3), and C_{q_b} = 4.0

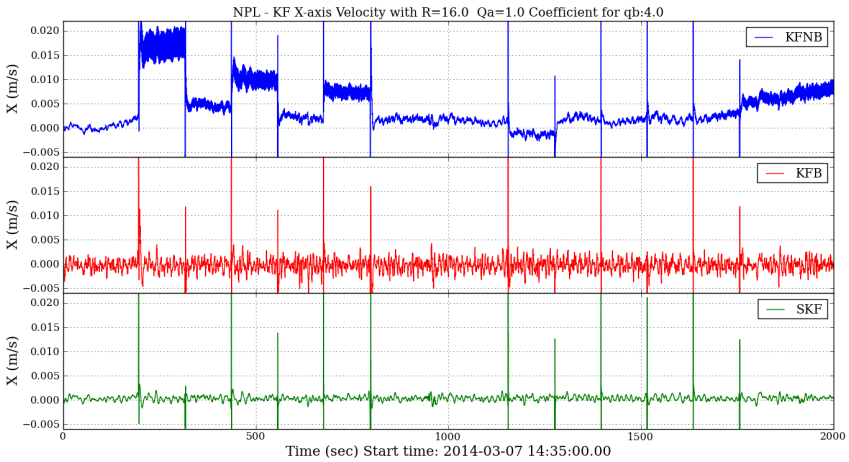

Figure 5.22: KFB and KFNB tuning: velocity error results with respect to the zero-velocity truth with with $\boldsymbol{R}$ =16.0 (m^2), $\boldsymbol{q_a}$=1.0 (m^2/s^3), and C_{q_b} = 4.0

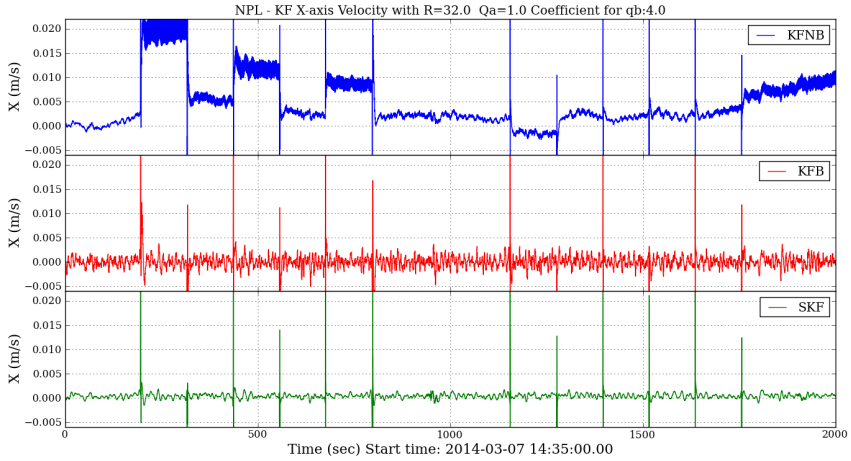

Figure 5.23: KFB and KFNB tuning: velocity error results with respect to the zero-velocity truth with with $\boldsymbol{R}$ =32.0 (m^2), $\boldsymbol{q_a}$=1.0 (m^2/s^3), and C_{q_b} = 4.0

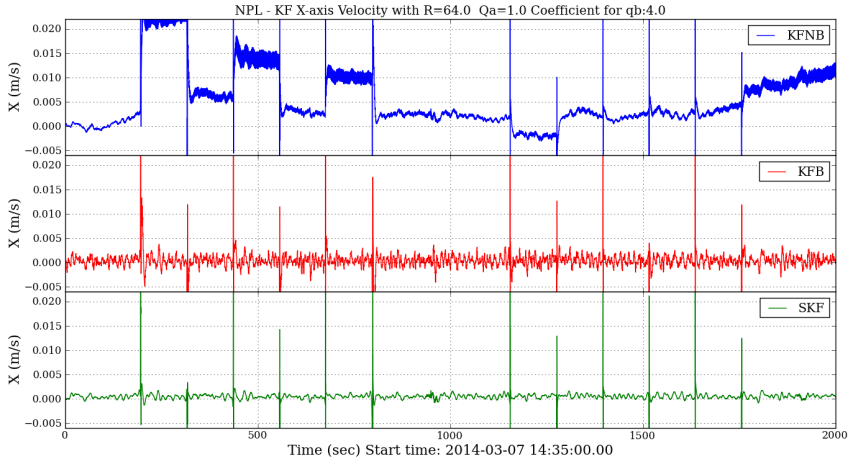

Figure 5.24: KFB and KFNB tuning: velocity error results with respect to the zero-velocity truth with with $\boldsymbol{R}$ =64.0 (m^2), $\boldsymbol{q_a}$=1.0 (m^2/s^3), and C_{q_b} = 4.0

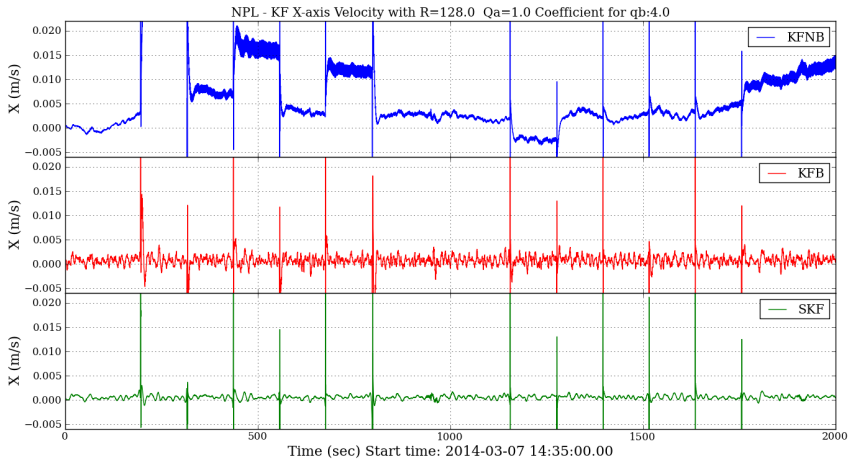

Figure 5.25: KFB and KFNB tuning: velocity error results with respect to the zero-velocity truth with with $\boldsymbol{R}$ =128.0 (m^2), $\boldsymbol{q_a}$=1.0 (m^2/s^3), and C_{q_b} = 4.0

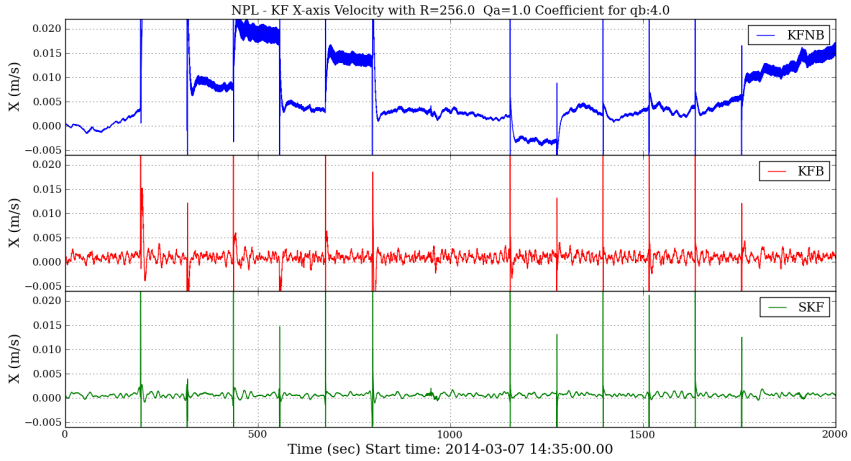

Figure 5.26: KFB and KFNB tuning: velocity error results with respect to the zero-velocity truth with with $\boldsymbol{R}$ =256.0 (m^2), $\boldsymbol{q_a}$=1.0 (m^2/s^3), and C_{q_b} = 4.0

The results clearly show that low values of $\boldsymbol{R}$ are better for KFNB. However, the GNSS measurements in KFNB need to be weighted strongly to compensate for the lack of baseline error states. Hence, as the value of $\boldsymbol{R}$ is increasing from Figure 5.19 to Figure 5.26, the KFNB velocity errors are drifting more rapidly. Unlike the LHPOST experiment in Chapter 4, the GNSS solutions in the NPL experiment are considered relatively stable, as the movable steel plate on the platform was kept static for most of time. When $\boldsymbol{R}$ becomes larger in the Kalman filter algorithms, the Kalman filter trusts and weights the strong motion seismometer observations more than the GNSS solutions. At the same time, the baseline errors of the strong motion seismometer in the Kalman filter system model have been doubly integrated as well and lead the rapid linear drifts and sawtooth-like effects in the velocity solutions. Thus, by estimating and correcting the baseline errors in KFB, the drifts and sawtooth-like effects are reduced effectively in the KFB solutions compared to the KFNB solutions. Notably, although the baseline error state estimates the acceleration bias, it also increases the noise level of KFB solutions. Similarly, the noise level of KFB can be decreased by increasing the value of $\boldsymbol{R}$ as shown in Figures 5.19~5.26. Moreover, the SKF results show that the noises of KFB are significantly reduced after applying an RTS smoother. The accelerometer outputs and Kalman filtered results related to tuning $\boldsymbol{R}$ are also plotted and shown in **Appendix A.2** for more information.

5.4.3 Fixed R and q_a with varied q_b

After tuning $\boldsymbol{q_a}$ and $\boldsymbol{R}$, the third parameter to tune is the value of $\boldsymbol{q_b}$ in the system noise matrix. As described with Eq. (5-8) in Section 5.4, the technique to tune $\boldsymbol{q_b}$ is to vary the standard deviation of the accelerometer baseline error by changing the coefficient C_{q_b}. The fixed $\boldsymbol{q_a}$ and $\boldsymbol{R}$ are set as 1.0 (m^2/s^3) and 128.0 (m^2) according to the results in Sections 5.4.1 and 5.4.2, respectively. C_{q_b} is varied in this tuning process and set as 4.0 initially. Table 5.4 shows the KFNB, KFB, and SKF velocity error statistics of tuning $\boldsymbol{q_b}$ with respect to the zero-velocity truth. Noted that $\boldsymbol{q_b}$ only exists in the system noise

matrix in the KFB and SKF with the corresponding baseline error state. Therefore, the velocity and displacement solutions from the KFNB are not changing from tuning $\boldsymbol{q_b}$ as there is no baseline error state and no $\boldsymbol{q_b}$ in the KFNB. Thus, the tuning of $\boldsymbol{q_b}$ in this section is focusing more on the stability of the baseline error state in the KFB.

Table 5.4: The performance of the KFB, KFNB, and SKF velocity solutions by fixing $\boldsymbol{q_a}$ = 1.0 (m^2/s^3) and $\boldsymbol{R}$ = 16.0 (m^2) and setting different $\boldsymbol{C_{qb}}$ with respect to the zero-velocity truth

	KFNB X Velocity Error (m/s)			KFB X Velocity Error (m/s)			SKF X Velocity Error (m/s)		
C_{qb}	Mean	STD	RMS	Mean	STD	RMS	Mean	STD	RMS
0.04	0.00616	0.00731	0.00956	1.50E-05	0.00196	0.00196	-1.29E-05	0.00034	0.00034
0.09	0.00616	0.00731	0.00956	1.58E-06	0.00170	0.00170	-1.33E-05	0.00034	0.00034
0.25	0.00616	0.00731	0.00956	-9.38E-06	0.00146	0.00146	-1.41E-05	0.00035	0.00035
1.0	0.00616	0.00731	0.00956	-1.85E-05	0.00126	0.00126	-1.56E-05	0.00037	0.00037
4.0	0.00616	0.00731	0.00956	-2.32E-05	0.00118	0.00118	-1.70E-05	0.00040	0.00040
9.0	0.00616	0.00731	0.00956	-2.38E-05	0.00120	0.00120	-1.73E-05	0.00043	0.00043
16.0	0.00616	0.00731	0.00956	-2.34E-05	0.00123	0.00123	-1.73E-05	0.00045	0.00045
25.0	0.00616	0.00731	0.00956	-2.27E-05	0.00127	0.00127	-1.72E-05	0.00047	0.00047

In Table 5.4, generally speaking, the performance of the KFB results is better compared to the KFNB results, and the SKF velocity results are the most stable compared to KFNB and KFB. Based on Table 5.4, the STD and RMS error of the KFB solutions have been improved 73.2~82.6% and 79.5~86.7%, respectively from the KFNB solutions. When setting C_{qb}= 4.0, the KFB can provide the smallest STD and RMS velocity errors in this case, whereas the smallest mean velocity error of KFB is when setting C_{qb}= 0.09. The velocity statistical results shown in Table 5.4 are only calculated when the sensors are static. As the $\boldsymbol{q_b}$ was designed for detecting the variation of the baseline error, ideally when the baseline error is not shifting greatly, the $\boldsymbol{q_b}$ can be set to a smaller value, for example, when the sensors are static. In contrast, for large changes of the baseline error, the larger the $\boldsymbol{q_b}$ is, the quicker the detection of the baseline error changes and the convergence of the displacement solutions can achieve. As in this experiment, there are some static periods and also some movements, the advantages and disadvantages of setting different $\boldsymbol{q_b}$ can be seen from Figures 5.27~5.34. Figure 5.27 to Figure 5.34 illustrate the KFB displacement solutions of the x-axis with varied $\boldsymbol{q_b}$ as well as the strong motion seismometer outputs with the baseline error state estimates of the x-component. The velocity error statistical results related to tuning $\boldsymbol{q_b}$ are also plotted as figures in **Appendix A.3** for more information.

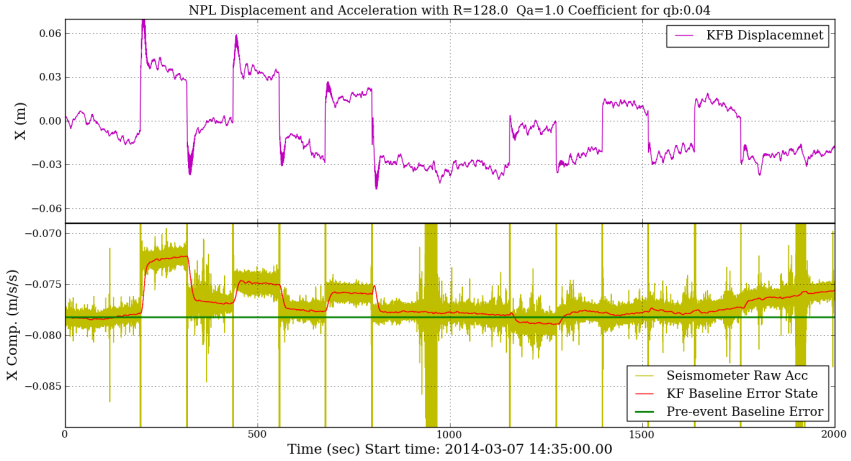

Figure 5.27: The KFB displacement solutions of the x-axis and the strong motion seismometer measurements with the baseline error state estimates along the x-component by setting $\boldsymbol{R}$ =128.0 (m^2), $\boldsymbol{q_a}$=1.0 (m^2/s^3), and C_{q_b} = 0.04

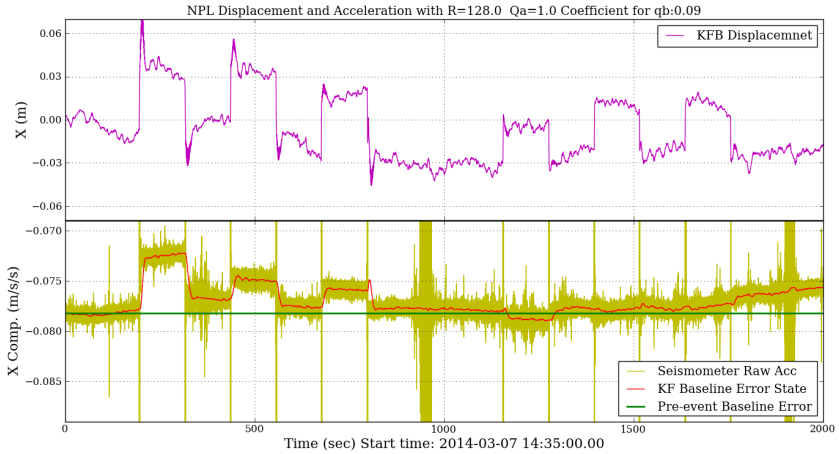

Figure 5.28: The KFB displacement solutions of the x-axis and the strong motion seismometer measurements with the baseline error state estimates along the x-component by setting $\boldsymbol{R}$ =128.0 (m^2), $\boldsymbol{q_a}$=1.0 (m^2/s^3), and C_{q_b} = 0.09

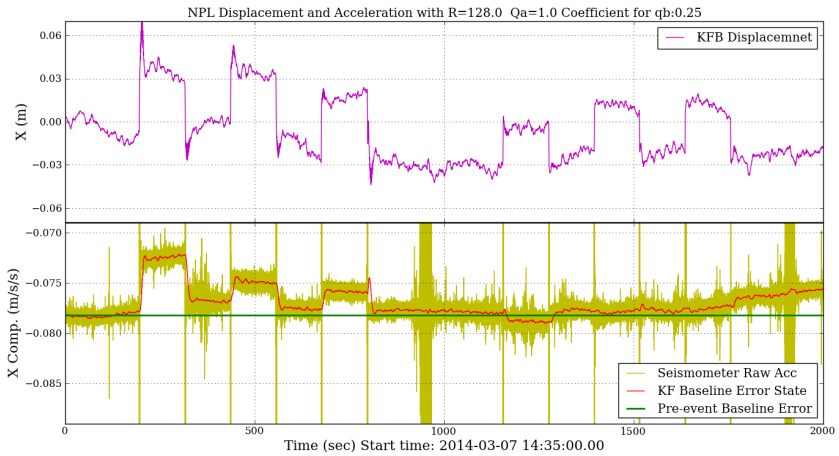

Figure 5.29: The KFB displacement solutions of the x-axis and the strong motion seismometer measurements with the baseline error state estimates along the x-component by setting $\boldsymbol{R}$ =128.0 (m^2), $\boldsymbol{q_a}$=1.0 (m^2/s^3), and C_{q_b} = 0.25

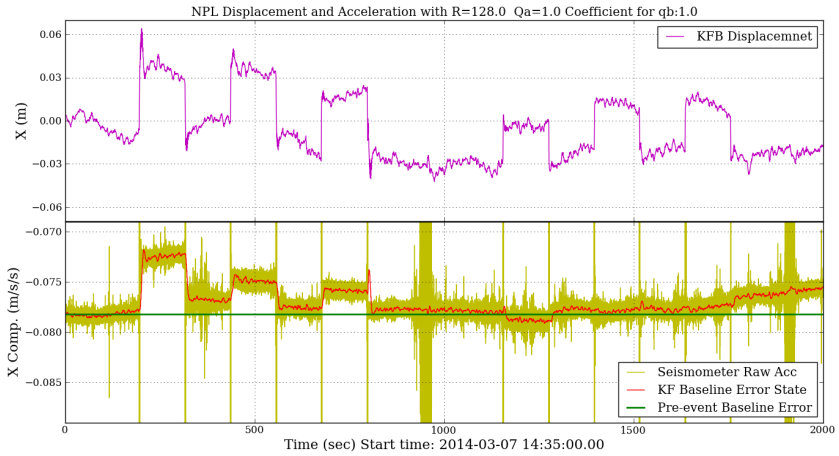

Figure 5.30: The KFB displacement solutions of the x-axis and the strong motion seismometer measurements with the baseline error state estimates along the x-component by setting $\boldsymbol{R}$ =128.0 (m^2), $\boldsymbol{q_a}$=1.0 (m^2/s^3), and C_{q_b} = 1.0

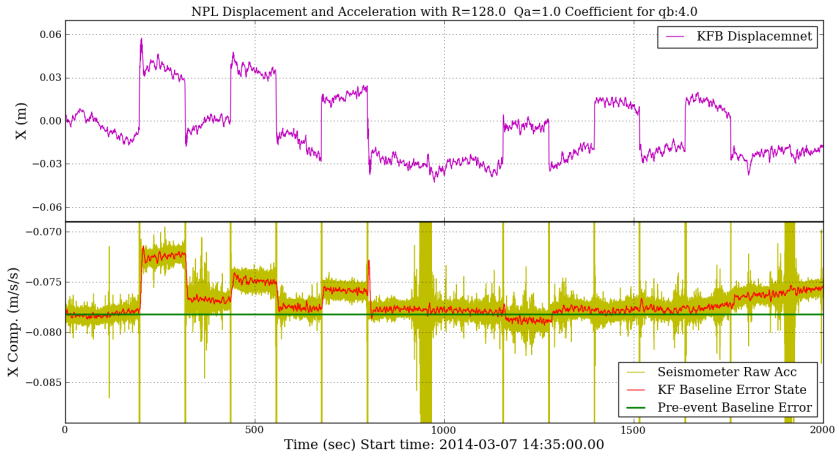

Figure 5.31: The KFB displacement solutions of the x-axis and the strong motion seismometer measurements with the baseline error state estimates along the x-component by setting $\boldsymbol{R}$ =128.0 (m^2), $\boldsymbol{q_a}$=1.0 (m^2/s^3), and C_{q_b} = 4.0

Figure 5.32: The KFB displacement solutions of the x-axis and the strong motion seismometer measurements with the baseline error state estimates along the x-component by setting $\boldsymbol{R}$ =128.0 (m^2), $\boldsymbol{q_a}$=1.0 (m^2/s^3), and C_{q_b} = 9.0

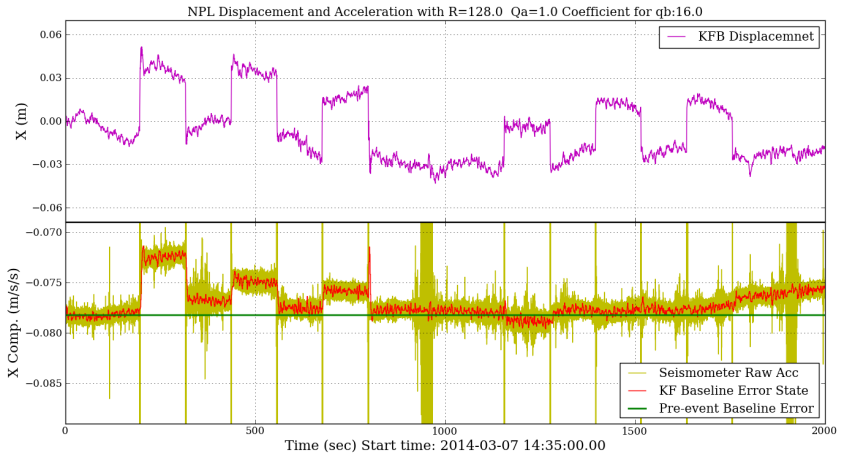

Figure 5.33: The KFB displacement solutions of the x-axis and the strong motion seismometer measurements with the baseline error state estimates along the x-component by setting $\boldsymbol{R}$ =128.0 (m^2), $\boldsymbol{q_a}$=1.0 (m^2/s^3), and C_{q_b} = 16.0

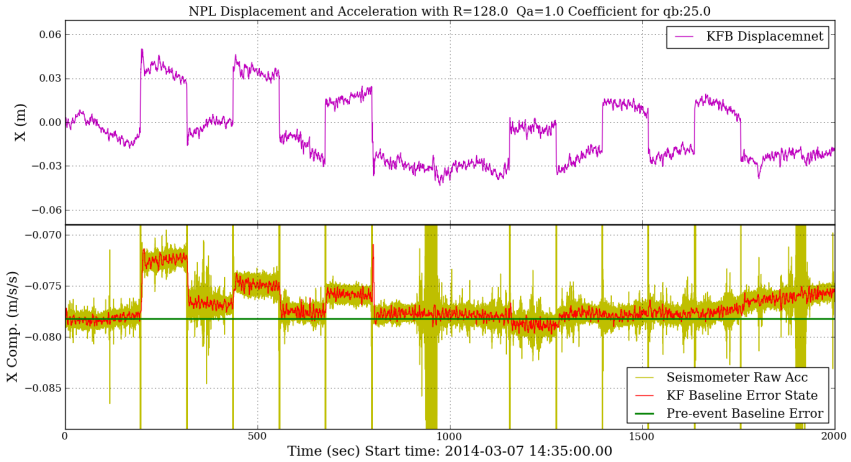

Figure 5.34: The KFB displacement solutions of the x-axis and the strong motion seismometer measurements with the baseline error state estimates along the x-component by setting $\boldsymbol{R}$ =128.0 (m^2), $\boldsymbol{q_a}$=1.0 (m^2/s^3), and C_{q_b} = 25.0

By increasing $\boldsymbol{q_b}$ in the KFB, the gradual changes of the tuned KFB displacement solutions and baseline error state estimates are shown from Figure 5.27 to Figure 5.34. In Figure 5.27, when the coefficient of $\boldsymbol{q_b}$ is set 0.04, the variation of the baseline error state estimate is smaller, especially during the static periods. However, Figure 5.27 also shows that when the movements are made, the displacement solutions drift more and take longer to converge. In contrast, when setting C_{q_b} = 25.0, as shown in Figure 5.34, the variation of the baseline error estimate becomes larger and noisier. Yet the convergence of the displacement solutions in Figure 5.34 takes less time to achieve after the shifts as the larger $\boldsymbol{q_b}$ can detect the rapid changes of the baseline error faster than the smaller $\boldsymbol{q_b}$. In addition, this also explains the increasing STD and RMS velocity errors and decreasing mean error in Table 5.4 when the value of C_{q_b} is smaller than 4.0.

Hence, a consensus value that is suitable for moving and static needs to be decided, and the optimal setting for $\boldsymbol{q_b}$ is C_{q^b} = 4.0 in this case.

5.4.4 Results after tuning

After the tuning process, a set of noise parameters in the Kalman filter has been decided for providing the optimised results, which are $\boldsymbol{R}$ =128.0 (m^2), $\boldsymbol{q_a}$=1.0 (m^2/s^3), and C_{q^b} = 4.0. The tuned displacement results of each method and their error analysis with respect to the AVG movements are shown in Table 5.5.

Table 5.5: The tuned displacements of GNSS, KFB, KFNB, and SKF from d1 to d12 (as marked in Figure 5.9) and their error statistics with respect to the AVG movements

(mm)	d1	d2	d3	d4	d5	d6	Displacement Error to AVG		
AVG	40.00	-40.00	40.00	-40.00	40.00	-40.00	**Mean**	**STD**	**RMS**
GNSS	40.32	-37.64	36.82	-49.52	31.14	-46.58	0.33	6.16	6.15
KFNB	104.46	-83.92	57.18	-79.50	49.60	-68.11	33.79	18.11	38.34
KFB	40.31	-38.21	37.08	-48.52	31.65	-46.33	0.35	5.67	5.68
SKF	40.14	-37.43	37.69	-48.49	32.47	-46.38	0.43	5.48	5.49
(mm)	**d7**	**d8**	**d9**	**d10**	**d11**	**d12**	**Displacement Error to AVG**		
AVG	30.00	-30.00	30.00	-30.00	30.00	-30.00	**Mean**	**STD**	**RMS**
GNSS	26.01	-20.72	36.52	-32.70	32.35	-35.51	0.63	5.59	5.55
KFNB	15.03	-10.55	36.20	-30.88	34.40	-17.01	-5.98	6.91	6.70
KFB	26.22	-20.83	36.63	-32.92	32.53	-35.57	0.78	5.58	5.53
SKF	26.18	-20.99	36.73	-33.03	32.60	-35.59	0.85	5.59	5.53

By comparing Table 5.1 and Table 5.5, the performance of the KFNB becomes worse after tuning as the noise parameters were decided based on the KFB results. The tuned KFB and SKF results in Table 5.5 perform similarly compared to the un-tuned results Table 5.1 and are still dominated by the GNSS errors. Thus, based on the results, for small displacements (e.g. < 50 mm) and no earthquake-like shaking, the KFB integrated results might not improve the performance of the displacement solutions compared to the GNSS results. However, the KFB can perform more stably before and after tuning compared to the existing Kalman filter method, KFNB.

5.5 Summary

An experiment which took place at the National Physical Laboratory (NPL) was designed to test the performance of the proposed Kalman filter algorithm. The work also sought to compare the KFB results with the KFNB results to test if the additional baseline error state increases the measurement accuracy as well as precision of small displacements of known magnitude and direction.

A strong motion seismometer and a Leica GNSS antenna were co-located and firmly mounted on a moveable platform. Observations of both sensors were logged for 5 hours in total and for 90 minutes when the platform was subjected to a series of small displacements of known magnitude and direction. The GNSS observations were processed using the method of PPP applied to each processing run. The GNSS PPP position solutions were turned into displacement in the body frame of the movable table. The GNSS displacement solutions and the strong motion seismometer observations were then input to the Kalman filter integrations to obtain the optimal displacement solutions at a high sampling rate.

The results show that all methods were unable to provide accurate solutions when the movements of the platform were less than 30 mm. Due to the design of the experiment, there were some unknown baseline errors or sensor biases within the accelerometer observations. The results showed that the baseline error state estimates in the KFB follow the trends of the strong motion seismometer observation and correct the baseline error in the Kalman filter calculations. When focusing on the 30 mm and 40 mm displacement results, the KFB can effectively reduce the quadratic drifts of the displacement compared to the KFNB, especially the sawtooth-like effects.

Three noise covariance parameters, $\boldsymbol{R}$, $\boldsymbol{q_a}$, and $\boldsymbol{q_b}$, in the Kalman filters were subjected to change to find out the most suitable value for each parameter in order to provide the potential optimal displacement solutions. In the tuning process, two of the parameters were fixed at one time, while the third was varied. The RTS smoothed results known as SKF results were also calculated and used to compare with both Kalman filter algorithms, KFB and KFNB. Statistics and figures of KFNB, KFB, and SKF velocity results with respect to zero-velocity truth when tuning different parameters were also performed.

The first tuning process began with, $\boldsymbol{q_a}$, in the system noise covariance matrix, which was tuned in the KFB, KFNB, and SKF algorithms. With setting a wide range of the values of $\boldsymbol{q_a}$, the impacts of tuning $\boldsymbol{q_a}$ in the Kalman filter were shown. The tuning results indicated that the KFNB displacement solutions were significantly affected by the value of $\boldsymbol{q_a}$, and the KFB solutions showed the stability and advantage of using a baseline error state in the Kalman filter integration. The optimal value of $\boldsymbol{q_a}$ is 1.0 (m^2/s^3) for this experiment.

The second tuning parameter was the measurement noise covariance, $\boldsymbol{R}$, in KFB, KFNB and SKF algorithms. By displaying the velocity error results with respect to zero-velocity truth, the advantages of applying a baseline error state in the KFB and SKF were shown in both statistical results and figures. Unlike the results shown in Chapter 4, the performance of the Kalman filters, especially KFNB, grew worse as $\boldsymbol{R}$ increased, and the results clearly show that low values of $\boldsymbol{R}$ are better for KFNB. However, the lack of baseline error states means the Kalman gain in the KFNB algorithm would weight the GNSS measurements heavily. Whereas the drifts and sawtooth-like effects are reduced effectively in the KFB solutions compared to the KFNB solutions. The results of tuning $\boldsymbol{R}$ also show that although the baseline error state estimates the acceleration bias, the additional state estimate might introduce some noise and increase the noise level of KFB solutions. Based on the statistical results and figures, the optimal $\boldsymbol{R}$ in this case is 128 (m^2).

The third parameter $\boldsymbol{q_b}$ in the system noise covariance matrix only exists in the KFB and SKF algorithms, as $\boldsymbol{q_b}$ is related to the baseline error state. $\boldsymbol{q_b}$ controls the stability of the baseline error state in the KFB and SKF. The velocity error statistical results helped to find out the optimal value of C_{q_b} during static periods. However, since the experiment actually involved several movements and static periods, a balanced value of $C_{q_b} = 4.0$ was selected to provide the optimal solutions in the entire experiment. Through plotting the baseline error state estimates together with the accelerometer observations and displacement solutions, the relationship between $\boldsymbol{q_b}$ and the baseline error estimates was shown.

Overall, although the KFB solutions are dominated by GNSS solutions, the KFB with the additional baseline error state can effectively reduce the sawtooth-like effects or other drifts in the velocity and displacement solutions and provide more reliable and accurate solutions compared to the KFNB. This KFB technique is expected to provide reliable displacement solutions even when the baseline error of the strong motion seismometer/accelerometer is changed or shifted during/after earthquake shaking. This assumption is tested in the next chapter, in which a real earthquake data set with a permanent displacement is tested with the proposed KFB.

Chapter 6 Sensor Integration Using Real Earthquake Data

In Chapter 4, the results generated by a loosely-coupled Kalman filter with a baseline error state were compared with the UCSD LHOST data to show both the improvement of using the proposed Kalman filter algorithm and the importance of the Kalman filter tuning process. The movable steel plate on the platform utilised in the NPL experiment described in Chapter 5 provided the opportunity to validate the proposed Kalman filter algorithm in the context of a permanent displacement after shaking. However, these experiments still differ from real earthquakes. Thus, in this chapter a large earthquake with significant permanent displacements after shaking has been selected as a test case for the application of the algorithm. The proposed Kalman filter algorithm is applied to observations of a real earthquake, the 2010 M_w 7.2 El Mayor-Cucapah Earthquake, Mexico.

6.1 Introduction and Data Sources

The M_w 7.2 El Mayor-Cucapah Earthquake occurred in northern Baja California, Mexico on April 4th, 2010; it was the largest earthquake in the area since 1892 (United States Geological Survey 2010). Figure 6.1 shows a terrain map that contextualizes the large earthquake and its aftershocks. The earthquakes occurred close to the border between the west coast of the United States and Mexico. A pair of collocated strong motion seismometer data and GPS observations was required from the existing seismic network and geodetic network, respectively, in order to validate the proposed Kalman filter integration during this large earthquake. The paired data sets for the El Mayor Cucapah Earthquake were taken from the advanced seismic networks and GPS networks that have been built in the west coast of the United States.

The California Real-Time Network (CRTN) GPS sites and earthquake displacements in Figure 6.1 show that during the earthquake, a certain area close to the active faults was moved by the main shock significantly. As the main earthquake shaking in the area was severe, the seismic measurements from many seismic stations clipped and were unable to provide earthquake information correctly, for example, the WES broadband seismic station results shown in Figure 6.2. The disadvantages of using seismic networks alone is highlighted in Figure 6.2, taken from the work of Brendan Crowell and Yehuda Bock at UCSD and Sharon Kedar at Jet Propulsion Laboratory (JPL). In Figure 6.2, the velocity measurements of the broadband seismic station WES clipped above the instrument range, whereas the 1 Hz GPS station P494 does not have this limitation so can provide dynamic deformation and permanent displacements of the large earthquake. Thus, to test if the integrated solutions can perform better than seismic stations or GPS stations alone, a pair of collocated stations in the vicinity with largest displacements were used in this experiment: GPS station P496 and strong motion seismometer station

5058. According to the distance function in Google Earth, the distance between both instruments was calculated as 138.56 metres from their longitudes and latitudes, as shown in Figure 6.3. The GPS station P496 collects 1 Hz GPS observations and is from the CRTN and Plate Boundary Observatory (PBO). The strong motion station 5058 provides 200 Hz strong motion seismometer data; it is 74.4 km away from the epicentre and a part of the Southern California Seismic Network (SCSN) operated by the United States Geological Survey (USGS) and the California Institute of Technology (Caltech).

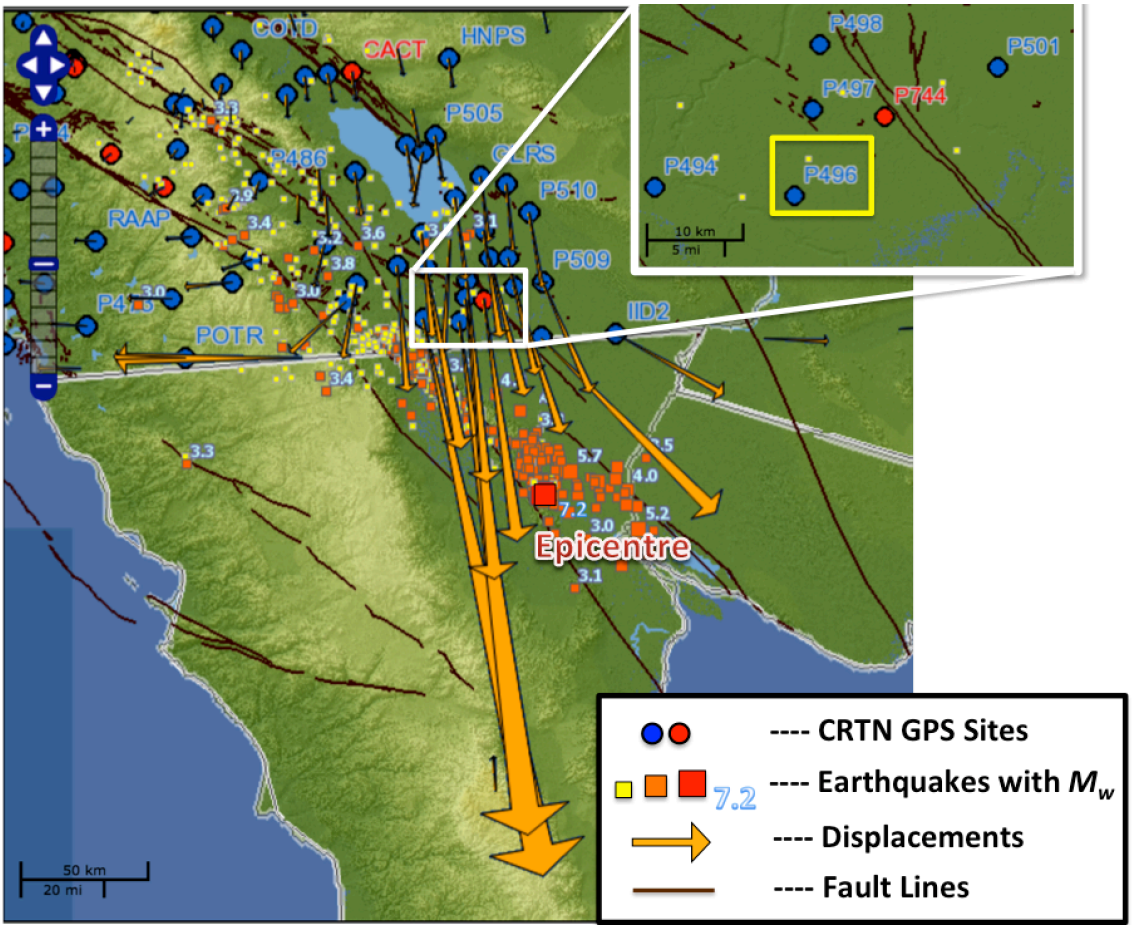

Figure 6.1: The El Mayor Cucapah Earthquake information on the terrain map, including fault lines, CRTN sites (blue and red circles), related earthquakes (yellow and orange squares) with moment magnitudes, and the measured displacements (orange arrows) during the main earthquake (figure adapted from http://geoapp03.ucsd.edu/gridsphere/gridsphere?cid=El+Mayor+Cucapah).

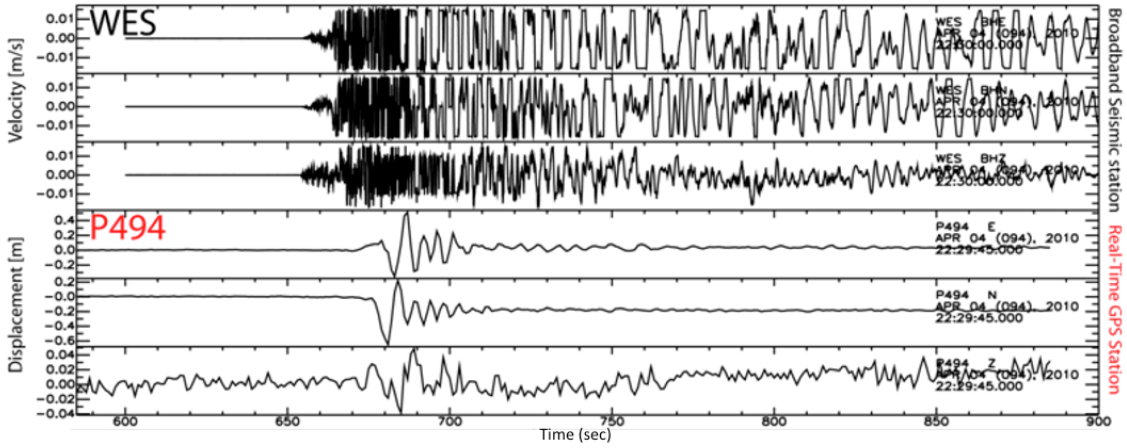

Figure 6.2: A comparison between the velocity measurements from the broadband seismic station WES and displacement solutions from the GPS station P494 in the largest displacement area during the El Mayor Cucapah Earthquake. (figure adapted from http://geoapp03.ucsd.edu/gridsphere/gridsphere?cid=El+Mayor+Cucapah)

Figure 6.3: The map and photographs of the collocated GPS and strong motion seismometer pair, the GPS station P496 and the strong motion seismometer station 5058 (photograph and figure adapted from Google Earth 2014)

Similar to the GNSS observations in the NPL experiment in Chapter 5, the 1 Hz GPS observations in this experiment were also processed by Christopher Atkins using the developed PPP software. Following the same procedure as introduced in Section 5.1.3, the PPP software provided 1 Hz GNSS position solutions of the GNSS receiver. The

position solutions were then converted into three-dimensional displacement solutions along the Easting, Northing, and vertical directions for later input to Kalman filter integrations. The GPS displacements were calculated from the average station position given by the CRTN and PBO from the long-term observations at the station.

The strong motion seismometer data in this experiment, including the raw data and the processed data, were downloaded from the Center for Engineering Strong Motion Data (CESMD) built by the USGS and the California Geological Survey (CGS). The term 'raw data' consists of the original accelerometer measurements, provided without application of any noise filters or baseline corrections to the data. The term 'processed data' refers the baseline corrected acceleration, velocity, and displacement of the strong motion seismometer, which have been noise filtered and baseline corrected from the raw data. Since the corrected data sets were given directly, the actual accelerometer data processing was not certain. As introduced in Section 2.4, it is most likely the accelerometer data was processed via the Basic Strong-Motion Accelerogram Processing Software (BAP) provided by USGS. In this experiment, the raw USGS data are used as inputs for the Kalman filter algorithms, and the processed USGS data are used to compare with the Kalman filter integrated estimates.

6.2 Time Synchronisation Between Instruments

In this study, one of the objectives is to solve the problem of time synchronisation between GPS and accelerometer-based instruments, as the time lags between sensors cause time synchronisation errors. The time synchronisation errors between sensors can potentially lead to false propagations and state estimates in Kalman filter algorithms. Based on Groves (2013), to effectively compensate the lags between observations, time-tagging the data is more ideal than using the nearest observations. Fortunately, most instruments in current geodetic and seismic networks are GPS time-tagged to allow a standard time reference. GPS time-tagging offset errors are usually within 10 nanoseconds for most modern electrical products using Coarse/Acquisition (C/A) code, which means a 3-metre error (Sadeghi & Gholami 2008). Assuming there are multipath errors of around 100 metres within the GPS observation, the GPS time offset error is about 0.3 microseconds, which is still much smaller than the normal sampling rates of GPS receiver (1 second) and accelerometers (0.01 second). In the previous experiments, the UCSD large outdoor shake table experiment in Chapter 4 and the NPL rooftop experiment in Chapter 5, the instruments were all GPS time-tagged and mounted on the same platform, which means the instruments experience the same movements. However, although most sensors are GPS time-tagged, in real earthquakes, the distances between instruments in the existing networks are critical as the earthquake waves might travel through stations at different times. Depending on the composition, temperature, and pressure of the Earth's crust, seismic waves travel with velocities between 200 and

800 m/s (Shearer 2009). Thus, within 0.01 second, seismic waves could travel between 20 and 80 m, which means the ideal distance between collocated instruments should be less than 20 m to minimise time lags between sensors. However, for GPS and accelerometer-based instruments in the existing geodetic and seismic networks, the short distance might not always be applicable, for example, the distance between the P496 GPS receiver and the strong motion station 5058 in this experiment is 138.56 m. Thus, to account the potential influences of the time synchronisation errors in the Kalman filter algorithms, one approach is to increase the measurement noise covariance, $\boldsymbol{R}$, in the Kalman filter algorithm (Groves 2013). Meanwhile, the baseline error state estimates in the implemented Kalman filter might also account for the time-lag effects and compensate for the time-synchronisation errors in the propagation or state estimates. As one of the Kalman filter tuning processes is the changing of the measurement noise covariance in the algorithm, Section 6.4 will explore the results of this process.

6.3 Kalman Filter Settings and Results

Similar to the NPL experiment in Chapter 5, the Kalman filter algorithm used in the real earthquake is also three-dimensional. The settings of the three-dimensional Kalman filter algorithm in this experiment are described in Section 5.2. The initial settings of the noise parameters in the Kalman filters are based on the tuning results in Chapter 5. Similarly, the noise parameters include the measurement noise covariance, $\boldsymbol{R}$, and the PSD, $\boldsymbol{q_a}$ and $\boldsymbol{q_b}$, in the system noise covariance, $\boldsymbol{Q}$. The initial C_{q_b} for the coefficient of $\boldsymbol{q_b}$ in this experiment was set as 4.0. The initial $\boldsymbol{q_a}$ = 1.0 (m^2/s^3) and $\boldsymbol{R}$ = 128.0 (m^2) were also set according to Eq. (5-4) and Eq. (5-7).

As described in Section 6.1, the observations of the GPS station P496 and strong motion station 5058 during the El Mayor-Cucapah Earthquake have been used in this experiment. The 1 Hz GPS PPP displacement solutions and the 200 Hz strong motion seismometer raw data are used as inputs in all Kalman filter algorithms, including the Kalman filter with baseline error state (KFB), the Kalman filter with no baseline error state (KFNB), and the smoothed Kalman filter (SKF). All three Kalman filter integrations output 200 Hz displacement solutions in this case. In addition, the 1 Hz GPS PPP displacement solutions and the 200 Hz USGS noise-filtered and baseline-corrected displacement solutions are also presented for comparison. Figures 6.4 to 6.6 show the Easting, Northing, and vertical displacement solutions of the collocated GPS station P496 and strong motion seismometer 5058 using different methods during the El Mayor-Cucapah Earthquake.

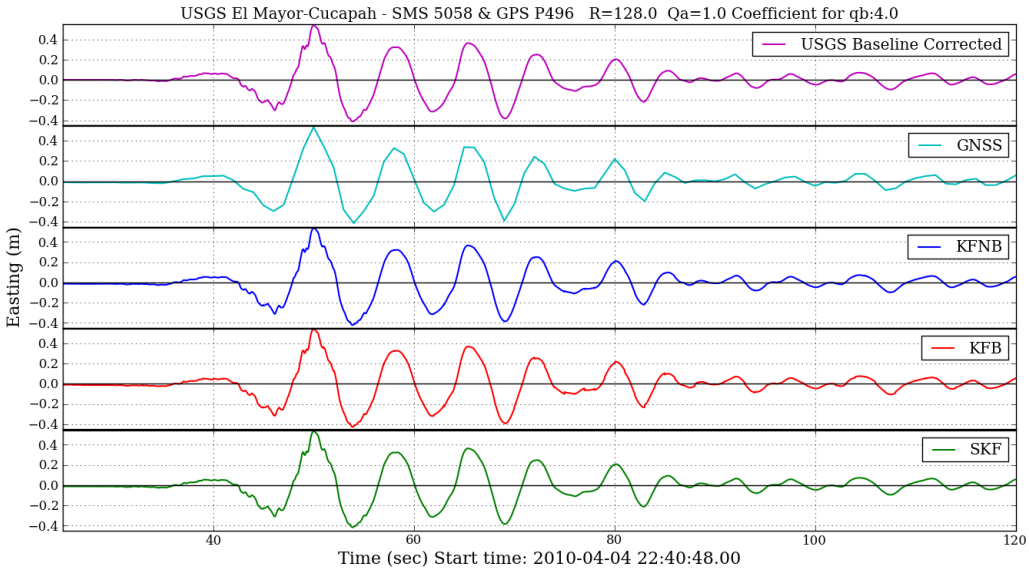

Figure 6.4: The Easting displacement results of the collocated GPS station P496 and strong motion seismometer 5058 during the El Mayor-Cucapah Earthquake

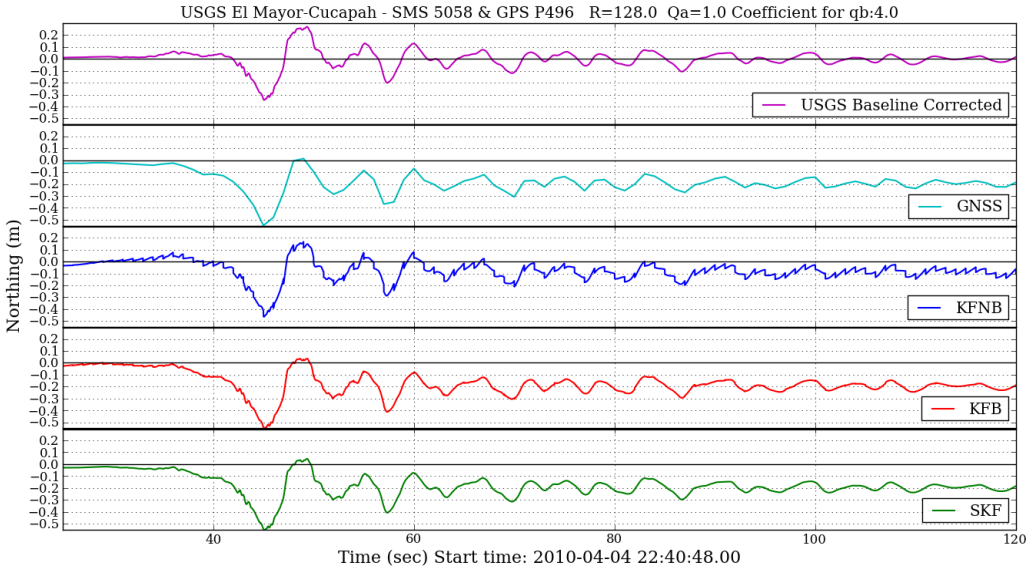

Figure 6.5: The Northing displacements of the collocated GPS station P496 and strong motion seismometer 5058 during the El Mayor-Cucapah Earthquake

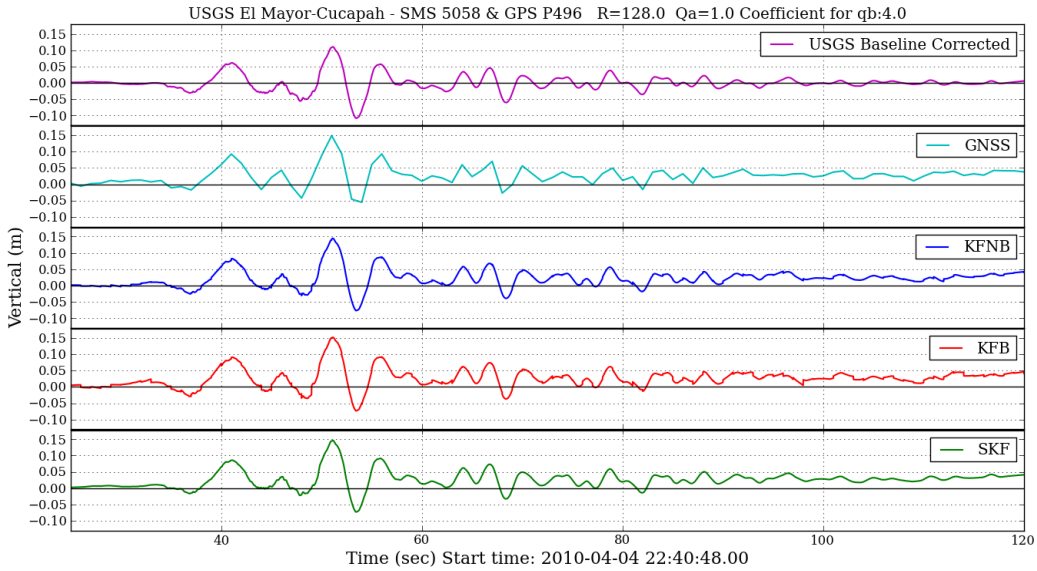

Figure 6.6: The vertical displacement results of the collocated GPS station P496 and strong motion seismometer 5058 during the El Mayor-Cucapah Earthquake

The displacement solutions in Figures 6.4 to 6.6 show that during the El Mayor-Cucapah Earthquake, the pair of GPS receiver P496 and strong motion seismometer 5058 has peak-to-trough amplitudes in the time series of ~90 cm, ~50 cm, and ~20 cm in the Easting, Northing, and vertical components, respectively. By plotting the displacement solutions together, the advantages of using the KFB are clearly shown. In Figure 6.5 and Figure 6.6 specifically, apart from the USGS baseline corrected and KFNB results, a ~20 cm and a ~5cm permanent (co-seismic) displacement in the Northing and vertical components have been measured by GPS alone, KFB, and SKF after the great earthquake.

The 200 Hz USGS acceleration baseline corrected results in Figure 6.5 can only show the high-frequency waveform but not the ~20 cm co-seismic displacement in the Northing after shaking. The seismological baseline correction on the accelerometer data has not only removed the pre-event accelerometer baseline error and filtered noise but also removed the co-seismic displacements. The 1 Hz GPS solutions in Figure 6.5 can show the ~20 cm co-seismic displacement in the Northing but not the high-frequency movements during shaking. Figure 6.4 and Figure 6.6 show that the KFNB can provide estimates smoothly when there are small permanent shifts in the Easting and the vertical components. However, in Figure 6.5, after the first main shock occurred, the KFNB displacement results started to drift and had sawtooth-like effects in the Northing. In contrast, the Northing displacement results in Figure 6.5 show that KFB and SKF can reduce the drifts and the sawtooth-like effects and provide high-frequency movements as well as the co-seismic displacements during the great earthquake. The advantages and disadvantages of each method under different circumstances are also summarized in Table 6.1.

Table 6.1: The pros and cons of using different methods under different circumstances during earthquakes

		USGS Baseline Corrected	GNSS	KFNB	KFB	SKF
Large co-seismic displacement	**Displacement**	✖	✔	✖	✔	✔
	Shaking	✔	✖	✖	✔	✔
Small co-seismic displacement	**Displacement**	✖	✔	✔	✔	✔
	Shaking	✔	✖	✔	✔	✔
No co-seismic displacement	**Displacement**	✔	✔	✔	✔	✔
	Shaking	✔	✖	✔	✔	✔

The sawtooth-like effects are particularly significant in the KFNB displacement solutions in the Northing in Figure 6.5, which suggests that the earthquake shaking might not only cause the ~20 cm co-seismic displacement in the Northing but also change the accelerometer baseline error within the strong motion seismometer. Hence, in order to investigate this assumption, the raw strong motion seismometer data, the pre-event accelerometer baseline error, the baseline error state estimates in the KFB and the displacements from all methods in the East, North, and vertical directions are presented in Figure 6.7, Figure 6.8 and Figure 6.9, respectively.

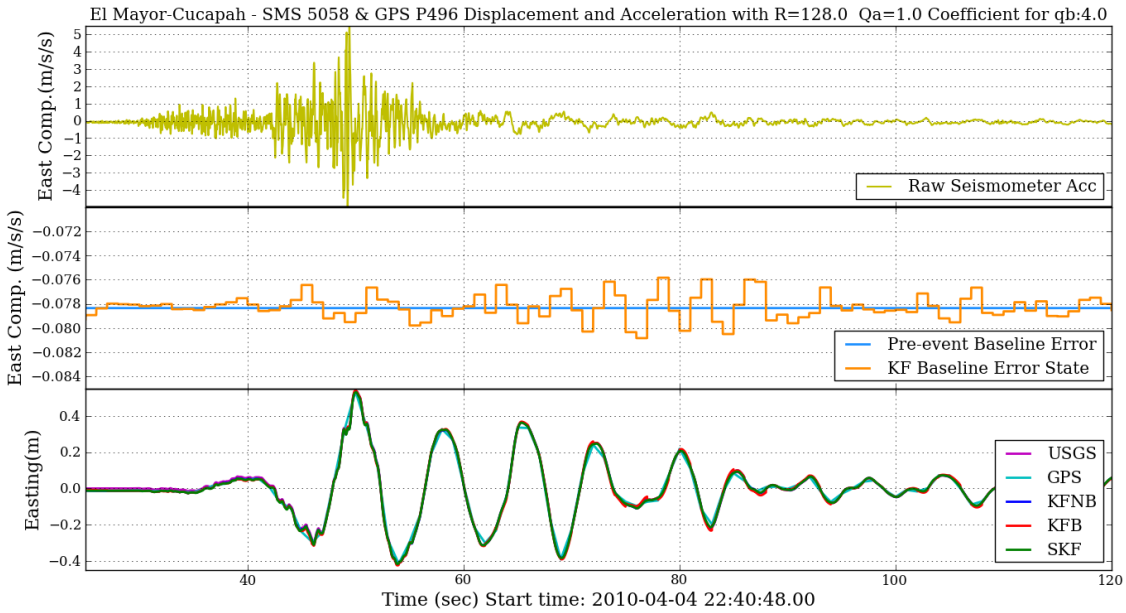

Figure 6.7: The strong motion seismometer 5058 raw accelerometer data from USGS, pre-event baseline error, and the KFB baseline error state for the Easting component. KFNB and KFB Easting displacement results of the collocated GPS station P496 and strong motion seismometer 5058 during the El Mayor-Cucapah Earthquake.

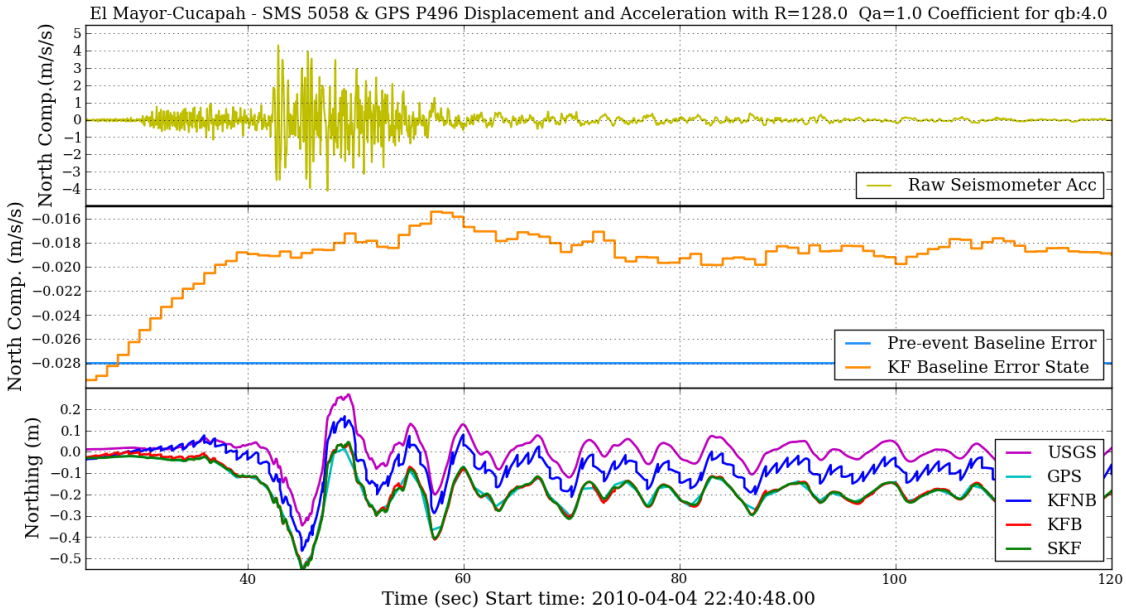

Figure 6.8: The strong motion seismometer 5058 raw accelerometer data from USGS, pre-event baseline error, and the KFB baseline error state for the Northing component. KFNB and KFB Northing displacement results of the collocated GPS station P496 and strong motion seismometer 5058 during the El Mayor-Cucapah Earthquake.

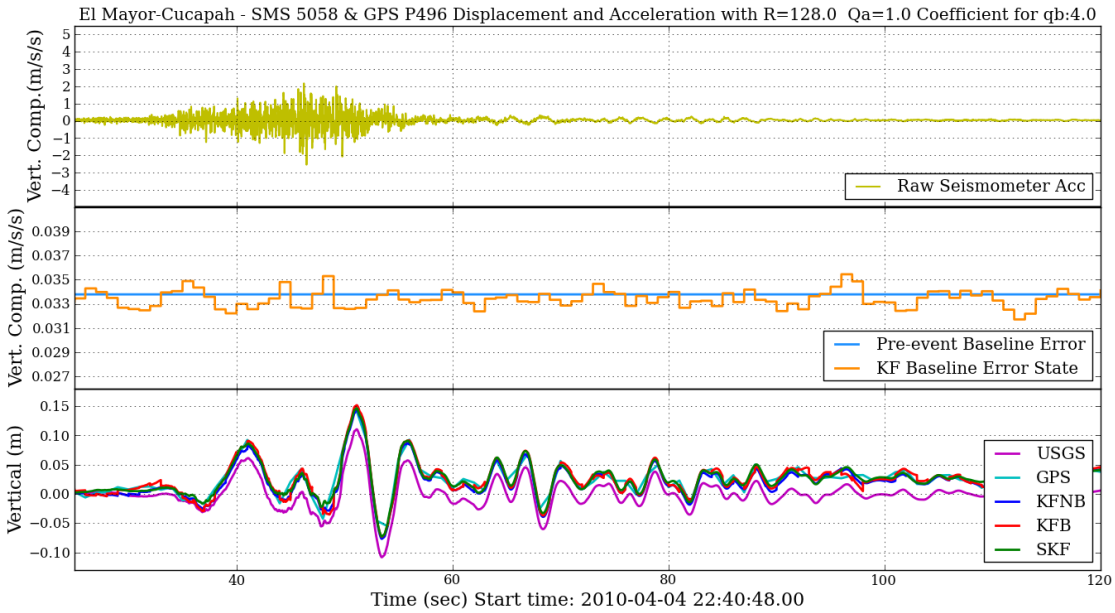

Figure 6.9: The strong motion seismometer 5058 raw accelerometer data from USGS, pre-event baseline error, and the KFB baseline error state for the vertical component. KFNB and KFB vertical displacement results of the collocated GPS station P496 and strong motion seismometer 5058 during the El Mayor-Cucapah Earthquake.

The raw accelerometer data in Figures 6.7 to 6.9 show the seismic waveforms during the earthquake. The pre-event baseline errors were the mean values of the 2000 epochs of static accelerometer observations before the earthquake. In Figure 6.7 and Figure 6.9, the KFB baseline error states generally follow the pre-event baseline error and vary within small ranges. Whereas in Figure 6.8, the maximum rate of baseline error state change is at the beginning of the shock and stabilised to new baseline error values during the earthquake. The KFB and KFNB displacement solutions in Figure 6.8 clearly show the advantages of having a baseline error state in the Kalman filter integration in this case. Without the baseline error state estimates, the KFNB solutions start to drift rapidly and show sawtooth-like effects from about 20 seconds in Figure 6.8. In addition, due to the drifts and sawtooth-like effects, the KFNB also fails to estimate the ~20 cm co-seismic displacement in the Northing.

By plotting the displacement results of all methods in Figure 6.7 to 6.9, the advantages and disadvantages of each method are clearer. All methods generally provide similar performance while there is no co-seismic displacement during the earthquake (e.g. the Easting). Small co-seismic displacements (~5cm) in the vertical component are measured by GPS alone and by all Kalman filter integrations. The USGS baseline-corrected solutions always show zero co-seismic displacements due to the removal of the mean measurement and application of noise filters. Despite the fact that the USGS baseline corrected solutions being unable to show the co-seismic displacements, the displacement waveforms are still useful for analysis of the high-frequency movements during the earthquake. The GPS solutions at 1 Hz, a low-sampling rate miss some

information during high-frequency movements - for example, the peaks at ~45 seconds in Figure 6.4 and at ~50 seconds in Figure 6.5. Although the KFB baseline error estimates correct the drifts in the Northing, there are some sawtooth-like effects within the Easting and vertical KFB displacement solutions. The small sawtooth-like effects in the KFB displacement solutions indicate that the $\boldsymbol{q_b}$ in the system noise covariance, $\boldsymbol{Q}$, should be set with smaller values as the baseline errors are relatively stable when there are no co-seismic displacements. By applying the RTS smoother after the KFB, the sawtooth-like effects in the KFB displacement solutions are eliminated. The smoothed displacement solutions are thought to be the most accurate solutions with the high-frequency movements during the earthquake and also the co-seismic displacements after the earthquake. Thus, as there is no displacement truth model available in a real earthquake, in this experiment, the RTS smoothed results are used to compare with KFNB and KFB solutions. The results of changing the noise parameters in the Kalman filter algorithms, known as the Kalman filter tuning process, are presented in the following section.

6.4 Kalman Filter Tuning

Similar to the previous experiments in Chapter 4 and Chapter 5, the Kalman filter tuning process also takes place for this experiment. One of the issues of using real earthquake data sets is that there is no truth model as in the specially designed experiments. Based on the results from the UCSD LHPOST and NPL rooftop experiments, the RTS smoothed solutions can potentially provide the most accurate solutions compared to the other investigated methods. The USGS baseline corrected solutions, GPS solutions, and Kalman filter integrated solutions presented in Section 6.3 have shown the advantages of using Kalman filter integrations in a real earthquake. As the KFNB method has been applied widely for integrated instruments in the seismological field (Hammond et al. 2010; Geng, Bock, et al. 2013; Bock et al. 2011; Tu et al. 2013; Smyth & Wu 2006), the tuning process in this section is comparing the KFNB and KFB solutions with the SKF solutions to show the advantages of using a baseline error state in the Kalman filter algorithm during a real earthquake.

As described in Section 5.4, the Kalman filter tuning process in a real earthquake event involves three parameters in the algorithms: the measurement noise covariance matrix, $\boldsymbol{R}$, and the $\boldsymbol{q_a}$ and $\boldsymbol{q_b}$ parameters in the system noise covariance matrix, $\boldsymbol{Q}$. The technique used to tune the Kalman filter is to fix two of the parameters and vary the third parameter. The $\boldsymbol{q_b}$ in KFB and SKF are the PSDs of the accelerometer baseline error variation obtained from the standard deviation of the baseline error from the mean values of the 2000 epochs of static strong motion seismometer 5058 observations. The initial settings are: C_{q_b} for the coefficient of $\boldsymbol{q_b}$ = 4.0, $\boldsymbol{q_a}$ = 1.0 (m^2/s^3), and $\boldsymbol{R}$ = 128.0 (m^2). Based on the displacement results presented in Section 6.3, the large earthquake

caused a near-zero displacement in the Easting, a 20 cm co-seismic displacement in the Northing, and a small 5 cm co-seismic displacement in the vertical component. Hence, the behaviours of both the KFNB and KFB methods under different co-seismic displacement circumstances will also be discussed in the tuning process.

6.4.1 Fixed R and q_b with varied q_a

Firstly, the PSD of the accelerometer noise, $\boldsymbol{q_a}$, in the system noise covariance matrix in the Kalman filter is tuned. The tuning process of $\boldsymbol{q_a}$ starts with initial value 1.0 (m^2/s^3) and increases/decreases the value of $\boldsymbol{q_a}$. The same noise parameters are set in KFB and KFNB for comparison, and the RTS smoother is implemented on the KFB solutions. The statistical results of the KFNB and KFB displacement errors in Easting, Northing, and Vertical directions with respect to the SKF solutions are presented in Table 6.2 to show the differences when using an additional baseline error state in KFB.

Table 6.2: The performance of the KFNB and KFB displacement by fixing $\boldsymbol{R}$ =128 (m^2) and C_{q_b} = 4.0 and setting different $\boldsymbol{q_a}$ with respect to the SKF results

	KFNB Easting Dis. Error (m)			KFNB Northing Dis. Error (m)			KFNB Vertical Dis. Error (m)		
q_a (m^2/s^3)	Mean	STD	RMS	Mean	STD	RMS	Mean	STD	RMS
1E-02	0.00287	0.00991	0.01032	0.89094	0.29226	0.93766	-0.03770	0.00848	0.03865
1E-01	0.00085	0.00749	0.00754	0.28782	0.08854	0.30113	-0.01218	0.00445	0.01297
1.0	0.00021	0.00713	0.00714	0.09283	0.02922	0.09732	-0.00390	0.00401	0.00560
10.0	2.2E-05	0.00735	0.00735	0.03045	0.01204	0.03275	-0.00124	0.00463	0.00480
100.0	-1.4E-05	0.00796	0.00796	0.01067	0.00770	0.01316	-0.00043	0.00566	0.00568
1000.0	-2.2E-05	0.00870	0.00870	0.00452	0.00754	0.00880	-0.00020	0.00748	0.00748

	KFB Easting Dis. Error (m)			KFB Northing Dis. Error (m)			KFB Vertical Dis. Error (m)		
q_a (m^2/s^3)	Mean	STD	RMS	Mean	STD	RMS	Mean	STD	RMS
1E-02	-8.2E-05	0.00773	0.00773	0.00030	0.00674	0.00674	3.0E-05	0.00594	0.00594
1E-01	-8.1E-05	0.00773	0.00773	0.00030	0.00672	0.00673	2.9E-05	0.00594	0.00594
1.0	-7.1E-05	0.00773	0.00773	0.00034	0.00662	0.00663	2.3E-05	0.00590	0.00590
10.0	-3.1E-05	0.00778	0.00778	0.00028	0.00614	0.00615	9.4E-06	0.00576	0.00576
100.0	-2.2E-05	0.00817	0.00817	0.00047	0.00643	0.00645	-1.3E-05	0.00605	0.00605
1000.0	-2.8E-05	0.00879	0.00879	0.00085	0.00727	0.00732	-4.2E-05	0.00760	0.00760

In Table 6.2, the performances of KFNB and KFB displacement solutions in the Easting and Vertical components are similar when there are no co-seismic displacements at the directions. With proper tuning values, some KFNB results in the Easting and Vertical components are even better than the KFB results, for example, $\boldsymbol{q_a}$ = 1 (m^2/s^3) and $\boldsymbol{q_a}$ = 10 (m^2/s^3) in the Easting. Yet, when there are co-seismic displacements in the Northing

component, the KFB is able to provide more stable and accurate solutions compared to KFNB. Figure 6.10 illustrates the Mean, STD, and RMS results in Table 6.2; as the scale of the q_a value is large, the x-axis is a logarithmic-scale.

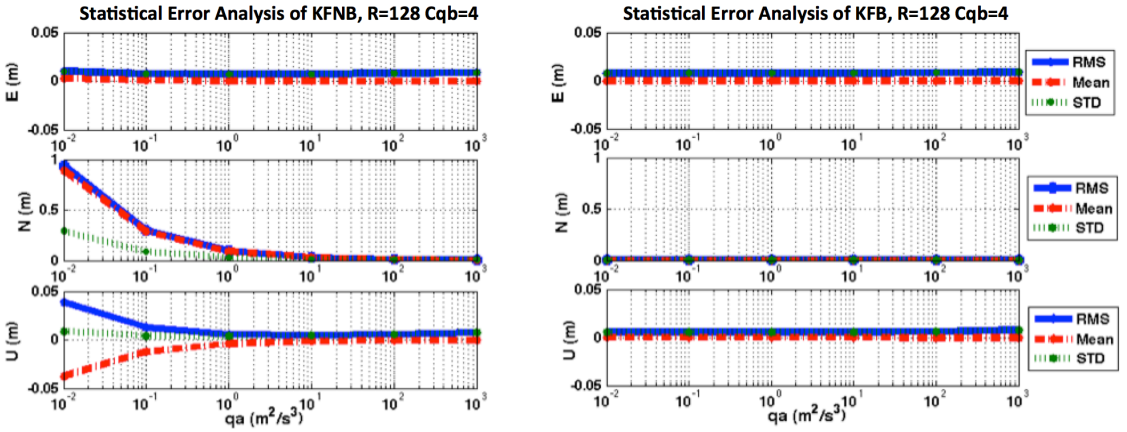

Figure 6.10: The statistical error analysis of the KFNB and KFB integrated displacement solutions by fixing $\boldsymbol{R}$ =128 (m^2) and C_{qb} =4 and varying q_a with respect to the SKF displacement solutions.

The plots in Figure 6.10 illustrate the stabilities of both KFNB and KFB methods when tuning q_a in the Kalman filters. Apart from the Northing component, the scales of the Easting and vertical components are set the same for comparison. In Figure 6.10, the KFB displacement error RMS and STD are nearly equal for all components as the mean error is near zero, which shows the stability of the KFB method when tuning q_a. On the other hand, the widely used method, KFNB, can only achieve similar stability when there is a near-zero co-seismic displacement (e.g. the Easting) but not when co-seismic displacements occurred (e.g. the Northing and Up). Figure 6.10 shows that when changing q_a, the displacement errors of KFB are consistent whether there are co-seismic displacements during the earthquake or not; whereas the displacement errors of KFNB are not only depending by the value of q_a but also significantly influenced by the co-seismic displacement, especially in the Northing component. Based on the tuning results in Table 6.2, the optimal value of q_a for the KFB is 10.0 (m^2/s^3) in this case.

6.4.2 Fixed q_a and q_b with varied R

The second parameter to be tuned in the Kalman filter is the measurement noise covariance matrix, $\boldsymbol{R}$. After tuning the q_a in the system noise matrix, $\boldsymbol{Q}$, in Section 6.4.1, the fixed q_a is set as 10.0 (m^2/s^3) in all Kalman filters. The fixed q_b in the system noise matrix is still set with C_{q_b} = 4.0. The initial $\boldsymbol{R}$ is set as 128.0 (m^2) with reference to the results in Chapter 5. Note that when tuning $\boldsymbol{R}$ in the Kalman filter, the $\boldsymbol{R}$ in both KFB and KFNB are also tuned to the same value, and the SKF solutions are the RTS smoothed KFB solutions. The KFB and KFNB displacement results are also compared

to the SKF displacement solutions due to the absence of the true displacements in real earthquakes. Table 6.3 presents the displacement error RMS, STD, and mean of the KFNB and KFB with a wide range of $\boldsymbol{R}$ with respect to the SKF solutions.

Table 6.3: The performance of the KFNB and KFB displacement by fixing $\boldsymbol{q_a}$ = 10.0 (m^2/s^3) and C_{q_b} = 4.0 and setting different $\boldsymbol{R}$ with respect to the SKF results

	KFNB E Dis. Error (m)			KFNB N Dis. Error (m)			KFNB U Dis. Error (m)		
$R(m^2)$	Mean	STD	RMS	Mean	STD	RMS	Mean	STD	RMS
2.0	-1.8E-05	0.00866	0.00866	0.00522	0.00742	0.00907	-0.00023	0.00703	0.00703
4.0	-1.7E-05	0.00849	0.00849	0.00667	0.00734	0.00992	-0.00028	0.00643	0.00644
8.0	-1.4E-05	0.00828	0.00828	0.00876	0.00746	0.01151	-0.00036	0.00593	0.00594
16.0	-1.0E-05	0.00805	0.00805	0.01175	0.00785	0.01413	-0.00047	0.00551	0.00553
32.0	-3.6E-06	0.00783	0.00783	0.01598	0.00862	0.01816	-0.00064	0.00515	0.00519
64.0	6.5E-06	0.00759	0.00759	0.02198	0.00994	0.02412	-0.00088	0.00486	0.00494
128.0	2.2E-05	0.00735	0.00735	0.03045	0.01204	0.03275	-0.00124	0.00463	0.00480
256.0	4.7E-05	0.00715	0.00715	0.04242	0.01524	0.04508	-0.00175	0.00445	0.00478
512.0	8.5E-05	0.00699	0.00699	0.05933	0.01995	0.06259	-0.00247	0.00429	0.00495

	KFB E Dis. Error (m)			KFB N Dis. Error (m)			KFB U Dis. Error (m)		
$R(m^2)$	Mean	STD	RMS	Mean	STD	RMS	Mean	STD	RMS
2.0	-1.6E-05	0.00950	0.00950	0.00010	0.00723	0.00723	-2.4E-05	0.00824	0.00824
4.0	-1.6E-05	0.00928	0.00928	0.00012	0.00689	0.00689	-2.2E-05	0.00759	0.00759
8.0	-1.6E-05	0.00897	0.00897	0.00014	0.00660	0.00660	-1.7E-05	0.00706	0.00706
16.0	-1.8E-05	0.00861	0.00861	0.00018	0.00638	0.00639	-9.7E-06	0.00662	0.00662
32.0	-2.1E-05	0.00828	0.00828	0.00023	0.00624	0.00624	-9.2E-07	0.00626	0.00626
64.0	-2.6E-05	0.00801	0.00801	0.00029	0.00620	0.00620	6.6E-06	0.00597	0.00597
128.0	-3.1E-05	0.00778	0.00778	0.00028	0.00614	0.00615	9.4E-06	0.00576	0.00576
256.0	-3.7E-05	0.00758	0.00758	0.00051	0.00678	0.00680	4.1E-06	0.00561	0.00561
512.0	-4.4E-05	0.00741	0.00741	0.00069	0.00769	0.00772	-9.9E-06	0.00552	0.00552

With reference to the results in Chapter 5, the measurement noise covariance matrix $\boldsymbol{R}$ was set to 128 m^2 in all Kalman filter algorithms initially and then increased/decreased to find the optimal setting. Table 6.3 shows that apart from the KFNB solutions in the Northing, the mean errors of other KFB and KFNB solutions are increasing, and the STD and RMS errors are decreasing. Generally speaking, when increasing the value of $\boldsymbol{R}$, the STD and RMS displacement errors are expected to be smaller as the $\boldsymbol{R}$ is the measurement noise covariance accounting for the GNSS observation noise level and also the effects of the data-lags. However, when the Kalman filter algorithm is not as

stable, increasing the value of $\boldsymbol{R}$ actually led to larger errors in the displacement solutions, for example, the effects of the changed baseline error (co-seismic displacement) in the Northing are too large for $\boldsymbol{R}$ to compensate in the KFNB. The mean, STD, and RMS results in Table 6.3 are also displayed in Figure 6.11, and similar to Figure 6.10, as the scale of the value $\boldsymbol{R}$ is large, the x-axis is a logarithmic-scale.

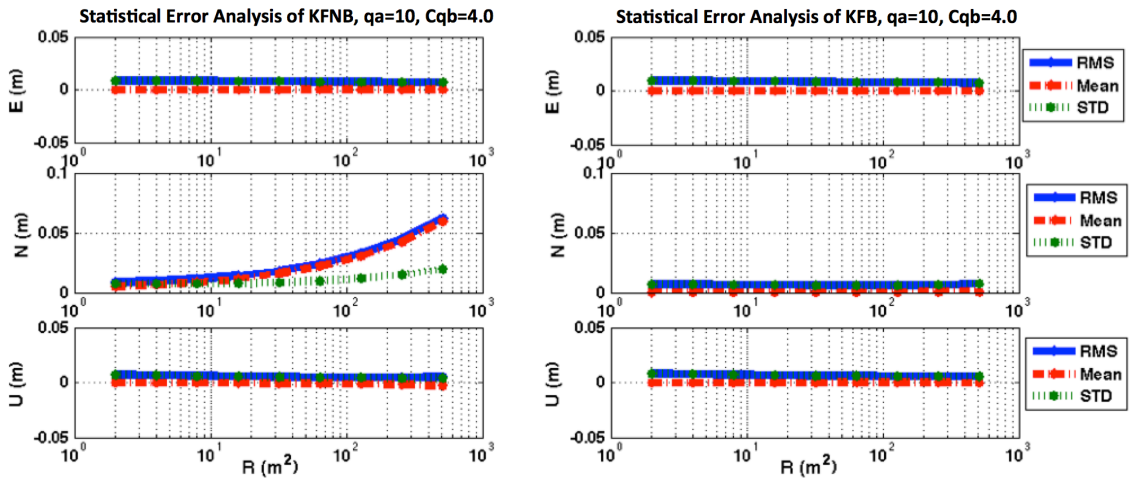

Figure 6.11: The statistical error analysis of the KFNB and KFB integrated displacement solutions by fixing $\boldsymbol{q_a}$ = 10 (m^2/s^3) and C_{qb} =4 and varying $\boldsymbol{R}$ with respect to the SKF displacement solutions.

The displacement error results in Figure 6.11 are plotted for comparison. Similarly, the RMS and STD errors are nearly the same in most plots in Figure 6.11 since the mean errors are close to zero. Table 6.3 and Figure 6.11 show that when tuning $\boldsymbol{R}$ in the KFNB and KFB, both methods can provide stable displacement solutions in the case of small co-seismic displacements during the earthquake, for example, the Easting and the Vertical component. However, in the case of larger permanent displacement (e.g. the Northing), the performance of the KFNB in this case is dominated by the value of $\boldsymbol{R}$, whereas the performance of the KFB is still consistent. Furthermore, based on the error results in Table 6.3, the error results of KFB actually do not vary much. Based on the results, $\boldsymbol{R}$=128.0 (m^2) has been decided for KFB to provide the relatively stable and optimal estimates during the earthquake in this case.

6.4.3 Fixed R and q_a with varied q_b

Finally, $\boldsymbol{q_b}$ in the system noise matrix is the third parameter to tune. As described by Eq. (5-8) in Section 5.4, the technique to tune $\boldsymbol{q_b}$ is to vary the standard deviation of the accelerometer baseline error by changing the coefficient of $\boldsymbol{q_b}$, C_{q_b}. The fixed $\boldsymbol{q_a}$ and $\boldsymbol{R}$ are set as 10.0 (m^2/s^3) and 128.0 (m^2) according to the results in Sections 6.4.1 and 6.4.2, respectively. The initial C_{q_b} is set as 4.0 with reference to the results in Section 5.4.3, and the value of C_{q_b} is varied in the tuning process. Table 6.4 shows the KFNB and KFB displacement error statistics of tuning $\boldsymbol{q_b}$ with respect to the SKF solutions. Note that $\boldsymbol{q_b}$ only exists in the system noise matrix in the KFB and SKF with the corresponding baseline error state. Therefore, the displacement solutions from the KFNB should not be changing significantly from tuning $\boldsymbol{q_b}$ as there is no baseline error state and no $\boldsymbol{q_b}$ in the KFNB. Thus, the process of tuning $\boldsymbol{q_b}$ is focusing more on the stability of the baseline error state in the KFB and the advantages of having the baseline error state in the Kalman filter algorithm.

As there is no baseline error state in the KFNB, the displacement error results of the KFNB with respect to the SKF in Table 6.4 only vary due to the small differences in the SKF solutions during tuning C_{qb}. In Table 6.4, the error results indicate that if the value of C_{qb} is not tuned properly, the performance of KFNB along one axis can actually be better than KFB, especially in the cases of small co-seismic displacement. The baseline error state improves the accuracy significantly when there is a co-seismic displacement in the Northing, however, the value of C_{qb} still needs to be set delicately based on the results in Table 6.4. The displacement error results of changing $\boldsymbol{q_b}$ in the system noise covariance with respect to the SKF solutions are also presented in Figure 6.12.

Table 6.4: The performance of the KFB and KFNB displacement by fixing $\boldsymbol{q_a}$ = 10.0 (m^2/s^3) and $\boldsymbol{R}$ = 128.0 (m^2) and setting different C_{qb} with respect to the SKF results

	KFNB E Dis. Error (m)			KFNB N Dis. Error (m)			KFNB U Dis. Error (m)		
C_{qb}	Mean	STD	RMS	Mean	STD	RMS	Mean	STD	RMS
0.01	1.4E-05	0.00720	0.00720	0.03045	0.01216	0.03279	-0.00124	0.00474	0.00490
0.04	1.4E-05	0.00720	0.00720	0.03044	0.01216	0.03278	-0.00124	0.00474	0.00490
0.09	1.4E-05	0.00720	0.00720	0.03044	0.01215	0.03278	-0.00124	0.00473	0.00489
0.25	1.5E-05	0.00721	0.00721	0.03044	0.01214	0.03277	-0.00124	0.00473	0.00489
1.0	1.7E-05	0.00724	0.00724	0.03044	0.01211	0.03276	-0.00124	0.00470	0.00486
4.0	2.2E-05	0.00735	0.00735	0.03045	0.01204	0.03275	-0.00124	0.00463	0.00480
9.0	2.8E-05	0.00752	0.00752	0.03046	0.01200	0.03274	-0.00124	0.00458	0.00475
16.0	3.4E-05	0.00770	0.00770	0.03046	0.01197	0.03273	-0.00124	0.00454	0.00471
25.0	3.9E-05	0.00789	0.00789	0.03047	0.01195	0.03273	-0.00124	0.00452	0.00469

	KFB E Dis. Error (m)			KFB N Dis. Error (m)			KFB U Dis. Error (m)		
C_{qb}	Mean	STD	RMS	Mean	STD	RMS	Mean	STD	RMS
0.01	-2.6E-05	0.00723	0.00723	0.01220	0.01395	0.01853	-3.6E-04	0.00482	0.00483
0.04	-2.8E-05	0.00727	0.00727	0.00559	0.01219	0.01342	-0.00016	0.00489	0.00489
0.09	-2.7E-05	0.00730	0.00730	0.00334	0.01057	0.01109	-9.7E-05	0.00496	0.00496
0.25	-2.3E-05	0.00737	0.00737	0.00172	0.00871	0.00888	-4.3E-05	0.00509	0.00509
1.0	-2.2E-05	0.00752	0.00752	0.00074	0.00707	0.00711	-5.3E-06	0.00537	0.00537
4.0	-3.1E-05	0.00778	0.00778	0.00028	0.00614	0.00615	9.4E-06	0.00576	0.00576
9.0	-3.8E-05	0.00800	0.00800	0.00028	0.00621	0.00622	1.2E-05	0.00604	0.00604
16.0	-4.2E-05	0.00820	0.00820	0.00022	0.00624	0.00624	1.3E-05	0.00626	0.00626
25.0	-4.4E-05	0.00839	0.00839	0.00018	0.00631	0.00631	1.5E-05	0.00645	0.00645

In Table 6.4 and Figure 6.12, the KFNB and KFB displacement results of tuning C_{qb} are generally steady. The relatively large KFNB displacement RMS and STD error results in the Northing in Figure 6.12 represent that the drifts and the sawtooth-like effect within the displacement solutions due to the co-seismic displacement. The baseline error state in KFB and SKF results from a mixture of accelerometer bias and levelling error. Based on the results in Table 6.4 and Figure 6.12, if not setting the C_{qb} appropriately, the use of baseline error state in the KFB would potentially introduce more errors or uncertainties in the algorithm.

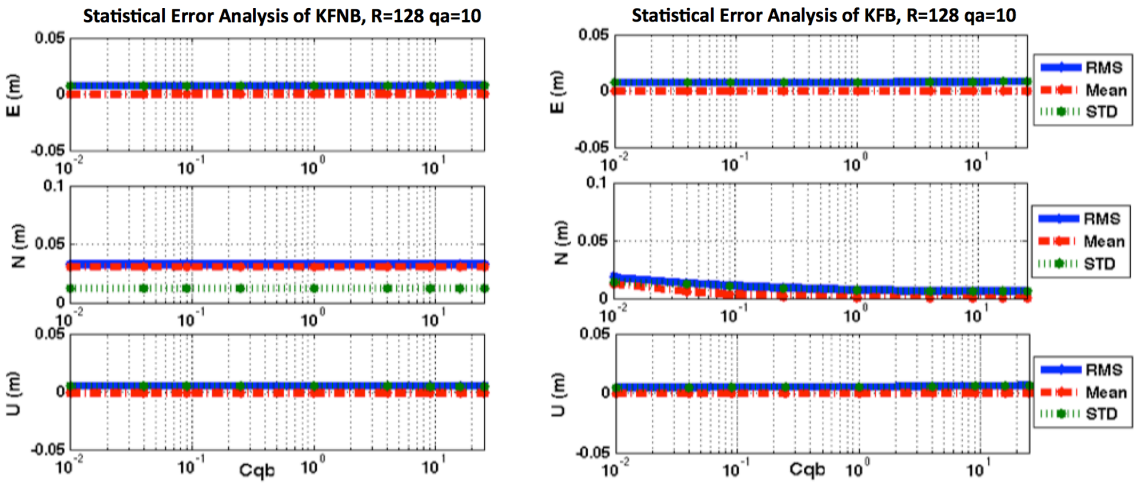

Figure 6.12: The statistical error analysis of the KFNB and KFB integrated displacement solutions by fixing $\boldsymbol{R}$ =128 (m^2) and $\boldsymbol{q_a}$ = 10 (m^2/s^3) and varying the coefficient of $\boldsymbol{q_b}$ with respect to the SKF displacement solutions.

Hence, in order to understand the changes of the baseline error state and tune C_{qb} properly, the KFB and KFNB displacement errors with respect to the SKF solutions, the KFB baseline error state estimates, and displacement solutions of all methods with varied C_{qb} in the Northing are shown in Figure 6.13 to Figure 6.20. In addition, the related results in the Easting and vertical components are also shown in **Appendix B.1** for more information.

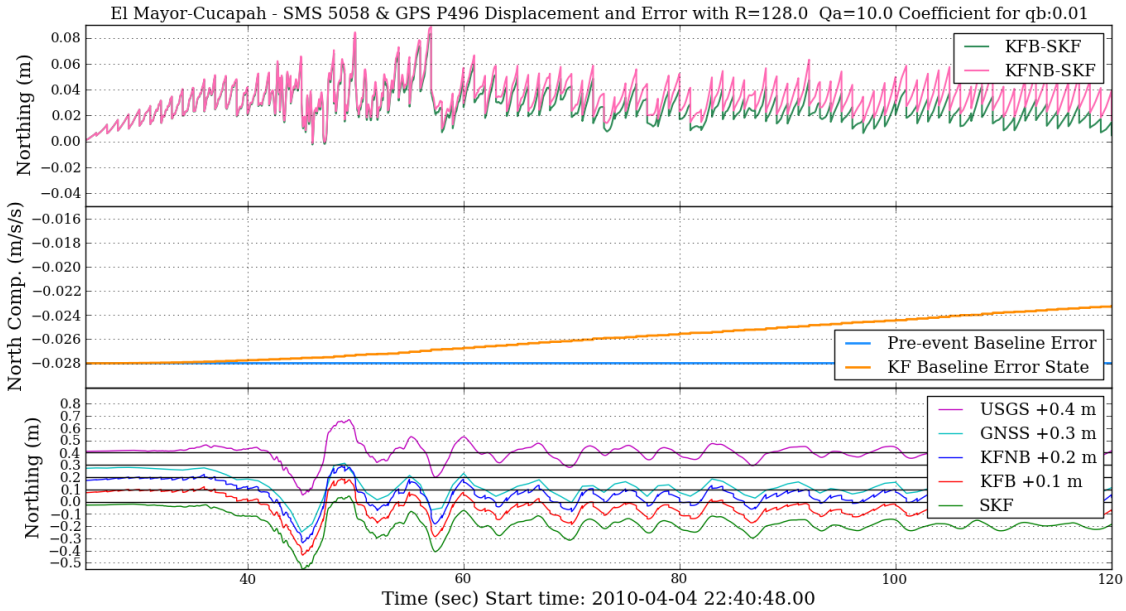

Figure 6.13: The displacement error results of the KFNB and KFB in the Northing with respect to the SKF, the pre-event accelerometer baseline error and the KFB baseline error state, and Northing displacement results of all methods by setting $\boldsymbol{R}$=128 (m^2), $\boldsymbol{q_a}$ = 10 (m^2/s^3), and C_{q_b} = 0.01.

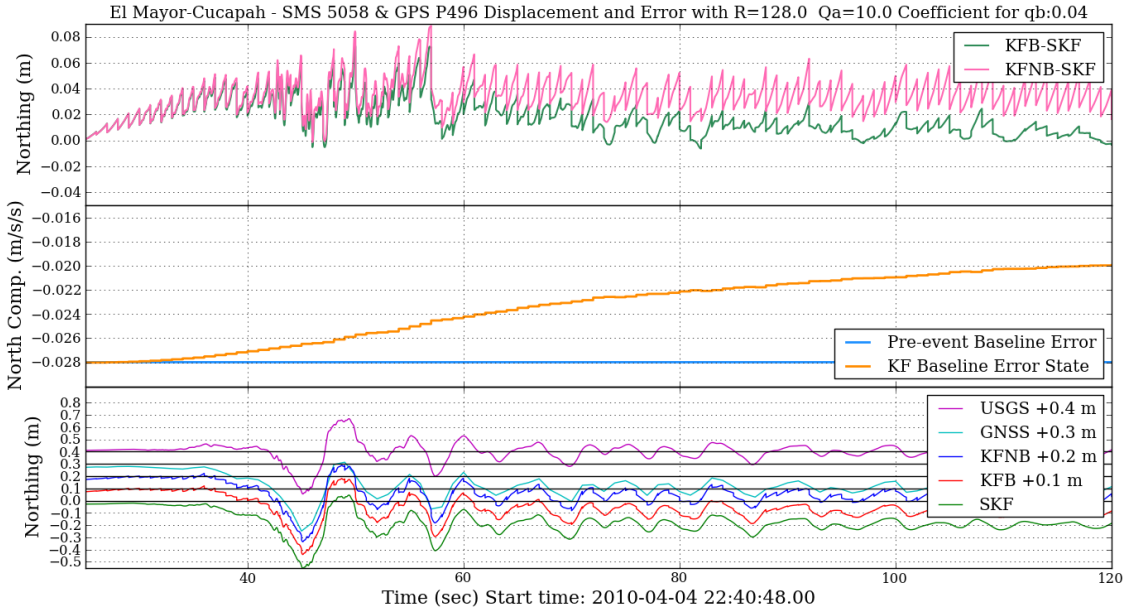

Figure 6.14: The displacement error results of the KFNB and KFB in the Northing with respect to the SKF, the pre-event accelerometer baseline error and the KFB baseline error state, and Northing displacement results of all methods by setting $\boldsymbol{R}$ =128 (m^2), $\boldsymbol{q_a}$ = 10 (m^2/s^3), and C_{q_b} = 0.04.

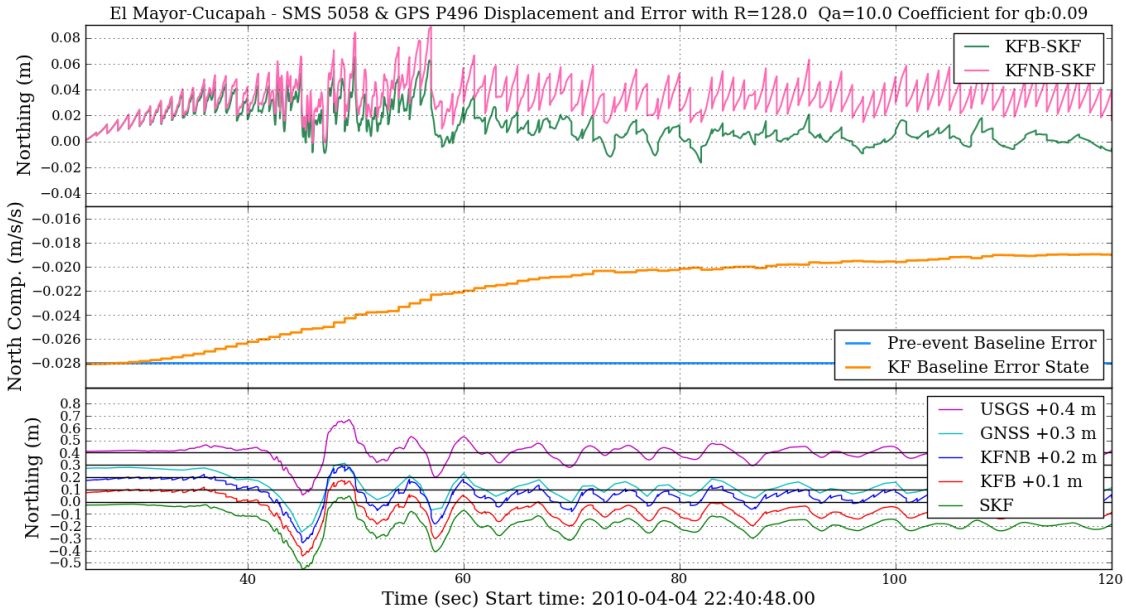

Figure 6.15: The displacement error results of the KFNB and KFB in the Northing with respect to the SKF, the pre-event accelerometer baseline error and the KFB baseline error state, and Northing displacement results of all methods by setting $\boldsymbol{R}$ =128 (m^2), $\boldsymbol{q_a}$ = 10 (m^2/s^3), and C_{q_b} = 0.09.

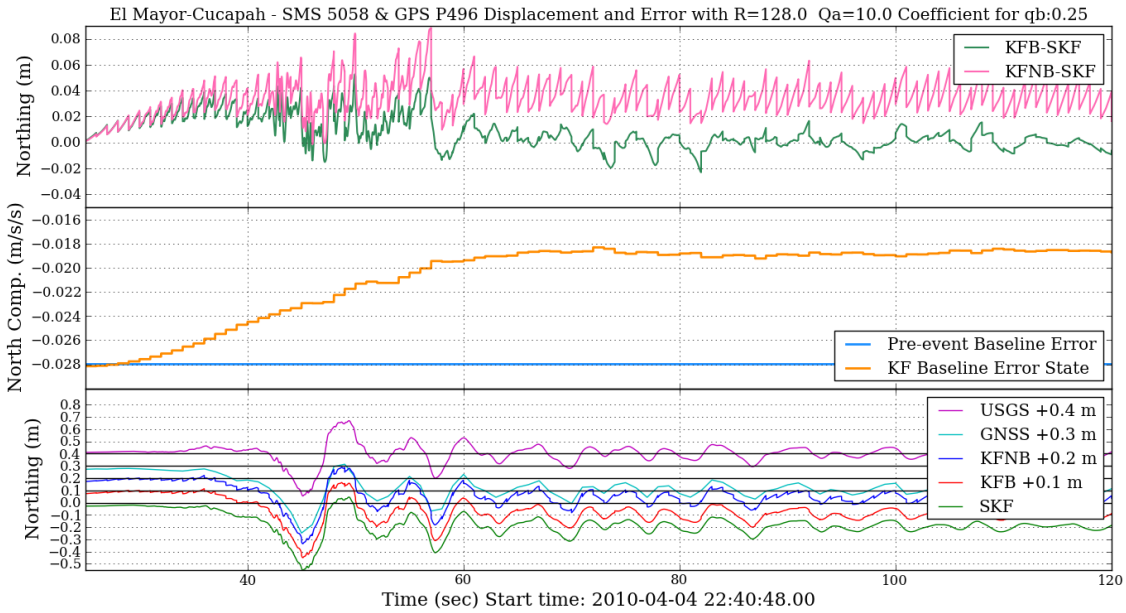

Figure 6.16: The displacement error results of the KFNB and KFB in the Northing with respect to the SKF, the pre-event accelerometer baseline error and the KFB baseline error state, and Northing displacement results of all methods by setting $\boldsymbol{R}$ =128 (m^2), $\boldsymbol{q_a}$ = 10 (m^2/s^3), and C_{q_b} = 0.25.

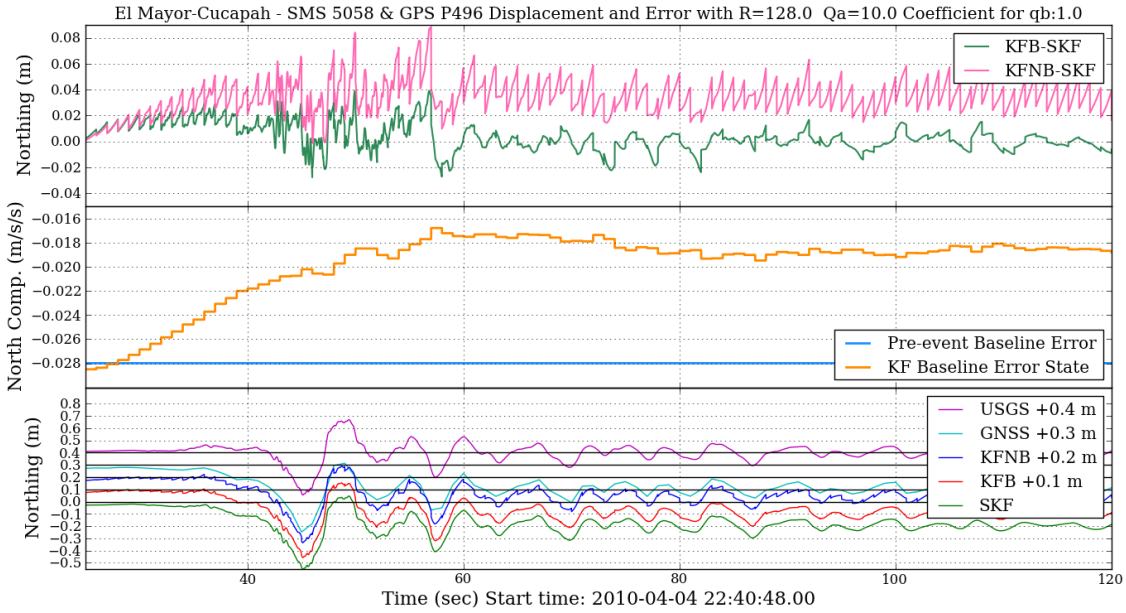

Figure 6.17: The displacement error results of the KFNB and KFB in the Northing with respect to the SKF, the pre-event accelerometer baseline error and the KFB baseline error state, and Northing displacement results of all methods by setting $\boldsymbol{R}$ =128 (m^2), $\boldsymbol{q_a}$ = 10 (m^2/s^3), and C_{q_b} = 1.0.

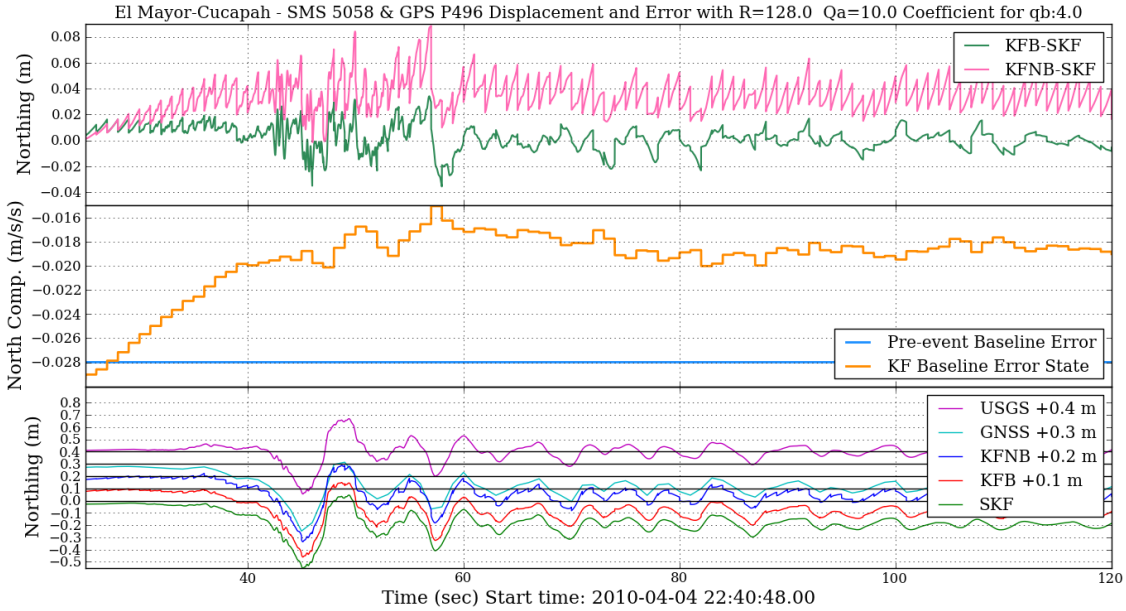

Figure 6.18: The displacement error results of the KFNB and KFB in the Northing with respect to the SKF, the pre-event accelerometer baseline error and the KFB baseline error state, and Northing displacement results of all methods by setting $\boldsymbol{R}$ =128 (m^2), $\boldsymbol{q_a}$ = 10 (m^2/s^3), and C_{q_b} = 4.0.

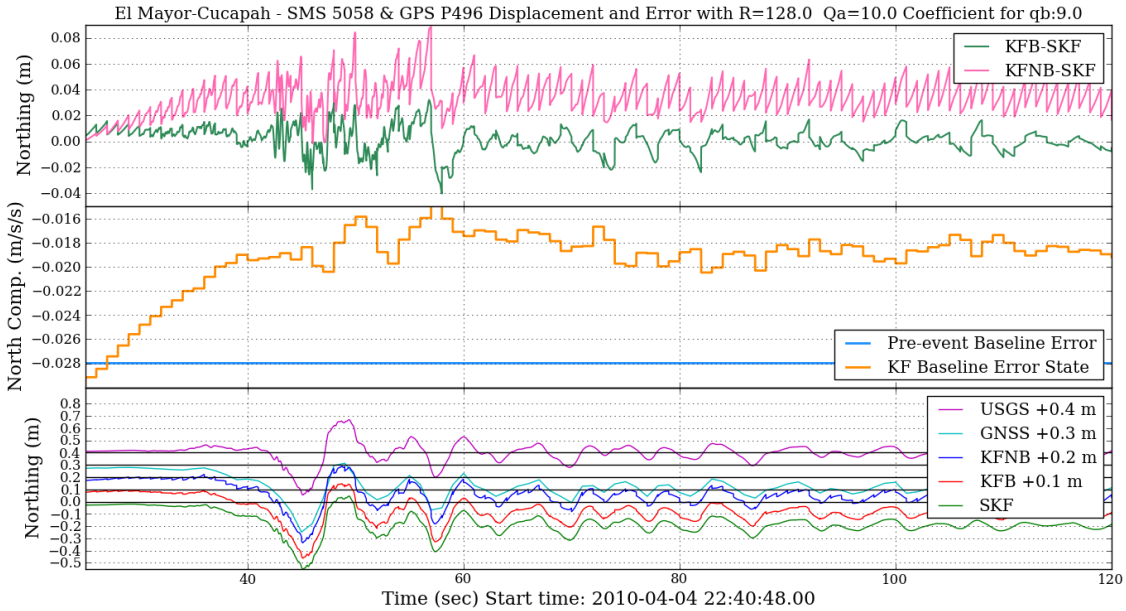

Figure 6.19: The displacement error results of the KFNB and KFB in the Northing with respect to the SKF, the pre-event accelerometer baseline error and the KFB baseline error state, and Northing displacement results of all methods by setting $\boldsymbol{R}$ =128 (m^2), $\boldsymbol{q_a}$ = 10 (m^2/s^3), and C_{q_b} = 9.0.

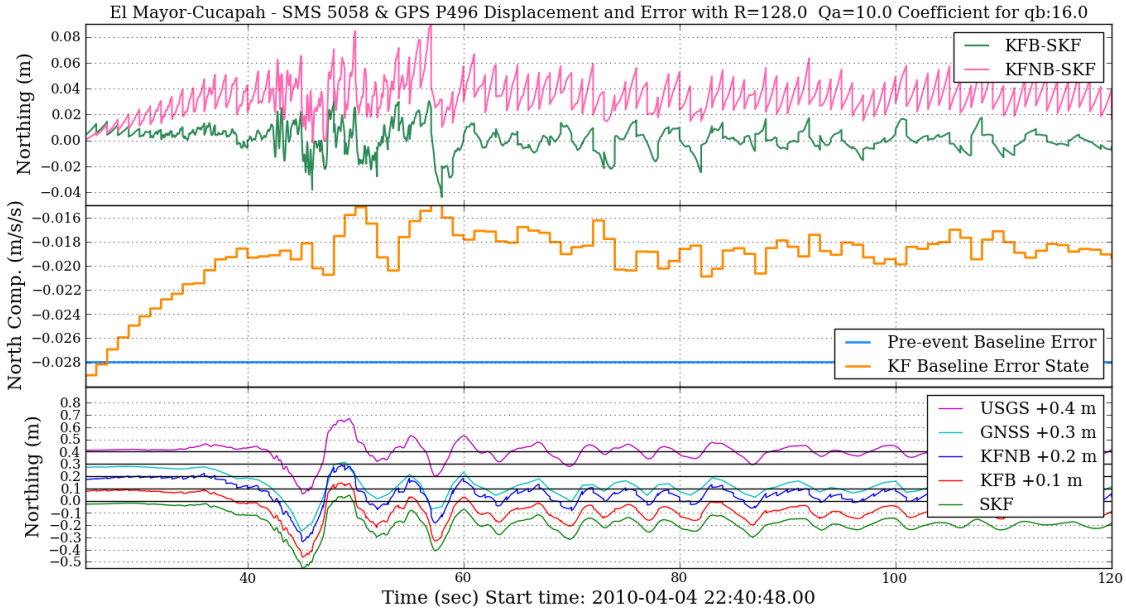

Figure 6.20: The displacement error results of the KFNB and KFB in the Northing with respect to the SKF, the pre-event accelerometer baseline error and the KFB baseline error state, and Northing displacement results of all methods by setting $\boldsymbol{R}$ =128 (m^2), $\boldsymbol{q_a}$ = 10 (m^2/s^3), and C_{q_b} = 16.0.

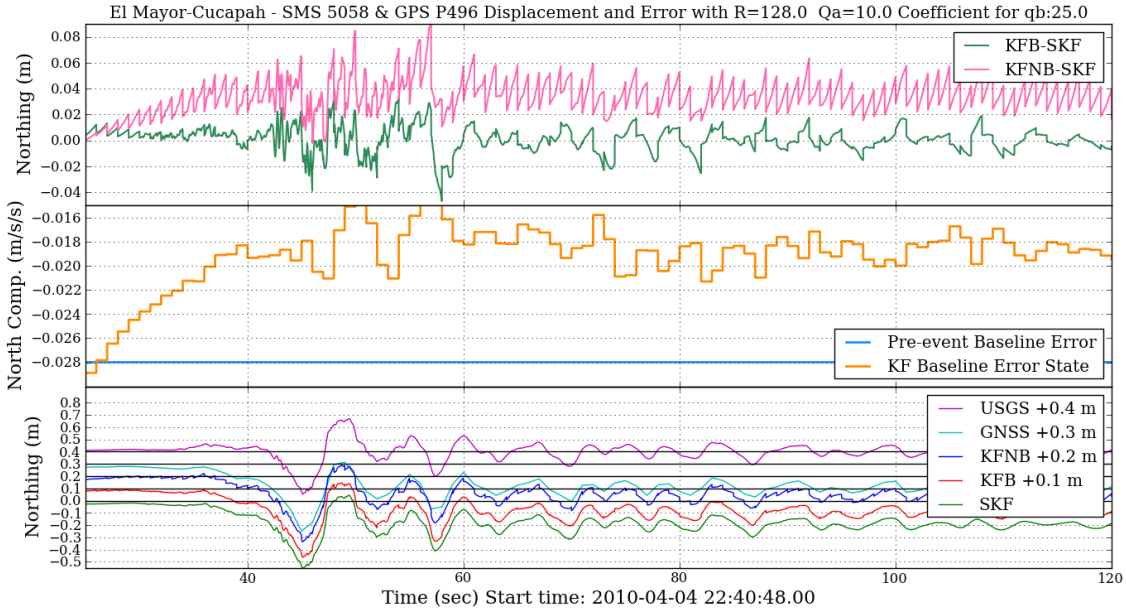

Figure 6.21: The displacement error results of the KFNB and KFB in the Northing with respect to the SKF, the pre-event accelerometer baseline error and the KFB baseline error state, and Northing displacement results of all methods by setting $\boldsymbol{R}$ =128 (m^2), $\boldsymbol{q_a}$ = 10 (m^2/s^3), and C_{q_b} = 25.0.

Figure 6.13 ~ Figure 6.21 illustrate the behaviour of the baseline error state in the KFB when setting different $\boldsymbol{q_b}$ in the system noise covariance, $\boldsymbol{Q}$. The KFNB and KFB displacement errors with respect to the SKF solutions show the importance of having a baseline error state when there are co-seismic displacements. The value of $\boldsymbol{q_b}$ represents the variations of the accelerometer baseline error, and the baseline error results from a mixture of accelerometer bias and levelling error. When the $\boldsymbol{q_b}$ term in the KFB is small,

it means the baseline error state does not vary much, and vice versa. In Figure 6.13, Figure 6.14 and Figure 6.15, when the values of $\boldsymbol{q_b}$ are small, the baseline error state can still at least estimate the linear drifts in the velocity and the quadratic drifts in the displacement gradually, at the same time, reduce the sawtooth-like effects compared to the KFNB displacement error. When $\boldsymbol{q_b}$ becomes larger in the KFB as shown in Figure 6.16 to Figure 6.21, the baseline error state senses the bias changes more rapidly. However, Figure 6.19 to Figure 6.21 also show that when the value of $\boldsymbol{q_b}$ is set larger, more variations and drifts occur on the KFB displacement errors. Moreover, based on the results of the Easting and the vertical component in **Appendix B**, the value of $\boldsymbol{q_b}$ should be set more delicately in the case of no or small co-seismic displacements during earthquakes as the bias changes might not vary much. Thus, based on the results produced by the analysis, the optimal value of C_{qb} is taken to be 1.0 in this case as a compromise to obtain optimal displacement solutions along the three axes. Furthermore, although there are still some small drifts in the displacement errors as shown in Figure 6.13 to Figure 6.21 and Figure B.1 to Figure B.18, compared to KFNB, GNSS, and the conventional seismological methods, the KFB can still provide a more accurate real-time solution under any circumstances.

6.5 Summary

In this chapter, the M_w 7.2 El Mayor-Cucapah Earthquake data sets of a collocated GNSS sensor and a strong motion have been tested with the proposed three-state Kalman filter integration. The selected GNSS station P496 and strong motion station 5058 are roughly collocated with a 138 metre separation. By using the data sets from the existing networks in a real earthquake, this experiment shows that the integrated GNSS and accelerometer-based instruments are still useful in real earthquakes, even when they are collocated within a short distance, but not combined.

The results presented in this chapter show that the implemented Kalman filter algorithm with an additional baseline error state (KFB) can determine high-frequency movements as well as the permanent (co-seismic) displacements in a real earthquake. Three different co-seismic displacements occurred along three axes in the M_w 7.2 El Mayor-Cucapah Earthquake, which provides an ideal environment to validate the KFB algorithm. The three co-seismic displacements after the earthquake are 20 cm in the Northing, 5 cm in the vertical component, and near-zero in the Easting. The displacement results of existing methods including GNSS, USGS baseline correction (USGS), a two-state Kalman filter integration (KFNB), and an RTS smoothed Kalman filter (SKF) have been compared with the KFB displacement solutions in this experiment to show the importance and improvements of using the baseline error state in the algorithm.

In this experiment, the USGS baseline-corrected acceleration results can only show the high-frequency shaking waveform but not the 20 cm permanent displacement in the Northing after shaking due to the applied seismological baseline correction and high-pass filter on the accelerometer measurements. The 1 Hz GNSS solutions can show the 20 cm displacement but not the high-frequency movements during the earthquake. The KFNB can only estimate smoothly when there is no co-seismic displacement (e.g. the Easting and Up). However, when the 20 cm permanent displacement was caused and the baseline error has changed, the KFNB solutions drifted and were biased by the accelerometer baseline change (e.g. in the Northing). The baseline error state in the KFB estimates and compensates for the varying accelerometer baseline errors and potential data lagging errors in the displacement solutions. Thus, the KFB can minimize the rapid drifts and the sawtooth-like effects to provide smooth and high-frequency displacement during the great earthquake.

Three noise covariance parameters, $\boldsymbol{R}$, $\boldsymbol{q_a}$, and $\boldsymbol{q_b}$, in the Kalman filters were also set individually to find out the most suitable value for each parameter in order to provide optimal displacement solutions. Similarly, in the tuning process, two of the parameters were fixed at one time, while the third was varied. As there is no displacement truth in the real earthquake, the RTS smoothed results (SKF) were taken as the most accurate solution and used to compare with both Kalman filter algorithms, KFB and KFNB. Statistics and figures of the KFNB and KFB displacement solutions with respect to SKF displacement solutions when tuning different parameters were also presented. With reference to the tuning results in Section 5.4, the initial settings of the noise parameters in the Kalman filters were: C_{q^b} for the coefficient of $\boldsymbol{q_b}$ = 4.0, $\boldsymbol{q_a}$ = 1.0 (m^2/s^3), and $\boldsymbol{R}$ = 128.0 (m^2).

Firstly, the tuning process of KFB and KFNB started with the PSD of the accelerometer noise, $\boldsymbol{q_a}$, in the system noise covariance, $\boldsymbol{Q}$, by setting a wide range of the values of $\boldsymbol{q_a}$. The tuned displacement results of KFB and KFNB with respect to the SKF displacement solutions indicated that the KFNB only performs stably along the Easting axis when no co-seismic displacement occurred in the earthquake. However, in the cases of the small co-seismic displacement (5 cm) in the vertical component and the larger co-seismic displacement (20 cm), the KFNB solutions are influenced by not only the value of $\boldsymbol{q_a}$ but also the co-seismic displacements, especially in the Northing component. Whereas, the KFB with the additional baseline error state can provide stable solutions and is less affected by the value of $\boldsymbol{q_a}$. Based on the KFB displacement error results with respect to the SKF solutions, the optimal value of $\boldsymbol{q_a}$ for the KFB is 10.0 (m^2/s^3) for this experiment.

Secondly, the measurement noise covariance, $\boldsymbol{R}$, in both KFB and KFNB algorithms was tuned, and the tuned KFB and KFNB were also compared to the SKF solutions. The statistical error results of the KFB and KFNB with respect to the SKF were

discussed under two circumstances: one axis with large co-seismic displacements in the Northing and two axes with no or small co-seismic displacements in the Easting and the vertical component. In the cases of the Easting and the vertical axis, the performances of both KFB and KFNB are similar. When increasing the value of $\boldsymbol{R}$, the mean errors of the KFB and KFNB solutions were increasing, whereas the STD and RMS were decreasing, since $\boldsymbol{R}$ (as the measurement noise covariance) accounts for the GNSS noise and the effects of the potential data-lags. On the other hand, with the substantial co-seismic displacement in the Northing, the KFB still can provide the same accuracy with varied $\boldsymbol{R}$. Whereas, the KFNB became unstable and failed to compensate the significant effects of the changed baseline errors (co-seismic displacement) when increasing the value of $\boldsymbol{R}$ in the Northing. Based on the error statistics, the error results of KFB were consistent under any circumstances. $\boldsymbol{R}$ = 128.0 (m^2) in KFB has been considered to provide relatively stable estimates during the earthquake in this case.

Thirdly, the parameter $\boldsymbol{q_b}$, which only features within the system noise covariance in the KFB and SKF algorithms, was tuned. The error statistics with respect to the SKF solutions were also provided when setting various $\boldsymbol{q_b}$ in the KFB algorithm. Since $\boldsymbol{q_b}$ presents the variations of the baseline error, although the KFB generally provides stable displacement solutions, the values of $\boldsymbol{q_b}$ still affected the accuracy of the displacement solutions. In the case of the large co-seismic displacements in the Northing, due to the significant and rapid baseline error changes, the KFB performed better when the $\boldsymbol{q_b}$ was set larger. However, in the cases of small or none co-seismic displacements, the variations of the baseline error were rather steady, thus, smaller values were more suitable for $\boldsymbol{q_b}$ to obtain more stable displacement solutions. Hence, the best choice of the $\boldsymbol{q_b}$ value depends on the kinds of requirements. Based on the results, a compromise value of the coefficient of $\boldsymbol{q_b}$ is considered to be 1.0 in this case, to obtain optimal displacement solutions along the three axes.

Overall, during the M_w 7.2 El Mayor-Cucapah Earthquake, the KFB with the additional baseline error state can effectively reduce the sawtooth-like effects or other drifts in the displacement solutions and provide accurate co-seismic displacement solutions compared to the existing methods, including the seismological baseline correction, GNSS, and KFNB. This implemented KFB technique is expected to provide reliable displacement solutions even when the baseline error of the strong motion seismometer/accelerometer is changed or shifted during/after earthquake shaking.

Chapter 7 Conclusions and Discussion

This chapter explores the conclusions of the research and provides a discussion of the results. First, Section 7.1 will address the overview of this study. Section 7.2 will discuss the overall conclusions of the research findings with the statement of general aims given in Chapter 2. Sections 7.3 will outline the findings associated with the three experiments in this study and detail the experimental conclusions relative to the specific objectives listed in Chapter 2. Discussion related to this study including the limitations of the methods and the applicability of this study will be discussed in Section 7.4. Furthermore, in Section 7.5, the research contributions of this study will be presented. Section 7.6 will discuss the follow-on work that can be continued potentially after this study. Finally, Section 7.7 closed this thesis by giving a general research overview.

7.1 Overview of the Study

The motivation for this study is the need to quantify and provide the rapid ground displacement immediately after an earthquake, to the end of determining the earthquake magnitude correctly and quickly. Existing work in the seismological field has dealt with seismic data during earthquakes but has failed to address problems with the quadratic drifting displacement solutions caused by accelerometer baseline error or no permanent (co-seismic) shifts after applying the seismological baseline correction. GNSS seismology has dealt with permanent shifts caused by earthquakes; however, the low-sampling rate (1-10 Hz) utilised by GNSS is unable to correct problems caused by the high-frequency movement during earthquakes. Although an integrated accelerometer based instrument and GNSS system has been investigated, the accelerometer baseline error still causes quadratic drifts in the displacement solutions when the accelerometer has moved during the shaking. Hence, the principal problem this work addresses is the combination of the seismological baseline correction method with the integrated system in order to provide a measure of ground displacement during earthquakes.

The principle innovation of this work is the utilisation of a baseline error state within a loosely-coupled Kalman filter integration. The proposed Kalman filter combines the accelerometer baseline error correction into the integrated Kalman filter algorithm. Three experiments have been carried out to validate this algorithm and the software developed to implement it. Firstly, tests and validations of the University of California San Diego (UCSD) Large High Performance Outdoor Shake Table (LHPOST) experiment were implemented using the proposed Kalman filter algorithm. Secondly, a designed displacement experiment with a pair of collocated strong motion seismometer and GNSS receiver has been carried out at the rooftop of NPL, and the results were analysed. Finally, the proposed Kalman filter algorithm was validated and tested against

data sets of a paired strong motion seismometer and GNSS from existing seismic and geodetic networks during a real earthquake, the M_w 7.2 El Mayor-Cucapah Earthquake.

7.2 General Conclusions in Relation to the Objectives

Accelerometer based instruments (strong motion seismometers and accelerometers) have been integrated with geodetic level GNSS receivers by a loosely-coupled Kalman filter integration with the aim of obtaining ground displacements rapidly for earthquake magnitude determination and earthquake early warning systems in the seismological field. During earthquakes, the frequent ground movements often cause the accelerometer baseline error to be unstable and changing during or after shaking, which will induce linear and quadratic drifts in the velocity and displacement solutions, respectively. The implemented Kalman filter algorithm is able to detect and correct the accelerometer baseline error when the acceleration bias is not stable, for example during or after shaking.

Based on the experiments and results in this study, there are two key principal conclusions. Firstly, the Kalman filter results depend sensitively upon the tuning process. The tuning process is changing the combination of the noise parameters in Kalman filter algorithms, which is critical and effective to the solutions. Secondly, including the baseline error state in the Kalman filter algorithm improves accuracy and information content in the outputs of the GNSS and accelerometer integrated system. With the baseline error state, no seismological baseline correction or noise filters are required for seismic data, which reduces pre-processing burdens and enables to provide the solutions quicker. The Kalman filter with the baseline error state gives both permanent displacements and earthquake waveforms during and after earthquakes, and both of which are vital in earthquake monitoring.

A software package that includes the loosely-coupled Kalman filter integration has been developed. Experiments have been carried out to validate the proposed algorithm and software. Meanwhile, observations from the existing geodetic network and seismic network of a real earthquake have also been tested. The following sections present detailed conclusions drawn from the experimental results.

7.3 Experiments and Their Conclusions

The detailed conclusions of each experiment in this study are given in the following sections. The outcomes in relation to the experiments are described, and the findings as well as limitations of each experiment are also summarised.

7.3.1 UCSD large shake table experiment

Professor Yehuda Bock from UCSD has provided GPS and MEMS accelerometer data sets from their large shake outdoor table experiment, the LHPOST. A seven-floor high

building was built on a controlled platform, and 7 GPS receivers and 15 MEMS accelerometers were located on different sites of the building. The DGPS displacement solutions and the MEMS accelerometers measurements were given and used as inputs for the Kalman filter integration. A high sampling rate (1024 Hz) displacement truth model was also provided to help assess the accuracy of the solutions. Moreover, the displacement solutions of UCSD's two-state (displacement and velocity) loosely-coupled Kalman filter integration were provided to compare with the displacement solutions of the implemented three-state (displacement, velocity, and baseline error) loosely-coupled Kalman filter method (KFB). This controlled platform can simulate the real earthquake waveforms in one direction with a high-sampling rate displacement truth model. These data sets have provided the ideal environment in which to test and validate the proposed Kalman filter algorithm.

1) Kalman filter tuning dominates the performance of the integrated results.

The results and analysis of UCSD's Kalman filter method published in Bock et al. (2011) were used in this research to compare with the proposed KFB results. Unlike the conclusions of Bock et al. (2011), the results have shown the importance of the Kalman filter tuning process by calculating the RMS errors of the displacement results with respect to the displacement truth model. The Kalman filter tuning process has been explored by changing the noise parameters in the algorithms, including the system noise covariance matrix ($\boldsymbol{Q}$) and measurement noise covariance matrix ($\boldsymbol{R}$). Since the Kalman filter tuning process is always semi-empirical, the algorithm has been validated with various combinations of the noise covariance matrices by varying one parameter at one time while fixing the other parameters. The results in this experiment show that the accuracy of the tuned Kalman filter integrations with correct noise parameters can improve the performance of the displacement solutions more than 36% and 20% on STD and RMS of the displacement error, respectively, with respect to the un-tuned Kalman filter integrations.

2) The limitation of the UCSD LHPOST experiment

Considering only the tuned results, there is no significant improvement from the KFB compared to the UCSD's two-state Kalman filter in this experiment when the same parameters are used in both Kalman filter algorithms. Since the large shake table was designed and controlled to return to the original position after shaking, the additional baseline error state is not very helpful because the accelerometer baseline error does not vary significantly in this experiment. Yet in reality, the accelerometer baseline errors often change considerably during or after shaking in real earthquakes. The additional baseline error state in KFB is used to detect and correct the change of the accelerometer baseline in the Kalman filter algorithm. A further experiment with considerably varied baseline errors during or after shaking is necessary to show the impact of the additional term.

Meanwhile, although the large shake table can simulate real earthquake waveforms, because of the design of the shake table the controlled platform can only simulate the waveform in one axis, moving laterally along one direction. More importantly, no permanent shifts occur during the shaking. In real earthquakes, the movements are always in three dimensions, and permanent displacements after shaking are common. In this case, another controlled experiment that processes the measurements in three dimensions with permanent displacements after shaking is used to validate the proposed KFB algorithm.

7.3.2 NPL rooftop experiment

An integrated strong motion seismometer and GNSS experiment was carried out on the rooftop of the NPL. A Leica Viva GNSS antenna and a Güralp CMG-5TD strong motion seismometer were mounted on a movable steel plate on the platform. Observations were logged for the same 5-hour period on two consecutive days. During the last 90 minutes of the second day, the platform was subjected to a series of small displacements of known magnitude and direction. The GNSS observations were processed several times using PPP, and the PPP solutions were used as inputs for Kalman filter integrations. The purposes of this experiment are to validate the three-dimensional Kalman filter algorithm with additional baseline error state (KFB) and to prove that the proposed Kalman filter integration algorithm could reach centimetre-level accuracy within short time periods. The nine-state (tri-axial displacement, velocity, and accelerometer baseline error) KFB results have been compared with the six-state (tri-axial displacement and velocity) Kalman filter (KFNB) integrated the results of the GNSS and the strong motion seismometer. In the following sections, the RTS smoothed results (SKF) are compared with the KFB and KFNB of these experiments. The velocity state estimates of each Kalman filter are used to validate the performance of the methods with respect to the zero-velocity truth in the experiment.

1) Small displacement 30 mm was detected, however the results are dominated by GNSS solutions.

The displacement results have shown that, with the assistance of GNSS solutions, the KFB can successfully detect small movements (30 mm and 40 mm), especially compared with the KFNB results. When estimating the baseline error of the strong motion seismometer as an additional state in the KFB and SKF algorithms, the accuracy of KFB and SKF estimates are significantly improved compared to KFNB. The zero-velocity truth showed that the Kalman filter tuning process has more impact on KFNB outputs than on those of KFB and SKF since the GNSS measurements in KFNB need to be weighted strongly for the lack of baseline error states in the algorithm. Hence, KFB and SKF with additional baseline error states produce results that are more stable compared to KFNB. However, the tuning results also showed that tuned KFB and SKF were dominated by the GNSS errors. Thus, based on the results, for small displacements

(e.g. < 50 mm) and no earthquake-like shaking, the KFB integrated results might not improve the performance of the displacement solutions compared to the GNSS results.

2) The introduced baseline error states in the proposed KFB and SKF detect and correct accelerometer baseline changes during and after shaking.

The strong motion seismometer data in this experiment has shown that the acceleration bias changed significantly after every shifting of the platform. The varied acceleration bias in the strong motion seismometer data has been taken as the baseline error. As this experiment was designed purposely not to level the sensor carefully so as to allow potential accelerometer baseline errors, it has provided the opportunity to test whether the proposed KFB algorithm can detect and correct the shifts. The baseline errors within accelerometer based instrument data have always been an important and undeniable issue when processing the strong motion seismometer or accelerometer data in a seismology field. Currently, the baseline error correction has been applied to remove the linear and quadratic drifts affected by the baseline error in the velocity and displacement solutions. However, the applied baseline error correction might also filter out the permanent displacements caused by earthquakes. The results in this experiment show that the additional baseline error state in KFB and SKF can detect the baseline error within the accelerometer data and correct the baseline error during the integration. This shows the potential of using and processing raw accelerometer data directly without traditional baseline correction to avoid the potential loss of high-frequency movements during real earthquakes.

3) The limitation of the NPL rooftop experiment

The experiment tests whether the designed Kalman filter algorithm can measure centimetre movements in a short time period and as well as detect the baseline error changes within the seismometer data. However, although the platform provided the small movements, there was no earthquake-like shaking during this experiment. To validate the KFB and prove the algorithm could reach the same accuracy during real earthquakes, it is necessary to consider the results of the method on GNSS and strong motion seismometer data taken from real earthquakes.

7.3.3 2010 El Mayor-Cucapah Earthquake data analysis

In this experiment, the proposed Kalman filter algorithm was applied to data from a real earthquake, the M_w 7.2 El Mayor-Cucapah Earthquake. The great El Mayor-Cucapah Earthquake occurred in northern Baja California, Mexico on April 4th 2010. The strong motion seismometer data and the GNSS observations recorded during the earthquake were obtained from a pair of collocated stations from the existing seismic network and geodetic network, respectively. Here, the displacement solutions of the Kalman filter with the baseline error state (KFB) are compared with the GNSS displacement solutions, the United State Geological Survey (USGS) acceleration baseline error

corrected displacement solutions, and the displacement solutions of the Kalman filter with no baseline error state (KFNB).

1) The implemented KFB algorithm provides high-frequency movements and permanent (co-seismic) displacements in a real earthquake.

This experiment shows the ability of using the proposed Kalman filter to provide accurate three-dimensional displacement solutions during a real earthquake. The results show that the KFB can provide optimal displacement solutions, including the high-frequency movements during shaking and the permanent displacements after shaking, during a large earthquake compared to all the existing methods. The USGS baseline correction method provides the smooth high-frequency movements during shaking after applying the seismological baseline correction and a high-pass filter on the accelerometer measurements. However, the USGS baseline corrected solutions cannot show the 20 cm and 5 cm co-seismic displacements to the North and the vertical component after shaking. GNSS provides 1 Hz displacement solutions and shows the 20 cm and 5 cm permanent displacements along the Northing and vertical axis successfully; nevertheless, the high-frequency movements during shaking are missed due to the low sampling rate of GNSS. The KFNB can provide the smooth high-frequency movements displacement solutions when the acceleration baseline error is not changed significantly (e.g. the Easting and Up in this experiment). However, when a co-seismic displacement along the Northing occurred in the earthquake, the KFNB solutions significantly drift and are biased by the changed acceleration baseline error.

2) Existing seismic and geodetic networks of instruments can be used.

Tests have been carried out of data processing techniques on real earthquake data. A similar level of performance improvement has been achieved for real earthquakes using the GNSS observations from the existing geodetic networks and the strong motion seismometer data from the existing seismic networks. In the rapid determination of ground displacement immediately after an earthquake, the centimetre-level accuracy outputs at high sampling rate can be achieved by integrating GNSS and accelerometer based instruments using KFB compared to existing methods.

3) Instruments collocated but not combined are still useful.

The strong motion seismometer data and the GNSS observations were obtained from the existing seismic network and geodetic network, respectively. A collocated strong motion seismometer and GNSS station were selected, with the distance between both instruments being about 138 metres. The results show that by focusing on the movements of sensors, the implemented Kalman filter can still provide ground displacements even with a short distance between sensors.

4) The limitations of this experiment

The experimental results of Chapter 6 are based on one paired strong motion seismometer and GNSS receiver. The high-rate earthquake data sets are not always available in reality. Firstly, it is difficult to find collocated instruments from existing seismic and geodetic networks because both networks were initially built for different purposes. Secondly, unlike the strong motion seismometers automatically recording the earthquake events, the GNSS observations from geodetic networks are usually archived manually and separately by various associates after earthquakes. The separate data resources increase the difficulty of finding the available and desired data sets. Thirdly, most GNSS stations during the El Mayor-Cucapah Earthquake in 2010 provide GNSS observations with sampling rate of 30 seconds, and few GNSS stations provide 1 Hz or 5 Hz GNSS observations. Since the 1 Hz GNSS observation is required in the proposed Kalman filter algorithm in this study, the available GNSS observations during the El Mayor-Cucapah Earthquake are actually very limited. Thus, at the end, only one pair of strong motion seismometer and GNSS receiver is suitable and tested in this study. The available data sets indicate that the proposed Kalman filter algorithm improved the accuracy of displacement solutions and provided baseline error changes for corrections during earthquakes. For further use in real applied contexts, more data sets from different earthquakes should be tested.

7.4 Discussion

7.4.1 Limitations of the implementation in this study

1) The technical challenge of the Kalman filter tuning process

In this thesis, every experiment explores the tuning process used to find the best combination of the noise covariance matrices in the Kalman filter algorithm in order to increase the performance of the Kalman filter integration. The experimental results in this thesis all suggest the importance and the need of tuning Kalman filter algorithms. Nevertheless, there is still not an over-arching theory of the Kalman filter tuning process. The level of expertise required for the Kalman filter tuning process became a key limitation of the method in this study. The setting of the noise parameters, including system noise and measurement noise variance matrices, is still semi-empirical and only based on experiments. The results of one experiment can only provide approximate initial settings for other experiments or events. Although the tuning process is needed in all Kalman filter integrations, the additional baseline error state in the proposed three-state Kalman filter in this study has significantly decreased the influence of the tuning process compared to the existing two-state Kalman filter method. The proposed Kalman filter with the accelerometer baseline error state can still reduce the time to approach the tuning process and provide more stable displacement solutions during earthquakes.

2) No truth model available for real earthquakes

As the Kalman filter tuning process took place in every experiment in this study, a key factor to validate the performance of different combinations of noise parameters is to compare the results with a truth model. In Chapter 4, the MTS three-variable controller (TVC) was used in the UCSD large shake table experiment to provide a high-rate displacement, velocity, and acceleration truth model during the simulation. In the NPL experiment in Chapter 5, a spacer was used to give the true movements of the instruments and the platform. However, one of the facts of using real earthquake data sets is that there is no truth model as in the other experiments. In Chapter 6, the RTS smoothed results were used as the near-truth solutions during the real earthquake. Since the RTS smoothed results were actually the smoothed results from the KFB solutions, the smoother cannot provide independent solutions like the MTS truth model or the spacer. Based on the results from the experiments in Chapter 4 and Chapter 5, the RTS smoothed solutions were trusted to provide the most accurate solutions during the earthquake compared to all other methods. As the KFNB method has been applied widely for integrated instruments in the seismological field (Hammond et al. 2010; Geng, Bock, et al. 2013; Bock et al. 2011; Tu et al. 2013; Smyth & Wu 2006), the tuning process in Chapter 6 is comparing the KFNB and KFB solutions with the smoothed solutions to show the advantages of using a baseline error state in the Kalman filter algorithm during real earthquakes.

3) For earthquake magnitude determination only, the question of whether the combined instrument improves upon GPS alone if higher-rate GPS observations (> 1 Hz) are available.

Improving the mean displacement of the slipped faults during earthquakes is necessary for rapid earthquake magnitude determination in a real world context. The displacements obtained by high-rate accelerometer-based instruments in seismology are either drifting rapidly or unable to show the permanent displacements. Thus, the application of the integrated instruments can certainly improve the performance of displacement solutions during earthquakes compared to accelerometer-based sensors alone. On the other hand, the experiments in this study have shown that GPS displacement solutions can provide similar performance compared to the proposed Kalman filter integrated solutions. As described in Section 2.2, the mean displacement can currently be derived directly from GPS solutions of geodetic networks. GPS networks provide consecutive observations, which can indicate the position changes of GPS stations after earthquakes. As shown by Table 2.1 in Section 2.2, the low-frequency GPS observations (≤ 1 Hz) can still be useful for detecting large earthquakes, for example, earthquakes with $M_w > 6$. However, for earthquakes with $M_w \leq 6$, the assistance of high-rate accelerometer based instruments (≤ 100 Hz) is preferred to show the high-frequency movements of earthquakes. For example, Wright et al. (2012)

indicate the danger of using seismic networks alone and of underestimating the magnitude of a large earthquake such as the 2011 M_w 9.0 Tohoku-Oki Earthquake in Japan. In Wright et al. (2012), the Japanese national seismic network estimated the earthquake magnitude M_w 7.1 at 28 seconds and increased the magnitude to M_w 8.1 at 120 seconds. However, with the dense 1 Hz GPS networks in Japan, the magnitude of the Tohoku-Oki earthquake was estimated as M_w 7.5 at 40 seconds and rapidly upgraded to M_w 8.0 and M_w 8.8 at 60 and 90 seconds, respectively. Although GPS still underestimated the magnitude compared to the final moment magnitude M_w 9.0, the magnitude determined by the GPS network was still more accurate and valuable than that provided by the seismic network alone. This rapid detection is extremely important given that, for example, the potential of a tsunami from M_w 8.8 is much higher than M_w 8.1. Hence, for large earthquakes, the GPS networks are able to provide accurate positions for rapid earthquake magnitude determination. However, the integrated instruments with high rate outputs (100 Hz) are still more useful for earthquakes with $M_w \leq 6$ and other applications in seismology (e.g. recognising different seismic waveforms and understanding the rapid movements of faults).

4) Data accessibility for real earthquakes poses a challenge to researchers.

When using the data from existing networks, it is more difficult to obtain high-rate GPS observations than high-rate strong motion seismometer/accelerometer data. The seismic network can record data at 100~200 Hz and save events when the strong motion seismometer or accelerometer measurements cross certain thresholds. Unlike the accelerometer based instruments, the existing GPS infrastructure rarely records at rates of 1 Hz or higher. GPS receivers receive signals and output the position solutions continuously; this large amount of GPS data means large data storage and more data processing. Thus, GPS data are often saved at a 30-second sampling rate and archived manually after earthquake events occur. The low sampling rate GPS observations are useful for long-term monitoring of seismology, for example, to monitor the movements of faults and crusts. Since most seismic events happen instantly, the higher rate of GPS observation can help to understand the seismic waves more precisely and quickly. Nevertheless, the high-rate (more than 1 Hz) GPS observations during earthquakes are not easy to find and access, especially for collocated GPS receivers and strong motion seismometers. As most GPS geodetic networks and seismic networks are still managed separately by several institutions, the data resources and information are relatively sparse and limited. Thus, the data collection for real earthquakes was one of the main difficulties in this study.

Finding useful earthquake data sets for testing the proposed algorithms is not always easy in practice. It is not only hard to find collocated instruments from seismic and geodetic networks but also difficult to arrange access to data sets for real earthquakes. During this study, other real earthquake data were identified and requested, including

the 2011 M_w 6.3 Christchurch Earthquake in New Zealand, the 2011 M_w 9.0 Tohoku Earthquake in Japan, and some medium earthquakes with M_w 5.0~6.0 in Taiwan. However, as some countries do not provide open data for national seismic and geodetic networks, it can be difficult to obtain real earthquake observations. Difficulties in coordinating extremely technical data sharing agreements due to language and varying privacy concerns are found, for example, Japan and Taiwan, possibly as a result of questions of language and authorisation. Furthermore, even when earthquake data for collocated instruments was generously provided, known pathologies of the data sets might prevent them from being usable for the purposes of this work. For example, paired GPS and strong motion seismometer data sets pertaining to the 2011 M_w 6.3 Christchurch Earthquake were provided by New Zealand's national geological network, GeoNet, but unknown technical problems in the GPS observation files prevented the provided GPS data from being processed to position solutions. More experiments should be carried out to test and validate the proposed integrated algorithm in this study before it is applied in a real world context, but real earthquake data resources might become a critical impediment to further research if most of the national seismic and geodetic networks in the countries are unable to provide open data.

7.4.2 Applicability and further discussion of this study

1) A combined GNSS and strong motion seismometer instrument has been produced by a commercial company, Trimble, for seismic monitoring.

When this study began in 2010, there was not yet a complete integrated system or product in the seismological community. In December of 2014, an integrated GNSS and accelerometer system was presented during the American Geophysical Union (AGU) Fall Meeting by Trimble Navigation Limited and REF TEK, a Division of Trimble (Passmore et al. 2014; Zimakov et al. 2014). REF TEK has produced accelerometer-based systems for over 40 years in the United States, and their seismic instruments are trusted and used by the seismological community, including the Global Seismological Network (GSN) and Incorporated Research Institutions for Seismology (IRIS) (TEK REF 2015).

In their presentation at the 2014 AGU Meeting, the core method used in the application was a two-state (displacement and velocity) loosely-coupled Kalman filter algorithm. The Trimble team has developed the software, and the engineer in the exhibition mentioned that the drifting displacement remained one of the difficulties they are facing. Currently, a tightly-coupled Kalman filter integration has been investigated by REF TEK as a method to solve the drifting problem in the displacement solutions. REF TEK also presented a shake table experiment in the meeting. While other shake tables usually simulate seismic acceleration waveforms without permanent displacements after shaking, the REF TEK shake table simulates the displacement waveforms for real earthquakes and also the permanent displacements caused by the earthquakes.

The presentation has shown the current applicability of the findings of this study in the geological and seismological community. The proposed Kalman filter algorithms with the additional baseline error state in this study should solve the drifting problem in their displacement solutions. The shake table that can simulate earthquake displacement waveforms would provide an excellent environment to test and validate the proposed algorithm.

2) Dense seismic monitoring networks are not always available in all countries, especially developing countries.

At this point in history, most countries in the world have built some seismic and GPS networks for earthquake monitoring; this is especially true for places with records of frequent earthquakes. However, the density of the seismic networks is not always proportional to the amount of the past earthquake activity. In fact, the density of the seismic stations in different countries is related to not only earthquakes or seismic events in the past but to the wealth of the countries. Figure 7.1 shows the distribution of recorded earthquakes and seismic monitoring stations around the world. In Figure 7.1, the sizes and colours of circles represent the earthquake magnitudes and recentness, respectively; blue triangles represent seismic monitoring stations; magenta dots show earthquakes of all magnitudes that have occurred in the past five years. Two large earthquakes and their aftershocks are shown as several large yellow and red circles on maps (a) and (b) in Figure 7.1, including the 2015 M_w 7.8 Nepal Earthquake in the Central Asian map and the 2015 M_w 7.2 Papua New Guinea Earthquake in the Australia/New Zealand (NZ) map. In addition to these two recent large earthquakes, the magenta dots in maps (a) to (b) in Figure 7.1 highlight the fact that there was extensive seismic activity in the areas in the past five years. However, despite many more earthquakes occurring in the vicinities in maps (a) and (b), the amounts of the seismic monitoring stations (blue triangles) in maps (a) and (b) are rather sparse compared to maps (c) and (d).

The four maps in Figure 7.1 show that in most developed countries with frequent earthquakes, the densities of the seismic monitoring stations are high; for example, Japan and Taiwan in map (a), the west coast of the United States in map (c), and Greece in map (d). However, Figure 7.1 also shows that the densities of seismic monitoring stations are much lower in seismically active developing compared to similarly seismically active developed countries; compare, for example, Nepal and Iran in map (a) and Papua New Guinea in map (b). Because building and maintaining seismic networks is expensive, some developing countries cannot afford to build high-density networks. Hence, poorer countries can only afford sparse networks. As mentioned previously, even with a dense seismic network, earthquake magnitudes can be underestimated significantly, which also means underestimating the damage caused by earthquakes. The sparse networks provide insufficient information for monitoring earthquakes, so

that their aftershocks could be more fatal, especially in the case of large earthquakes ($M_w \geq 7.0$). Therefore, in order to provide sufficient seismic information during earthquakes in poorer countries, one suggestion is to replace the sparse networks with the combined instruments to provide sufficient seismic and geodetic information (e.g. rapidly accurate velocities and displacements during and after earthquakes) and determine the earthquake magnitudes quickly, as the combined instruments are more flexible in different applications compared to GPS or seismic network alone.

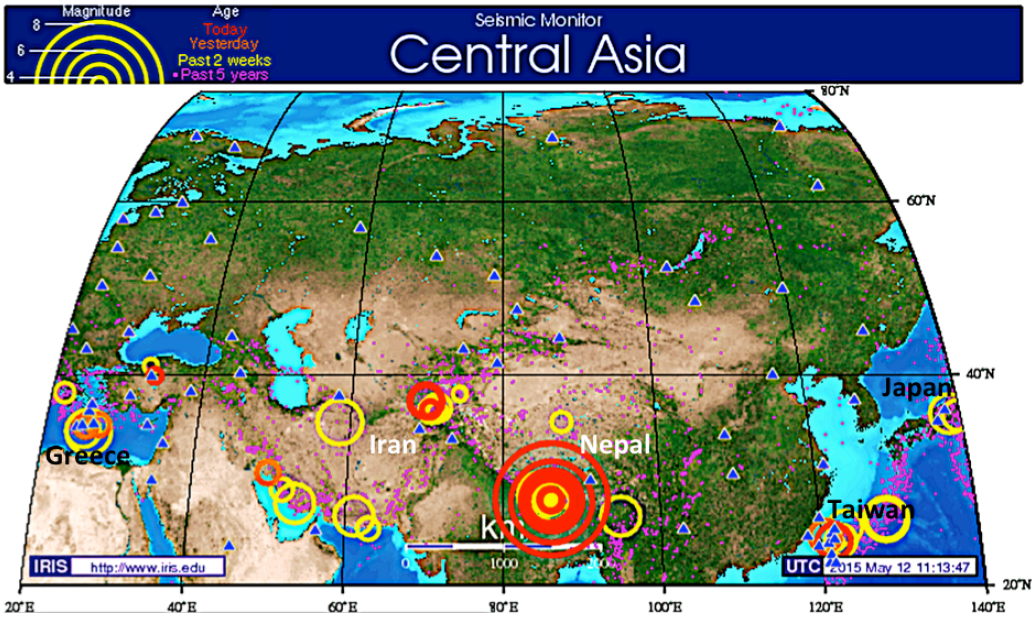

(a)

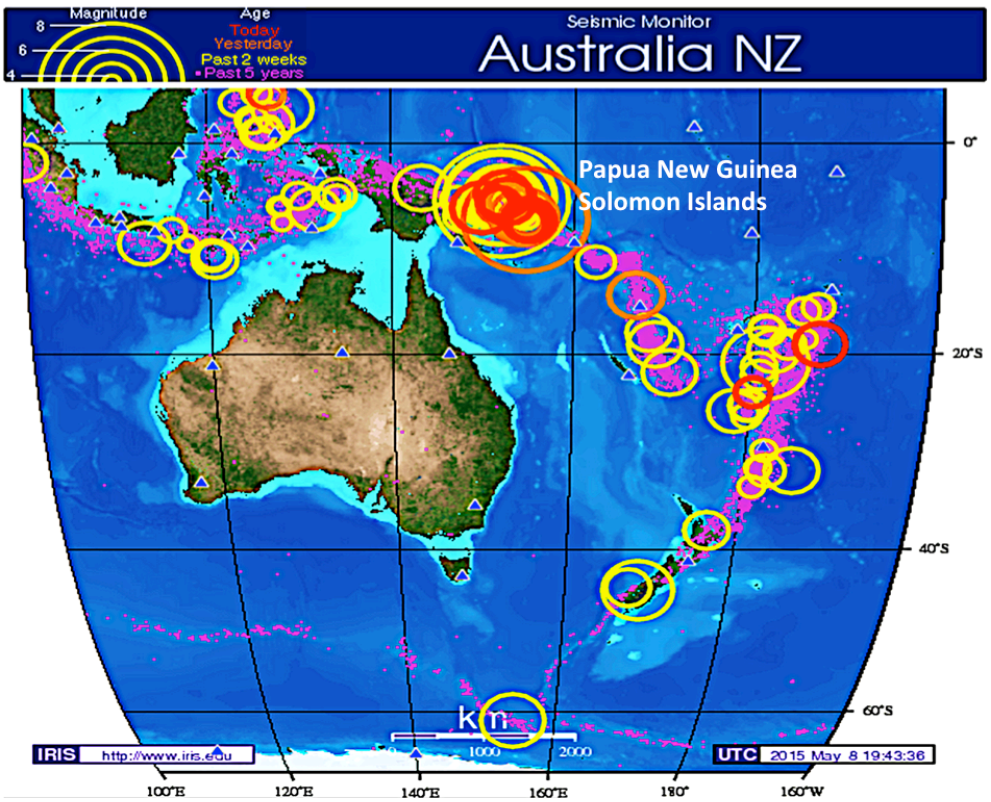

(b)

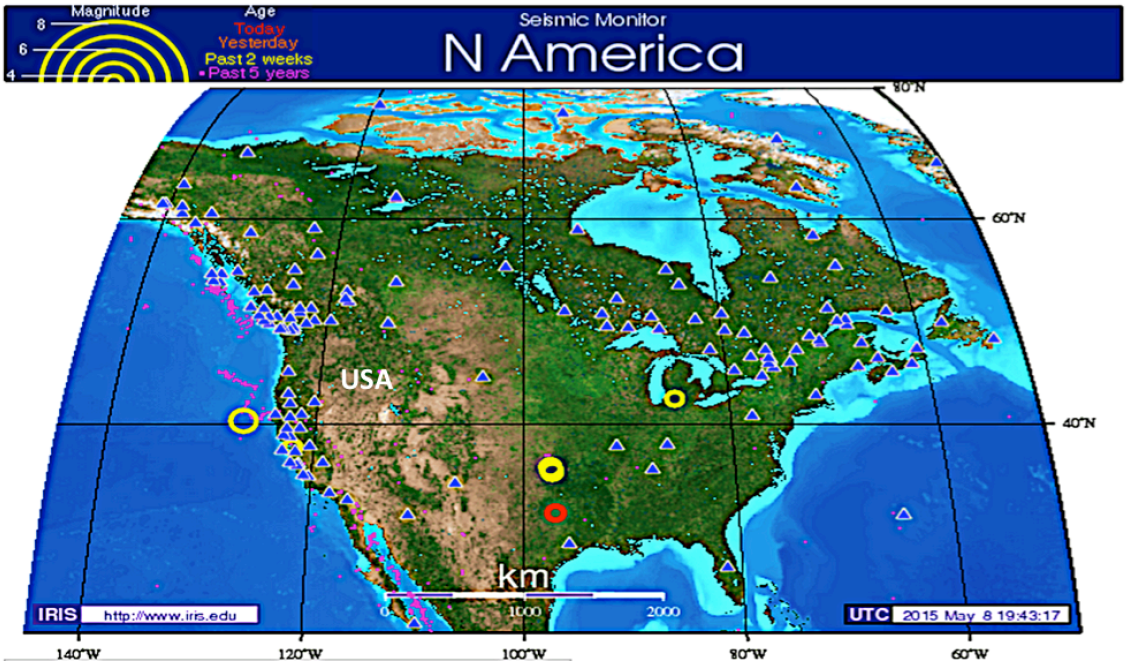

(c)

(d)

Figure 7.1: Maps of world earthquakes from the IRIS website, accessed in May 2015. The sizes and colours of circles represent the earthquake magnitudes and recentness, respectively. The blue triangles represent seismic monitoring stations. The magenta dots show all of the earthquakes that have occurred in the past five years. (http://ds.iris.edu/seismon/)

7.5 Research Contributions

During this study, the following original work was conducted:

- A Kalman filter algorithm for GNSS/accelerometer-based instruments has been proposed and improved compared to the existing methods. In existing Kalman filter integrations, accelerometer baseline errors usually cause rapid linear and quadratic drifts in the velocity and displacement solutions, respectively. The proposed Kalman filter in this study estimates and corrects the accelerometer baseline errors in the algorithm. Combining the Kalman filter algorithm with the baseline error state has reduced the impact of the acceleration bias from the accelerometer-based instruments. Furthermore, the proposed Kalman filter algorithm reduces the rapid sawtooth-like effects in the displacements and provides high-rate accurate displacement solutions during and after earthquakes for earthquake magnitude determination.
- Three experiments have been implemented in this study: the UCSD large outdoor shake table experiment with a high-rate displacement truth model, the NPL rooftop experiment with a moveable platform to move several small displacements, and a real earthquake, 2010 El Mayor Cucapah Earthquake. Each experiment utilised recordings of one pair of GNSS and strong motion seismometer from the existing geodetic and seismic networks, respectively. The results and performance analyses of the proposed Kalman filter algorithm in these three experiments have been presented in Chapter 4, Chapter 5, and Chapter 6, individually.
- The development, demonstration, testing, and analysis of the proposed Kalman filter have been implemented to address the limitations of the current existing methods and also the advantages of using the proposed Kalman filter with the additional accelerometer baseline error state.
- A substantial software package has been developed to implement the proposed algorithm and output the high-rate displacement solutions. All of the data processes in every experiment, including data collection, file reading, algorithm calculations, Kalman filter tuning process, and data analysis, were conducted within this software package.

7.6 Further Work

Some ideas for further developments and validations related to this study have been addressed as following:

- An adaptive Kalman filter that can change the measurement noise matrix ($\boldsymbol{R}$) and system noise matrix ($\boldsymbol{Q}$) could be used to improve the performance of the

proposed Kalman filter algorithm. Given that the noise covariance and uncertainties of both the GNSS and accelerometer-based instruments might behave differently before, during, and after earthquakes, the current fixed noise covariance parameters used in Kalman filter algorithms represent a limitation of current practice. Hence, an adaptive Kalman filter algorithm can be implemented and validated through further experiments and real earthquakes.

- As there is only one pair of collocated GNSS and strong motion seismometer in this study, it would be preferable to obtain more real earthquake data sets with collocated GNSS and accelerometer-based instruments from existing networks for the purpose of further testing and validation. Earthquake data sets with diverse magnitudes are also required to explore the potential for the proposed Kalman filter algorithm to be used in real earthquakes.
- Controlled shake table experiments that simulate real earthquake displacement waveforms and are observed by a combined GNSS and accelerometer system, such as those of Trimble REF TEK, are ideal to test and validate the performance of the implemented algorithm in this study. The three-state (displacement, velocity, and accelerometer baseline error) Kalman filter algorithm that implemented in this study is believed to improve the performance compared to the two-state (displacement and velocity) algorithm that is currently used in the combined instrument.
- Further study can explore the optimal density of the combined instruments for rapid earthquake magnitude determination. For example, researchers might determine the maximum distance between combined instruments, so that when building sparse networks in the developing countries, costs can be reduced while the network retains the ability to provide sufficient seismic and geodetic information during earthquakes.
- It is also valuable to investigate the use of the algorithm in conjunction with lower-cost sensors, such as low-cost GNSS receivers and accelerometers. Since current seismic networks are expensive, a further object of this research is reducing the cost of instruments and installation while keeping the same accuracy of the solutions. If the similar performance can be achieved for less cost, it would be helpful for poorer countries to build substantial geodetic and seismic networks or to upgrade the existing monitoring networks.

7.7 Research Overview

Earthquake monitoring and early warning systems have been an active research area for many years, involving rapid earthquake co-seismic displacements and magnitude determinations. The limitations of the sensors restricted the developments by using

either GNSS/GPS networks or seismic networks alone. This study has developed a method to integrate the observations of GNSS/GPS and accelerometer-based sensors and to combine the seismological baseline correction into the implemented algorithm. The developed method has improved the performance of co-seismic displacements and earthquake movements compared to the existing methods. Further related researches should focus on the real-time earthquake magnitude determination and tsunami early warning system due to its implications for protecting human lives and properties. Finally, it is hoped that such research will be investigated and developed in near future to ensure the safety of humans in earthquakes.

Appendix A: More Tuning Results in the NPL Experiment

A.1 Fixed q_b and R with varied q_a

The velocity error results of KFB, KFNB, and SKF of varied $\boldsymbol{q_a}$ with respect to the zero-velocity truth discussed in Section 5.4.1 are displayed in the figures below.

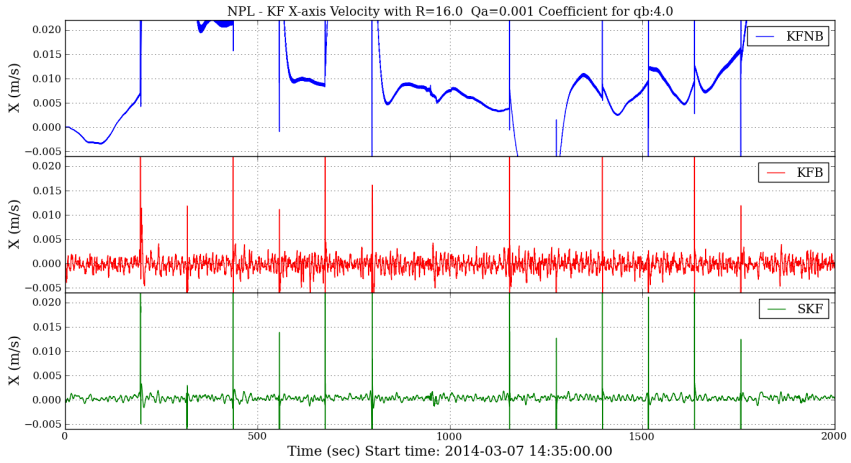

Figure A.1: KFB, KFNB, and SKF tuning: velocity error results with respect to the zero-velocity truth by setting $\boldsymbol{R}$ =16.0 (m^2), $\boldsymbol{q_a}$=0.001 (m^2/s^3), and C_{q^b} = 4.0

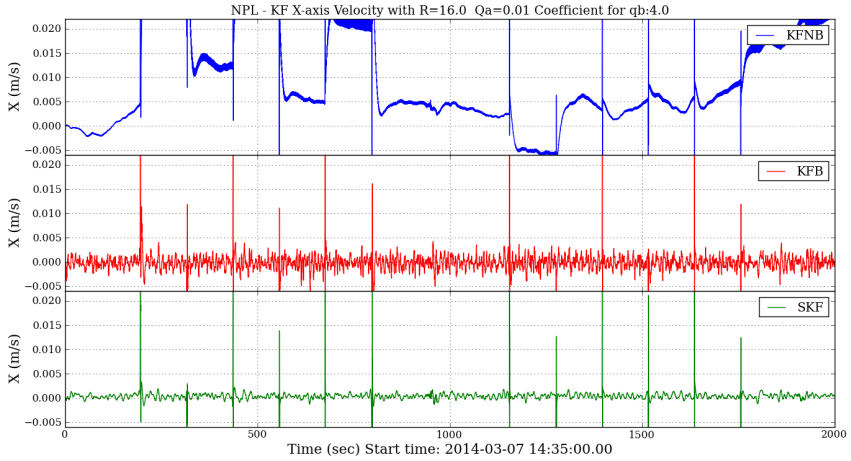

Figure A.2: KFB, KFNB, and SKF tuning: velocity error results with respect to the zero-velocity truth by setting $\boldsymbol{R}$ =16.0 (m^2), $\boldsymbol{q_a}$=0.01 (m^2/s^3), and C_{q^b} = 4.0

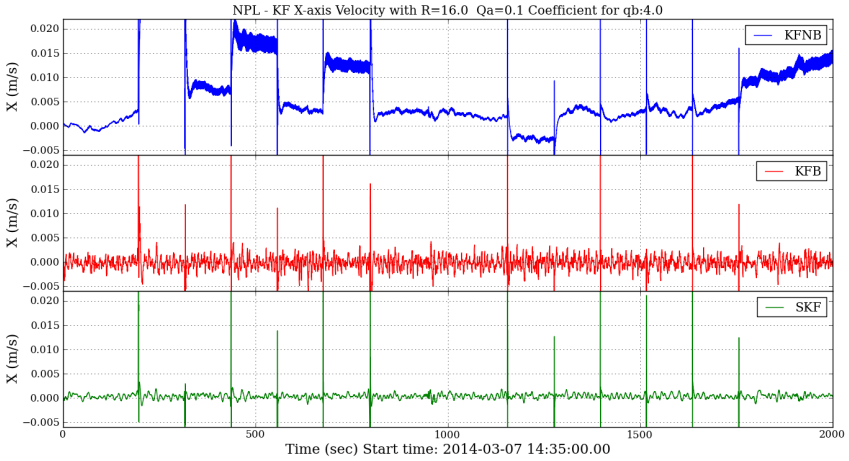

Figure A.3: KFB, KFNB, and SKF tuning: velocity error results with respect to the zero-velocity truth by setting $\boldsymbol{R}$ =16.0 (m^2), $\boldsymbol{q_a}$=0.1 (m^2/s^3), and C_{q_b} = 4.0

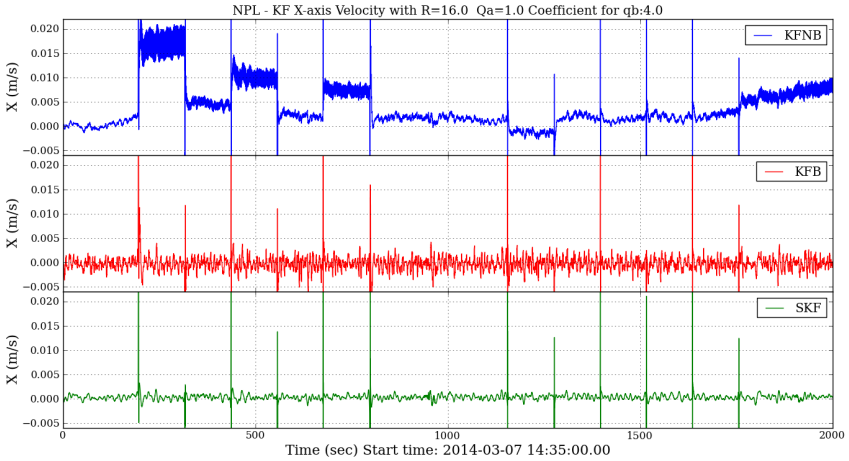

Figure A.4: KFB, KFNB, and SKF tuning: velocity error results with respect to the zero-velocity truth by setting $\boldsymbol{R}$ =16.0 (m^2), $\boldsymbol{q_a}$=1.0 (m^2/s^3), and C_{q_b} = 4.0

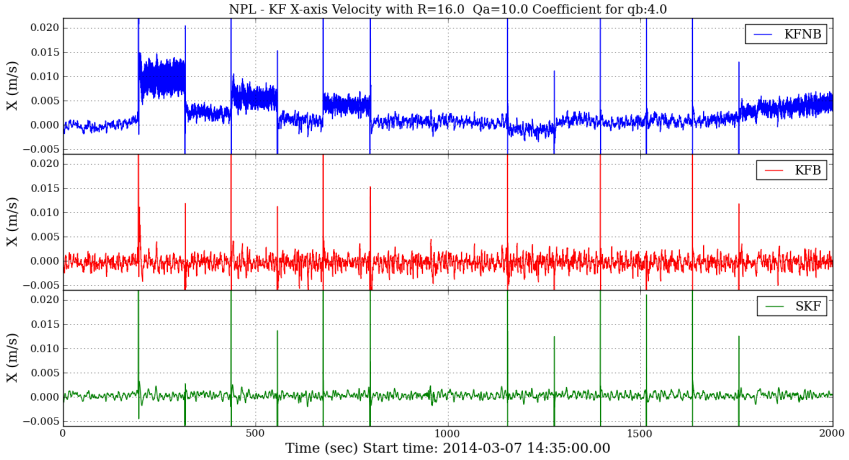

Figure A.5: KFB, KFNB, and SKF tuning: velocity error results with respect to the zero-velocity truth by setting $\boldsymbol{R}$ =16.0 (m^2), $\boldsymbol{q_a}$=10.0 (m^2/s^3), and C_{q_b} = 4.0

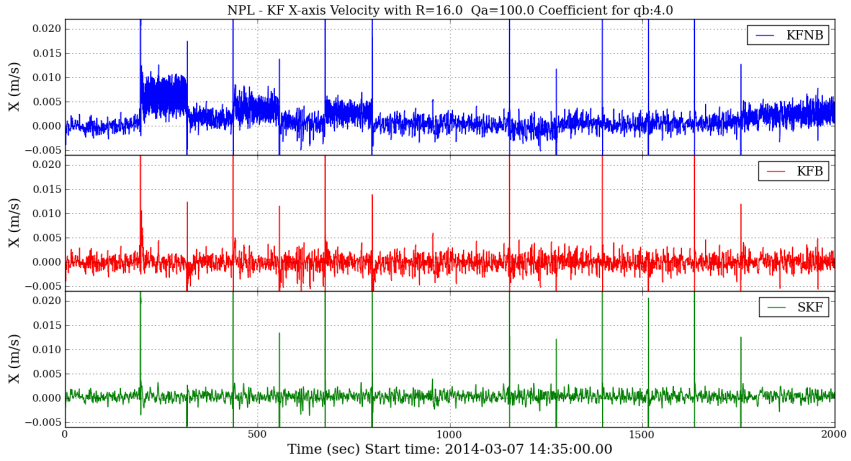

Figure A.6: KFB, KFNB, and SKF tuning: velocity error results with respect to the zero-velocity truth by setting $\boldsymbol{R}$ =16.0 (m^2), $\boldsymbol{q_a}$=100.0 (m^2/s^3), and C_{q^b} = 4.0

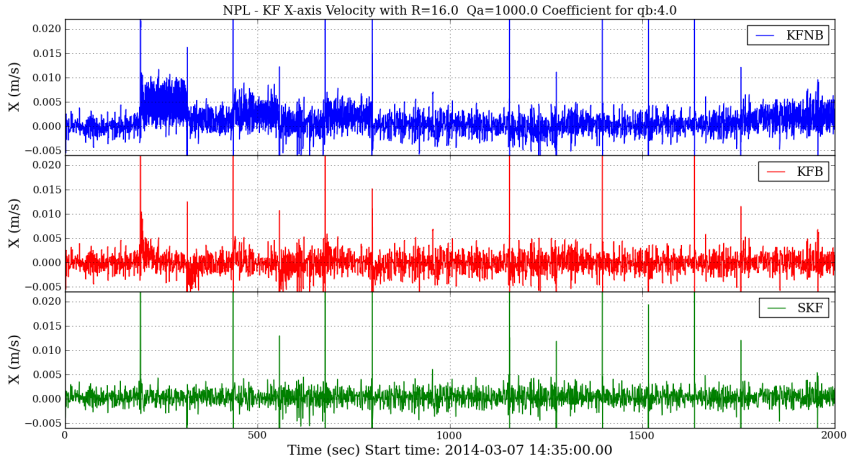

Figure A.7: KFB, KFNB, and SKF tuning: velocity error results with respect to the zero-velocity truth by setting $\boldsymbol{R}$ =16.0 (m^2), $\boldsymbol{q_a}$=1000.0 (m^2/s^3), and C_{q^b} = 4.0

A.2 Fixed q_a and q_b with varied R

The accelerometer outputs and Kalman filtered results related to tuning $\boldsymbol{R}$ in Section 5.4.2 are plotted and shown in Figures A.8~A.15.

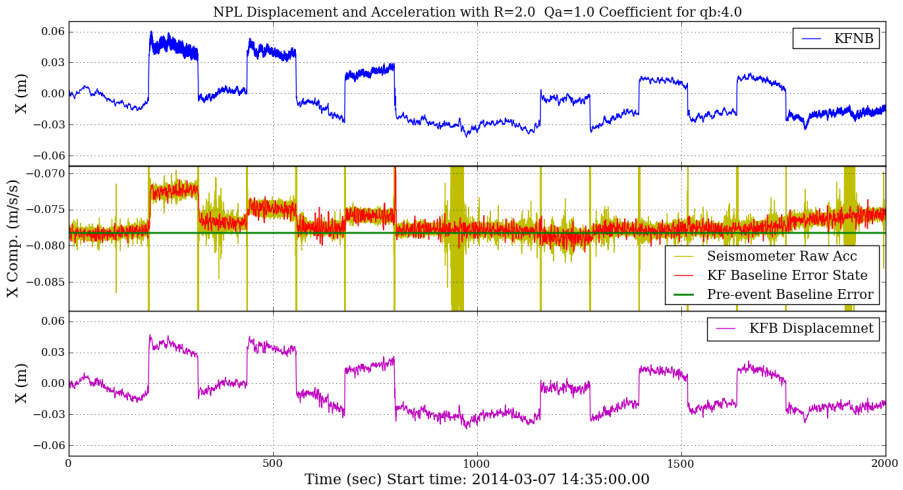

Figure A.8: Tuning $\boldsymbol{R}$: KFNB and KFB displacement and corresponding acceleration results with $\boldsymbol{R}$ =2.0 (m^2), $\boldsymbol{q_a}$=1.0 (m^2/s^3), and C_{q_b} = 4.0

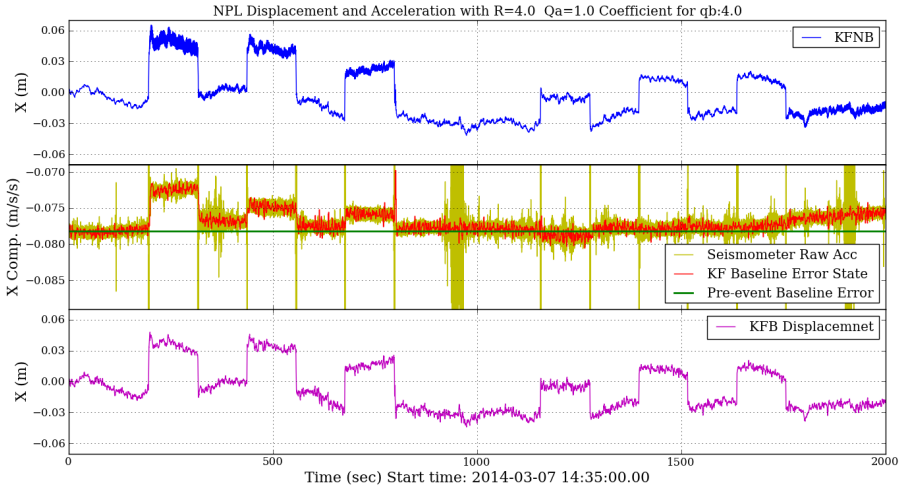

Figure A.9: Tuning $\boldsymbol{R}$: KFNB and KFB displacement and corresponding acceleration results with $\boldsymbol{R}$ =4.0 (m^2), $\boldsymbol{q_a}$=1.0 (m^2/s^3), and C_{q_b} = 4.0

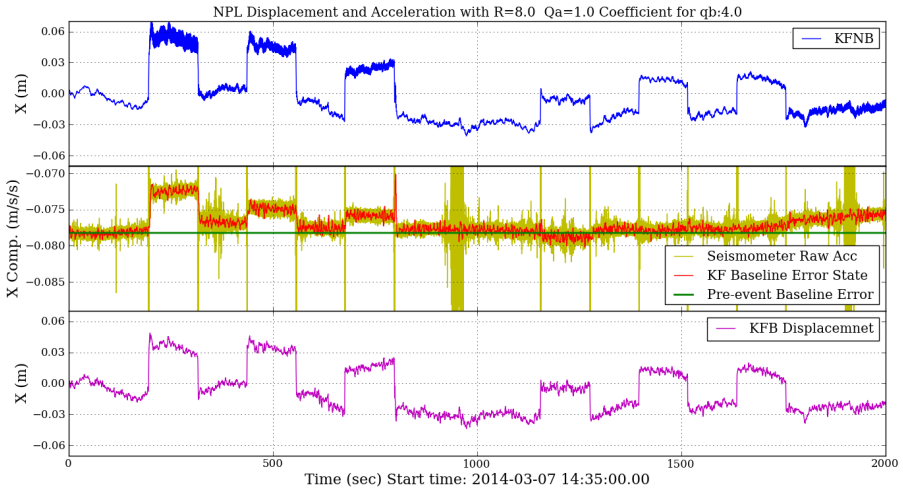

Figure A.10: Tuning $\boldsymbol{R}$: KFNB and KFB displacement and corresponding acceleration results with $\boldsymbol{R}$ =8.0 (m^2), $\boldsymbol{q_a}$=1.0 (m^2/s^3), and C_{q_b} = 4.0

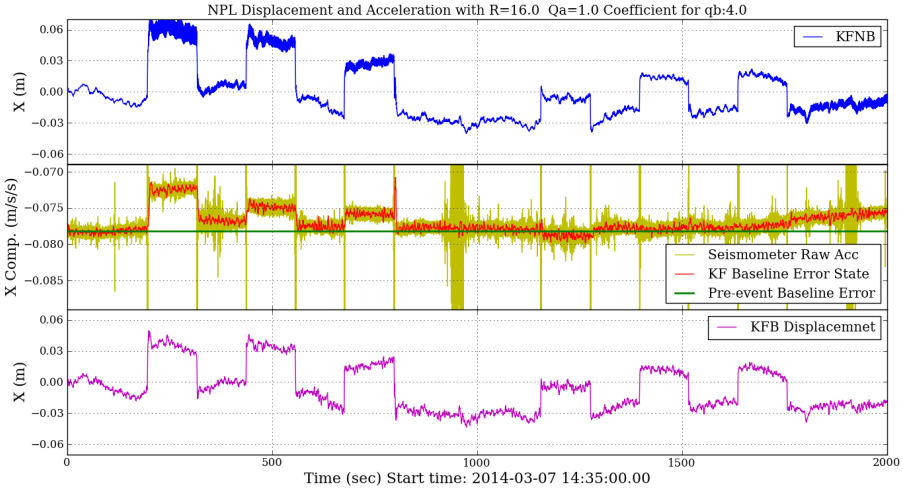

Figure A.11: Tuning $\boldsymbol{R}$: KFNB and KFB displacement and corresponding acceleration results with $\boldsymbol{R}$ =16.0 (m^2), $\boldsymbol{q_a}$=1.0 (m^2/s^3), and C_{q_b} = 4.0

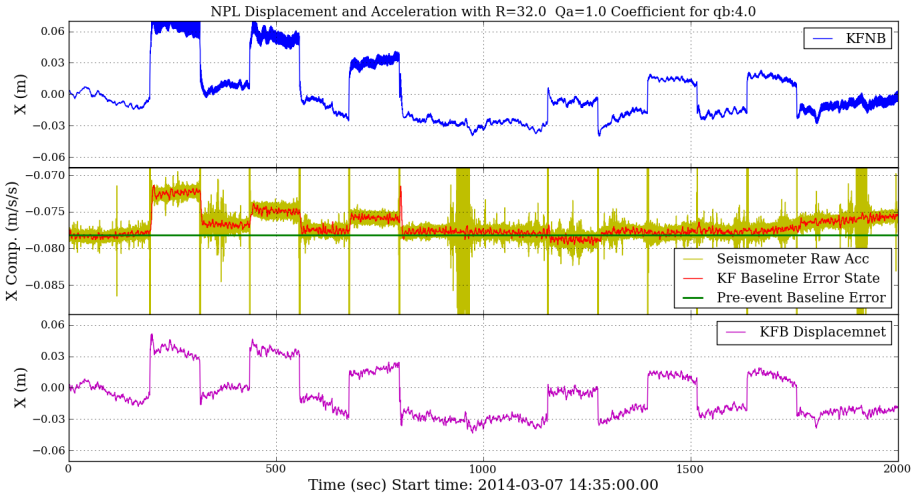

Figure A.12: Tuning $\boldsymbol{R}$: KFNB and KFB displacement and corresponding acceleration results with $\boldsymbol{R}$ =32.0 (m^2), $\boldsymbol{q_a}$=1.0 (m^2/s^3), and C_{q_b} = 4.0

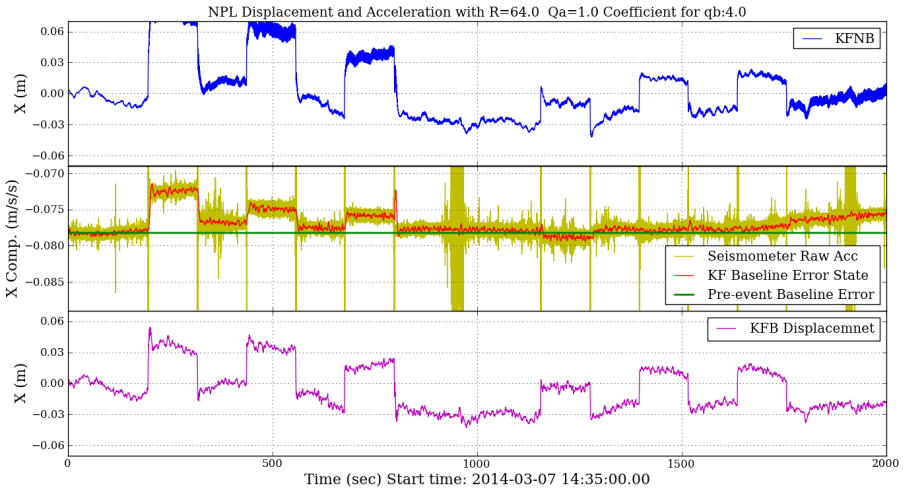

Figure A.13: Tuning $\boldsymbol{R}$: KFNB and KFB displacement and corresponding acceleration results with $\boldsymbol{R}$ =64.0 (m^2), $\boldsymbol{q_a}$=1.0 (m^2/s^3), and C_{q_b} = 4.0

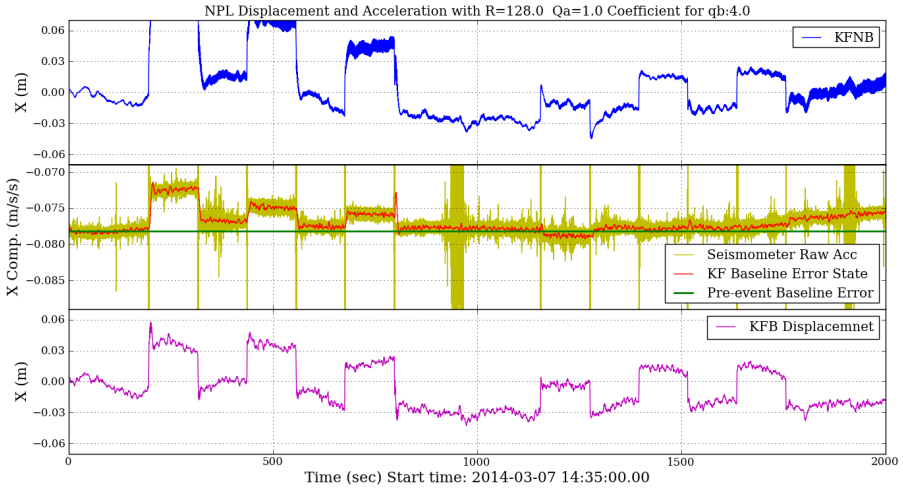

Figure A.14: Tuning $\boldsymbol{R}$: KFNB and KFB displacement and corresponding acceleration results with $\boldsymbol{R}$ =128.0 (m^2), $\boldsymbol{q_a}$=1.0 (m^2/s^3), and C_{q_b} = 4.0

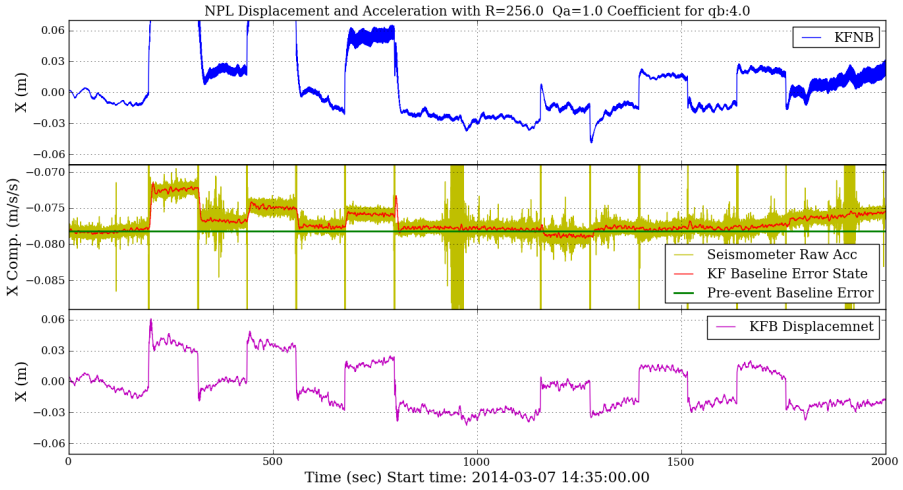

Figure A.15: Tuning $\boldsymbol{R}$: KFNB and KFB displacement and corresponding acceleration results with $\boldsymbol{R}$ =2.0 (m^2), $\boldsymbol{q_a}$=1.0 (m^2/s^3), and C_{q_b} = 4.0

A.3 Fixed R and q_b with varied q_a

The velocity error statistical results of KFB, KFNB, and SKF related to the $\boldsymbol{q_b}$ tuning process in Section 5.4.3 are plotted as figures below.

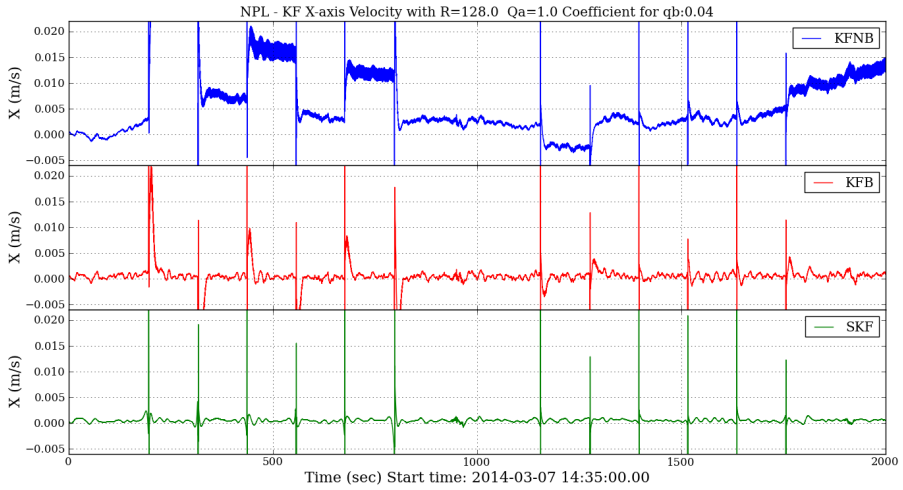

Figure A.16: KFB, KFNB, and SKF tuning: velocity error results with respect to the zero-velocity truth with $\boldsymbol{R}$ =128.0 (m^2), $\boldsymbol{q_a}$=1.0 (m^2/s^3), and C_{q_b} = 0.04

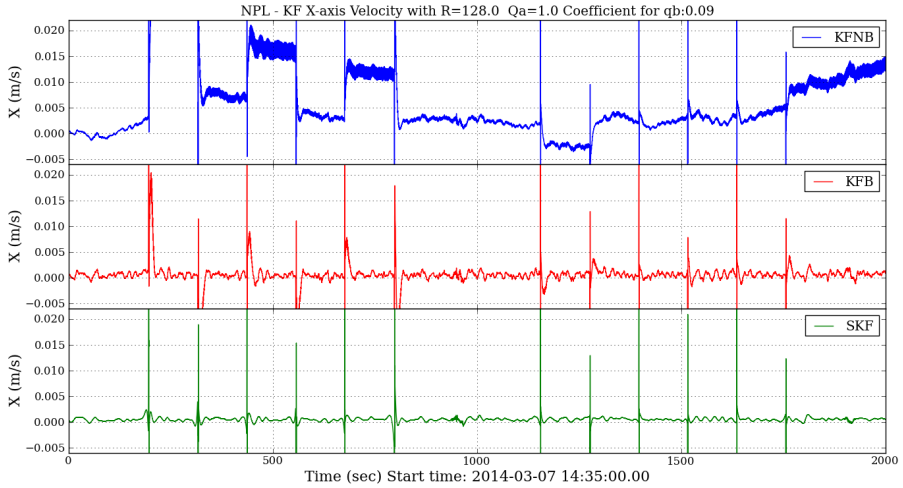

Figure A.17: KFB, KFNB, and SKF tuning: velocity error results with respect to the zero-velocity truth with $\boldsymbol{R}$ =128.0 (m^2), $\boldsymbol{q_a}$=1.0 (m^2/s^3), and C_{q_b} = 0.09

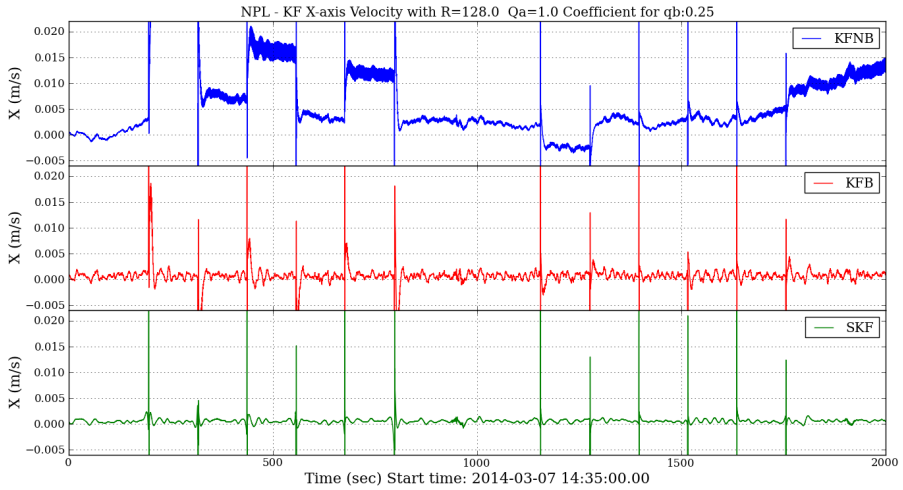

Figure A.18: KFB, KFNB, and SKF tuning: velocity error results with respect to the zero-velocity truth with $\boldsymbol{R}$ =128.0 (m^2), $\boldsymbol{q_a}$=1.0 (m^2/s^3), and C_{q_b} = 0.25

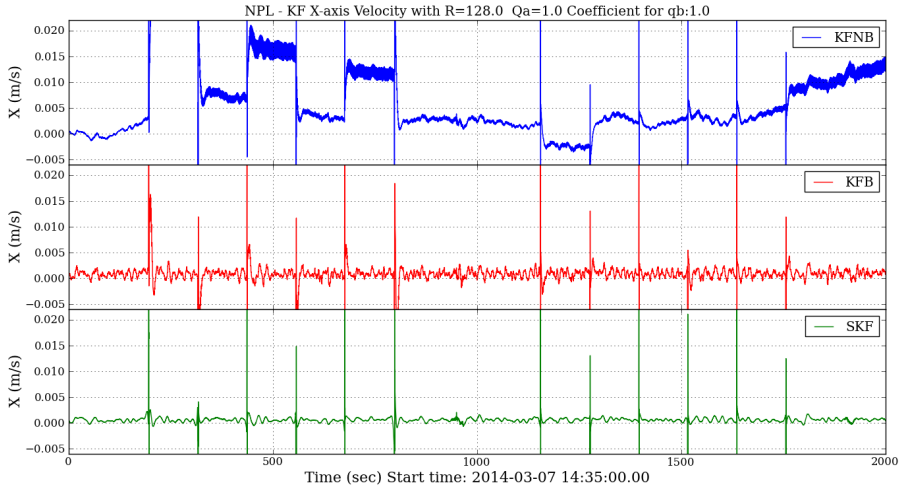

Figure A.19: KFB, KFNB, and SKF tuning: velocity error results with respect to the zero-velocity truth with $\boldsymbol{R}$ =128.0 (m^2), $\boldsymbol{q_a}$=1.0 (m^2/s^3), and C_{q_b} = 1.0

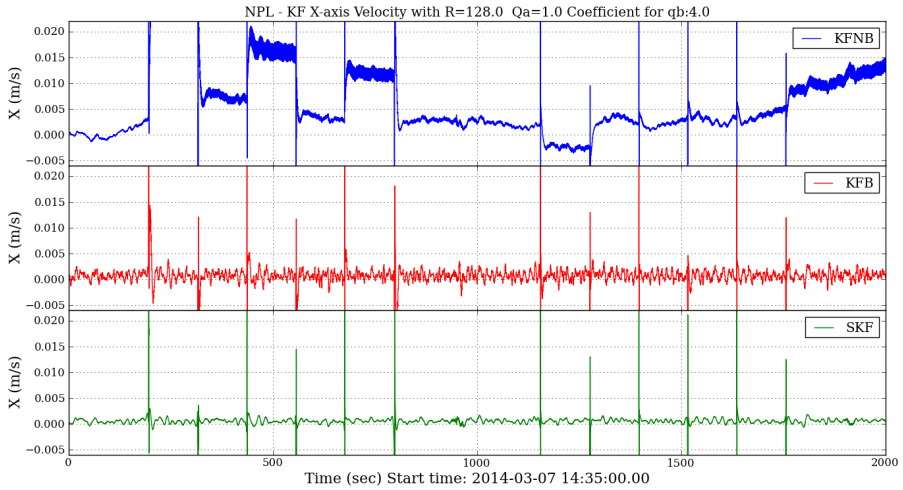

Figure A.20: KFB, KFNB, and SKF tuning: velocity error results with respect to the zero-velocity truth with $\boldsymbol{R}$ =128.0 (m^2), $\boldsymbol{q_a}$=1.0 (m^2/s^3), and C_{q_b} = 4.0

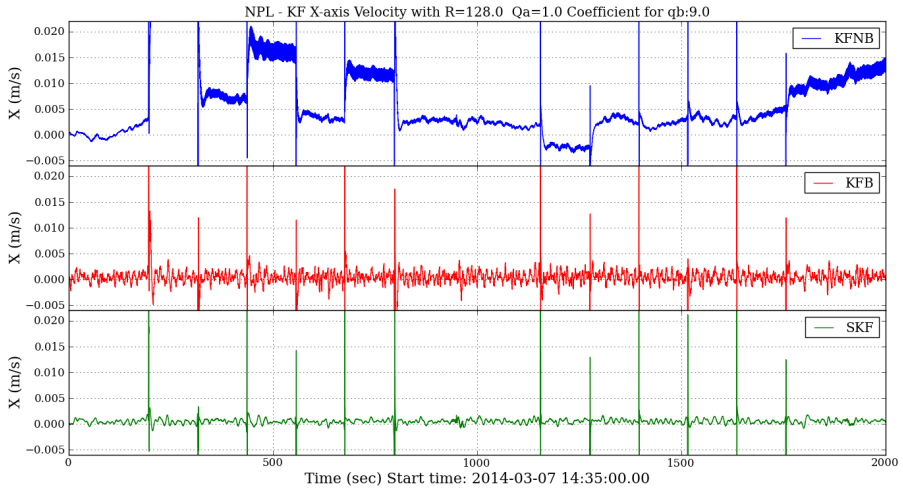

Figure A.21: KFB, KFNB, and SKF tuning: velocity error results with respect to the zero-velocity truth with $\boldsymbol{R}$ =128.0 (m^2), $\boldsymbol{q_a}$=1.0 (m^2/s^3), and C_{q_b} = 9.0

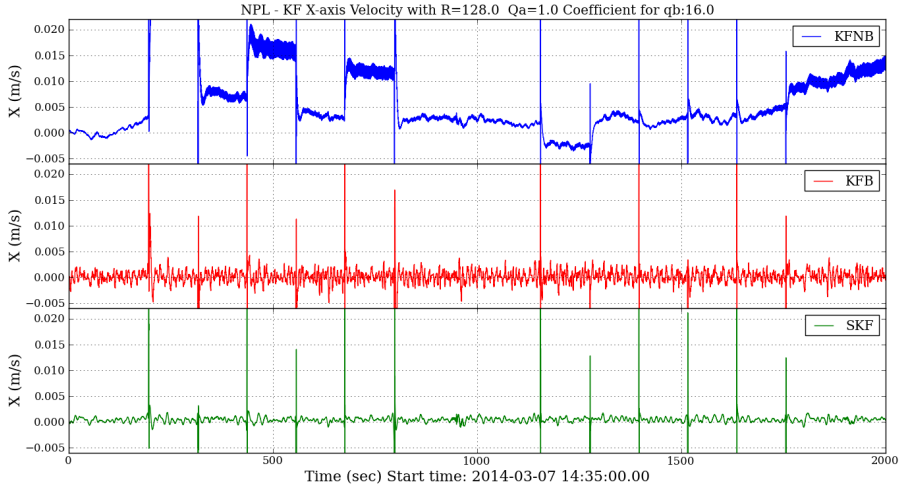

Figure A.22: KFB, KFNB, and SKF tuning: velocity error results with respect to the zero-velocity truth with $\boldsymbol{R}$ =128.0 (m^2), $\boldsymbol{q_a}$=1.0 (m^2/s^3), and C_{q_b} = 16.0

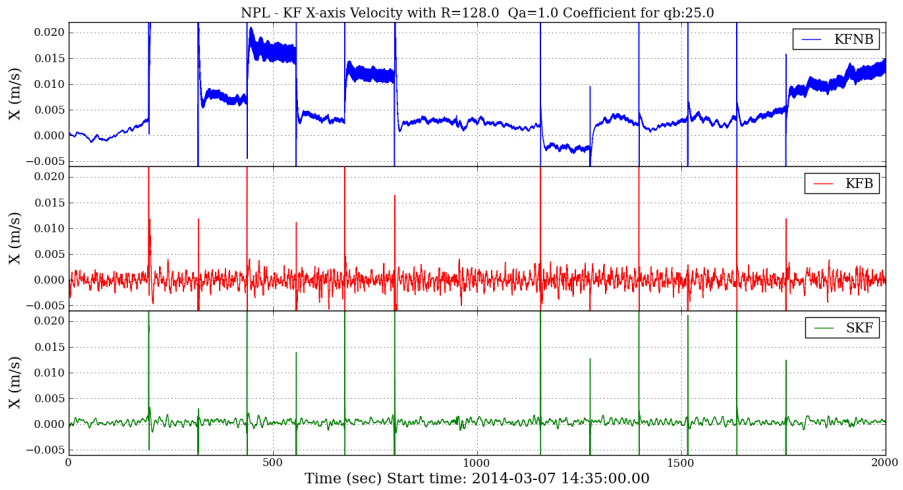

Figure A.23: KFB, KFNB, and SKF tuning: velocity error results with respect to the zero-velocity truth with $\boldsymbol{R}$ =128.0 (m^2), $\boldsymbol{q_a}$=1.0 (m^2/s^3), and C_{q_b} = 25.0

Appendix B: More Tuning Results Using Real Earthquake Data

B.1 Fixed R and q_a with varied q_b

The displacement error results of the KFNB and KFB in the Easting with respect to the SKF, the pre-event accelerometer baseline error and the KFB baseline error state, and Easting displacement results of all methods with varied $\boldsymbol{q_b}$ related to the discussion in Section 6.4.3 are displayed in the figures below.

B.1.1 The Easting with a near-zero co-seismic displacement

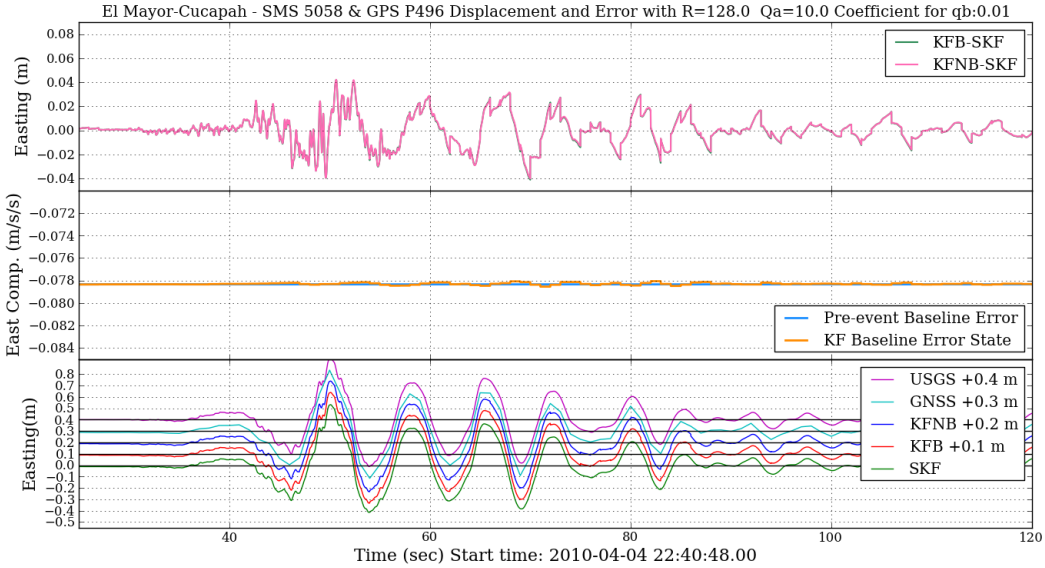

Figure B.1: The displacement error results of the KFNB and KFB in the Easting with respect to the SKF, the pre-event accelerometer baseline error and the KFB baseline error state, and Easting displacement results of all methods by setting $\boldsymbol{R}$ =128 (m^2), $\boldsymbol{q_a}$ = 10 (m^2/s^3), and C_{q_b} = 0.01.

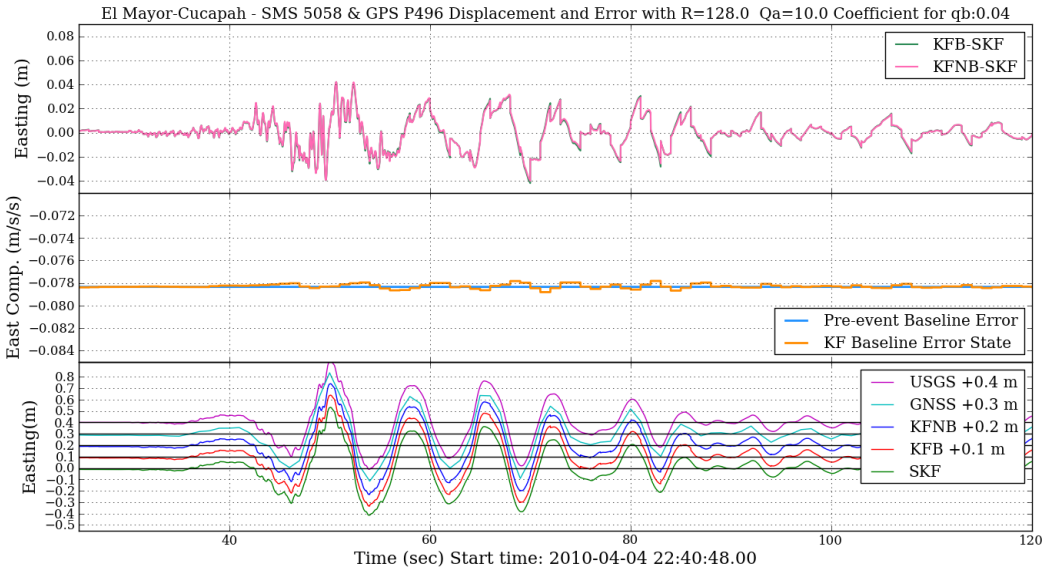

Figure B.2: The displacement error results of the KFNB and KFB in the Easting with respect to the SKF, the pre-event accelerometer baseline error and the KFB baseline error state, and Easting displacement results of all methods by setting $\boldsymbol{R}$ =128 (m^2), $\boldsymbol{q_a}$ = 10 (m^2/s^3), and C_{q_b} = 0.04.

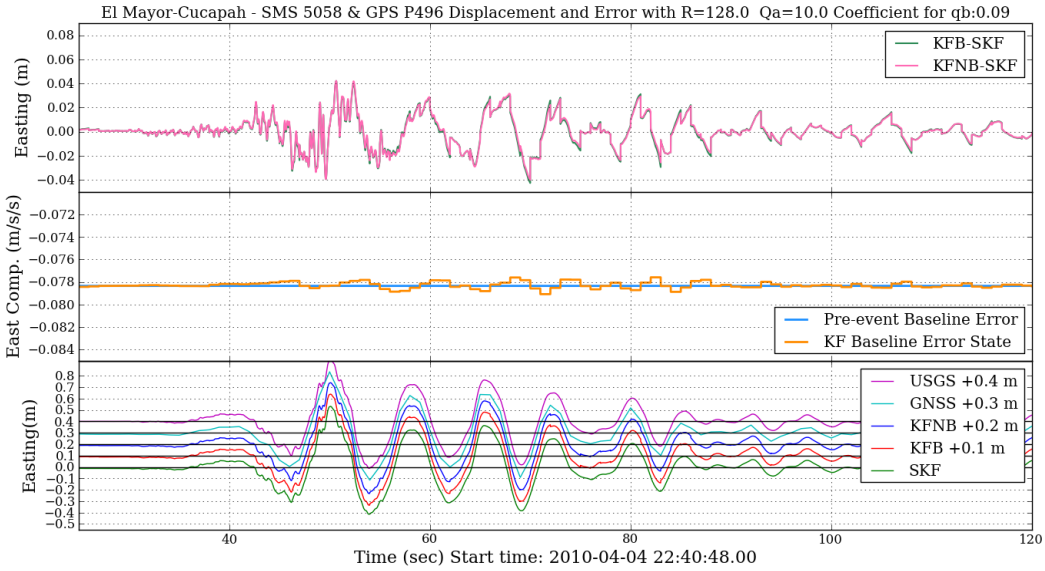

Figure B.3: The displacement error results of the KFNB and KFB in the Easting with respect to the SKF, the pre-event accelerometer baseline error and the KFB baseline error state, and Easting displacement results of all methods by setting $\boldsymbol{R}$ =128 (m^2), $\boldsymbol{q_a}$ = 10 (m^2/s^3), and C_{q_b} = 0.09.

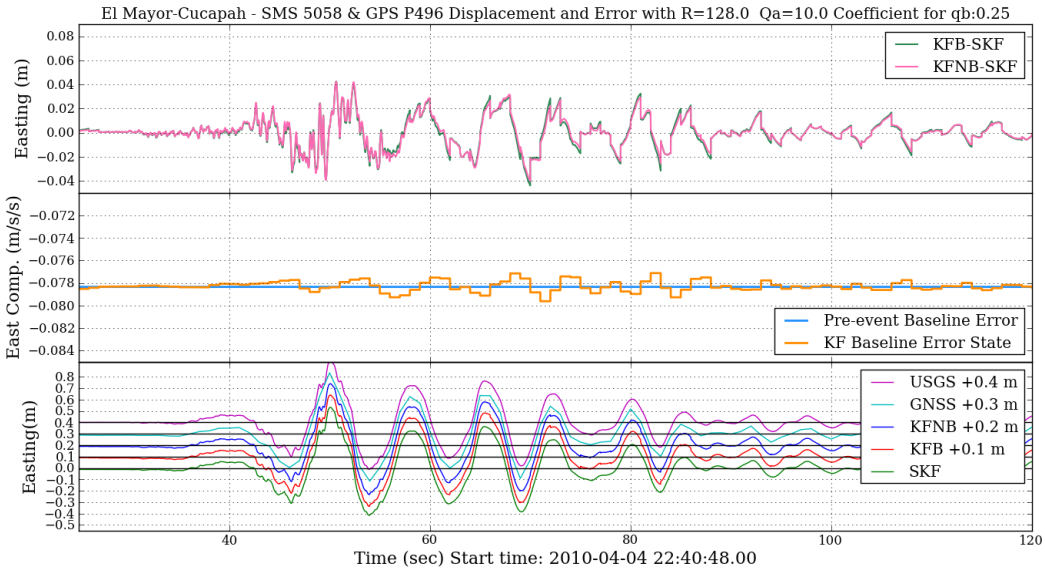

Figure B.4: The displacement error results of the KFNB and KFB in the Easting with respect to the SKF, the pre-event accelerometer baseline error and the KFB baseline error state, and Easting displacement results of all methods by setting $\boldsymbol{R}$ =128 (m^2), $\boldsymbol{q_a}$ = 10 (m^2/s^3), and C_{q_b} = 0.25.

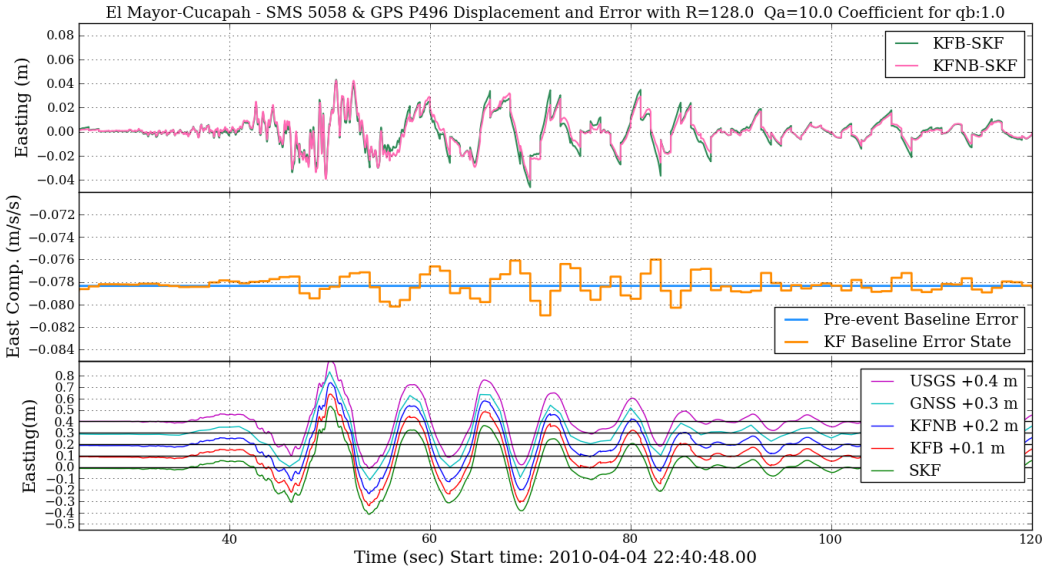

Figure B.5: The displacement error results of the KFNB and KFB in the Easting with respect to the SKF, the pre-event accelerometer baseline error and the KFB baseline error state, and Easting displacement results of all methods by setting $\boldsymbol{R}$ =128 (m^2), $\boldsymbol{q_a}$ = 10 (m^2/s^3), and C_{q_b} = 1.0.

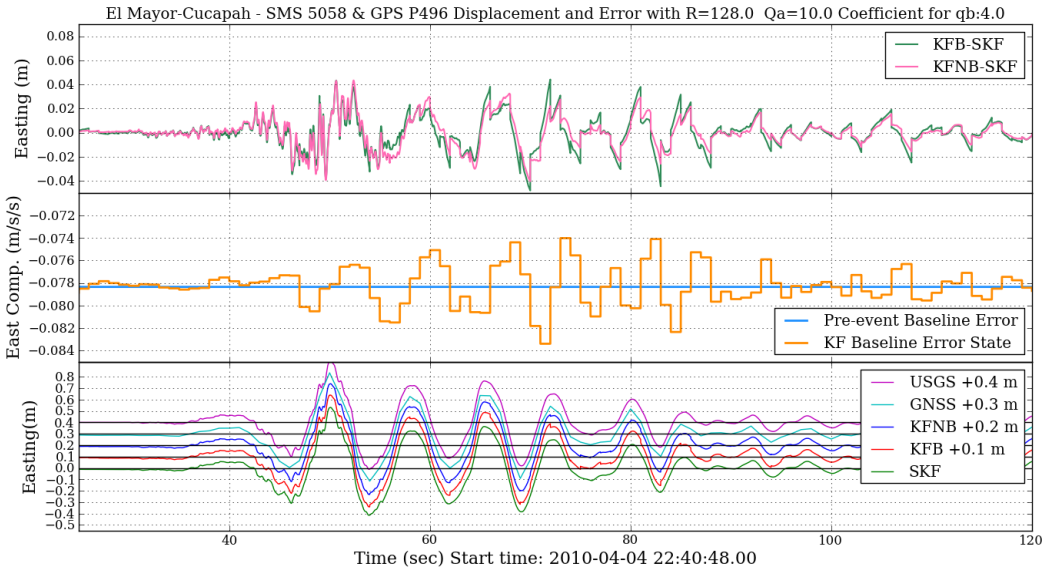

Figure B.6: The displacement error results of the KFNB and KFB in the Easting with respect to the SKF, the pre-event accelerometer baseline error and the KFB baseline error state, and Easting displacement results of all methods by setting $\boldsymbol{R}$ =128 (m^2), $\boldsymbol{q_a}$ = 10 (m^2/s^3), and C_{q_b} = 4.0.

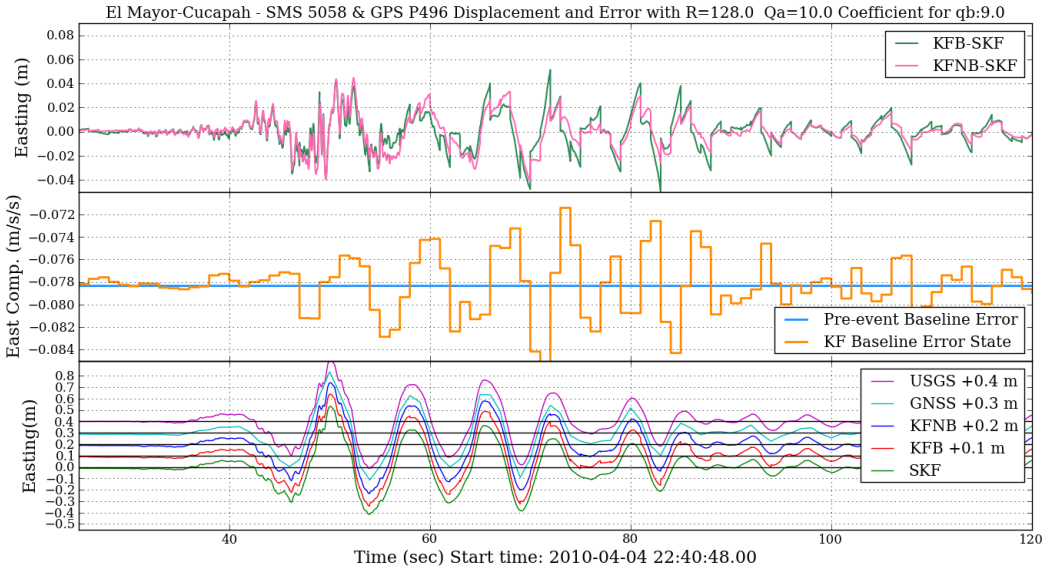

Figure B.7: The displacement error results of the KFNB and KFB in the Easting with respect to the SKF, the pre-event accelerometer baseline error and the KFB baseline error state, and Easting displacement results of all methods by setting $\boldsymbol{R}$ =128 (m^2), $\boldsymbol{q_a}$ = 10 (m^2/s^3), and C_{q_b} = 9.0.

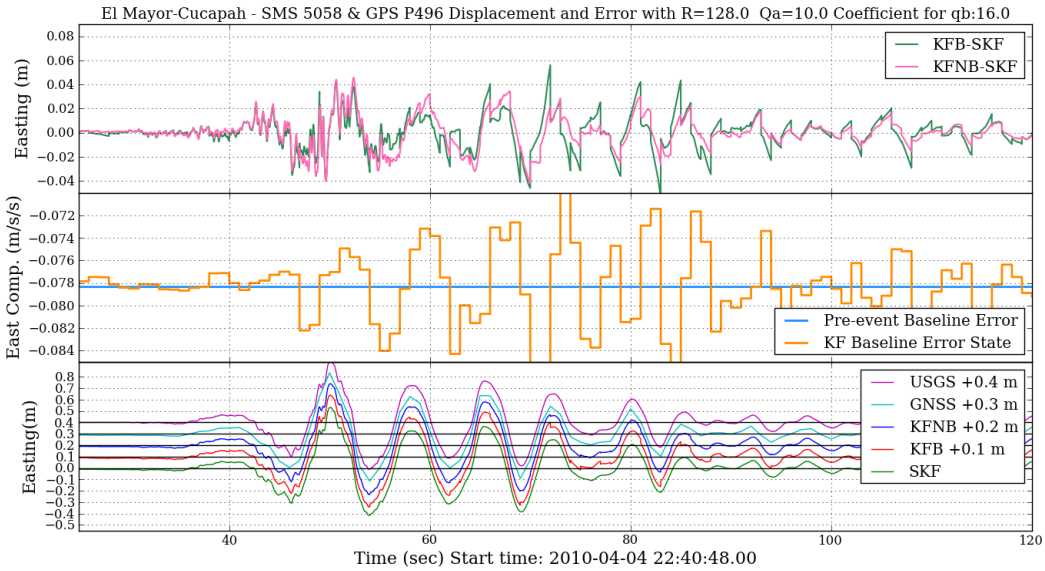

Figure B.8: The displacement error results of the KFNB and KFB in the Easting with respect to the SKF, the pre-event accelerometer baseline error and the KFB baseline error state, and Easting displacement results of all methods by setting $\boldsymbol{R}$ =128 (m^2), $\boldsymbol{q_a}$ = 10 (m^2/s^3), and C_{q_b} = 16.0.

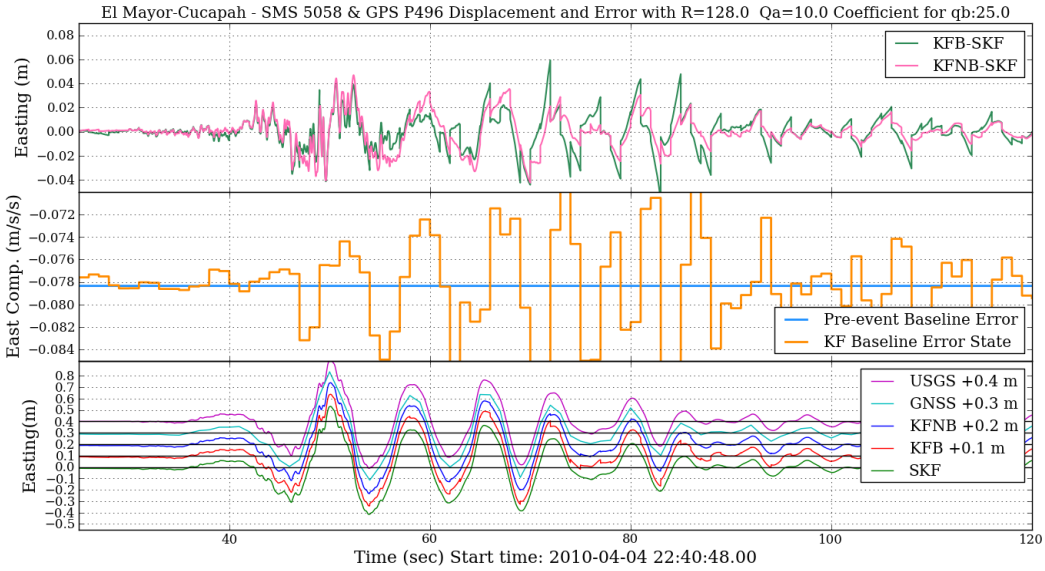

Figure B.9: The displacement error results of the KFNB and KFB in the Easting with respect to the SKF, the pre-event accelerometer baseline error and the KFB baseline error state, and Easting displacement results of all methods by setting $\boldsymbol{R}$ =128 (m^2), $\boldsymbol{q_a}$ = 10 (m^2/s^3), and C_{q_b} = 25.0.

B.1.2 The vertical component with a 5 cm co-seismic displacement

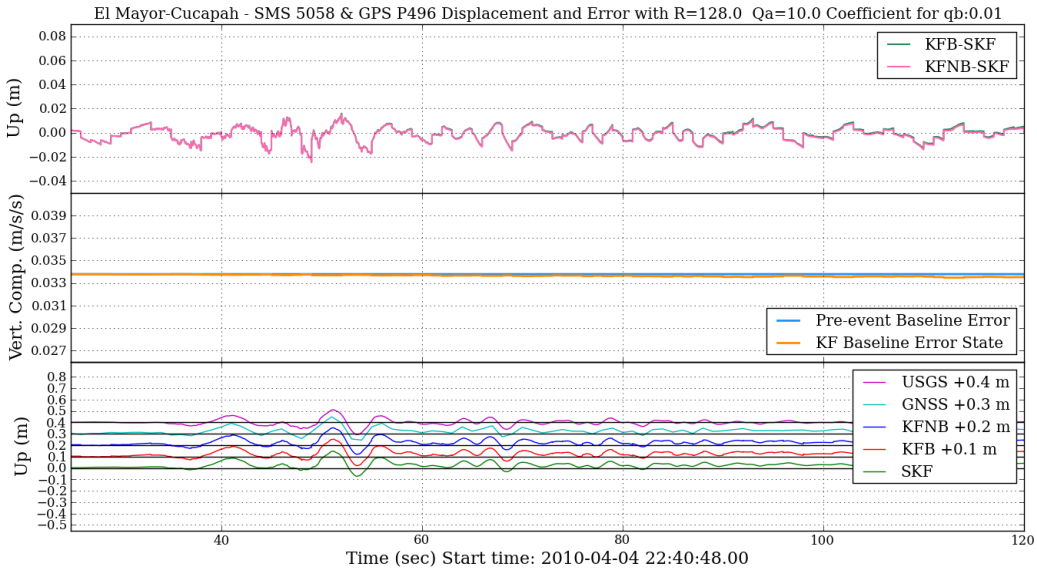

Figure B.10: The displacement error results of the KFNB and KFB in the vertical component with respect to the SKF, the pre-event accelerometer baseline error and the KFB baseline error state, and vertical displacement results of all methods by setting $\boldsymbol{R}$ =128 (m^2), $\boldsymbol{q_a}$ = 10 (m^2/s^3), and C_{qb} = 0.01.

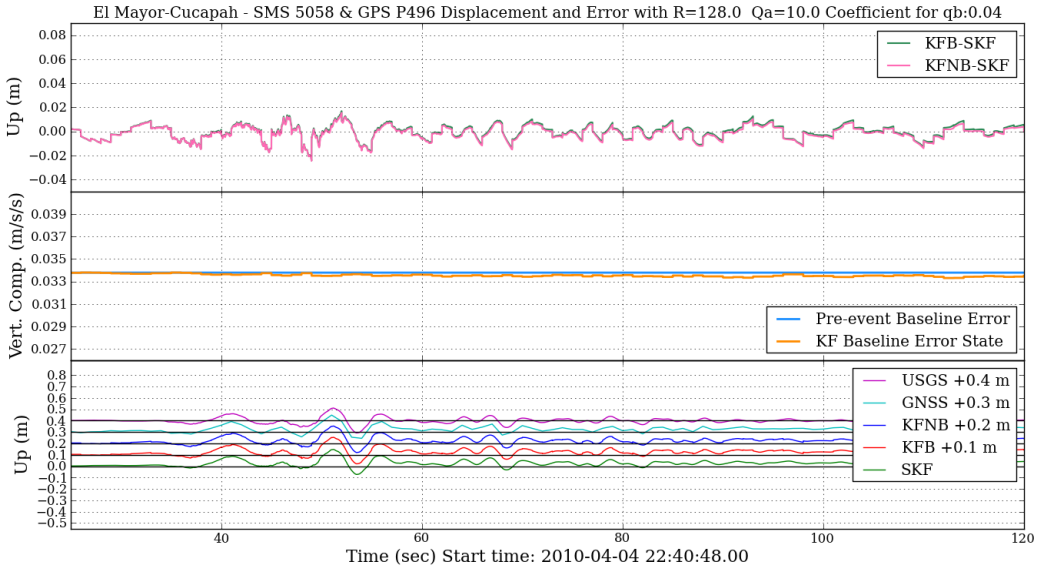

Figure B.11: The displacement error results of the KFNB and KFB in the vertical component with respect to the SKF, the pre-event accelerometer baseline error and the KFB baseline error state, and vertical displacement results of all methods by setting $\boldsymbol{R}$ =128 (m^2), $\boldsymbol{q_a}$ = 10 (m^2/s^3), and C_{qb} = 0.04.

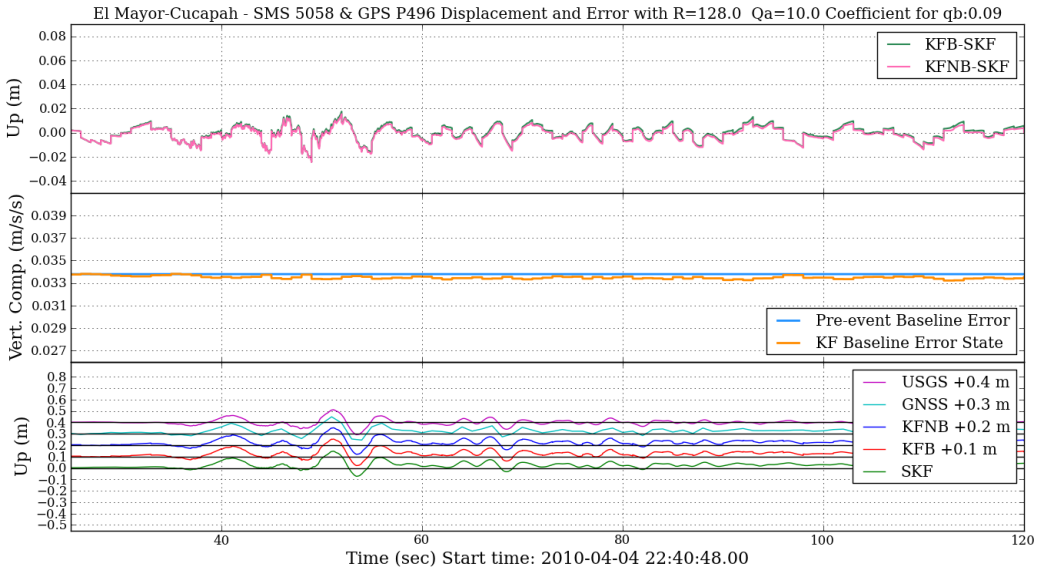

Figure B.12: The displacement error results of the KFNB and KFB in the vertical component with respect to the SKF, the pre-event accelerometer baseline error and the KFB baseline error state, and vertical displacement results of all methods by setting $\boldsymbol{R}$ =128 (m^2), $\boldsymbol{q_a}$ = 10 (m^2/s^3), and C_{q_b} = 0.09.

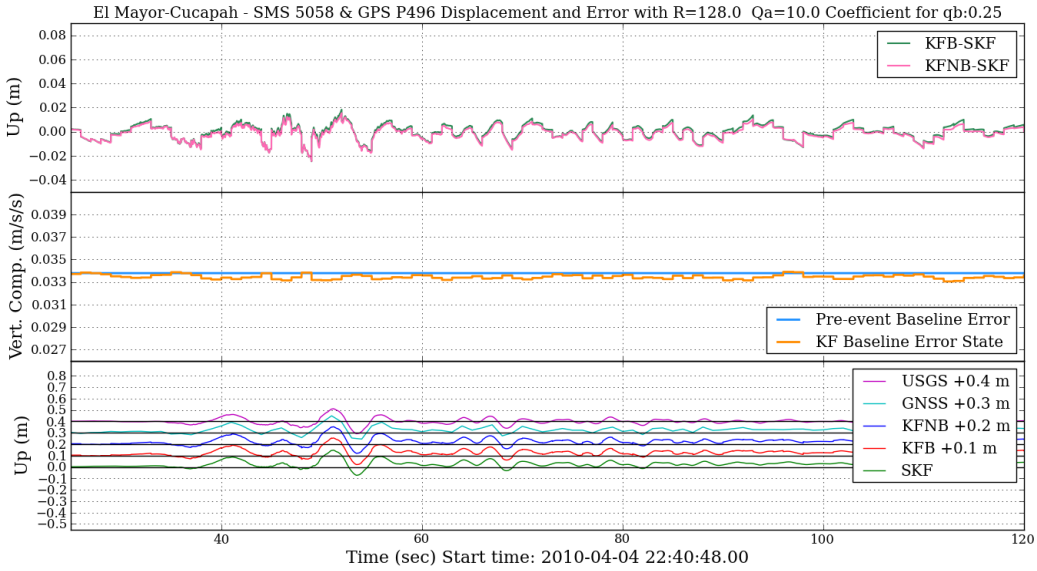

Figure B.13: The displacement error results of the KFNB and KFB in the vertical component with respect to the SKF, the pre-event accelerometer baseline error and the KFB baseline error state, and vertical displacement results of all methods by setting $\boldsymbol{R}$ =128 (m^2), $\boldsymbol{q_a}$ = 10 (m^2/s^3), and C_{q_b} = 0.25.

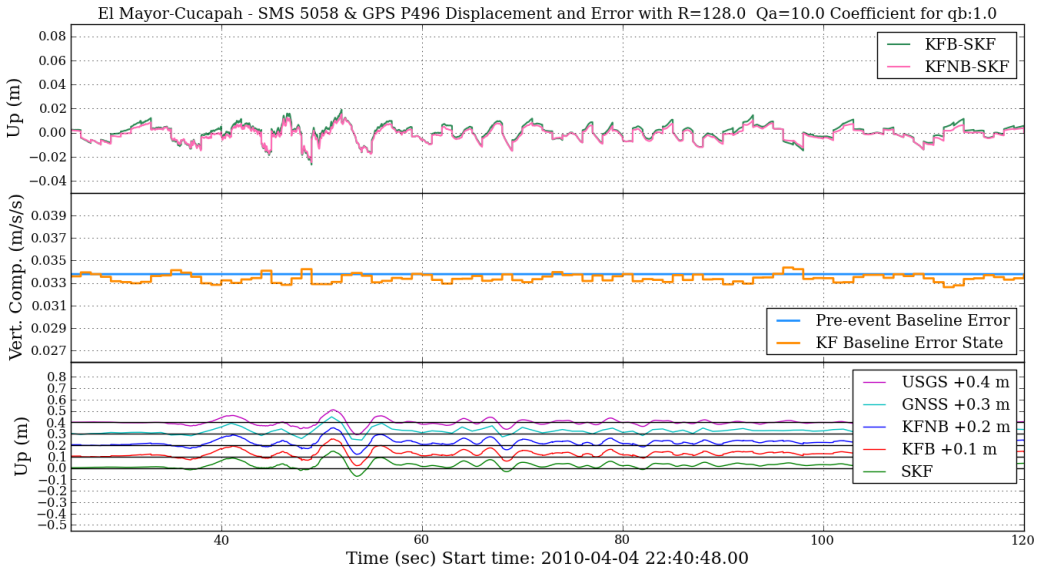

Figure B.14: The displacement error results of the KFNB and KFB in the vertical component with respect to the SKF, the pre-event accelerometer baseline error and the KFB baseline error state, and vertical displacement results of all methods by setting $\boldsymbol{R}$ =128 (m^2), $\boldsymbol{q_a}$ = 10 (m^2/s^3), and C_{q_b} = 1.0.

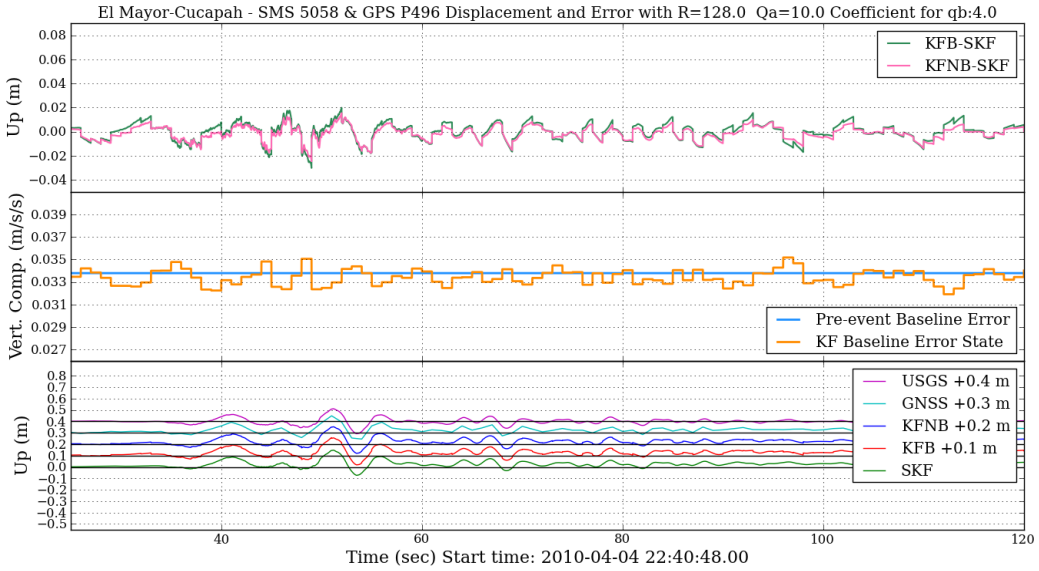

Figure B.15: The displacement error results of the KFNB and KFB in the vertical component with respect to the SKF, the pre-event accelerometer baseline error and the KFB baseline error state, and vertical displacement results of all methods by setting $\boldsymbol{R}$ =128 (m^2), $\boldsymbol{q_a}$ = 10 (m^2/s^3), and C_{q_b} = 4.0.

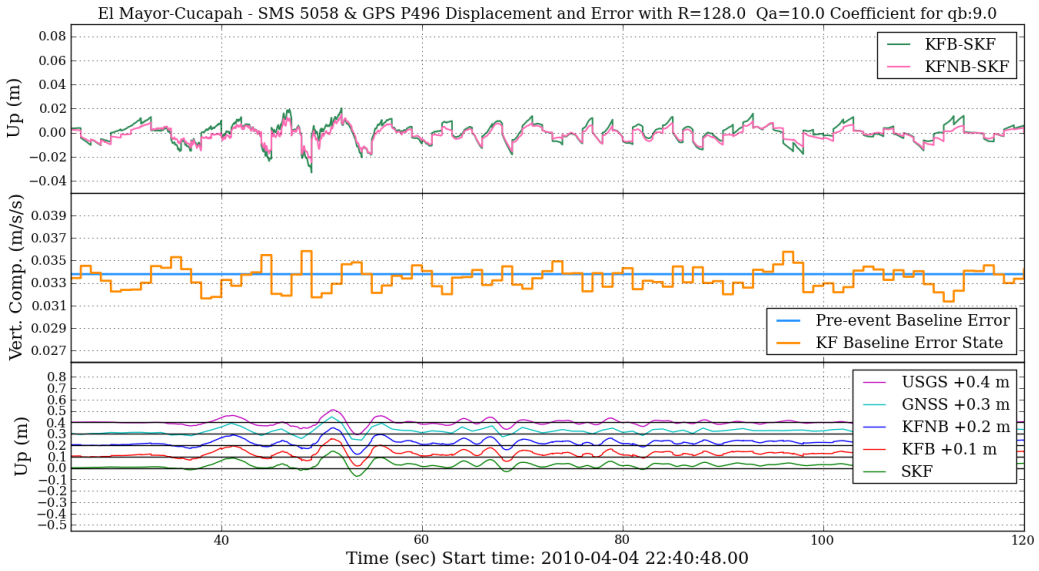

Figure B.16: The displacement error results of the KFNB and KFB in the vertical component with respect to the SKF, the pre-event accelerometer baseline error and the KFB baseline error state, and vertical displacement results of all methods by setting $\boldsymbol{R}$ =128 (m^2), $\boldsymbol{q_a}$ = 10 (m^2/s^3), and C_{q_b} = 9.0.

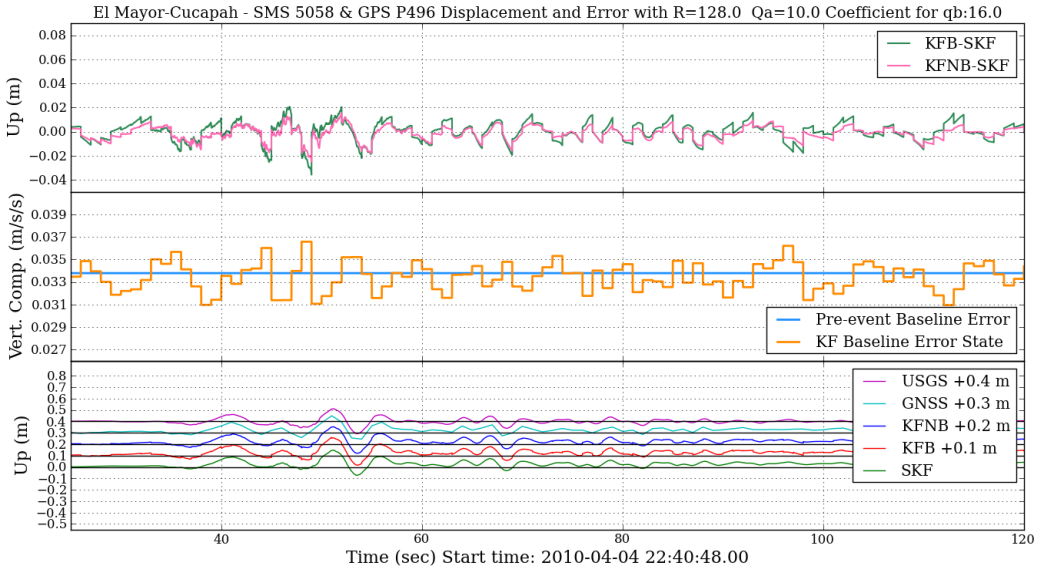

Figure B.17: The displacement error results of the KFNB and KFB in the vertical component with respect to the SKF, the pre-event accelerometer baseline error and the KFB baseline error state, and vertical displacement results of all methods by setting $\boldsymbol{R}$ =128 (m^2), $\boldsymbol{q_a}$ = 10 (m^2/s^3), and C_{q_b} = 16.0.

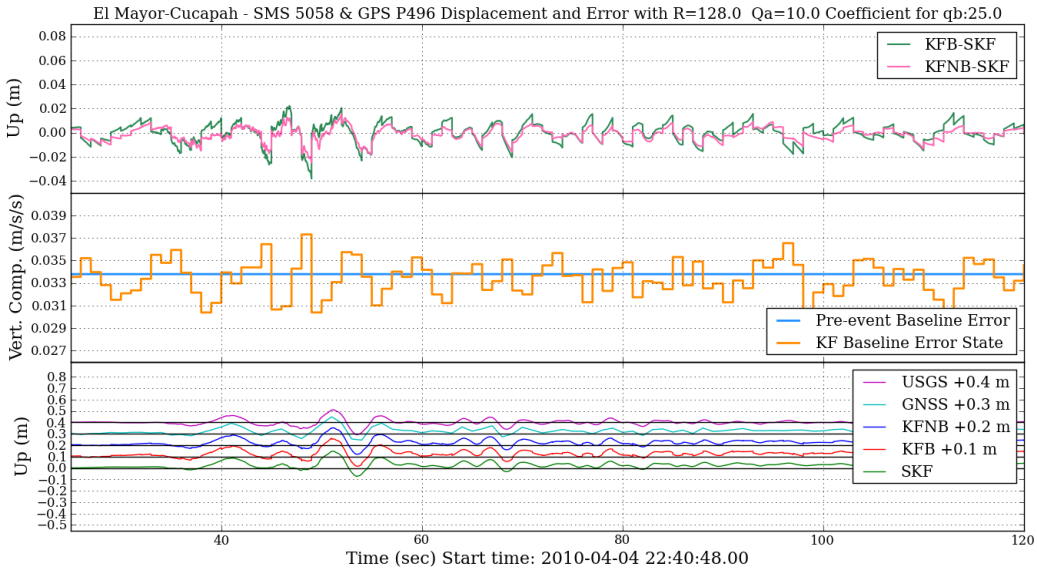

Figure B.18: The displacement error results of the KFNB and KFB in the vertical component with respect to the SKF, the pre-event accelerometer baseline error and the KFB baseline error state, and vertical displacement results of all methods by setting $\boldsymbol{R}$ =128 (m^2), $\boldsymbol{q_a}$ = 10 (m^2/s^3), and C_{q_b} = 25.0.

References

Atkins, C. & Ziebart, M., 2015. Effectiveness of observation-domain sidereal filtering for GPS precise point positioning. *GPS Solutions*, pp.1–12. Available at: http://dx.doi.org/10.1007/s10291-015-0473-1.

Bilich, A., Cassidy, J.F. & Larson, K.M., 2008. GPS Seismology: Application to the 2002 Mw 7.9 Denali Fault Earthquake. *Bulletin of the Seismological Society of America*, 98(2), pp.593–606.

Blewitt, G. et al., 2006. Rapid determination of earthquake magnitude using GPS for tsunami warning systems. *Geophysical Research Letters*, 33(11), pp.6–9. Available at: http://www.agu.org/pubs/crossref/2006/2006GL026145.shtml [Accessed July 23, 2012].

Bock, Y. et al., 1997. Southern California Permanent GPS Geodetic Array : Continuous measurements of regional crustal deformation between the 1992 Landers and 1994 Northridge earthquakes. *Journal of Geophysical Research*, 102(B8), pp.18013–18033.

Bock, Y., Melgar, D. & Crowell, B.W., 2011. Real-Time Strong-Motion Broadband Displacements from Collocated GPS and Accelerometers. *Bulletin of the Seismological Society of America*, 101(6), pp.2904–2925. Available at: http://www.bssaonline.org/cgi/doi/10.1785/0120110007 [Accessed December 9, 2011].

Bock, Y., Prawirodirdjo, L. & Melbourne, T.I., 2004. Detection of arbitrarily large dynamic ground motions with a dense high-rate GPS network. *Geophysical Research Letters*, 31, p.L06604.

Bock, Y., Prawirodirdjo, L. & Melbourne, T.I., 2004. Detection of arbitrarily large dynamic ground motions with a dense high-rate GPS network. *Geophysical Research Letters*, 31, p.L06604.

Bolt, B., 2006. *Earthquakes: 2006 Centennial Update* 5th ed., W. H. Freeman.

Boore, D.M. & Bommer, J.J., 2005. Processing of strong-motion accelerograms: needs, options and consequences. *Soil Dynamics and Earthquake Engineering*, 25(2), pp.93–115.

Boore, D.M., Stephens, C.D. & Joyner, W.B., 2002. Comments on baseline correction of digital strong-motion data: examples from the 1999 Hector Mine, California, earthquake. *Bulletin of the Seismological Society of America*, 92(4), pp.1543–1560.

Boroschek, R.L. & Legrand, D., 2006. Tilt Motion Effects on the Double-Time Integration of Linear Accelerometers: An Experimental Approach. *Bulletin of the Seismological Society of America*, 96(6), pp.2072–2089. Available at: http://www.bssaonline.org/cgi/doi/10.1785/0120050167 [Accessed August 18,

2011].

Brady, A.G., 2009. Strong-motion accelerographs: Early history. *Earthquake Engineering & Structural Dynamics*, 38(9), pp.1121–1134. Available at: http://dx.doi.org/10.1002/eqe.913.

Brown, R.G. & Hwang, P.Y.C., 2012. *Introduction to Random Signals and Applied Kalman Filtering with Matlab Exercises* 4th ed., John Wiley & Sons, Inc.

Chiang, K.W. et al., 2010. An ANN–RTS smoother scheme for accurate INS/GPS integrated attitude determination. *GPS Solutions*. Available at: http://dx.doi.org/10.1007/s10291-008-0113-0.

Chiu, H.-C., 1997. Stable Baseline Correction of Digital Strong-Motion Data. *Bulletin of the Seismological Society of America*, 87(4), pp.932–944.

Choi, K. et al., 2004. Modified sidereal filtering: Implications for high-rate GPS positioning. *Geophysical Research Letters*, 31(L22608), p.4.

Clinton, J.F., 2004. *Modern digital seismology-instrumentation, and small amplitude studues in the engineering world*. California Institute of Technology.

Converse, A.M. & Brady, A.G., 1992. BAP: Basic Strong-Motion Accelerogram Processing Software Report; Version 1.0. , p.180.

Douglas, J. & Boore, D.M., 2010. High-frequency filtering of strong-motion records. *Bulletin of Earthquake Engineering*, 9(2), pp.395–409. Available at: http://link.springer.com/10.1007/s10518-010-9208-4 [Accessed August 23, 2013].

Einde, L. Vanden et al., 2004. Development of the George E. Brown Jr. Network for Earthquake Engineering Simulation (NEES) Large High Performance Outdoor Shake Table at the University of California, San Diego. In *13th World Conference on Earthquake Engineering*. Vancouver, B.C., Canada.

Emore, G.L. et al., 2007. Recovering Seismic Displacements through Combined Use of 1-Hz GPS and Strong-Motion Accelerometers. *Bulletin of the Seismological Society of America*, 97(2), p.357.

Farrell, J. & Barth, M., 1999. *The global positioning system and inertial navigation*, New York, N.Y.: McGraw-Hill.

Farrell, J.A., 2008. *Aided Navigation: GPS with High Rate Sensors* 1st ed., McGraw-Hill Professional.

Fraser, D.C. & Potter, J.E., 1969. The optimum linear smoother as a combination of two optimum linear filters. *Automatic Control, IEEE Transactions*, 14(4), pp.387–390.

Gao, Y. & Chen, K., 2004. Performance Analysis of Precise Point Positioning Using Real-Time Orbit and Clock Products. *Journal of Global Positioning Systems*, 3(1-2), pp.95–100.

Gelb, A., 1974. *Applied Optimal Estimation*, The MIT Press.

Geng, J., Bock, Y., et al., 2013. A new seismogeodetic approach applied to GPS and accelerometer observations of the 2012 Brawley seismic swarm: Implications for earthquake early warning. *Geochemistry, Geophysics, Geosystems*, 14(7).

Geng, J., Melgar, D., et al., 2013. Recovering coseismic point ground tilts from collocated high-rate GPS and accelerometers. *Geophysical Research Letters*, 40(19), pp.5095–5100. Available at: http://doi.wiley.com/10.1002/grl.51001 [Accessed July 22, 2014].

Genrich, J.F. & Bock, Y., 2006. Instantaneous geodetic positioning with 10–50 Hz GPS measurements: Noise characteristics and implications for monitoring networks. *Journal of Geophysical Research*, 111(B3). Available at: http://www.agu.org/pubs/crossref/2006/2005JB003617.shtml [Accessed July 27, 2012].

Genrich, J.F. & Bock, Y., 1992. Rapid resolution of crustal motion at short ranges with the global positioning system. *Journal of Geophysical Research*, 97(B3), pp.3261–3269.

Gleason, S. & Gebre-Egziabher, D., 2009. *GNSS Applications and Methods*, Artech House Publishers.

GNS Science, 2011a. GeoNet – Home. Available at: http://www.geonet.org.nz/ [Accessed November 28, 2011].

GNS Science, 2011b. GeoNet – Strong Motion Data. Available at: http://www.geonet.org.nz/resources/basic-data/strong-motion-data/ [Accessed November 28, 2011].

Graizer, V.M., 2005. Effect of tilt on strong motion data processing. *Soil Dynamics and Earthquake Engineering*, 25(3), pp.197–204.

Grewal, M.S., Weill, L.R. & Andrews, A.P., 2001. *Global Positioning Systems, Inertial Navigation, and Integration* 1st ed., Wiley-Interscience.

Grewal, M.S., Weill, L.R. & Andrews, A.P., 2007. *Global Positioning Systems, Inertial Navigation, and Integration* 2nd ed., Wiley-Interscience.

Groves, P.D., 2013. *Principles of GNSS, Inertial, and Multisensor Integrated Navigation Systems* 2nd ed., London, UK: Artech House.

Gutenberg, B. & Richter, C.F., 1956. Earthquake Magnitude, Intensity, Energy, and Acceleration. *Bulleitn of the Seismological Society of America*, 1956(46), p.105.

Gutenberg, B. & Richter, C.F., 1955. Magnitude and Energy of Earthquakes. *Nature*, 176, p.795.

Hammond, W.C., Bürgmann, R. & Heaton, T., 2010. *The scientific value of high-rate, low-latency GPS data*, Nevada, USA: Nevada Geodetic Laboratory.

Hanks, T.C. & Kanamori, H., 1979. A moment magnitude scale. *Journal of Geophysical Research*, 84, pp.2348–2350.

Havskov, J. & Alguacil, G., 2010. *Instrumentation in Earthquake Seismology*, Available at: http://www.springerlink.com/index/10.1007/s00024-009-0538-6.

Howell, B.F., 1990. *An Introduction to Seismological Research: History and Development*, Cambridge University Press. Available at: http://books.google.co.uk/books?id=4e1Cc-nqcGoC.

Javelaud, E.H., Ohmachi, T. & Inoue, S., 2011. A Quantitative Approach for Estimating Coseismic Displacements in the Near Field from Strong-Motion Accelerographs. *Bulletin of the Seismological Society of America*, 101(3), pp.1182–1198. Available at: http://www.bssaonline.org/cgi/doi/10.1785/0120100146 [Accessed July 30, 2011].

Ji, C. et al., 2004. Slip history of the 2003 San Simeon earthquake constrained by combining 1-Hz GPS, strong motion, and teleseismic data. *Geophysical Research Letters*, 31, p.17608.

Kalman, R.E., 1960. A New Approach to Linear Filtering and Prediction Problems. *Transactions of the ASME–Journal of Basic Engineering*, 82(Series D), pp.35–45.

Kanamori, H., 1978. Quantification of Earthquakes. *Nature*, 271(2), pp.411–414.

Kaplan, E.D., 2005. *Understanding GPS: Principles and Applications* 2nd ed., Artech House Publishers.

Kouba, J., 2003. Measuring seismic waves induced by large earthquakes with GPS. *Studia Geophysica et Geodaetica*, 47 (4), pp.741–755.

Lam, N. & Wilson, J., 2004. Displacement Modelling of Intraplate Earthquakes. *ISET Journal of Earthquake Technology*, 41(439), pp.15–52.

Langbein, J. & Bock, Y., 2004. High-rate real-time GPS network at Parkfield: Utility for detecting fault slip and seismic displacements. *Geophys. Res. Lett*, 31, p.15.

Larson, K., 2007. *Final Technical Report: The Tokachi Oki earthquake: evaluation of GPS as a strong motion instrument*, University of Colorado.

Larson, K.M., 1993. Application of the Global Positioning System to Crustal Deformation Measurements 3. Result From the Southern California Borderlands. *J. Geophys. Res.*, 98(B12), pp.21713–21726. Available at: http://dx.doi.org/10.1029/92JB02116.

Larson, K.M., 2009. GPS seismology. *Journal of Geodesy*, 83(3), pp.227–233.

Larson, K.M. & Agnew, D.C., 1991. Application of the Global Positioning System to Crustal Deformation Measurement 1. Precision and Accuracy. *J. Geophys. Res.*, 96(B10), pp.16547–16565. Available at: http://dx.doi.org/10.1029/91JB01275.

Larson, K.M., Bodin, P. & Gomberg, J., 2003. Using 1-Hz GPS data to measure deformations caused by the Denali fault earthquake. *Science*, 300(5624), p.1421.

Larson, K.M., Webb, F.H. & Agnew, D.C., 1991. Application of the Global Positioning

System to Crustal Deformation Measurement 2. The Influence of Errors in Orbit Determination Networks. *J. Geophys. Res.*, 96(B10), pp.16567–16584. Available at: http://dx.doi.org/10.1029/91JB01276.

Lewis, F.L., Xie, L. & Popa, D., 2007. *Optimal and Robust Estimation: With an Introduction to Stochastic Control Theory* 2nd ed., CRC Press.

Li, C.-Y., 2010. *Skyscrapers Watch Using an INS/GPS Integrated POS Grid*. National Cheng Kung University.

Li, C.-Y., 2009. Skyscrapers Watch Using an INS/GPS Integrated POS Grid. *ION GNSS 22nd International Technical Meeting*.

Li, X. et al., 2006. Full-scale structural monitoring using an integrated GPS and accelerometer system. *GPS Solutions*, 10 (4), pp.233–247.

Li, X. et al., 2013. Real-time high-rate co-seismic displacement from ambiguity-fixed precise point positioning: Application to earthquake early warning. *Geophysical Research Letters*, 40, pp.295–300.

Luco, J.E. et al., 2011. Experimental study of the dynamic interaction between the foundation of the NEES/UCSD Shake Table and the surrounding soil: Reaction block response. *Soil Dynamics and Earthquake Engineering*, 31(7), pp.954–973. Available at: http://linkinghub.elsevier.com/retrieve/pii/S0267726111000984 [Accessed September 15, 2014].

Maybeck, P.S., 1982. *Stochastic Models, Estimation, and Control*, Elsevier. Available at: http://www.sciencedirect.com/science/article/pii/S0076539208632129 [Accessed September 27, 2014].

Misra, P. & Enge, P., 2010. *Global Positioning System: Signals, Measurements and Performance* 2nd ed., Ganga-Jamuna Pr.

Mostov, K.S., Soloviev, A.A. & Koo, T.J., 1997. Initial Attitude Determination and Correction of Gyro-Free INS angular Orientation on the Basis of GPS Linear Navigation Parameters. In *Intelligent Transportation System IEEE Conference*. pp. 1034–1039.

National Research Institute for Earth Science and Disaster Prevention, 2011. Digital Strong-Motion Seismograph Network - KiK-net. Available at: http://www.kik.bosai.go.jp/ [Accessed November 28, 2011].

Niu, J. & Xu, C., 2014. Real-Time Assessment of the Broadband Coseismic Deformation of the 2011 Tohoku-Oki Earthquake Using an Adaptive Kalman Filter. *Seismological Research Letters*, 85(4), pp.836–843. Available at: http://srl.geoscienceworld.org/cgi/doi/10.1785/0220130178 [Accessed July 23, 2014].

Ozcelik, O., 2008. *A Mechanics-based Virtual Model of NEES-UCSD Shake Table: Theoretical Development and Experimental Validation*. University of California,

San Diego. Available at: https://books.google.co.uk/books?id=UAbEAZFqyBcC.

Ozcelik, O., Luco, J.E., Conte, J.P., et al., 2008. Experimental characterization , modeling and identification of the NEES-UCSD shake table mechanical system. *Earthquake Engng Struct. Dyn.*, 37(September 2007), pp.243–264.

Ozcelik, O., Luco, J.E. & Conte, J.P., 2008. Identification of the Mechanical Subsystem of the NEES-UCSD Shake Table by a Least-Squares Approach. *Journal of Engineering Mechanics*, (January), pp.23–34.

Passmore, P. et al., 2014. Integrated SeismoGeodetic Systsem with High-Resolution, Real-Time GNSS and Accelerometer Observation For Earthquake Early Warning Application. In *AGU 2014 Fall Meeting Abstracts*.

Rauch, H.E., Striebel, C.T. & Tung, F., 1965. Maximum likelihood estimates of linear dynamic systems. *AIAA Journal*, 3(8), pp.1445–1450. Available at: http://dx.doi.org/10.2514/3.3166.

Richter, C.F., 1935. An instrumental earthquake magnitude scale. *Bulletin of the Seismological Society of America*, 25, pp.1–32.

Rios, J.A. & White, E., 2002. Fusion Filter Algorithm Enhancements For a MEMS GPS / IMU. In *ION GPS 2002, National Technical Meeting of The Institute of Navigation*.

Roberts, G.W., Meng, X. & Dodson, A.H., 2004. Integrating a Global Positioning System and Accelerometers to Monitor the Deflection of Bridges. *Journal of Surveying Engineering*, 130(2), pp.65–72. Available at: http://link.aip.org/link/?QSU/130/65/1.

Ruge, A.C. & McComb, H.E., 1937. Tests of Earthquake Accelerometers on a Shaking Table. *Bulletin of the Seismological Society of America*, (27), pp.325–329.

Sadeghi, M. & Gholami, M., 2008. Time synchronizing signal by GPS satellites. *WSEAS Transactions on Communications*, 7(5), pp.521–530.

Shakal, A.F., Huang, M.J. & Graizer, V.M., 2003. Strong-Motion Data Processing. In W. H. Lee et al., eds. *International Handbook of Earthquake and Engineering Seismology Part B*. Academic Press for International Association of Seismology and Pysics of the Earth's Interior, pp. 967–981.

Shearer, P.M., 2009. *Introduction to Seismology*, Cambridge: Cambridge University Press. Available at: http://ebooks.cambridge.org/ref/id/CBO9780511841552.

Shin, E.-H., 2005. *Estimation Techniques for Low-Cost Inertial Navigation*. Calgary, Canada: University of Calgary.

Singhal, T., Harit, A. & Vishwakarma, D.N., 2012. Kalman Filter Implementation on an Accelerometer sensor data for three state estimation of a dynamic system. *International Journal of Research in Engineering and Technology*, 1(6), pp.330–334.

Smyth, A. & Wu, M., 2006. Multi-rate Kalman filtering for the data fusion of displacement and acceleration response measurements in dynamic system monitoring. *Mechanical systems and signal processing*, 21(2), pp.706–723.

Stein, S. & Wysession, M., 2003. *An Introduction to Seismology, Earthquakes, and Earth Structure*,

Takasu, T., 2006. High-rate precise point positioning: observation of crustal deformation by using 1-Hz GPS data. In *GPS/ GNSS Symposium 2006, Tokyo University of Marine Science and Technology*. Tokyo.

TEK REF, 2015. About REF TEK. Available at: http://www.reftek.com/about.htm.

Thoen, B.K., 2004. *469D Seismic Digital Control Software*, MTS Corporation.

Thoen, B.K. & Laplace, P.N., 2004. Offline Tuning of Shaking Tables. In *13th World Conference on Earthquake Engineering*. Vancouver, B.C., Canada.

Towhata, I., 2008. *Geotechnical Earthquake Engineering*, Springer-Verlag. Available at: http://books.google.co.uk/books?id=wRxhiHf-ieIC.

Trifunac, M.D., 1971. Zero Baseline Correction of Strong-Motion Accelerogranis. *Bulletin of the Seismological Society of America*, 61(5), pp.1201–1211.

Trifunac, M.D. & Lee, V.W., 1974. A Note of the Accuracy of Computed Ground Displacements from Strong-Motion Accelerogram. *Bulletin of the Seismological Society of America*, 64(4), pp.1209–1219.

Trifunac, M.D. & Todorovska, M.I., 2001. Evolution of accelerographs, data processing, strong motion arrays and amplitude and spatial resolution in recording strong earthquake motion. *Soil Dynamics and Earthquake Engineering*, 21(6), pp.537–555.

Trifunac, M.D., Udwadia, F.E. & Brady, A.G., 1973. Analysis of Errors in Digitized Strong-Motion Accelerograms. *Bulletin of the Seismological Society of America*, 63(1), pp.157–187.

Tu, R. et al., 2013. A new algorithm for tight integration of real-time GPS and strong-motion records, demonstrated on simulated, experimental, and real seismic data. *Journal of Seismology*, 18(1), pp.151–161. Available at: http://link.springer.com/10.1007/s10950-013-9408-x [Accessed September 13, 2014].

Tu, R. & Chen, K., 2014. Tightly Integrated Processing of High-Rate GPS and Accelerometer Observations by Real-Time Estimation of Transient Baseline Shifts. *Journal of Navigation*, 67(05), pp.869–880. Available at: http://www.journals.cambridge.org/abstract_S0373463314000150 [Accessed September 12, 2014].

United States Geological Survey, 2011. U.S. Geological Survey - National Strong-Motion Project. Available at: http://nsmp.wr.usgs.gov/ [Accessed November 28,

2011].

United States Geological Survey, 2010. *USGS Poster of the Baja, Mexico Earthquake of 04 April 2010 - Magnitude 7.2*, Available at: http://earthquake.usgs.gov/earthquakes/eqarchives/poster/2010/20100404.php.

USGS NSMP Data Center, 2012. USGS NSMP Data processing. , 6(Vol 6). Available at: http://nsmp.wr.usgs.gov/processing.html#notes.

Vallina, A.U., 1999. *Principles of Seismology*, Cambridge University Press. Available at: http://books.google.co.uk/books?id=UoXQnDt6MooC.

Vigny, C. et al., 2005. Insight into the 2004 Sumatra-Andaman earthquake from GPS measurements in southeast Asia. *Nature*, 436(7048), pp.201–206.

Welch, G. & Bishop, G., 1995. *An Introduction to the Kalman Filter*,

Wielandt, E., 2002. Seismometry. In W. H. Lee et al., eds. *International Handbook of Earthquake and Engineering Seismology Part A*. Academic Press for International Association of Seismology and Pysics of the Earth's Interior, pp. 283–304.

Wright, T.J. et al., 2012. Real-time, reliable magnitudes for large earthquakes from 1 Hz GPS Precise Point Positioning: the 2011 Tohoku-Oki (Japan) earthquake. *Geophysical Research Letters*, 39. Available at: http://www.agu.org/pubs/crossref/pip/2012GL051894.shtml [Accessed August 13, 2012].

Wu, Y.-M. & Wu, C.-F., 2007. Approximate recovery of coseismic deformation from Taiwan strong-motion records. *Journal of Seismology*, 11(2), pp.159–170. Available at: http://www.springerlink.com/index/10.1007/s10950-006-9043-x [Accessed August 23, 2011].

Yeats, R., 2012. *Active Faults of the World*, Cambridge: Cambridge University Press. Available at: http://ebooks.cambridge.org/ref/id/CBO9781139035644.

Zimakov, L. et al., 2014. Combination of High Rate, Real - Time GNSS and Accelerometer Observations and Rapid Seismic Event Notification for Earthquake Early Warning and Volcano Monitoring with a Focus on the Pacific Rim. In *AGU 2014 Fall Meeting Abstracts*.

Zumberge, J.F. et al., 1997. Precise point positioning for the efficient and robust analysis of GPS data from large networks. *Journal of Geophysical Research-Solid Earth*, 102(B3).